Nanobiotechnology in Energy, Environment, and Electronics

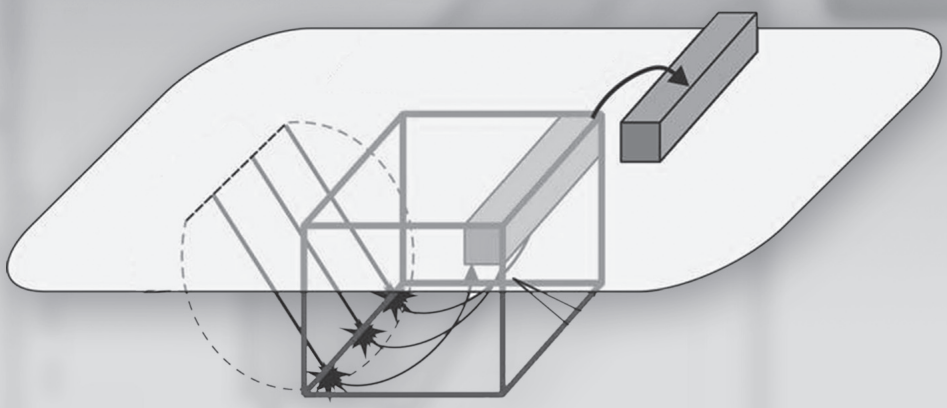

Pan Stanford Series on Nanobiotechnology

Series Editor
Claudio Nicolini

Titles in the Series

Vol. 1

Nanobiotechnology and Nanobiosciences
Claudio Nicolini
2008
978-981-4241-38-0 (Hardcover)
978-981-4241-39-7 (eBook)

Vol. 2

Functional Proteomics and Nanotechnology-Based Microarrays
Claudio Nicolini and Joshua LaBaer, eds.
2010
978-981-4267-76-2 (Hardcover)
978-981-4267-77-9 (eBook)

Vol. 3

Synchrotron Radiation and Structural Proteomics
Eugenia Pechkova and Christian Riekel, eds.
2011
978-981-4267-38-0 (Hardcover)
978-981-4267-93-9 (eBook)

Vol. 4

Nanobiotechnology in Energy, Environment, and Electronics: Methods and Applications
Claudio Nicolini, ed.
2015
978-981-4463-96-6 (Hardcover)
978-981-4463-97-3 (eBook)

Nanobiotechnology in Energy, Environment, and Electronics

Methods and Applications

edited by

Claudio Nicolini

CRC Press
Taylor & Francis Group
6000 Broken Sound Parkway NW, Suite 300
Boca Raton, FL 33487-2742

Version Date: 20150128

International Standard Book Number-13: 978-981-4463-97-3 (eBook - PDF)

Visit the Taylor & Francis Web site at
http://www.taylorandfrancis.com

and the CRC Press Web site at
http://www.crcpress.com

© 2015 by Taylor & Francis Group, LLC

To the memory of Dr. Alexey A. Peshkov, my very dear friend, outstanding Russian scientist, and correspondent member of the Russian Academy of Sciences, for his long scientific activity towards new megatechnologies—namely the development of mineral deposits by the technogenic initiation of directed geological processes—that a premature departure has suddenly terminated, leaving, however, to us his important scientific contribution witnessed also in this volume.

Contents

Introduction: Present Challenges and Future Solutions via Nanotechnology for Electronics, Environment and Energy

Claudio Nicolini

Fondazione Nanoworld Institute ELBA Nicolini, Largo Redaelli 7, 24020, Pradalunga, Bergamo, Italy

claudio.nicolini@unige.it

Oil fuels the modern world, but oil is a finite resource. It brought great changes to economies and lifestyles in less than 200 years and nothing else to date equals the enormous impact which the use of oil has had on so many people in so many ways around the world. The critical question is, however, "When is or was the maximum daily amount of world oil production at its peak?" After that, oil is going to become an irreversibly declining resource facing an increasing demand, which will not be met. The world passed its peak of rate of oil discoveries in the 1960s, and it seems that the peak of world oil production will then be reached by 2020, and possibly within the next decade (Campbell, 1997; Campbell and Laherrere, 1998; Ivanhoe, 1995).

What are then going to be realistic alternative energy sources for humanity among the existing renewable or non-renewable one (Table 1)?

Fusion involves the fusion of either of two hydrogen isotopes, deuterium or tritium. Deuterium exists in great quantities in ordinary water, and from that perspective fusion is theoretically an almost infinitely renewable energy resource. This is the holy grail of ultimate energy. Fusion is the energy that powers the Sun, and that is the problem. The temperature of the Sun ranges from about

10,000 degrees Celsius on its surface to an estimated 15–18 million degree Celsius in the interior where fusion takes place. Containing such a temperature on Earth in a sustainable way and harnessing the heat to somehow produce power has so far escaped our search. However, even if commercial fusion will be accomplished, the end product again is likely to be electricity, and not a replacement for fuel sources such as oil and gas.

Table 1 Alternative energy sources

Non-renewable	Renewable
Oil sands, heavy oil	Wood/other biomass
Coal	Hydropower
Shale oil	Solar energy
Gas hydrates	Wind energy
Nuclear fission	Wave energy
Geothermal	Tidal power
	Fusion
	Ocean thermal energy conversion

Questions are sometimes raised as to using **hydrogen and fuel cells** for fuel sources. Neither is a primary energy source. Hydrogen must be obtained by using some other energy source. Usually it is obtained by the electrolysis of water, or by breaking down natural gas (methane CH_4). Hydrogen is highly explosive, and to be contained and carried in significantly usable amounts, it has to be compressed to hundreds of pounds per square inch. Hydrogen is not easy to handle, and it is not a replacement for pouring 10 gallons of gasoline into an automobile tank. Fuel cells have to be fuelled; most use hydrogen or some derivative of oil. Fuel cells are not a source of energy in themselves.

Oil appears to be a unique energy source that up to now has no complete replacement in all its varied end uses. British scientist Sir Crispin Tickell concludes, "…we have done remarkably little to reduce our dependence on a fuel [oil] which is a limited resource, and for which there is *no comprehensive substitute in prospect*." Coming to realize that oil is finite, any and all suggestions of means to replace oil are obviously welcomed, but so far only cheerful myths are enthusiastically embraced. These include: that there are two trillion

barrels of economically recoverable oil in the Colorado Plateau oil shales; that dams and their reservoirs are a source of indefinitely renewable energy and that they are environmentally benign; that solar, wind, geothermal and hydro-electric power can supply the electrical needs, from the Arctic to the tropics, of the Earth's **over six billion people** (likely to further grow in the near future); that coal, oil from oil sands, and biofuels can replace the 72 million barrels of oil the world now uses daily; and that somehow electricity produced from various alternative energy sources can readily provide the great mobility which oil now gives to the more than 600 million vehicles worldwide. Regrettably, **none** of these cheerful myths appear up to now to be valid, including the mega-myth which represents the most popular public placebo that "The scientists will think of something" as I did witnessed myself few months ago at Orlando during a short visit to Disneyworld. The energy spectrum from burning wood to fusion that fuels the Sun (Table 1) is now well known. If there is some major exotic energy source beyond what is here listed, we have no evidence of it and the reality appears to be that the world is rapidly running out of a resource (oil) that in many ways appears irreplaceable. We have been living on a great fossil fuel inheritance accumulated during more than 500 million years that humanity has incredibly exhausted in the last period in less than 200 years. We will soon exhaust this capital, and we will have to go to work to try to live on current energy income. It will not be a simple easy transition as pointed out in a remarkably perceptive book written by Darwin in 1952, where were described historic changes in the human condition, calling them "revolutions." Darwin wrote that there is one more revolution clearly in sight: "The fifth revolution will come when we have spent the stores of coal and oil that have been accumulating in the earth during hundreds of millions of years…it is obvious that there will be a very great difference in ways of life… ."

The present energy situation is exemplified in Figs. 1 and 2 from what has been occurring in the United States in the recent time.

Similarly, the **natural disasters** have been increasing in number and frequency in the last few years permitted by the wrong myth that humanity could do without the Kyoto agreement attempting to control the devastating **carbon dioxide** effects. As in the preservation of oil reserve, the humanity and its governments have

failed also in the protection of natural environment. In summary, the result could become very shortly a great change in economies, social structures and lifestyles, and the opportunities for science and technology to make a difference are becoming constantly narrower. And this despite the striking development in **electronics at the nanoscale**, through the construction of new effective nanosensors and nanoactuators.

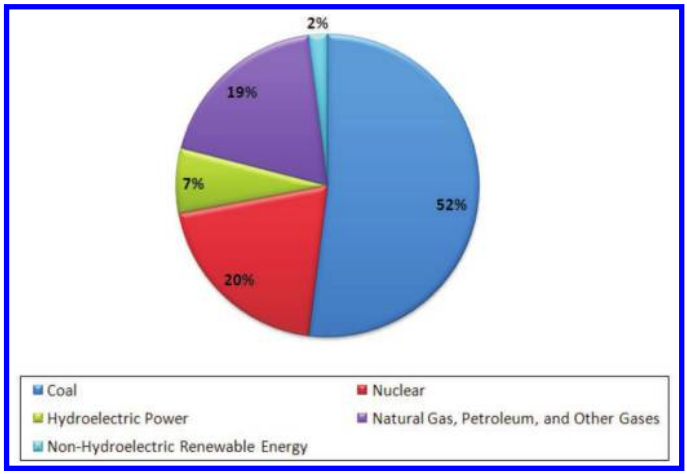

Figure 1 US electricity net generation by source for 2000 (EIA Annual Energy Review) *Source*: International Energy Agency.

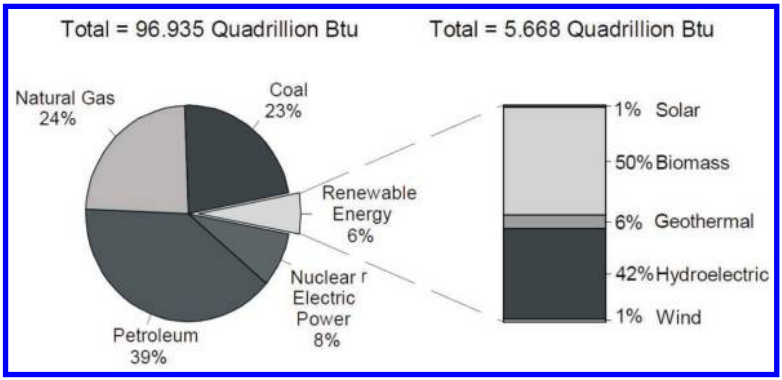

Figure 2 Renewable energy in proportion to total US energy supply. *Source*: Energy Information Administration (EIA).

It is, therefore, essential to find concrete solutions to the growing problems in all sectors of the economy, such as energy,

environment and electronics, and worldwide the situation could be overcome only by a wide internationalisation involving the leading countries in economic, military and financial terms, namely the **Russian Federation**, the **United States of America and Europe**. Furthermore, only at the nanoscale, we can hope to embark on such undertaking with some degree of success. It is the right moment for the United States and Russia to unite with Europe their forces and to concentrate all the possible resources to solve the dramatic problems affecting the entire world as those illustrated above, involving resources and facilities from leading multinational companies, as well manpower coming from citizens of the above three large countries which should change their priorities and return to science and technology as for the past full of long stories of successes. I know this will work for the entire world's benefit and for my personal direct experience having passed my entire life in these three large communities extremely productive in R&D. Attempt to do this at the national scale with large recruitment from underdeveloped countries is bound to failure because the magnitude of the crisis induced by the derivatives has far lasting devastating effects (continuously coming to light) and because the magnitude of the technological problems long time underestimated is unmatchable at any single isolated nation scale. The scheme based on multinational companies, that in the past was able to work for Italy in Bioelectronics with Polo Nazionale Bioelettronica and CIREF (both centred around Italian-based multinational companies as ABB, Montedison, FIAT, ST Microelectronics, Olivetti, Farmitalia, Elsag-Bailey), may still be valid but this time only if the above named three large countries, frequently in the past on opposite sites, find means to cooperate in order to achieve the required critical mass at the world scale. An institution (Fondazione EL.B.A.) indeed in the past was born and did grow with participation of organizations at the crossing of Europe, Russia and the United States and constitute the proof of principle that something similar (Nanoworld Institute) could become again the triggering factor between Europe, Russia and the United States. In the past, the Biochip Project initiated by President Gorbachev through Academician Velikov (USSR) and President Craxi through myself (Italy) did work and I do not see why should not work now, despite the larger scale and the more ambitious objectives. I hope that the time has passed for science to be at the service of arms race

among between the United States and Russia, and the reduction of nuclear arsenals and waste being pursued in START (STrategic Arms Reduction Treaty) should further aim not only to avoid their falling in wrong hands and to increase global security (as suggested by President Obama in the 2013 State of the Union), but also to transfer all these military resources in **joint civilian project**. Recently in an open debate with President Putin organized by Russian television I raised via the Internet a question (subsequently acknowledged) about the opportunity of final disarmament within the "Measures to Further Reductions and Limitation of Strategic Offensive Arms" treaty between Russia and the United States such that the enormous resources spent could be used for the development of joint projects in nanoscience and nanotechnology for energy, health, electronics and environment.

Cancer at the molecular scale is strongly interlinked to differentiation, ageing and proliferation, but also to ecology, and solving it we will solve major correlated problems in life sciences. Energy is strongly interlinked with power generation, automation and environment, while similarly is happening (at the nanoscale) for really intelligent hardware, being strongly interlinked to communication, defence and environment. Indeed the risk of upcoming ecological disasters, including global warming, can be reduced or avoided with the development of new energy sources nanotechnology-based from sun, wind and hydrogen. The far-reaching effects will be beneficial for the entire humanity and for the survival and growth of earth. Last but not least is the objective to bring back the prestige of science among young people to correct the economical disasters caused by bankers and financial institutions.

References

Campbell C. *The Coming Oil Crisis*. Independent Publishers Group, April 1, 2004. ISBN 0-906522-11-0 (first edition 1997).

Campbell C, Laherrère J. *The End of Cheap Oil*. Scientific American, March 1998.

Darwin, CG. *The Next Million Years*, 209 pages. London: Rupert Hart-Davis, 1952.

Ivanhoe LE. Future world oil supplies: there is a finite limit. *World Oil*, October 1995, pp. 77–88.

Part A

Methods

Chapter 1

Influence of Chromosome Translocation on Yeast Life Span: Implications for Long-Term Industrial Biofermentation

Jason Sims,[a] Dmitri Nikitin,[a,b] and Carlo V. Bruschi[a]

[a]*International Centre for Genetic Engineering and Biotechnology, Area Science Park, Padriciano 99, I-34149 Trieste, Italy*
[b]*Institute of Biochemistry and Physiology of Microorganisms, RAS, Nauki Av., 5, Pushchino, Russia*

bruschi@icgeb.org

Ageing as always been part of the biological life and a topic that we understand very little of. In particular, ageing in microbial cultures undergoing long-term industrial fermentation is a very important factor determining the overall efficiency and in final analysis the economic outcome of the bio-production process. On the other hand, gross chromosomal rearrangements (GCR), specifically translocations, are genomic alteration well known to occur in fungal cells undergoing long-term growth. This work focuses primarily on the effects of chromosome translocation on the chronological life span (CLS) of *Saccharomyces cerevisiae* (SC), a model organism used both, for understanding the ageing process as well as for industrial large-scale production of re-cyclable

Nanobiotechnology in Energy, Environment, and Electronics: Methods and Applications
Edited by Claudio Nicolini

ISBN 978-981-4463-96-6 (Hardcover), 978-981-4463-97-3 (eBook)
www.panstanford.com

biomass. A secondary goal of the research was to verify the feasibility of using telomeric DNA sequence length as a molecular marker to monitor population ageing during long-term fermentation. Therefore, a comparison between telomere length and CLS was performed. The data that have been gathered show that chromosome translocation has a different and sometimes opposite effect on the CLS of the budding yeast; furthermore, it was demonstrated that in some cases telomere length does not correlate with the life span of SC. This finding refutes the postulate that age and life expectancy can be deduced from the length of the telomeric DNA and thus precludes the possibility to use this parameter to monitor the health and viability of a long-term industrial fermentation process.

1.1 Introduction

1.1.1 The Yeast *Saccharomyces cerevisiae*

Saccharomyces cerevisiae, also known as the budding yeast, has been used since the dawn of the great civilizations for its fermentation properties in the production of bread, beer, and wine (Fig. 1.1).

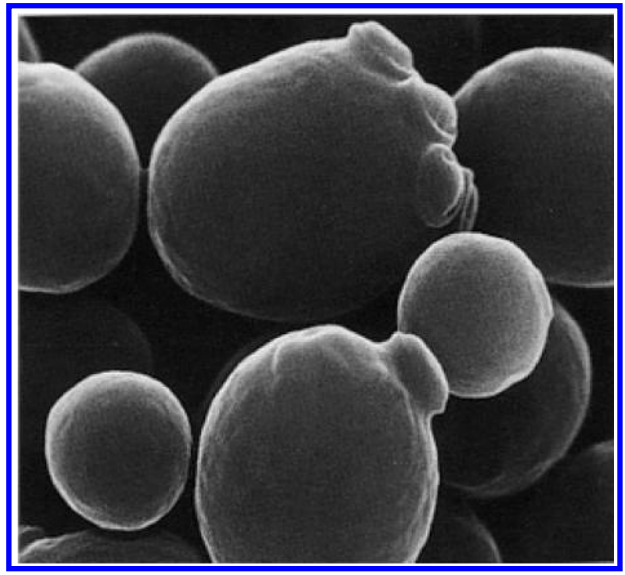

Figure 1.1 Electron microscope picture of *Saccharomyces cerevisiae*.

It is one the eukaryotic models of choice for the easiness with which it can be handled; in fact, it is one of the most studied eukaryotic microorganisms in the fields of molecular and cell biology.

Major discoveries have been made working on SC such as cell-cycle and genome instability, which have greatly contributed to the development of the recent techniques used in laboratories; furthermore, it presents the same structural complexity of plant and mammal cells.

Going deeper into the structural and molecular content of SC, it is important to understand some major characteristics that define the budding yeast.

SC cells differ from ovoid to round and have a diameter that varies from 5–10 depending if it is haploid or diploid.

The haploid form is due to the fact that it has gone into starvation, meaning that it has fewer nutrients on which it can survive and therefore it must conserve itself by using less energy as possible. This is achieved thanks to the production of four haploid spores, which remain held in a capsule called ascus. Since the different sexes are expressed by a couple of heterozygous alleles *MAT*a/*MAT*α, every ascus will hold two haploid cells for every sex type; this means two a and two α. If the amount of nutrients is re-established to normal, it returns to the diploid form by mating one α with one a.

1.1.2 The Yeast Genome

The yeast genome is organized in 16 chromosomes that vary in length between 200 and 1800 kb. The total amount of the genome is 12 Mb with approximately 6400 ORFs. Furthermore, there is the presence of extra-nuclear DNA such as 2 μ, which is an endogenous plasmid, and mitochondrial DNA. However, the yeast genome is very different from any other organism because it is very condensed; as a result, 72% of it is encoded.

One of the reasons why SC has become so important is that it was the first eukaryotic genome to be sequenced. The completed sequence has been published in 1996 (Goffeau et al., 1996).

The availability of the genome has turned SC in an optimal model for the studies concerning homologous genes in humans, plants and other organisms. In addition, presumably 50% of the yeast genes have a homologous gene in humans.

1.1.3 DNA Double-Strand Break

Different DNA lesions can occur; one of them is the double-strand break (DSB). This break can be induced by different kinds of factors: endogenous such as accumulation of oxygen reactive species, replication stresses and replication errors, whereas the exogenous factors are chemical reagents, different kinds of drug species and IR radiation.

In human cells, these breaks normally occur during the entire life span of the cell due to their metabolism and environmental factors therefore by leading to a major structural damage of the DNA molecule, which can dramatically change how the cell reads the gene information. Consequently, the cell needs to frequently repair the damage using different repair mechanisms. However, when the cell ages these repair mechanism become slower and less efficient to a point that it cannot repair itself anymore, now the cell can choose different paths to follow, such as senescence, apoptosis or carcinogenesis.

The majority of the cells in our body are senescent. However, if they are hit by a non-repairable DNA damage, they will follow the path of apoptosis, this is the last resort to prevent the formation of tumorigenic cells.

In somatic tissues, since the recurrence of repair is high, the genome instability can lead to the loss of heterozygosity and carcinogenesis.

This means that you can have the activation of proto-oncogenes through an allelic mutation or the inactivation of oncosuppressor (i.e. the alteration of the gene that gives mammary gland cancer *BRCA1*).

When a DSB occurs in a eukaryotic cell a complex web of proteins activate, these are damage sensor enzymes, signal transductors and effectors. Some of the proteins that are activated are kinases (Mec1 and Tel1), which in terms activate by phosphorylation Rad9 and Rad53.

Rad53, moreover, acts on a series of substrates (Brca1, Nbs1, p53 and Cdc25C) activating the damage response mechanism. Therefore, Rad53 stops the cell-cycle and enhances the repair mechanism and if necessary triggers apoptosis (Zhou et al., 2000).

1.1.4 DBS Repair Mechanisms

There are different DBS repair mechanisms (Fig. 1.2):

- homologous recombination (HR)
- single-strand annealing (SSA)
- synthesis-dependent strand annealing (SDSA)
- break-induced replication (BIR)
- crossing over
- non-homologous end joining (NHEJ)

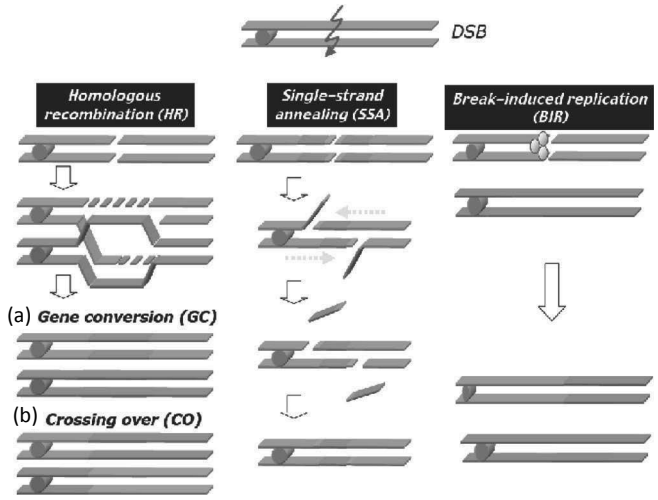

Figure 1.2 Schematic representations of some DNA repair mechanisms.

The different repair mechanisms that arise after the DSB are used differently in the different cells; NHEJ is used by the mammalian cells, whereas HR is used by the yeast (Kanaar et al., 1998; Kolodner, 2002). In addition, the HR is more efficient in the diploid yeast cell rather than the haploid yeast (Shrivastav et al., 2008).

Defects in these repair systems cause genome instability, which can lead to tumorigenesis.

DSB in SC activates different repair mechanisms, which are kinetically different but all activated by Mec1 and Tel1. Mutations to Mec1 and Tel1 cause different chromosome alterations such as the shortening of the telomeres, the increase in mitotic recombination,

chromosome loss, and the sticking of the telomere ends, which ultimately leads to translocations and circular chromosomes (Craven et al., 2002).

1.1.5 Homologous Recombination

The term "homologous recombination" describes a set of mechanisms, all of which use homologous sequences to repair DNA. Most current models of HR are initiated by a DSB; the most common models are double-strand break repair (DSBR), SDSA, SSA, and BIR models. These HR mechanisms have several common features: All HR reactions are catalyzed by a number of proteins that belong to the *RAD*52 epistasis group, although some enzymes are more important for specific pathways.

An important point in the HR is the formation of the Holliday junction, which is a mobile cross formation of DNA with four different strands paired in two duplex. This formation is achieved because when a DSB occurs, one strand of the duplex anneals with the strand of the other duplex (Agmon et al., 2009).

1.1.6 Synthesis-Dependent Strand Annealing

Homologous recombination via the SDSA pathway occurs in cells that mitotically divide and results in non-crossover products. The invading 3′ strand is extended along the recipient DNA duplex by a DNA polymerase and is released as the Holliday junction between the donor and recipient DNA molecules slides in a process called branch migration. The newly synthesized 3′ end of the invading strand is then able to anneal to the other 3′ overhang in the damaged chromosome through complementary base pairing. After the strands anneal, a small flap of DNA can sometimes remain. Any such flaps are removed, and the SDSA pathway finishes with the resealing, also known as ligation, of any remaining single-stranded gaps (Helleday et al., 2007).

1.1.7 Break-Induced Replication

During DNA replication, double-strand breaks can sometimes be encountered at replication forks as DNA helicase unzips the template strand. These defects are repaired in the BIR pathway of HR. The

precise molecular mechanisms of the BIR pathway remain unclear. Three proposed mechanisms have strand invasion as an initial step, but differ in how they model the migration of the D-loop and later phases of recombination (McEachern and Haber, 2006).

The BIR pathway can also help to maintain the length of telomeres, regions of DNA at the end of eukaryotic chromosomes, in the absence of (or in cooperation with) telomerase. Without working copies of the telomerase enzyme, telomeres typically shorten with each cycle of mitosis, which eventually blocks and leads to senescence. In budding yeast cells, where telomerase has been inactivated through mutations, two types of "survivor" cells have been observed to avoid senescence longer than expected by elongating their telomeres through BIR pathways (McEachern and Haber, 2006).

Maintaining telomere length is critical for cell immortalization, a key feature of cancer. Most cancers maintain telomeres by upregulating telomerase. However, in several types of human cancer, a BIR-like pathway helps to sustain some tumors by acting as an alternative mechanism of telomere maintenance (Morrish et al., 2009).

1.1.8 Single-Strand Annealing

The SSA pathway of HR repairs double-strand breaks between two repeat sequences. The SSA pathway is unique in that it does not require a separate similar or identical molecule of DNA, like the DSBR or SDSA pathways of HR. Instead, the SSA pathway only requires a single DNA duplex, and uses the repeat sequences as the identical sequences that HR needs for repair. The pathway is relatively simple in concept: After two strands of the same DNA duplex are cut back around the site of the double-strand break, the two resulting 3′ overhangs then align and anneal to each other, restoring the DNA as a continuous duplex (Haber et al., 2010; West, 2003).

1.1.9 Non-Homologous End Joining

NHEJ is referred to as "non-homologous" because the break ends are directly ligated without the need for a homologous template, in contrast to HR, which requires a homologous sequence to guide repair. The term "non-homologous end joining" was coined in 1996 by Moore and Haber.

NHEJ typically utilizes short homologous DNA sequences called micro-homologies to guide repair. These micro-homologies are often present in single-stranded overhangs on the ends of double-strand breaks. When the overhangs are perfectly compatible, NHEJ usually repairs the break accurately. Imprecise repair leading to loss of nucleotides can also occur but is much more common when the overhangs are not compatible. Inappropriate NHEJ can lead to translocations and telomere fusion, hallmarks of tumor cells (Boulton et al., 1996; Moore et al., 1996; Wilson et al., 1999; Budman et al., 2005).

1.1.10 Chromosome Translocation

Chromosome translocation is a rearrangement of parts between two non-homologous chromosomes (Fig. 1.3). When the two breaking points are within a gene coding sequence this could lead to the fusion of two genes, that is very common in cancer cells, and also is known to bring diseases such as the chronic myelogenous (or myeloid) leukemia (CML) which is the union between the *BCR* and the *ABL* protein genes (Klein et al., 1982).

There are two different main types of chromosome translocations in humans: the reciprocal translocation or non-Robertsonian translocation, which is usually an exchange of material between two non-homologous chromosomes, and the Robertsonian translocations, which are the fusion of the two acrocentric chromosomes near the centromere with loss of the short arm that therefore lead to an unbalanced karyotype of 45 chromosomes.

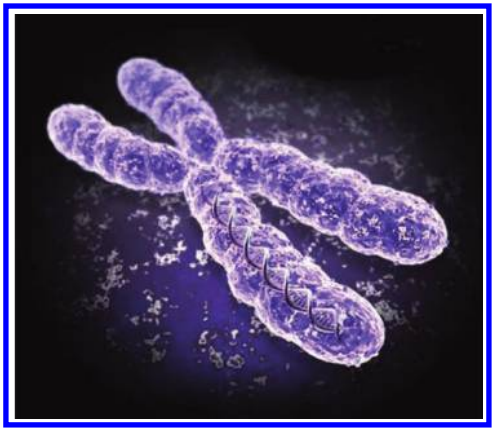

Figure 1.3 Three-dimensional image of a chromosome.

Carriers of Robertsonian translocations are not associated with any phenotypic abnormalities, but there is a risk of unbalanced gametes, which lead to miscarriages or abnormal offspring. For example, carriers of Robertsonian translocations involving chromosome 21 have a higher chance of having a child with Down syndrome. These chromosome translocations can also be seen in yeast and can represent a way to evolve.

1.1.11 BIT Bridge-Induced Translocation

Bridge-Induced translocation method (Fig. 1.4), which was developed in this laboratory, induces chromosome translocation in unmodified yeast cells through targeted DNA cassette integration of the KANr selectable marker flanked by sequences homologous to two chromosomal loci randomly chosen on the genome (Tosato et al., 2005).

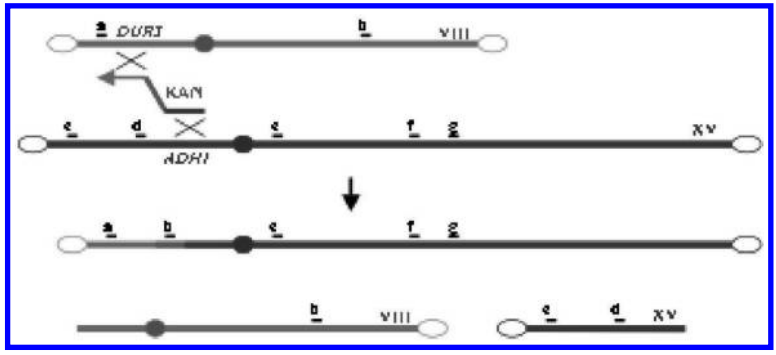

Figure 1.4 Scheme of a bridge-induced translocation between the gene ADH1 on chr. XV and the gene DUR3 on chr VIII.

The cassette carried at its ends two nucleotide sequences homologous to two distinct genomic loci each located on a different chromosome. Thus, once integrated, the selectable linear DNA fragment becomes a molecular bridge between two unique, naturally occurring pre-selected loci.

This method gives chromosome translocations without the need of previously engineering the cells. In literature, there are different techniques used to induce chromosome translocation, but in these cases, it is necessary to insert a site for an endonuclease such as HO or Sce1 by therefore promoting a DBS and a translocation, but they all occur between homologous chromosomes.

The length of the homology deeply influences the BIT system. In fact, a 40 nt homology has an efficiency of 1.6% integration into the desired locus, but by lengthening the homology to 65 nt the efficiency doubles. The low percentage in the desired translocation means that probably there is mechanism that suppresses the whole processes during mitosis.

Furthermore, the efficiency of the translocation is influenced by the region of homology. This means that the regions that regulate this process, also known as the promoter and the terminator regions, are more recombinogenic compared to the ORF.

The mechanism with which probably the translocation occurs follows two steps: First, one end pairs with its homologous sequence; second, the other end searches for its homology on the same chromosome, and if the homology is not met, the cell activates the mechanism to suppress the mitotic recombination. At this point, the free end is able to pair itself with the homology sequence found on the other chromosome and therefore induces a translocation. The pieces of DNA that are cut during the translocation can follow different paths such as degradation or chromosome rearrangements.

In most cases, the cassette can integrate ectopically in the genome, or with just one end of targeted locus. In this case, the free end can integrate in another chromosome using a micro-homology or it can integrate itself on the same chromosome without any homology at all. Finally, it can also integrate itself in the endogenous plasmid 2 μ.

It is also known that only 10–20% of the translocants show phenotype abnormalities such as polynucleated cells, longer buds, anucleated cells. In most cases the actin1 protein seems to be modified, this could explain in part the phenotype abnormalities. There is also a decrease of the Rad53p protein used in DNA repair mechanisms and also the missed phosphorylation of the same protein. These data suggest that the cells have undergone an adaptation after their arrest in the G2/M phase checkpoint (Nikitin et al., 2008).

It has been observed that from the same chromosome translocation you can obtain 10 translocants with different phenotype, morphology and different gene expression (Rossi et al., 2009).

1.1.12 Telomeres

Chromosomes to be determined as such need three essential structures: origin of replication, centromere, and a telomere.

The telomere (Fig. 1.5) has different functions in the chromosome, which differ from the maintenance of the chromosome structure to the protection of the ends. It has been known since the 1970s that the conventional DNA polymerase is unable to replicate the ends; therefore, the cell is unable to keep the telomere from shortening each round of cell division.

Figure 1.5 Representation of a chromosome and its telomere.

However, some cells such as stem and tumor cells have a very important protein that is expressed called the telomerase, which can increase the length of the telomeres every time they shorten since it carries a RNA template used for this task, this gives the cell a certain immortality, thereby the cell is able to divide limitlessly without entering senescence or a non-dividing stage.

In addition, there are some proteins that are associated to the telomere such as the TRF proteins that are considered the "ruler" of the telomere because they are used by the cell to understand how long is the telomere. Furthermore, another family of proteins known as sirtuins have shown to play an important role in the processes that bring the cell to senescence.

The Sir2 protein (silent information regulator) is known to suppress the rDNA recombination and extend the life span by 40% if an extra copy of the gene is added. However, if the telomeres are too long—and therefore there are a large number of sirtuin proteins attached, Sir2 could suppress essential genes of the cell

bringing it to a premature death (Kass-Eisler and Greider, 2000; Bitterman et al., 2003; Cheol Woong Ha and Won-Ki Huh, 2011).

1.2 Material and Methods

1.2.1 Materials

Table 1.1 Some of the translocants that were studied in this manuscript Yeast Strains

Yeast Strains Name	Chromosomes involved	Genotypic background	Produced by
D10	XV-VIII	SAN1	BIT with 40 nt of homology
D3	XV-VIII	SAN1	BIT with 40 nt of homology
D11	XV-VIII	SAN1	BIT with 65 nt of homology
T5	XV-VIII	Trisomic N2 (SAN1 + VIII)	BIT with 65 nt of homology
T12	XV-VIII	Trisomic N2 (SAN1 + VIII)	BIT with 40 nt of homology
AD5	V-VIII	SAN1	BIT with 65 nt of homology
N2	V-VIII	Trisomic N2	BIT with 40 nt of homology
POLY	XIII-XV	BY4743	Excision by Scel in vitro; transformation with 50 nt homology
Val	VII-II	SAN1	BIT with 40 nt of homology
Susu1	IX-XVI	SAN1	BIT with 40 nt of homology
Susu4	IX-XVI	SAN1	BIT with 40 nt of homology
Susu5	IX-XVI	SAN1	BIT with 40 nt of homology
77	VIII-VIII	SAN1	BIT with 40 nt of homology
San1	None	Wt	

1.2.1.1 Media

The media compositions follow the standards of "methods in yeast genetics" (Kaiser et al., 1994). Yeast used for genomic extraction was grown in YPD + G418 (final concentration 200 μg/mL) for selection, whereas for the CLS, all strains were grown in synthetic complete medium with G418 for those that needed selection.

Synthetic Complete Medium

Ingredients	% w/v
Bacto-yeast nitrogen base w/o amino acids	0.67
Ammonium sulfate	0.5
Glucose	2
Drop-out mix	0.2

Synthetic Complete Medium: Add 1000 mL of distilled water.
Dropout mix

Ingredients	mg. in 1000 mL
Adenine	18
Arginine	76
Histidine	76
Leucine	380
Lysine	76
Methionine	76
Proline	76
Threonine	76
Tryptophan	76
Tyrosine	76
Uracil	76

Adenine, threonine, and tryptophane were added after autoclaving the media, since they are thermolabile.

1.2.1.2 Solutions and enzymes

- Herring sperm (HS) (Roche), DNA MB grade, 10 mg/mL, for hybridization
- Marker 1 Kb plus 1 µg/mL
- Geneticine G418 50 mg/mL
- Stock solutions: ethanol, ethanol 70%, TBE 10×, ammonium acetate 4 M, maleic acid 0.5 M, Tween 20, NaOH 0.4 N, HCl 0.25 N, SSC 20×, SDS 10%
- Enzyme use for genomic digestion BanI

- Enzyme used for ligation with buffer: T4 DNA ligase with neb1 buffer + ATP (25×)
- Hepes buffer, 2% glucose

1.2.1.3 Kits and provided solutions

Wizard® Genomic DNA Purification Kit

- Cell lysis solution
- Nuclei lysis solution
- Protein precipitation solution
- DNA rehydration solution
- RNase solution

PCR DIG Probe Synthesis Kit

- Enzyme Mix, Expand High Fidelity, 30 µL (105 U) Enzyme Mix, 3.5 U/µL in storage buffer, 20 mM Tris-HCl, pH 7.5 (25°C), 100 mM KCl, 1 mM dithiothreitol (DDT), 0.1 mM EDTA, 0.5% Tween 20 (v/v), 0.5% Nonidet P40 (v/v), 50% glycerol (v/v)
- PCR DIG Probe Synthesis Mix, 10× conc., 125 µL of a mixture containing dATP, dCTP, dGTP (2 mM each), 1.3 mM dTTP, 0.7 mM DIG-11-dUTP, alkali-labile, pH 7.0
- PCR Buffer with MgCl2, 10× conc., 1 mL Expand High Fidelity Buffer, 10× conc. with MgCl2
- dNTP Stock Solution, 10× conc., 125 µL of a mixture containing dATP, dCTP, dGTP, dTTP (2 mM each), pH 7.0
- Control Template, 50 µL (1 ng) plasmid DNA (20 pg/µL) in Tris/EDTA buffer, pH 8.0. The 5 kb plasmid contains the cDNA for the human tissue-type plasminogen activator (tPA)
- Control PCR Primer Mix, 25 µL (containing 50 pmol of each primer) control PCR primer 1 and 2 (2 mM each)

LIVE/DEAD Yeast viability kit (molecular probes)

- Fun Stain 10 mM

Primers used for generating the probe

These primers were used for generating the probe and are specific for the subtelomeric region.

Forward primer

5′-CCCACACTTTTCACATCTACCTCTACTCTCGCTGTCACTCC TTACCCGGC-3′

Reverse primer
5′-CCCCGAATTCCGGCATTCCTGTCGATGCTGATAGGG-3′

1.2.2 Methods

1.2.2.1 Polymerase chain reaction and its applications

The PCR (polymerase chain reaction) is a technique used to amplify the DNA template of choice, which can vary from a plasmid, genomic DNA and cDNA. The region of interest can be amplified thanks to short length oligonucleotides called primers that find homology on the ends of desired region. These oligonucleotides give the possibility to the enzyme, the polymerase, to begin the amplification of the region.

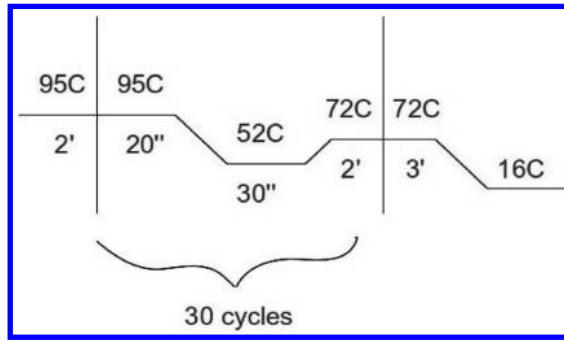

Figure 1.6 Representation of the PCR timetable with its temperatures.

There are three main steps (Fig. 1.6):

- The denaturation step is needed to separate the DNA double-strand filaments in to single strand filaments. This is due to high temperatures such as 95°C for 2 min.
- Annealing step is the cycle that is repeated 30 times, and it consists of first a quick denaturation of 30 sec at 95°C and second the actual annealing of the primers to their homologous sequence at a temperature that is calculated through this simplified formula $T_a = T_m - 2$ for 30 sec, finally the elongation of the chain where the time is calculated based on the length of the sequence and the throughput of the enzyme used.
- Elongation step is the last elongation in which the temperature is 72°C and the timing varies from 2 to 3 min.

- This technique enables an exponential amplification of the DNA sequence. Moreover, with 30 cycles, you can achieve an amplification growth of 109 times. The DNA concentration can be verified by electrophoresis gel run stained with ethidium bromide.
- This technique was created by K. B. Mullis in 1986.

1.2.2.2 Probe synthesis

The probe was synthetized using the PCR technique. The template for the amplification is any genomic DNA since the subtelomeric sequences are conserved, whereas the primers used were specifically designed to probe the repetitive sequence. The dNTPs used for amplification are marked dNTPs provided with the kit and the enzyme used was GoTaq polymerase with its buffer.

1.2.2.3 Genomic DNA extraction

The extraction of the genomic DNA was performed using the kit provided by Promega and its protocol.

- Add 1 mL of culture grown for 20 h in YPD broth to a 1.5 mL tube.
- Centrifuge at 13,000–16,000 rpm for 2 min. Remove supernatant;
- Resuspend the cells in 293 µL of 50 mM EDTA.
- Add 7.5 µL of 20 mg/mL lyticase and gently pipet four times to mix.
- Incubate the sample at 37°C for 30–60 min to digest cell wall.
- After cooling to room temperature, Centrifuge at 13,000–16,000 rpm for 2 min and remove supernatant.
- Add 300 µL of nuclei lysis solution.
- Add 100 µL of protein Precipitation solution and vortex for 20 sec.
- Let the sample sit on ice for 5 min.
- Centrifuge for 3 min.
- Transfer supernatant to clean Eppendorf tube with 300 µL of isopropanol at room temperature.
- Mix by inversion until the thread-like strands of DNA appeared.
- Centrifuge for 5 min at 13,000 rpm.

- Decant the supernatant and drain the tube on clean absorbent paper. Add 300 µL of room temperature of 70% ethanol and invert to wash the DNA pellet.
- Centrifuge at 13,000 rpm for 2 min, aspirate the ethanol.
- Drain tube on clean absorbent paper and allow the pellet to air dry for 10–15 min;
- Add 50 µL of DNA rehydration solution;
- Add 1.5 µL of RNase solution to the purified DNA sample, vortex the sample for 1 sec; centrifuge briefly for 5 sec to collect the liquid and incubate at 37°C for 15 min;
- Rehydrate DNA by incubating at 65°C for 1 h, periodically mix the solution or rehydrate the DNA by incubating the solution overnight at room temperature or at 4°C.

1.2.2.4 Genomic DNA hydrolysis

The genomic DNA digestion was performed using the enzyme BanI (Seidel et al., 2008) using its provided buffer NEB4 (New England Biolabs).

In 50 µL → 5 µL of genomic DNA
5 µL of buffer (NEB4)
1 µL of BSA
37 µL of H_2O
2 µL of enzyme

The digestion was performed for 3 h at 37°C.

1.2.2.5 DNA electrophoresis

The digested genomic DNA was electrophoresed on 0.8% agarose gel submerged in TBE 0.5× (Tris-HCl pH8 90 mM, Boric Acid 90 mM, EDTA 2.5 mM). The gel was left to run for 2–3 h at 100 V (Seidel et al., 2008) and stained with ethidium bromide.

1.2.2.6 Southern blot

The Southern blot was performed using the protocol described below.

Step 1

- The gel has to be washed two times with 0.25 N HCl for 10 min.

- Rinse with water and neutralize the acid by washing with 0.4 N NaOH for 15 min.
- Prepare the Hybond-N^+ (GE Healthcare) membrane by putting it on the surface of the water at let it submerged for 5 min.
- Wash with 0.4N NaOH for 15 min.
- Place the membrane and the gel in the Southern blotting vacuum camera at leave the vacuum for 1 h or more.
- After transferring the DNA to the membrane, wash the membrane with 1 M ammonium acetate for 15 min.
- Place the membrane between absorbent paper sheets and place it at +70°C overnight.

Step 2

- Submerge membrane in 6× SSC for 2 min.
- Place membrane in a sealed bag with 6 mL of prehybridization solution (6× SSC, 5× Denhard solution, 0.5% SDS, 100 ug/mL herring sperm DNA) for 2 h at 68°C.
- Change prehybridization solution with hybridization solution (6× SSC, 0.5% SDS, 100 ug/mL herring sperm DNA, Probe (2 μL in 100 μL of H_2O) and place it at 68°C for overnight incubation.

Step 3

- Wash the membrane with 2× SSC and 0.5% SDS for 5 min.
- Wash membrane with 2× SSC and 0.1% SDS for 15 min.
- Wash membrane with 0.1× SSC and 0.5% SDS at 68°C for 1 h with gentle shaking.
- Wash the membrane with washing buffer (0.1 M maleic acid, 0.15 M NaCl, Tween 20, pH 7.5) for 5 min.
- Submerge the membrane in blocking solution (0.1 M maleic acid, 0.15 M NaCl, 1× blocking Buffer) for 30 min.
- Submerge the membrane in antibody solution (0.1 M maleic acid, 0.15 M NaCl, 1× Blocking Buffer, 1 μL of anti-digoxigenine Abs) for 30 min.
- Wash membrane two times with washing buffer for 15 min each;

- Equilibrate membrane with detection buffer (0.1 M Tris-HCl pH 9.5, 0.1 M NaCl) for 5 min.
- Place the membrane in a plastic bag and add CDP-star (Roche), keep it for 5 min in the dark.
- Discard the liquid in excess.
- Seal the membrane and place it for 10 min at 37°C in the dark.
- Develop pictures using high-performance chemiluminescence film (GE Healthcare).

1.2.2.7 Yeast viability assay

The yeast viability assay uses red stain that brightens the metabolism of the cell, therefore only metabolically active cells are marked clearly with fluorescent intravacuolar structures, while dead cells exhibit extremely bright, diffuse, green-yellow fluorescence (Fig. 1.7).

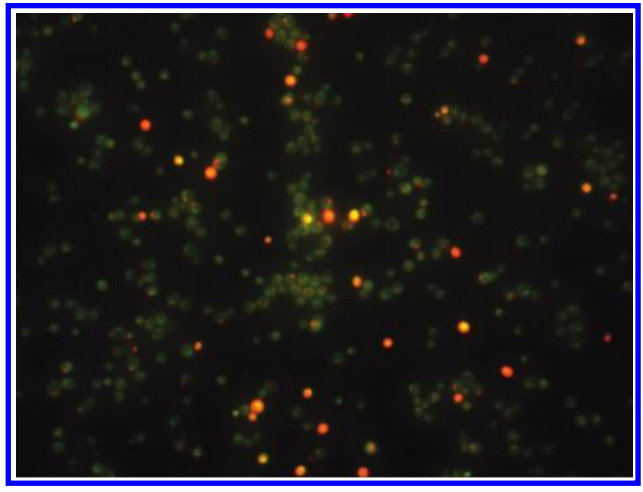

Figure 1.7 Picture taken with fluorescent microscope of translucent D11 at day 3. The cells in green are alive, whereas the cells in bright orange are dead.

Furthermore, the green stain brightens cells with intact membranes but with little or no metabolic activity, these present diffuse green cytoplasmic fluorescence and lack fluorescent intravacuolar bodies.

Fluorescent light is emitted between 470–590 nm UV light.

- Cells must to be washed two times with water;
- Add Hepes medium and 12.5 uM of FUN stain (10 mM stock).
- Incubate at 30°C for 1 h.
- Place on glass microscope slide.
- Look at fluorescent microscope.

All pictures were taken with a Leica inverted laboratory microscope with LED light, and UV illumination. The provided software (Leica Application Suite) was used for the acquisition and merging of the pictures.

1.3 Results

All the mutants that were analyzed were previously generated in this lab. The first step was to define the different length of the telomeres of every strain.

1.3.1 Genome Extraction

The genome extraction was performed with the Wizard® Genomic DNA Purification Kit, with some minute modifications to the original protocol to have the DNA as pure as possible. The protein precipitation step was performed more than one time to eliminate most of the proteins.

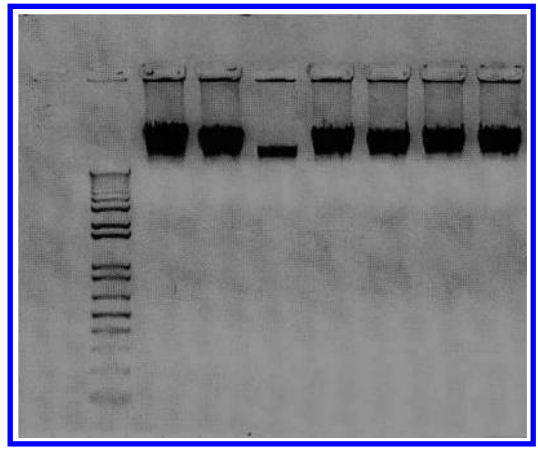

Figure 1.8 Genomic DNA extraction of different strains.

In Fig. 1.8, the strong bands of the genomic extraction are clearly visible.

1.3.2 DNA Hydrolysis

Afterward, the genomic DNA was digested with BanI for 3 h at 37°C. The digested genomic DNA was separated on 0.8% agarose gels for 3 h at 100 V. The electrophoresis gel was rinsed in Milli-Q water and then treated for depurination by 0.25 N HCl twice for 10 min and neutralized with 0.4 N NaOH buffer for 15 min. The DNA was then transferred to Hybond-N membrane (GE healthcare) by vacuum blotter.

In Fig. 1.9, the smearing and the digestion of the DNA are visible in every sample defining a clear cut of the DNA.

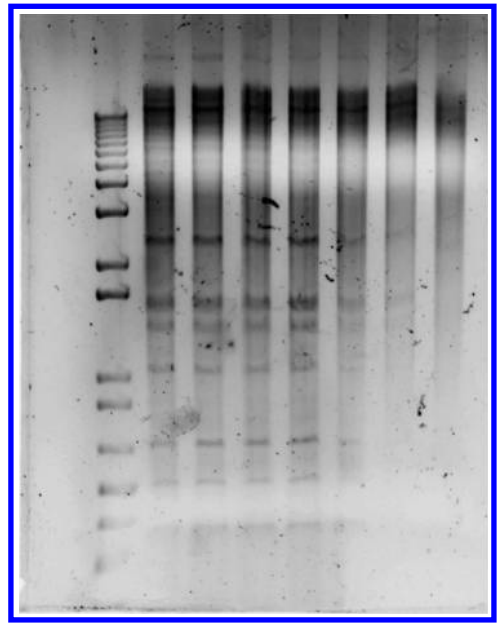

Figure 1.9 Genomic DNA digested with enzyme BanI for 3 h at 37°C.

1.3.3 Probe Synthesis

The probe used for the Southern blot (Fig. 1.10) was synthetized using the Probe DIG synthesis kit with specifically designed primers:

Forward primer

5′-CCCACACTTTTCACATCTACCTCTACTCTC

GCTGTCACTCCTTACCCGGC-3′

Reverse primer

5′-CCCCGAATTCCGGCATTCCTGTCGATGCTGATAGGG-3′

The DNA template is any *S. cerevisiae* genomic DNA since the subtelomeric sequence is conserved.

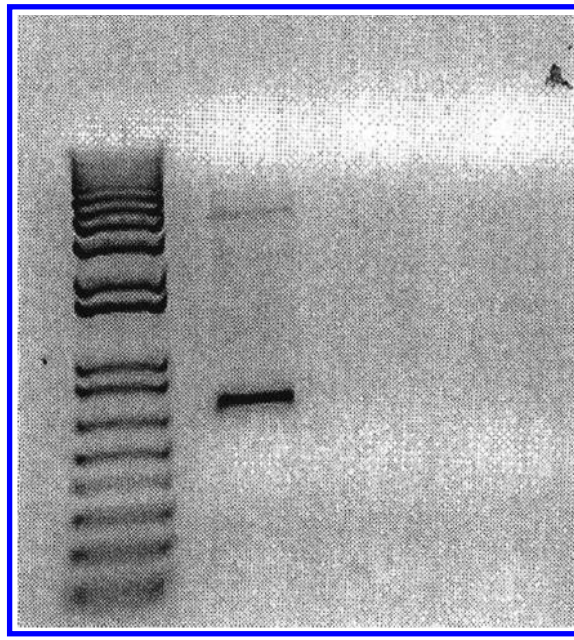

Figure 1.10 Gel check of PCR for probe synthesis. The probe was synthetized using the DIG kit.

1.3.4 Southern Blot

The results of the Southern blot (Fig. 1.11), performed with the probe of our production, show that chromosome translocation had an effect on the chromosome length of the different translocants if we compare them with the wild-type strain. The smearing of the telomeres is due to the fact that each cell of the colony has a different length of the telomere. What is to consider the average length of entire cell colony.

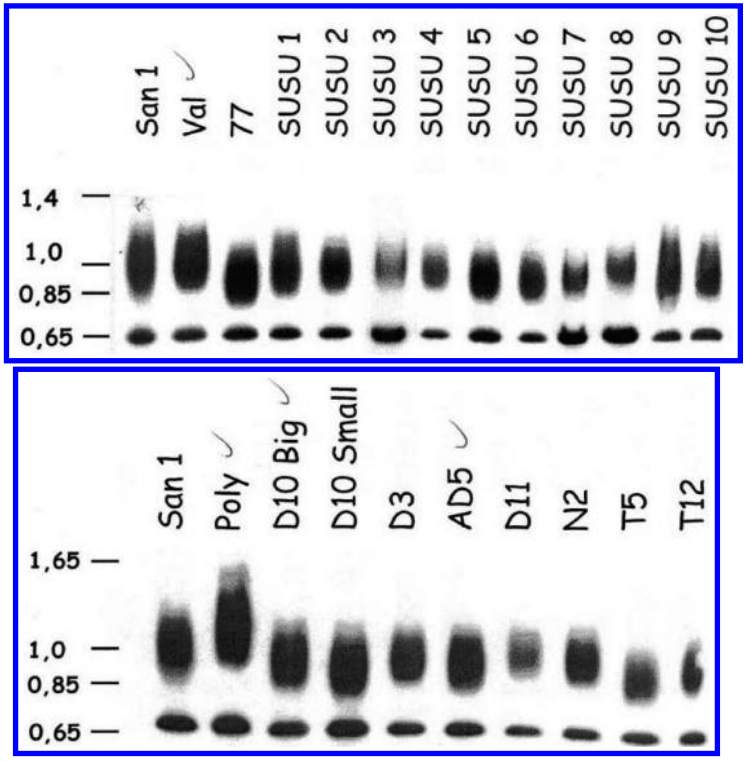

Figure 1.11 Southern Blot, showing the different telomere length of the strains and underwent CLS analysis.

1.3.5 Chronological Life Span

The CLS is used to measure the means and maximum survival time of a population of non-dividing cells in a restrictive medium, such is a medium for industrial, large-scale fermentation. Yeast CLS may be a suitable model for the ageing process of post-mitotic cells, such as neurons in multicellular organism.

It was measured by growing the cells in a synthetic complete medium and, after 3 days of growth in which they all reach the plateau phase, every 2 days a sample was retrieved for yeast viability assay analysis. To normalize the results, two sessions of 500 cells for each strain were photographed. The viability assay was performed using FUN staining (Fig. 1.12).

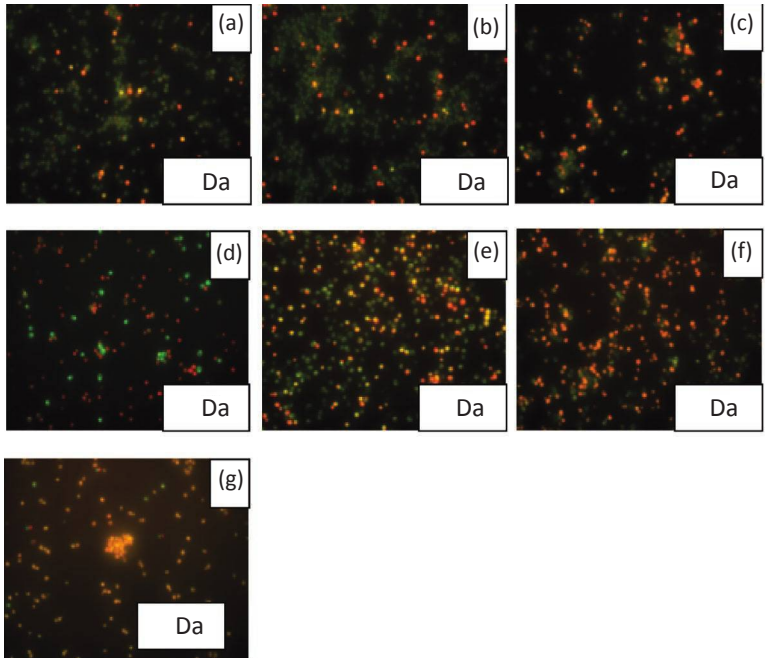

Figure 1.12 (a–g) Pictures of the CLS of strain D11, starting from day 3 and finishing with day 17. The cells colored in green are alive, and the cells displayed in orange are dead. It is easy to note the increase of number of the dead cells from session to session until total death on day 17.

1.3.6 Translocants between XV-VIII (D10, D3, D11, T5, T12)

The translocants between chromosomes XV and chromosome VIII, where the targeted genes for translocation are *ADH5* and *DUR3*, show different phenotypes: D10 has cell cycle defects and nuclei segregation impaired, whereas D3 and D11 show no or light defects. Furthermore, D10 can be divided into two different phenotypes—Big and Small—where Big has a trisomic chromosome and forms big colonies on YPD agar plates unlike D10 Small.

T5 and T12 were not observed in detail, but they present a different genomic background because they have an additional chromosome VIII (Tosato et al., 2005). As shown in Fig. 1.13, the same translocation can have a different and sometimes opposite effect on the CLS of the budding yeast.

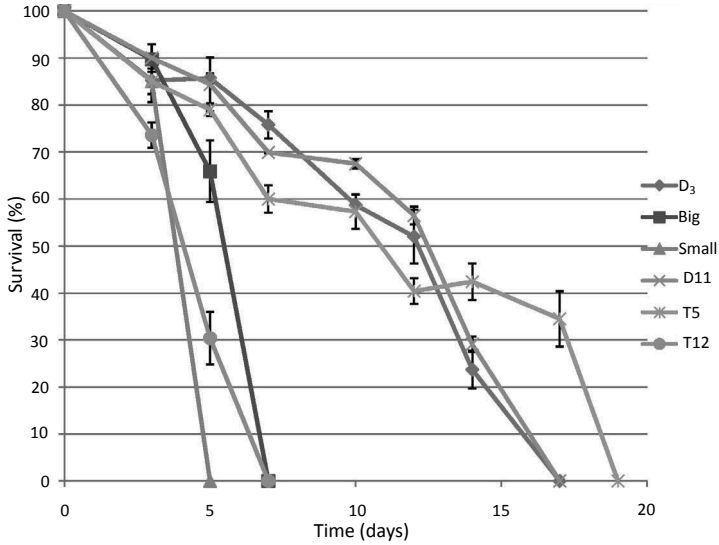

Figure 1.13 Chronological life span of strains that had a chromosome translocation between chr. XV and chr. VIII.

1.3.7 Between V-VIII (AD5)

The translocants between chromosomes V and VIII (Fig. 1.14), where the genes targeted are *ALD5* and *DUR3*, show no or little defects, but their CLS is much different.

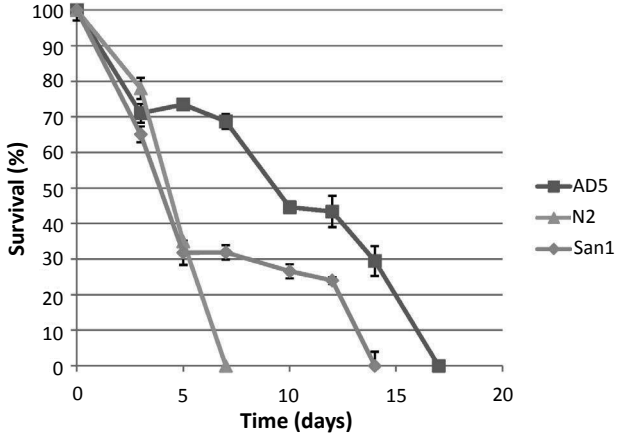

Figure 1.14 Chronological life span of strains that had a chromosome translocation between chr. V and chr. VIII.

1.3.8 Between XIII-XV & VII-II (Poly, Val)

The translocants between chromosomes XIII-XV and VII-II (Fig. 1.15), where the genes targeted were *RIT1* and *APC5*, were *RDH54* and *MRPS35*, respectively. Poly shows cell cycle defects, whereas Val is a polyploidic cell.

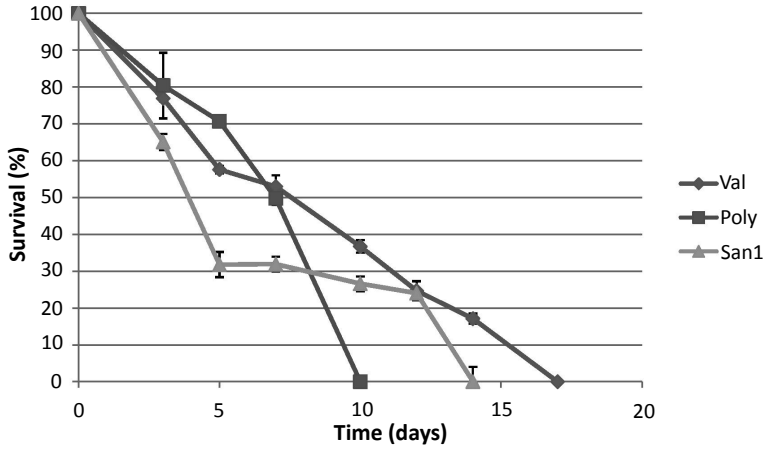

Figure 1.15 Chronological life span of strains that had a chromosome translocation between chr. XIII and XV (Poly), and between chr. VII and chr. II (Val).

1.3.9 Between IX-XVI (Susu1, Susu4, Susu5)

The translocants between chromosomes IX and XV, where the genes targeted where *SUC2* and *SSU1*, show different phenotypes: Susu1 and Susu4 have cell cycle defects with slow growth in glycerol, but Susu5 has nucleus fragmentation, is a putative petit and cannot grow in glycerol (Rossi et al., 2010).

Different results arise after all the cells have been counted and the data normalized.

Chromosome translocation is a stress for the cells that not only involves movement of genetic material between chromosomes but also alters the three-dimensional structure and spacing of the chromatin and expression of many genes and, in addition, changes the metabolism of the cell. Thereby all the translocants analyzed have a diverse response to the translocation. The strains with similar pattern have been grouped together to facilitate the understanding of the effects.

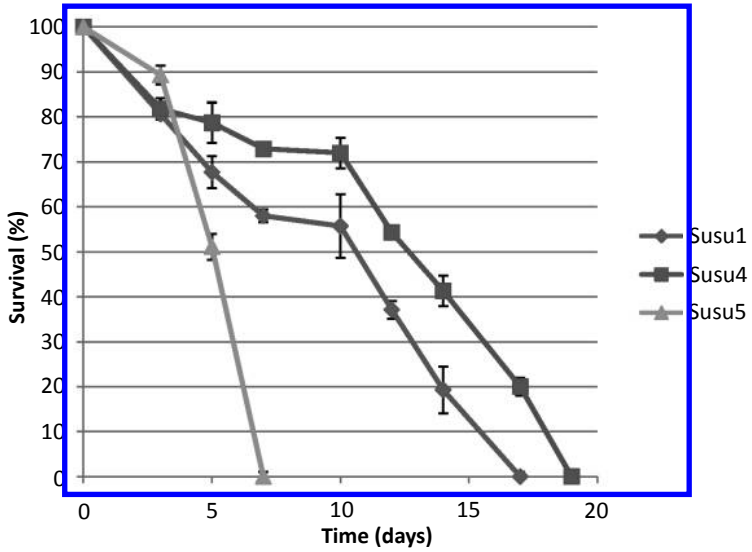

Figure 1.16 Chronological Life Span of strains that had a chromosome translocation between chr. IX and chr. XVI. Even though the translocation is the same the effect on the CLS is much different.

Long-living strains (Fig. 1.17) were able to live up to 50% longer than the wild-type strain, whereas short-living strains (Fig. 1.18) can live up to 65% less than the wild type.

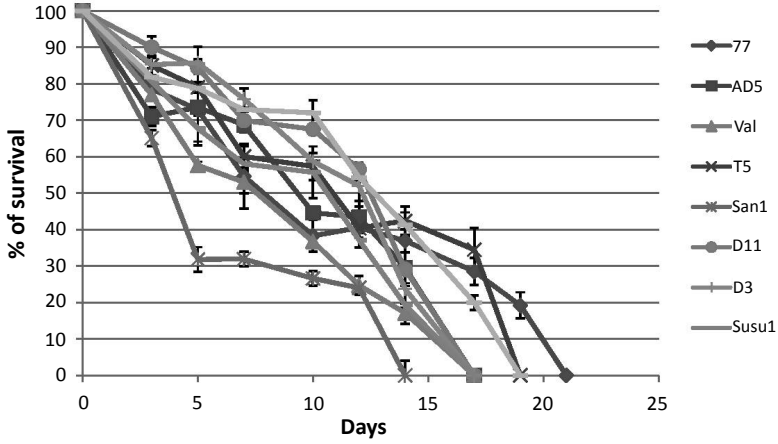

Figure 1.17 Chronological life span of strains that lived longer than the wild type (san1).

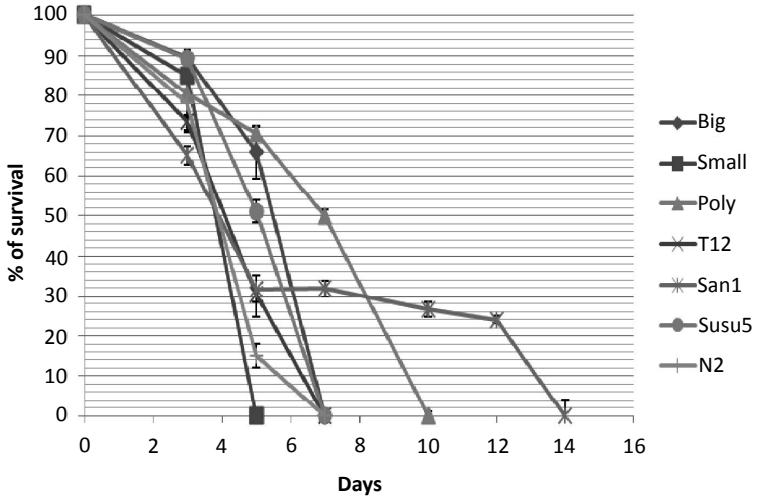

Figure 1.18 Chronological life span of strains that lived less than the wild type (san1).

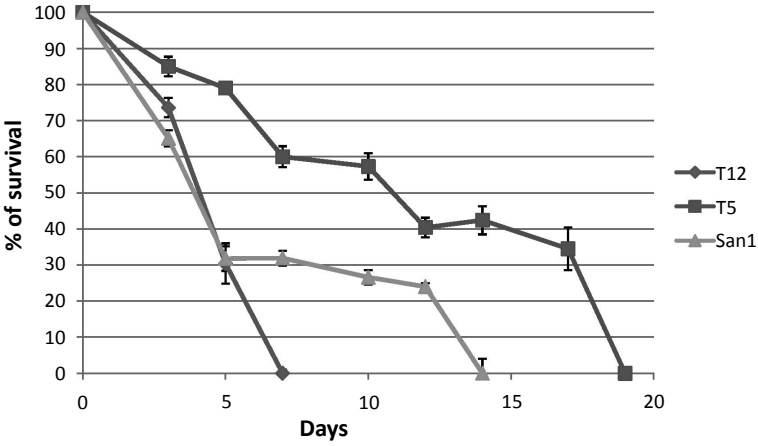

Figure 1.19 Comparison of the CLS between T12 and T5, which have the same chromosome translocation.

This demonstrates that chromosome translocation has a different and opposite effect on the cell, even if the translocation occurs between the same chromosomes in the same loci. A very clear example is T12 and T5 (Fig. 1.19), where the chromosome translocation was induced between chromosome XV and

chromosome VIII, targeting, respectively, the *ADH1* gene and the *DUR3* gene; even if the loci are identical, their CLS is dramatically different.

1.4 Conclusions

This chapter explains some chromosome translocation effects on the CLS of SC, demonstrating that a translocation is much more than a simple movement of genetic material from a chromosome to another, but it has a deep and profound effect on the cell functioning. It is able to modify the metabolism, CLS, cell cycle and more that still needs to be defined. Therefore, it is a novel and interesting tool to use to improve a strain and benefit from the long life span in a biofermentation process.

The results from the study presented in this chapter show that the following:

- Chronological life span had an effect on the telomere length of the cells. The shortening and lengthening were both observed defining that the cells reacted differently to the chromosome translocation even if it was between the same loci. Furthermore, the CLS does not correlate with length of the telomere demonstrating that the telomeres are not always to be concerned for measuring the "age" of the cell. Therefore, telomere length is just the tip of the iceberg of a more complex pathway that has to be yet completely understood.
- Chromosome translocation had a different and opposite effect on the CLS of SC, even if the translocation was achieved between the same chromosomes targeting the same genes. This means that cells can react differently to the same translocation, and that there are more than one pathway that control chromosome translocation and its consequences.
- The CLS of some cells was increased up to 50% compared to the wild type, whereas others had their CLS decreased down to 65% less. Furthermore, literature confirms that there could be a correlation between the less living translocants, and respiratory deficiency, since it has been proven that respiratory deficient cells live much less in SC complete medium (Fabrizio et al., 2010). There is much to speculate on

this topic, since respiratory deficiency is a sign of cells that undergo apoptosis, raising the questions that also SC could undergo apoptosis.

- Selection of a highly viable strain could be appropriate for industrial use, such as biofermentation, thereby limiting the cost of replacing the dead yeast with new ones. Furthermore, it opens the possibility of cutting the costs of re-growing new yeast.
- The future prospective of this project is to improve the strain, always by translocation, by making it resistant to higher levels of alcohol and to yeast-harmful compounds.

References

Agmon N., Pur S., Liefshitz B., et al., Analysis of repair mechanism choice during homologous recombination. *Nucl*. *Acids Res*. 2009, **37**(15), 5081–5092.

Bitterman K. J., Medvedik O., Sinclair D. A., Longevity regulation in *Saccharomyces cerevisiae*: Linking metabolism, genome stability, and heterochromatin. *Microbiol*. *Mol*. *Biol*. *Rev*. 2003, **67**(3), 376–399.

Boulton S. J., Jackson S. P., *Saccharomyces cerevisiae* Ku70 potentiates illegitimate DNA double-strand break repair and serves as a barrier to error-prone DNA repair pathways. *EMBO J*. 1996, **15**(18), 5093–103 PMID 8890183.

Budman J., Chu G., Processing of DNA for nonhomologous end-joining by cell-free extract. *EMBO J*. 2005, **24**(4), 849–860.

Cabib E., Silverman, J. S., Shaw, J. A., et al., Carbohydrates as structural constituents of yeast cell wall and septum. *Pure Appl*. *Chem*. 1991, **63–64**(4), 483–489.

Craven R., Greenwell P., Dominska M., Regulation of genome stability by TEL_1 and MEC, yeast homologous of the mammalian ATM and ATR genes. *Genetics*. 2002, **161**(2), 493–507.

De Klein A., Van Kessel A. G., Grosveld G., et al., A cellular oncogene is translocated to the Philadelphia chromosome in chronic myeloid leukaemia. *Nature*. 1982, **300**(5894), 765–767.

Fabrizio P., Hoon S., Shamalnasab M., et al., Genome-wide screen in *Saccharomyces cerevisiae* identifies vacuolar protein sorting, autophagy, biosynthetic, and tRNA methylation genes involved in life span regulation. *PLoS Genet*. 2010, **6**(7), e1001024.

Fabrizio P., Longo V., The chronological life span of *Saccharomyces cerevisiae*. *Aging Cell*. 2003, **2**(2), 73–81.

Goffeau A., Barrell B. G., Bussey H., et al., Life with 6000 genes, *Science*. 1996, **274**(5287), 546–552.

Ha C. W., Huh W.-K., The implication of Sir2 in replicative aging and senescence in *Saccharomyces cerevisiae*. *Aging*. 2011, **3**(3), 319–324.

Haber Lab. *Single-Strand Annealing*. Brandeis University. Retrieved 3 July 2010.

Helleday T., Lo J., Van Gent D. C., et al., DNA double-strand break repair: From mechanistic understanding to cancer treatment. *DNA Repair* (*Amst*). 2007, **6**(7), 923–935 doi: 10.1016/j.dnarep.2007.02.006. PMID 17363343.

Kanaar R., Hoeijmaster J. H., van Gent D. C., Molecular mechanism of double strand break repair. *Trends Cell Biol*. 1998, **8**(12), 207–217.

Kass-Eisler A., Greider, C. W., Recombination in telomere length maintenance. *Trends Biochem*. *Sci*. 2000, **25**(4), 200–204.

Kolodner R. D. Putam C. D., Myund K., Maintenance of Genome stability in *Saccharomyces cerevisiae*. *Science*. 2002, **297**(5581), 552–557.

McEachern, M. J., Haber, J. E., Break-induced replication and recombinational telomere elongation in yeast. *Ann*. *Rev*. *Biochem*. 2006, **75**, 111–135. doi:10.1146/annurev.biochem.74.082803.133234. PMID 16756487.

Moore J. K., Haber J. E., Cell cycle and genetic requirements of two pathways of non-homologous end-joining repair of double-strand breaks in *Saccharomyces cerevisiae*. *Mol*. *Cell Biol*. 1996, **16**(5), 2164–2173. PMID 8628283.

Morrish T. A., Greider C. W., Short telomeres initiate telomere recombination in primary and tumor cells. *PLoS Genet*. 2009, **5**(1), e1000357.

Nikitin D., Tosato V., Zavec A. B., et al., Cellular and molecular effects of nonreciprocal chromosome translocations in *Saccharomyces cerevisiae*, *Proc*. *Natl*. *Acad*. *Sci*. *U*. *S*. *A*. 2008, **105**(28), 9703–9708.

Rossi B., Noel P. E., Bruschi C. V., Different aneuploidies can arise from the same bridge-induced chromosomal translocation event in *Saccharomyces cerevisiae*. *Genetics*. 2009, **186**(3), 775–790.

Seidel J. J., Anderson C. M., Blackburn E. H., A novel tel1/ATM N-terminal motif, TAN, is essential for telomere length maintenance and a DNA damage response. *Mol*. *Cell*. *Biol*. 2008, **28**(18), 5736–5746.

Shrivastav M., De Haro L. P., Nickoloff J. A., Regulation of DNA double-strand break repair pathway choice., *Cell Res*. 2008, **18**(1), 134–147.

Tosato V., Waghmare S. K., Bruschi C. V., Non reciprocal chromosome bridge-induced translocation (BIT) by targeted DNA integration in yeast, *Chromosoma*. 2005, **114**(1), 15–27.

West S. C., Molecular views of recombination proteins and their control, *Nat. Rev. Mol. Cell. Biol.* 2003, **4**(6), 435–445.

Wilson, T. E., Lieber, M. R., Efficient processing of DNA ends during yeast nonhomologous end joining. Evidence for a DNA polymerase beta (Pol4)-dependent pathway. *J. Biol. Chem*. 1999, **274**(33), 23599–23609.

Zhou B. B., Elledge S. J., The DNA damage response: Putting checkpoints in perspective, *Nature*. 2000, **408**(6811), 433–439.

Chapter 2

Pulsed Power Nanotechnologies for Disintegration and Breaking Up of Refractory Precious Metals Ores

Valentin A. Chanturiya and Igor Zh. Bunin

Research Institute of Comprehensive Exploitation of Mineral Resources (*IPKON RAS*), *Russian Academy of Sciences*, *4 Kryukovsky Tupik*, *Moscow*, *111020 Russia*

bunin_i@mail.ru

This chapter reviews current research in high pulsed power technologies for processing of precious metals containing refractory ores and natural mineral aggregates, a branch of experimental engineering physics that critically depends on national priority research projects for its dynamic development. The aim of the chapter is to show progress in the study of *nanosecond* processes involved in the disintegration and breaking up of mineral complexes with fine disseminated precious metals. It presents the results of theoretical and experimental studies of the mechanisms of non-thermal action of high-power electromagnetic pulses (**HPEMP**) with nanosecond leading edge and pulse duration and high electric field strength on natural mineral media. It presents experimental data to confirm the formation of breakdown channels and selective disintegration of mineral complexes as a result of pulse irradiation, which makes for efficient access of lixiviant solutions to precious

Nanobiotechnology in Energy, Environment, and Electronics: Methods and Applications
Edited by Claudio Nicolini

ISBN 978-981-4463-96-6 (Hardcover), 978-981-4463-97-3 (eBook)
www.panstanford.com

metal particles and enhanced precious metal recovery into lixivia during leaching. The chapter shows the advantages of high-energy pulse treatment, which, when in the processing of resistant gold-containing ores and beneficiation products from Russian deposits, provides for stable gain in valuable components recovery (5–80% gain for gold and 20–50% for silver), therewith helping reduce energy consumption and cost of products.

2.1 Introduction

Pulse electrotechnologies (named also "pulsed power") are the major direction of the development of various manufactures of XXI centuries (Mesyats, 2004). The effect of superstrong electromagnetic fields on materials (for example, no-thermal action of strong electric fields on medical, biologic and *natural mineral* objects) is one of the "pulsed power" technological-process directions.

An analysis of modern condition of source of iron (gold and others) ore raw materials (Chanturiya, 1999a, 2001a) has shown a negative tendency of reducing the mineral resources extraction and worsening the quality of extracted ores. In the nearest future, the deposits presented mainly by fine-disseminated and rebellious ores will be developed; it demands essentially new solutions in the technology and technique of their beneficiation. In Russia, like elsewhere in the world, development of primary gold deposits is considered a first-priority line of development for the gold mining industry. Most of the gold-containing ores characteristic of Russian gold deposits are resistant ores with gold content varying between 3 and 5 ppm, usually showing quite low gold and silver recovery by cyanidation. Processing resistance of gold-containing mineral complexes is related to the presence of gold particles of submicrometric (<1.0–10 μm) and nanometric size (~10–100 nm), mostly associated with pyrite and arsenopyrite. The problem of proper utilization of resistant ores and enhancement of precious metal recovery presently takes on ever-increasing significance.

Processing of resistant ores involves certain difficulties related to their "physical" and "chemical" resistance (Chanturiya, 2003a). The "chemical" resistance of such ores is being fought against by flotation concentration, oxidative roasting, autoclave oxidation, biohydrometallurgical leaching, etc. The "physical" resistance of ores is being countered by traditional energy-intensive methods of

grinding ores down to −40 μm (up to 90%), thermal processing of sulfides concentrates, and *non-traditional high-energetic techniques* of breaking up of sulfides minerals.

During the beneficiation of a mineral raw material, about 70% of the energy is used in crushing and grinding the ore. The consumption of electrical energy during grinding ranges between 20 kW·h/t to 60 kW·h/t depending on the type of ore. In a number of cases, an increase in the fineness of the mineral particles does not lead to an increase in the level of mineral exposure, whereas there is an increase in the number of finest particles (<10 μm). Analysis of the main gold losses during primary processing shows that 35–40% of gold is connected with aggregates and 30–35% of gold is connected with fine particles less than 40 μm. In order to reduce these losses during processing of finely-disseminated ores without forming aggregates and simultaneously without excessive overgrinding, the non-selective traditional processes of crushing and grinding in jaw and cone crushers, and ball mills should be replaced by selective disintegration. The physical meaning of the changeover to selective disintegration involves organizing the process so that crushing occurs not over the random directions of compressive forces, but predominantly over the boundaries of mineral grains as a result of developing shear and tensile loads at their boundaries. These methods are realized in dynamic self-grinding mills, conical inertial crushers, gas stream and spring mills (Abouzeid and Fuerstenau, 2000; Sander and Schonert, 2000), for ultrafine grinding ("Mekhanobr" Int. Stk. Co).

Let us review some kinds of modern technique of natural media modifications, which are closely related to the method proposed in this chapter (Table 2.1; Chanturiya and Bunin, 2007).

The *electrochemical* methods should be mentioned first (Chanturiya and Vigdergauz, 1993). The essence of these methods consists in the increase of defects concentration and arising of a great number of microcracks under the polarization processes of sulfide and oxide minerals with semiconductor properties. The defects concentration raise and microcracks emergence are caused under these conditions by the electrochemical reactions that take place on the mineral grain boundaries. In practice, the electrochemical action is performed in the process of grinding by the application of direct current of 3–6 A/m^2 density and of 6–12 V voltage inside the ball mill. The electric power consumption in this case amounts to 0.2–0.4 kWh/ton and the degree of disclosure increases by 20–25%.

Table 2.1 Non-traditional high-energetic methods of disintegration and breaking up of mineral complexes

Action; process (operation); technological effect	Limitations (by-effects)	Energy consumption (kWh/t)	Introduction (stage); raw material	Authors, year
Electrochemical treatment				
Leaching; improved recovery of Au and Ag by 10–25%	Higher energy consumption; inhibition of disintegration due to formation of S^o; passivation of electrode systems; necessary combination with chemical effect to higher electroconductivity of a medium	50–60 (aqueous medium); 20–30 (alkaline or acid medium)	Laboratory and pilot commercial tests; sulfide ores bearing noble metals	V. A. Chanturiya, V. E. Vigdergaus, T. V. Chekushina, 1993
Accelerated electron beam				
Disintegration of mineral complexes; higher productivity of grinding circuit	High capital outlays; technical problems of introduction into operational mineral	5–10	Laboratory and semi-commercial tests at the continuously operating machine with production capacity of 40 kg/h;	G. P. Bochkarev, V. I. Rostovtsev, Yu. P. Veigel't, V. A. Chanturiya, V. E. Vigdergaus, 1983

(1.5–2 times), Zn, Cu, Pb recovery at flotation by 5–10%; Au and Ag recovery at cyanidation by 25–30%	processing flowsheets; higher energy consumption; sample heating; alteration of surface and volume properties		sulfide, iron ores, etc.	
Microwave frequency treatment				
Weakening of mineral complexes; less grinding durability by 20–25%; higher recovery of Au by 10%	Complexity of realization under commercial conditions; sample heating, fusion, treatment of exclusively dry samples; alteration of surface and volume properties of minerals	5–7	Laboratory tests; gold-bearing quartz-feldspar ores; pyrite flotation concentrates; gold-arsenic gravity concentrates ores bearing platinum-group metals (PGM)	K. E. Haque, et al. 1999; A. V. Khwan, V. I. Solovév, V. M. Petrov, G. V. Sedelńikova, et al., 2001–2004
Electric impulse treatment				
Failure due to electrical explosion within material volume; higher exposure of mineral joints	High energy consumption; limitations in treatment of finely dispersed mineral raw material before cyanidation	Energy in an impulse 0.5–20 kJ	Laboratory tests; grinding-milling commercial machines; any raw materials	U. Andres, 1977–2000; V. I. Kurets, A. F. Usov, V. A. Tsukerman, 1970–2007

(*Continued*)

Table 2.1 (*Continued*)

Action; process (operation); technological effect	Limitations (by-effects)	Energy consumption (kWh/t)	Introduction (stage); raw material	Authors, year
Electric hydrodynamic effect				
Nanosecond breakdown of water, containing suspended microparticles; higher recovery of Au at cyanidation by 60–70%	Random alteration of ion composition of liquid phase; impossibility of treatment of dry or wetted (by 10–15%) material; size of at least 90–100% of material is 74 μm class	3–5	Pilot laboratory machine; gold-bearing tailings of copper-zinc ore processing	Yu. A. Kotov, G. A. Mesyats, A. L. Filatov, et al., 2000
Superpowerful hyperimpact waves				
Micro-resonance disintegration of mineral complexes; higher yield by 20%	High energy consumption, insufficient selectivity of the effect	Maximum pressure in impact wave is ~ 1000 MPa	Pilot machine, any raw materials	V. Yu. Veroman, 1996

Magnetic impulse treatment				
Fracturing	Exclusively for minerals-ferromagnetics; low increase in recovery	Lower total energy consumption by 3–5 kWh/t	Laboratory and pilot commercial tests; ferriferous quartzites	S. A. Goncharov, et al., 2000–2005
Nanosecond high-power electromagnetic pulses (HPEMP)				
Disintegration and exposure of finely dispersed mineral complexes; higher recovery of noble metals at cyanidation by 10–80%; platinum-group metals (PGM) at centrifugal concentrators; at upgrading of rough concentrates by 5−6% at upgrading of tailings by 60−70%	Minimum size of a sample is ~100 μm; protective screening of impulse generator location is required; material humidity is less than 30%	2–3	Laboratory tests, semi-commercial tests at continuous-operating machine of 100 kg/h in production capacity; sulfide ores, quartzites, concentrated products (concentrates, tailings), containing noble metals and PGM	V. A. Chanturiya, Yu. V. Gulyaev, I. Zh. Bunin, V. D. Lunin, et al., IPKON RAN, IRE RAN, TsNIGRI, OOO "ITsPT", GMK "Norilsk Nickel", 1997–2007

Considerably better results were obtained under the ore exposure to the *accelerated electron beam* with energy of 1–2 MeV and current density of 1–5 μA/cm^2 before grinding (Chanturiya and Vigdergauz, 1995; Bochkarev et al., 1997). The physical background of the effect is the electric charge of the natural media of weak conductivity. This causes the emergence of microcracks, which lead to the softening of mineral components. The 20–80% increase of grinding efficiency, as well as the 15–20% raise of technological characteristics is observed under these conditions for all types of ores.

It is noteworthy that the most complicated technological process is the disintegration process of refractory (resistant) ores and beneficiation products. For example, 50–60% of precious metals contained in the raw material cannot be extracted in spite of the increased fineness of grinding. One of the noteworthy attempts to solve this problem was the irradiation of the ore by the *microwave* generator (Solovyev, 2001; Khvan et al., 2002; Kingman, 2004). The microwave generator provided a continuous radiation of 0.9–2.5 GHz frequency. The roast of the medium up to 360°C increased the yield of gold in several experiments, but no convincing results were obtained. In UHF treatment, heterogeneous (non-uniform) absorption of microwave energy by different components of the mineral complex results in embrittlement of the mineral matrix and destruction of its skeleton along the intergrowth boundaries, which "unseals" the valuable components, making them easier to extract. In addition, intense physicochemical processes occur on the surfaces of the sulfide samples exposed to UHF treatment: Pyrite oxidizes to hematite and elemental sulfur, and arsenopyrite oxidizes to magnetite, arsenic sulfide, and (minor) SO_2, which helps increase gold recovery up to 95%. However, excessive UHP heating results in unwanted effects, such as fusion and sintering of the material and closure of as-formed cracks. In addition, this procedure is energy-intensive, with energy consumption of at least 3–5 kWh per ton required to provide for plant capacity of 5–10 tons per day.

Magnetic pulse treatment of gold-containing ores is meant to reduce energy expenditure for milling and increase gold recovery (Goncharov et al., 2004). This technique is realized by passing the ore (or pulp) through a dielectric pipeline segment enclosed in a system of electromagnetic coils, which constantly generates

electromagnetic field pulses with repetition frequency up to 50 Hz. It is worthwhile to implement this technique in ore processing just before milling and to include it in the cyanidation procedure, which proves to yield a 1–1.5% gain in gold recovery in all.

A group of researchers affiliated in the Electrophysical Institute of the Uralian Branch of the Russian Academy of Sciences (Yekaterinburg) designed a plant for *electrohydraulic treatment* of resistant materials by nanosecond pulses with a positive polarity, a magnitude of up to 250 kV, and a repetition rate of up to 300 Hz (Kotov et al., 2000). This device does perform the mechanism of nanosecond breakdown of water (the electrohydraulic method proposed by L. A. Yutkin) with suspended microparticles, yet having significant limitations on efficiency, capacity, and energy consumption, and some other technological restrictions. In essence, electrohydraulic treatment is realized through exposing the test material immersed in liquid, to shock waves generated by electrical breakdown of the liquid, with an aim to destruct the resistant particles. The essential disadvantages of this method are the necessity of performing the process in a liquid medium with solid-to-liquid ratio S:L = 1:1, which decreases plant capacity and increases energy consumption, and non-controllable changes in ionic composition of the aqueous phase of the pulp. In particular, experiments with samples of stale tailings from the Uchala concentration plant revealed a sizable increase in concentration of Cu, Zn, and Fe ions in the aqueous phase of the pulp after electrohydraulic pulse treatment, which may disturb further processing and have negative environmental sequels.

All the high-energy treatment methods discussed above have the following disadvantages in common: high energy consumption, overheating of the material subject to processing, and certain intensification of sulfide leaching with uncontrollable passage of metal ions into the liquid pulp phase.

In this chapter, we present an advanced treatment method developed by IPKON RAS (Moscow) researchers in collaboration with specialists from IRE RAS, TsNIGRI (Moscow) and other organizations, which appears to be free of the disadvantages listed above. This non-traditional, highly efficient, and environmentally safe method of breaking up fine disseminated mineral complexes of precious metals is based on non-thermal action of *nanosecond high-power electromagnetic pulses* upon refractory precious metals

containing ores and beneficiation products (Chanturiya et al., 1999b, 2001b,c, 2003b; Bunin et al., 2001). The application of HPEMP irradiation in dressing of refractory gold-containing ores appears attractive as this technique provides for a significant increase in precious metal recovery (5–80% for gold and 20–50% for silver).

2.2 Mechanisms of Disintegration of Mineral Complexes Exposed to High-Power Electromagnetic Pulses

The main idea of using high-energy effects in the processing of resistant mineral complexes with an aim to selectively break up mineral intergrowths and provide free access of lixiviant solutions to finely dispersed precious metal particles consists in creating proper conditions for maximum concentration of mechanical stresses or energy promoting host rock disintegration sufficient for effective "unsealing" of valuable components. The application of HPEMP irradiation in dressing of resistant gold-containing ores appears attractive as this technique provides for a significant increase in precious metal recovery, therewith helping reduce both energy consumption and the cost of products. However, the diversified physical processes involved in the interaction of HPEMP with complex mineral media are as yet scantily known.

This study deals with three plausible mechanisms of disintegration of mineral particles under the action of nanosecond HPEMP with short leading edge (~1–5 ns) and pulse duration (~10–50 ns) and high electric field strength $E_p \sim 10^7$ V/m (comparable to or exceeding the electric strength of the test material in a static field). The first mechanism consists of loosening of the mineral structure due to electrical breakdown effects, which only occurs in cases where small, highly conductive inclusions are hosted in dielectric media. The second mechanism is related to development of thermomechanical stresses at the boundary (interface) between the dielectric and conductive mineral components. The third mechanism, assuming essentially non-thermal action of HPEMP on mineral complexes, is related to electromagnetic energy absorption by thin metallic films or layers much thinner than the characteristic skin layer.

2.2.1 Disintegration of Mineral Media Due to Electrical Breakdown

The action of HPEMP on a sample with conductive inclusions is accompanied by electric field strengthening in the vicinity of the boundary with maximum curvature. As a result, electrical breakdown occurs at lower E_p values (Fig. 2.1).

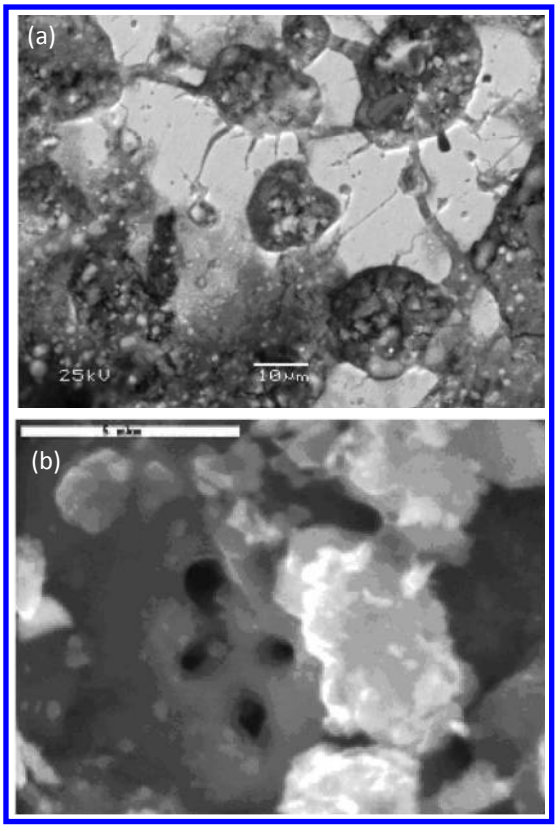

Figure 2.1 SEM image of the microstructure of destructive zones of sulfides surface after HPEMP irradiation: partial breakdown of arsenopyrite surface; scale bar is 10 μm (a) and output of the breakdown channel on the pyrite surface; scale bar is 5 μm (b).

The as-formed breakdown channels connect the conductive inclusions to each other and to the surface of the sample. Figure 2.2a presents experimental data, according to which the boundaries

of Au microinclusions in FeAsS (arsenopyrite) grains are initially (prior to irradiation) out of contact with joints in the host mineral matrix. Originally the joints in arsenopyrite grains have a spallation (cleavage) appearance, most of them being filled with some dust-like material. After HPEMP irradiation, the cracks prove to be empty of filling, and appear discontinuous (Fig. 2.2b). Most of these cracks are confined to boundaries between secondary mineral phase segregations and the arsenopyrite matrix, which suggests that HPEMP have a selective effect on the host mineral matrix.

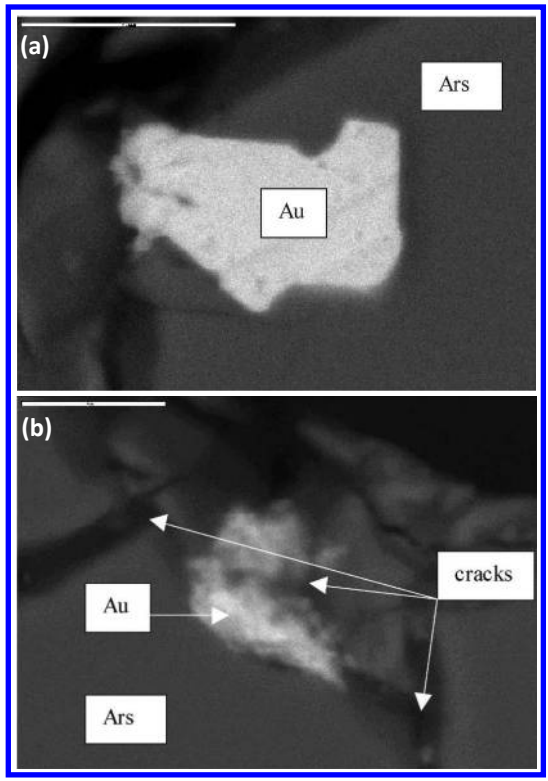

Figure 2.2 Native gold grain (Au) in arsenopyrite matrix (Ars) before (a) and after (b) irradiation with HPEMP; SEM images, scale bar is 10 μm.

The average per pulse amount of energy released in the developing breakdown channel is estimated as $w \approx W_0 t_p / t_0$, where $W_0 = \int_V d^3x (\varepsilon \vec{E}^2 / 8\pi)$ is electric field energy of the pulse in a particle of volume V, t_p is pulse duration, and t_0 is the time during which

the channel develops a length equal to the linear dimension of the particle (L). In essence, t_0 depends on the rate of channel development v_d, which is governed by the drift velocity of electrons in the avalanche at the head cusp of the developing channel, and depends on local field strength as $\propto\sqrt{E}$. For dielectrics with electrical strength about 50 MV/m, $v_d \cong$ 3–5 km/s, such that more than one pulse with t_p = 30 ns would be required to break down through a particle with L > 1 mm. Once the developing channel reaches the surface of the particle, the discharge becomes creeping, tending to neutralize the electric field throughout the entire particle volume. The total energy released in the channel is limited by the W_0 value (assuming that the particle under consideration is isolated from all other particles).

The size of the zone occupied by cracks (r_c) depends on energy density in the breakdown channel (Fig. 2.3). To calculate r_c, we used the following model considerations. Energy is released in the channel somewhat instantaneously as compared to the time it takes for the channel to expand, stress waves to propagate through the sample and the heated matter to flow out from the channel. The zone occupied by evaporated matter takes on the form of explosion cavity. Beyond the zone of evaporation, the material undergoes crushing, and in farther-away zones cracking due to azimuthal (radial) rupture stresses predominates.

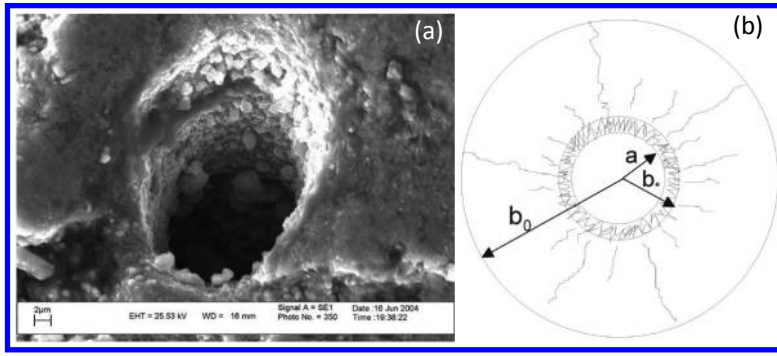

Figure 2.3 Breakdown channel in pyrite particle (a) and schematic image of damage zone around breakdown channel (b).

While a problem of cylindrical shock wave propagation is being solved in the zones of evaporation and crushing, for the cracking zone we use a quasi-static approximation based on equilibrium

equations. The relationship of r_c to initial gas pressure in the channel (P_0) can be approximately expressed as follows:

$$r_c = a_0 \frac{\sigma_* \kappa}{\sigma_c} \left(\frac{p_0}{\sigma_* \sqrt{\kappa}} \right)^{1/2\gamma'} \qquad \kappa^2 \equiv \frac{E}{2\sigma_*} \left[1 + \nu + \ln \frac{\sigma_*}{\sigma_c} \right]^{-1}, \tag{2.1}$$

where a_0 is the initial channel radius, γ is an adiabatic index for the gas in the channel, σ_* and σ_c denote the compression (crushing) and rupture strength parameters of the material exposed to HPEMP, E is Young's modulus, and ν is Poisson's ratio. For quartz samples with L = 0.3, 1, and 10 mm and HPEMP with E_p = 20 MV/m, we obtained r_c = 0.005, 0.08, and 0.5 mm, respectively. This mechanism would only work for relatively large particles (larger than L_{min} varying from 10^{-4} to 10^{-3} m) subject to disintegration, its efficiency increasing with increasing L and E_p.

2.2.2 Mechanism of Disintegration of Mineral Aggregates Subjected to Pulse-Heating

Disintegration of mineral particles through irradiation-induced cracking is possible for particles consisting of substances with differing conductivity, when subjected to pulse-heating (Fig. 2.4). Intensity of thermomechanical stresses is governed by heating contrast and dissimilarity of thermoelastic properties of the different material components.

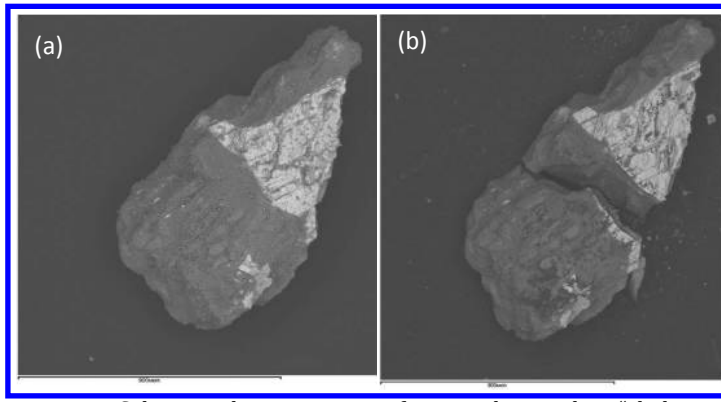

Figure 2.4 Selective disintegration of mineral complex "chalcopyrite (light color)–aluminum silicate" along grains boundary under HPEMP irradiation; SEM images; scale bar is 100 μm.

In the simplest case with axial symmetry, where two cylindrical parts (1 and 2) are in contact in the $z = 0$ plane, the quantities $u(r,z)$ and $s(r,z)$, respectively, characterizing displacement in the r and z directions, and the $\sigma_{\alpha\beta}$ (r,z) values characterizing stresses within each of the contacting parts are determined by the following equations of motion:

$$\frac{\partial\sigma_{rr}}{\partial r}+\frac{\partial\sigma_{rz}}{\partial z}+\frac{\sigma_{rr}-\sigma_{zz}}{r}=\rho\frac{\partial^2 u}{\partial t^2}, \tag{2.2}$$

$$\frac{\partial\sigma_{zz}}{\partial z}+\frac{\partial\sigma_{rz}}{\partial r}+\frac{\sigma_{zr}}{r}=\rho\frac{\partial^2 s}{\partial t^2} \tag{2.3}$$

with the following boundary conjugation (continuity) conditions: $u^{(1)}(r, z = 0) = u^{(2)}(r, z = 0)$.

The components of the deformation tensor

$$e_{rr} = \partial u/\partial r,\ e_{zz} = \partial s/\partial z,\ e_{\phi\varphi} = u/r,\ e_{rz} = \tfrac{1}{2}(\partial u/\partial z + \partial s/\partial r) \tag{2.4}$$

are related to $\sigma_{\alpha\beta}(r,z)$ as follows:

$$\sigma_{\alpha\beta} = 2Ge_{\alpha\beta} + (\lambda e - \beta\theta)\delta_{\alpha\beta},\ \sigma_{r\varphi} = \sigma_{z\varphi} = 0,\ e_{r\phi} = e_{z\phi} = 0, \tag{2.5}$$

where $\theta = \Delta T$ denotes the amount of heating of part 1 (or part 2), and G, λ, and β are related to Young's modulus E, Poisson's ratio ν, and thermal expansion coefficient α by the following expression:

$$G = E/2(\nu + 1),\ \lambda = E\nu/(1 + \nu)(1 - 2\nu),\ \text{and}\ \beta = \alpha E/(1 - 2\nu).$$

Shear stresses at the boundary between parts 1 and 2 can be determined approximately from the condition of equal displacement at the boundary, assuming that in the vicinity of the interface $u(r,z)$ can be considered independent of r and $s(r,z)$ independent of z, neglecting the acceleration, and disregarding temperature gradient within each of the contacting parts:

$$\tau = \frac{\beta_2\theta_2(2G_1+\lambda_1)-\beta_1\theta_1(2G_2+\lambda_2)}{2(G_1+G_2)+\lambda_2+\lambda_1},\ \cong \tilde{\mathrm{E}}\cdot\frac{3}{2}(\alpha_2\theta_2-\alpha_1\theta_1) \tag{2.6}$$

where $\tilde{\mathrm{E}} = 2E_1E_2/(E_1 + E_2)$. Stress values are maximum in cases where $\alpha_2 > \alpha_1, \theta_2 > \theta_1$ or $\alpha_2 < \alpha_1, \theta_2 < \theta_1$, (for example, in the FeS–Al_2O_3

complex FeS heats up stronger than Al_2O_3); in such situation, 30×10^{-6} Ẽθ_2. Owing to heat conduction, θ_2 at the boundary becomes nearly equal to θ_1 within $\sim 10^{-8}$ s of the pulse, such that only stresses related to dissimilarity of thermoelastic properties remain significant.

A single pulse with $E \sim 10^7$ V/m and $t_p \sim (3–10) \times 10^{-9}$ s generates stresses of 0.3 to 3 MPa at pyrite–gold or pyrite–quartz boundaries in complex samples, which would be insufficient for spallation along an ideal (perfect) boundary between the different components. However, in the presence of initial damage, small as it is, failure can build up in a sample irradiated with a series of pulses. For stress varying between 0.3 and 3 MPa, a small initiating crack of length $l_0 \times (l_0 < L)$ proves to be about $(0.2–2) \times 10^{-3}$ m. Since the linear dimension of the particle $L > l_0$, only particles with $L > (0.2–2) \times 10^{-3}$ m would be expected to disintegrate. For example, when dealing with pyrite–quartz or pyrite–gold contacts, 15 to 50 pulses with $E_p \sim 10^7$ V/m and $t_p = (3–10) \times 10^{-9}$ s suffice to break down a sample of size 3×10^{-3} m, and 100 to 300 pulses with the same parameters would be required to disintegrate a sample of size 10^{-2} m.

2.2.3 Non-Thermal Absorption of Electromagnetic Energy by Precious Metal Particles

One of the plausible mechanisms of nonthermal action of HPEMP on mineral complexes is related to the effect of electromagnetic energy absorption by thin metallic films or layers thinner than the characteristic skin layer. This particular case is suitable for describing the interaction of HPEMP with precious metal particles disseminated in resistant ores because the characteristic size of precious metal particles is very small (from submicrometric size ~0.01–0.1 μm to nanometric size ~10–100 nm), which may be significantly smaller than the characteristic wavelength of the irradiating pulse and the skin layer thickness (for particles of size 10^{-9} to 10^{-7} m, skin layer thickness is about 10^{-6} m).

Theoretical analysis of a simple 1D model, which considers an electromagnetic pulse striking a flat metallic layer of arbitrary thickness enclosed within a dielectric medium, allows the following conclusions. Interaction of high-power electromagnetic radiation with precious metal particles hosted in resistant ores may involve

highly efficient non-thermal absorption of electromagnetic energy by metal particles, which, at irradiating power high enough, may result in fast energy release and cause certain, changes in the host mineral structure. In particular, field strength within the mineral samples may increase significantly, and micro-breakdown features may develop between metal particles, which would result in microcracking, thus promoting the disintegration of mineral complexes.

To summarize, a feature in common to the disintegration mechanisms described above is the limitation on the minimum size of mineral complex related to low concentration of the irradiating energy. Increasing this concentration by increasing E_p or t_p would result in unwanted through breakdown of the discharge gap and decrease in heating contrast. The material would disintegrate efficiently provided that the pulse irradiation energy suffices for matter sublimation in the channel and the time it takes for this energy to be released is significantly shorter than the time required for heat transfer and dissipation of heat in surrounding zones. Maintaining the discharge further would result in redistribution of the permanently generated heat in the volume of the sample. As a result of *electrothermal breakdown*, this may give rise to unwanted effects, such as overheating, sintering of particles, fusion of particle surfaces and closure of as-formed microdamage, which would subsequently hinder the access of lixiviant solutions to valuable components hosted within the mineral particles.

2.3 Experimental

For industrial realization of nanosecond HPEMP method, the specialists affiliated in IPKON RAS (Moscow) and Ltd "FON" (Ryazan') designed a plant with capacity of 100–300 kg (of ore subject to processing) per hour using a conveyer mode of conveying ore into the zone of electromagnetic pulse treatment (Fig. 2.5).

The plant includes the following units: voltage converter, master pulse generator, capacitive energy accumulator, transportation system, and electrode unit. The efficiency of disintegration of mineral complexes and breaking up ("unsealing") of precious metal particles is controlled by the development of a streamer discharge in the gap between the electrodes through proper selection of the magnitude, duration, and shape of pulses. The required "dose" of

electromagnetic pulse effect for the specified mass of the mineral material to be processed is attained by varying the speed of conveyer belt movement and repetition frequency of pulses from the pulse shaper. The flow of the material subject to processing is conveyed (with equalized thickness and limited width) into the unit of high-energy treatment with nanosecond high-voltage pulses with the following characteristics: voltage amplitude 20–50 kV; pulse duration 10–20 ns pulse repetition frequency 10–500 Hz, with total plant power consumption not greater than 3 kW. Thus, setting the appropriate electrophysical parameters from the control panel, one can obtain the desired technological effect, therewith providing for proper plant capacity depending on the sort of mineral material being processed.

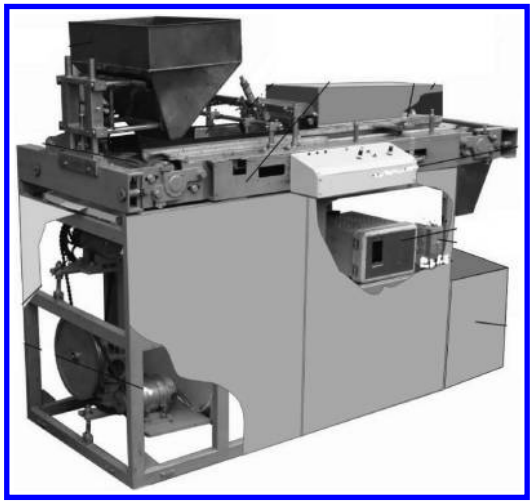

Figure 2.5 Pulsed power installation for nanosecond HPEMP treatment of rebellious precious metals containing ores and beneficiation products.

We carried out a series of experiments with an aim to examine the effect of recurring HPEMP on the processing (technological) characteristics of particles of gold-(silver-)containing materials. Experiments on HPEMP-induced effects were performed with various materials, including samples of resistant ores, beneficiation products (gravitational and flotation concentrates) and stale tailings from concentration plants. A feature in common to all the materials selected for study was the presence of finely dispersed

gold, much of this gold being related to sulfide minerals, predominantly pyrite and arsenopyrite.

Experiments on breaking-up by HPEMP were made with resistant pyrite-arsenopyrite concentrates of ores from the Nezhdaninskoye (gravity concentrate, gold content—80 ppm, particle sizes—500 μm) and Klyuchevskoye (flotation concentrate, gold content—29 ppm, particle sizes—100 μm) deposits and samples of stale sulfide tailings from the Aleksandrinskoye (Au—2.34 ppm, particle sizes—74 μm), Gai (Au—2.0 ppm, 315 μm), Uchala (Au—2.1 ppm, 74 μm), Urup (Au—1.0 ppm, 315 μm), and Uzelga (Au—2.24 ppm, 74 μm) integrated mining-and-dressing works.

The experimental procedure included pre-treatment of mineral particles with a series of HPEMP, followed by cyanidation to extract precious metals. The experiments involved both dry samples and samples wetted with water in amount not greater than enough to fill the pores in mineral particles, i.e., to attain the solid-to-liquid ratio S:L = (5–10):1. The number of pulses in a series and the irradiation parameters (pulse shape and duration) varied depending on particular experimental conditions. The appropriate value of electric field strength magnitude of the electromagnetic field (varying from 5 to 50 MV/m) exceeding the electrical strength of the material was attained through adjusting the gap between the electrodes and their insulation.

The assessment of breaking-up efficiency for gold-containing mineral products was based on the results of cyanidation of the samples of gold-containing sulfides before and after (with and without) irradiation with high-power electromagnetic pulses. Gold content of solid products (initial specimens and cyanidation tailings) was determined by assaying. Gold content of pregnant (post-cyanidation) lixivia was determined by the atomic absorption method using a Perkin-Elmer spectrometer.

The employment of HPEMP in dressing-resistant gold-containing ores and beneficiation products appears attractive as it provides for maximum breaking-up efficiency for the mineral complexes being processed and a significant gain in valuable components recovery (5–80% for gold and 20–50% for silver). Data on gain in gold recovery by sorption cyanidation during 36 h from gold-containing ores, concentrates and other processing products from different deposits after HPEMP treatment are given in Table 2.2.

Table 2.2 Effect of HPEMP irradiation on gold extraction by cyanidation from resistant gold-containing ores and beneficiation products from Russian deposits

Deposit; gold content (ppm)	Size class (μm)	Gain in gold recovery (from → to) (%)
Initial ore		
Kyuchus, 24.2	−1000	12.1 (66.7 → 78.8)
Nevskoye, 1.3–1.8	−500	4.4 (91.2 → 95.6)
Olimpiadinskoye, 2.4	−100	8.3 (60.0 → 68.3)
Products (concentrates) Gravitational		
Nezhdaninskoye, 80	−50	6.41 (77 → 83.4)
	−500	31.1 (51.2 → 82.3)
Flotation		
Klyuchevskoye, 29	−100	47 (40 → 87)
Kumtor (Kyrgyzstan), 45	−20	5.7 (82 → 87.7)
	−140	8 (63 → 71)
Tailing from concentration plants		
Aleksandrinskoye, 2.34	−74	31.2 (52.6 → 83.8)
Gai, 2	−315	80 (11 → 91)
Uchala, 2.1	−74	30 (13 → 43)
Urup, 1.1	−315	71.1 (8.5 → 79.6)
Uzelga, 2.24	−74	36.8 (6.2 → 43)

A series of process experiments confirmed the theoretical assumption that maximum breaking-up efficiency after HPEMP treatment would be expected from gold-containing sulfides not finer grained than 200–100 μm, and that the effect of formation of breakdown channels and selective disintegration is enhanced predominantly for wet samples.

In particular, for a gravitational concentrate of ore from the Nezhdaninskoye deposit exposed to HPEMP rather high gain in precious metal recovery was obtained with minimum energy expenditure of just 2 kWh per ton of concentrate being processed and 0.064 kWh per gram of additionally recovered gold, while

energy consumption in a process involving mechanical grinding of the −500 μm ore to −50 μm were about 20–25 kWh per ton of ore and 0.9 kWh per gram of additionally recovered gold. This fact indicates that the proposed technique provides for highly efficient breaking up of resistant ore products, primarily owing to partial destruction of mineral complexes and generation of breakdown channels promoting the access of lixiviant to gold and silver particles, which would help radically reduce energy consumption for additional comminution of coarse-grained disperse products. Comparison of data on gold and silver extraction by cyanidation from the gravity ore concentrate from the Nezhdaninskoye deposit obtained with and without irradiation with HPEMP (Table 2.3) confirms the obvious advantage of the electromagnetic pulse processing over mechanical comminution.

Table 2.3 Gold and silver extraction by cyanidation from a resistant gold-containing concentrate of Nezhdaninskoye deposit ores

Pre–cyanidation processing	Recovery (%)	
	Gold	Silver
No processing (material in its initial state)		
−0.05 mm size class	79.4	44.0
−0.50 mm size class	51.2	21.8
Irradiation with HPEMP		
−0.05 mm size class	83.4	73.7
−0.50 mm size class	82.3	68.8

Preliminary processing of gravity concentrate of Nezhdaninskoye deposit ore with a series of HPEMP resulted in significant increase of gold and silver extraction into lixivia during the cyanidation stage, with gold recovery increased by 31.1% (from 51.2% in a blank test to 82.3% after irradiation) and silver recovery increased by 47% (from 21.8% to 68.8%). Gold recovery from flotation concentrate of Klyuchevskoye deposit ore increased after irradiation with HPEMP from 40% to 86.3%.

Gold recovery from stale gold-containing dressing tailings increased after pulses-irradiation from 6.3–52.6% to 43–91%.

Several series of tests performed in IPKON RAS together with Mining and Metallurgical Center of the Zapolyarnyi Affiliate of

"Norilsk Nickel" Corporation yielded an absolute gain in noble metals recovery from the beneficiation products of disseminated copper-nickel ores, up to 75% for gold and 52–67% for platinum-group metals, with resultant gold recovery as high as 88.3% and with resultant palladium recovery as high as 70% and resultant platinum recovery as high as 82%. In this case, the desired technological effect has been achieved due to use of a preliminary HPEMP-irradiation and the subsequent comminution during 15 min and specific gravity processing in the "Knelson" centrifugal concentrator.

Special experiments were carried out with the purpose to study the affect of HPEMP on subsequent *bioleaching* of pyrite-bearing gravity concentrate (FeS_2—80%; –1 + 0 mm) obtained from Kalarsky ore (Siberia, Russia). In this experiment, the concentrate initially subjected to nanosecond electric-pulse treatment was placed into a medium (solid-to-liquid ratio of 1:5), containing autotrophic thionic bacilli (*Acidithiobacillus thiooxidans*, *Acidithiobacillus ferrooxidans*, and *Leptospirillum ferrooxidans*) extracted from the sulfide ore. The results of measurements were compared with the data obtained from experiment with specimens subjected to biological treatment but without the previous energy attack.

Because of HPEMP treatment, the pyrite particles were observed to disintegrate, while their subsequent biological treatment caused their further fracture and liberation of the mineral matrix. Under the impact of nanosecond pulses, the yield of coarser fractions (–1 + 0.5 mm) tends to decrease from 13% to 5.7%. The bacterial leaching brought about an intensive formation of defects on the surfaces of the grains, as well as the growth of localized corroded patches on mineral surfaces. After impulse input and during biological treatment the pH and Eh parameters of the productive solution tend to decrease (pH) and to increase (Eh) (Fig. 2.6).

The combination of HPEMP impact and biological leaching added by enforced aeration (air blowing) decrease pyrite content by 25% compared with 13.3% in a check test. After HPEMP treatment with natural aeration (mechanical agitation), the leaching affected 7.2% of pyrite against a mere 2% in the check test. In this case, the amount of elementary sulfur on pyrite surface substantially increases when aeration is provided (from 12×10^{-2} mg/g for biological treatment to 40.6×10^{-2} mg/g for

HPEMP and biological treatment). The results so far obtained testify to a high efficiency of non-thermal HPEMP impact combined with bacterial leaching of sulfide minerals. This fact has allowed to develop a new technology for disintegration and breaking-up for refractory gold-bearing mineral products (patent RF 222 6560).

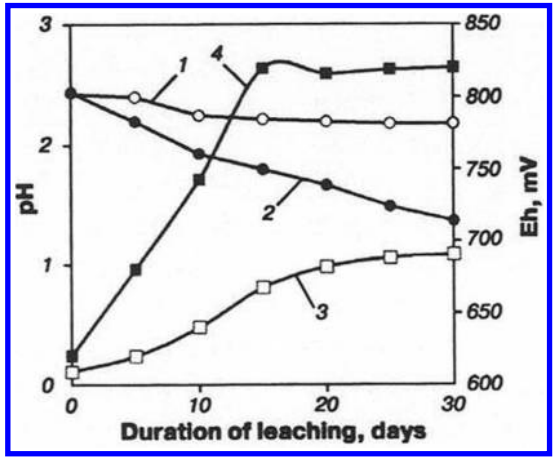

Figure 2.6 Changing of pH (1, 2) and Eh (3, 4) of liquid phase of bacterial leaching products depending on duration of leaching for various types of pyrite concentrate treatment: 1, 3—bacterial leaching; 2, 4—HPEMP + bacterial leaching.

2.4 Conclusions

A feasibility study of the principal non-traditional methods of high-energy treatment of resistant gold-containing mineral products designed to intensify the disintegration of mineral complexes with fine disseminated valuable components has been performed. The advantages of highly efficient and environmentally safe method based on non-thermal action of nanosecond HPEMP are shown.

The main plausible mechanisms of non-thermal action of nanosecond HPEMP on complex natural mineral media (like gold-containing sulfide and quartz ores and beneficiation products) have been analyzed. It was demonstrated that maximum breaking-up efficiency after HPEMP treatment would be expected from gold-containing sulfides not finer grained than 200–100 μm, and that the effect of formation of breakdown channels and selective disintegration is enhanced predominantly for wet samples.

Preliminary processing of dressing-resistant gold-containing ores and beneficiation products with a series of nanosecond HPEMP resulted in significant increase of gold and silver extraction into lixivia during the cyanidation stage (5–80% for gold and 20–50% for silver), therewith helping reduce both energy consumption and the cost of products.

Acknowledgments

The authors acknowledge the financial support from the Program of the Geoscience Branch of Russian Academy of Science "Nanoparticles in Natural and Technogenic Systems" and the Program of the Presidium of Russian Academy of Science "Development Engineering of Chemical Substance and Advanced Materials."

References

Abouzeid, A. Z. M., and Fuerstenau, D. W. (2000). *Proc. XXI Int. Miner. Process. Congress.* A4.

Bochkarev, G. R., et al. (1997). *Proc. XX Int. Miner. Process. Congress.*, **1**, 231–243.

Bunin, I. J., et al. (2001). *Proc. Rus. Acad. Sci. (Izvestiya RAN). Ser. Phys.*, **65**(12), 1788–1792.

Chanturiya, V. A., and Vigdergauz, V. E. (1993). *Electrochemistry of Sulphides. Theory and Practice of Flotation*, Nauka, Moscow.

Chanturiya, V. A., and Vigdergauz, V. E. (1995). *Mining J.* (Gorny Zhurnal), **7**, 53–57.

Chanturiya, V. A. (1999a). *J. Mining Sci.*, **3**, 107–121.

Chanturiya, V. A. (1999b). *Repts. Rus. Sci.* (Doklady RAN), **366**(5), 680–683.

Chanturiya, V. A., et al. (2000). *J. Mining Sci.*, **4**, 102–108.

Chanturiya, V. A., et al. (2001a). *Eur. J. Mineral Process. Environ. Prot.*, **1**(1), 25–41.

Chanturiya, V. A., et al. (2001b). *Repts. Rus. Acad. Sci.* (Doklady RAN), **379**(3), 372–376.

Chanturiya, V. A., et al. (2001c). *J. Mining Sci.*, **4**, 95–106.

Chanturiya, V. A. (2003a). *Geology Ore Deposits*, **45**(4), 321–328.

Chanturiya, V. A., et al. (2003b). *Proc. of XXII Int. Miner. Process. Congress*, Cape Town, **1**, 232–241.

Chanturiya, V. A., and Bunin, I. Z. (2007). *J. Mining Sci.*, **43**(3), 311–330.

Goncharov, S. A., et al. (2004). *Inf. Anal. Mining Bull.* (Gorny informatsionno-analiticheskiy byulleten'), **7**, 5–7.

Kingman, S. W., et al. (2004). *Int. J. Miner. Process*, **1–4**, 71–83.

Khvan, A. V., et al. (2002). *Mining Bull. Uzbekistan* (Gorny vestnik Uzbekistana), **2**(9), 56–60.

Kotov, Yu. A., et al. (2000). *Repts. Rus. Acad. Sci.* (Doklady RAN), **372**(5), 654–656.

Kurets, V. I., et al. (2002). *Electromagnetic-Pulse-Induced Disintegration of Materials*, Kola Scientific Center of RAS, Apatity.

Mesyats, G. A. (2004). *Pulsed Power: Methods and Applications*, Nauka, Moscow.

Sander, U., and Schonert, K. (2000). *Proc. XXI Int. Miner. Process. Congress*, A4.

Solovyev, V. I. (2001). *Ore Beneficiaton* (Obogashcheniye rud), **2**, 13–14.

Chapter 3

Modeling of Software Sensors in Bioprocess

Luca Belmonte and Claudio Nicolini

Laboratories of Biophysics and Nanobiotechnologies, Department of Experimental Medicine, University of Genoa, Via Pastore 3, Genoa 16130, Italy

claudio.nicolini@unige.it

The recent development of techniques such as nucleic acid programmable protein array (NAPPA) and SNAP for gene expression directly on quartz brought to the need to develop new technologies for compounds' identification. Indeed, these latter non-conventional methods lead to the need for a more sophisticated algorithm for peak recognition since they face the problem of master mix and lysate molecules spectra as background. A wide range of tools are available to identify protein mass spectra but are optimized for conventional MS analysis and spectra have to be composed of a few molecular species. None of them is optimized for background subtraction. A first attempt to overcome the troubles discussed so far was the development of *Spectrum Analyzer and DataSet manager (SpADS)*—an R script for MS data preprocessing—which is discussed here and adapted to provide software sensing for Quartz Crystal Microbalance with Dissipation factor

Nanobiotechnology in Energy, Environment, and Electronics: Methods and Applications
Edited by Claudio Nicolini

ISBN 978-981-4463-96-6 (Hardcover), 978-981-4463-97-3 (eBook)
www.panstanford.com

monitoring application. SpADS provides useful preprocessing functions such as binning and peak extractions, as an available tool, and is able to provide functions of spectra background subtraction and dataset managing. It is entirely developed in R and thus free of charge. Some features were added in order to provide an algorithm for Michaelis–Menten constant calculation and normalized *D*-Factor calculation. Finally, 3D plot functions were added, too.

3.1 Introduction: An Overview on Sensors

Sensors (or *detectors*) are usually considered a part of a device called *transducer*; the former is the device component able to detect a variation of the physical quantity to be measured and the latter is necessary to acquire and process those data. The two terms—sensor and transducer—are currently used with the same meaning and even in this book are referred to as being the same. A sensor is used to make a physical quantity more and more understandable by an observer changing from a physical quantity to another but without loss of information. With the expansion of electronics nowadays, such kind of devices are used even for the elaboration of "observed quantity"—through software processing of data—and not only for a simple physical quantity variation view. Indeed, software sensors combine both hardware and software approaches to provide estimation of variable unmeasurable otherwise, such as kinetic parameters [9]. Moreover, the integration of computational logic allows pervasive systems. Indeed, *ubiquitous computing* refers to software and computing integration in "everyday life" in a really invisible way to users [1–3], using Pad, PCs, and sensors. Context-aware systems catch user's needs in order to translate their requirements and activities in signals and information: *"machines that fit the human environment instead of forcing humans to enter theirs"* [4]. This latter paradigm is also called pervasive computing, ambient intelligence [5], or more recently everywhere [6]. Recent advances in micro-electro-mechanical-systems (MEMS) technology, wireless communications, and digital electronics have enabled the construction and development of wireless low-cost and low-power sensor networks [7]. Tiny sensors are used as nodes able to sense and process data and communicate with each other—or to a central unit—the results of their sensing. Sensor nodes are able to

process data due to an onboard processing unit, this allows one to send partially processed data to a central processing unit. This task can be accomplished only by using sensors. Thus, a computational section integrated into the transducer is needed to make new devices directly interact with humans and other devices.

Modern sensor applications can cover a wide range of application fields depending on the type of sensors applied. Sensor application can range from ambient conditions to health or from military applications to commercial and home applications. Sensors can be used for continuous sensing or event detection, they can generate response on real time or not, and moreover, they can be used for control actuators. As shown in [7], sensors application could be categorized as the following: military, environment, health, home, commercial, space exploration, chemical processing, and disaster relief. To summarize, a sensor is a device that shows different characteristics, i.e., sensibility to a physical quantity and selectivity. As for the hardware, even the software needs to show these latter different characteristics. Moreover, it has to be consistent with sensor characteristics, such as sensitivity, resolution, accuracy, reliability, response time, and hence forth. In this chapter, we will mainly focus on the so-called *software sensors*, a kind of software that is able to detect unmeasurable variables through algorithm implementation.

In the **first part** of this chapter, definitions of hardware and software sensors will be provided, and in the **second part** of the chapter, mathematical modeling will be discussed with an introduction to problem for software sensor implementation. Finally, a practical example will be given to the reader, discussing project and software implementation approaches for a new kind of QCM_D software sensor able to detect Michaelis–Menten constants.

3.1.1 Hardware Sensors

Although this chapter is mainly focused on software sensors, a brief description of a modern sensor architecture will be given here. In particular, we will focus on a general-purpose schema of the sensor architecture mainly used in wireless sensors and useful for our purposes. In a modern concept, a sensor is made up of four different sections [7], as shown in Fig. 3.1. Components of sensors are not only the sensing unit and the transducer unit, but modern

sensors are constituted even of a processing unit, a transceiver unit, and a power supply unit. To summarize, the basic configuration of a modern sensor architecture is made up of the following units:

(i) *Sensing unit*: It is the section that senses the variation of the physical quantity to be observed. Analog signals are then sent to an analog–digital converter (ADC) that encodes this signal to the digital form.
(ii) *Processing unit*: Fed by the ADC, it is able to process data, executing some dedicated algorithms. Usually it is coupled with a storage unit.
(iii) *Transceiver unit*: It connects the sensor with other sensors, calculator, or more generally with the Internet.
(iv) *Power supply unit*.

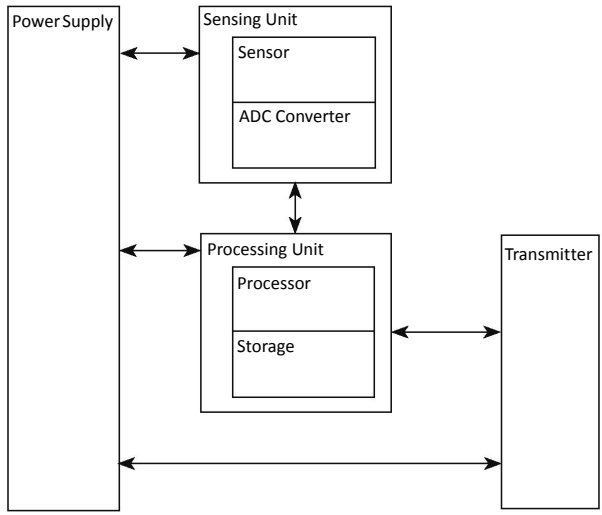

Figure 3.1 Diagram of hardware sensor components.

3.1.2 Software Sensors

Software sensors are able to detect hardware sensors' output signals and to process them with dedicated algorithms. Dedicated algorithms are the software piece of the software sensor and they could implement heuristics [10,11] or estimation algorithms. Thus, as shown in [9], software sensors are mainly composed of two main parts (Fig. 3.2):

(1) *Hardware sensor*: It provides the online measurement of the observed quantity in real time.
(2) *Software sensor*: It provides the estimation of unmeasurable quantity converging toward the real values of the unmeasured variables applying algorithms in real time to the data provided by hardware sensors.

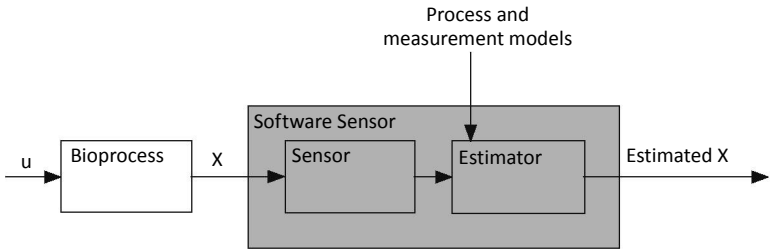

Figure 3.2 Software-sensor scheme as in Cheruy (1997).

Synthesis of this kind of estimation algorithm is not always possible, and a mathematical modeling of the target variables is needed. Software sensors are mainly used in biofields and are useful in the monitoring of the bioprocess. The development of sensors coupled with the central unit for cholesterol detection in blood is only an example of the power of this technique.

3.2 Mathematical Modeling of a Software Sensor

Software sensors are useful tools in the fields in which it is not possible to measure a particular variable or kinetic parameter. These types of sensors are widely used and are mainly used in bioprocessing control. To avoid bottleneck due to lack of hardware sensors, estimation algorithms should be provided for the estimation of these unmeasurable variable. Unfortunately, the implementation of an estimation algorithm is not always possible due to model knowledge limitation or reliability of the algorithm input parameters provided by the hardware sensor. Development of a mathematical model plays a key role in the implementation of this kind of software. The following sections discuss the estimation and indirect measurement of the target variables. Indeed, there are several ways in which these parameters can be retrieved [14].

A method called adaptive method is one of the more interesting ways for bioprocess control, and it is based on time-varying parameters. Bioprocess models are *"mainly based on mass balance equations with kinetics parameters which are badly known functions of process variable"* [9]. Considering these kinetic parameters as unknown, and time-varying, adaptive techniques for online estimation, state variables of the process should be used [12–14] as a generic nonlinear function. These are the following:

$$M = f(X, k) \tag{3.1}$$

$$\frac{dX}{dt} = g(X, u, k), \tag{3.2}$$

where k is the unknown kinetic parameters, M the measured variable, X the state variable, and u the control variable.

3.2.1 Indirect Measurement and Estimation

Indirect X state variables' measurements are given by simulating process model (Eq. 3.2). In this way, unknown kinetics parameters are deleted and substituted by a measurement function (M) [9]. This technique is applicable only if the models (Eqs. 3.1 and 3.2) have suitable structure properties [9]. An adaptive observer delivers estimated process variables by process model simulation with a corrective term that is proportional to the difference between the measurement and its prediction [9]. Moreover, the kinetic values, which are unknown, are updated at every time according to the measurement prediction error. The observer basic equations [9] are as follows:

$$\frac{dX_e}{dt} = g(X_e, u, k_e) + K_1(M - f(X_e + k_e)) \quad \text{for } X \text{ estimation} \tag{3.3}$$

$$\frac{dk_e}{dt} = K_2(M - f(X_e k_e)) \quad \text{for } k \text{ estimation} \tag{3.4}$$

where K_1 and K_2 are the designed observer parameters and have to be defined in order to ensure estimation convergence and performances. A solution can be theoretically guaranteed for such nonlinear systems only if the measurements M are state variables as proved under realistic conditions [13].

3.2.2 QCM_D-SNAP Combined Approach for Enzymatic Kinetic Calculation

Nucleic acid programmable protein array (NAPPA) is an innovative kind of self assembling protein microarray [34]. The NAPPA method allows for functional proteins to be synthesized in situ directly from printed cDNAs just in time for assay [34,35] using cDNA encoding the target proteins. The proteins are translated using a reconstituted *Escherichia coli* coupled in the cell-free expression system. The addition of a SNAP tag to each protein enables attachment to the array through an antibody printed simultaneously with the expression plasmid. This leads to irreversible covalent labeling of the SNAP-tag with a synthetic probe [36]. The whole system discussed so far was proposed on a nanogravimeter quartz in order to monitor protein expression directly in situ. The Michaelis–Menten approach will be discussed in this section in order to monitor the interaction of substrates and enzymes. Since these latter parameters are not directly measurable, the implementation of a software sensor was needed. The implementation of this software sensor implies two main troubles to be solved: a flux measurement in which the Michaelis–Menten constant will be calculated and a statistical measurement in which a *D* factor will be measured. Thus, two different mathematical models have to be built. These two models will be then translated into software classes; their definitions are provided in the following sections. For further details on QCM_D apparatus architecture, see [37].

3.2.2.1 Michaelis–Menten Kinetic

As discussed previously, an implementation of the kinetic of Michaelis–Menten will be implemented in order to implement a software sensor, and a brief discussion on the latter will be provided in the following.

The Michaelis–Menten kinetic is useful in understanding the affinity rate of a substrate and an enzyme. If enzyme concentration is much less than the substrate concentration, the rate of product formation is given by

$$v = \frac{d[P]}{dt} = V_{\max} \frac{[S]}{K_m + [S]} = k_{cat}[E]_0 \frac{[S]}{K_m + [S]} \tag{3.5}$$

The reaction rate increases with increasing substrate concentration [S], asymptotically approaching its maximum rate, V_{max} [28]. It also follows that

$$V_{max} = k_{cat} \times [E]_0. \tag{3.6}$$

Thus,

$$k_{cat} = \frac{V_{max}}{[E]_0}, \tag{3.7}$$

where $[E]_0$ is the enzyme concentration and k_{cat} is the maximum number of substrate molecules converted to product per enzyme molecule per second. The Michaelis constant, K_m, is the substrate concentration at which the reaction rate is at half-maximum and is an inverse measure of the substrate's enzyme affinity; the smaller the K_m, the higher the affinity. Thus, the rate will approach V_{max} quickly [22]. Moreover, the value of K_m is dependent on both the enzyme and the substrate. This model is used in a variety of biochemical fields. A few examples are enzyme–substrate interaction, antigen–antibody binding, DNA–DNA hybridization, and protein–protein interaction [22,23]. A typical method for V_{max} and K_m constant calculation is to run a series of enzyme assays at different substrate concentrations [S], with a known initial reaction rate, v_0. This latter means that the reaction rate is measured after a short time period in which the enzyme–substrate complex has formed and the substrate concentration is constant [27]. By plotting reaction rate against concentration, and using nonlinear regression of the Michaelis–Menten equation, the parameters may be obtained [24].

3.2.2.2 Normalized *D* factor definition

Dissipation factor—here called *Normalized D Factor*—is calculated by nanogravimetry measurement on a substrate interacting with an enzyme. It is calculated as ratio of *Half Width at Half Maximum* (HWHM) and the maximum frequency value on a frequency versus the *Gaussian*-shaped time function. A formal definition is given here as follows:

$$D_{norm} = \frac{\text{HWHM}}{f_0}, \tag{3.8}$$

where

$$\text{HWHM} = \frac{\text{FWHM}}{2}, \tag{3.9}$$

f_0 is the maximum frequency value on the Gaussian shape curve, and full width at half maximum (FWHM) is

$$\text{FWHM} = 2\sqrt{2\ln(2)}\sigma \approx 2.355\sigma \tag{3.10}$$

The Gaussian shape curve can be defined as

$$f(x) = \frac{1}{\sigma\sqrt{2\pi}} \exp - \left[\frac{(x - x_0)^2}{2\sigma^2} \right]. \tag{3.11}$$

3.3 Project of a Software Sensor

Before proceeding with software implementation details, in the following sections, we will show how the software package was projected. This will be done using unified modeling language (UML) diagrams. UML is a standardized general-purpose modeling language for object-oriented software engineering. This standard was created by the Object Management Group and became the industry standard for modeling software-intensive systems [20].

3.3.1 Use Case Diagram

The following use case diagram will show how main functionalities will be available for users. Indeed (Fig. 3.3), this kind of diagram is really easy to understand. The user can acquire a spectrum of both classical nanogravimetry measurements, i.e., in function of a frequency delta, and normalized *D* factor spectrum. Afterward, Michaelis–Menten kinetic parameters can be calculated.

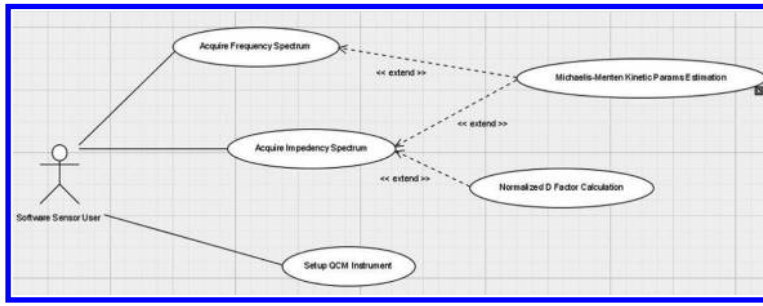

Figure 3.3 UML "use case" diagram for QCM_D usage.

3.3.2 Component Diagram

In this section, a UML component diagram is shown and discussed. As can be noticed, only the software sensor core component is discussed, since this is the main purpose of this chapter. For further details on other component please refer to [37]. Different classes are implemented for the making of this component, as described in the following:

(1) A dedicated section for the reading of a spectra provided by the QCM hardware/software is needed. Indeed, this kind of files are text files and discussed in details in the next section.
(2) A preprocessing section for the cleaning of the input signal: It includes different classes, normalization, binning, and smoothing, which are discussed in details in the software implementation section.
(3) A processing section: It is made up of two different main classes that are the normalized *D* factor class and the Michaelis–Menten kinetic class. The latter is based on the *D* factor class output.

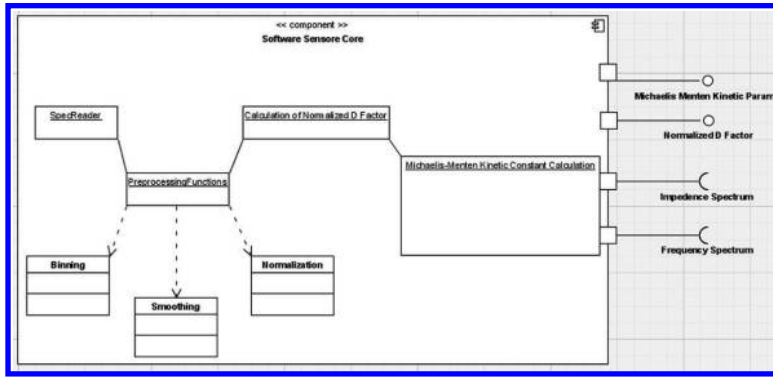

Figure 3.4 UML "Component diagram" for QCM_D software sensor core design.

3.3.3 Deployment Diagram

The UML deployment diagram is shown in this section, specifying input and output parameters for each component of the software sensor. Those parameters are expected on ports and shown in details in Fig. 3.5.

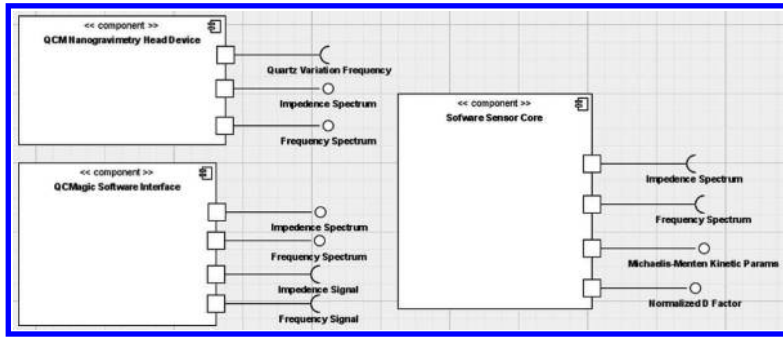

Figure 3.5 UML "Deployment Diagram" for a QCM_D software sensor.

A schematic device routing view is shown in Fig. 3.6, in which a flow pump linked to the quartz chamber is shown. Quartz frequency variation is monitored by a nanogravimetry head. The output is sent to a dedicated PC on which QCMagic software and the software sensor are running.

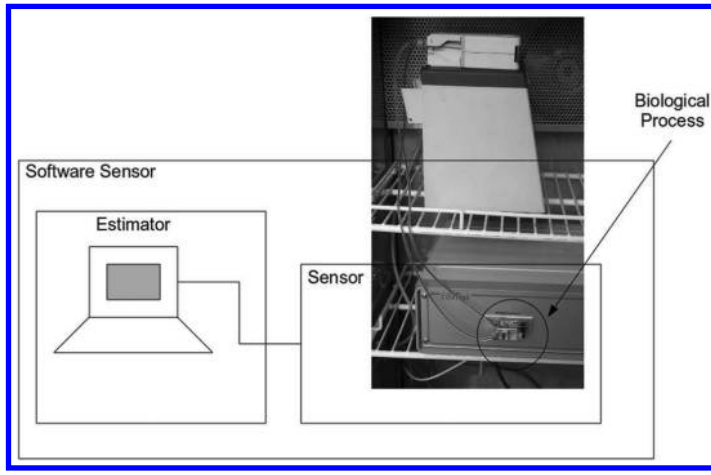

Figure 3.6 Schematic signal routing view of the QCM_D Sensor. Black boxes are shown.

3.4 Implementation of a QCM-D Software Sensor

This section shows the implementation of QCM_D software sensor. For the first trial, R language was used to implement mathematical

models discussed in Section 3.2. R is an open source programming language and software environment for statistical computing and graphics. It is widely used among statisticians for developing statistical software [15,16] and data analysis [16] and even in biological and scientific fields. R was created at the University of Auckland, New Zealand, by R. Ihaka and R. Gentleman [17]. A development team is still working on its update. R is part of the GNU project [18,19], and it uses a command line interface. In the following, an adapted version of SpADS [39] that implements all the functions discussed so far will be discussed. Moreover, this software was fed by the output of QCMagic software by Elbatech. For further details, please refer to [29–32].

3.4.1 Input File Format

In the chapter, we will assume the output of the QCM hardware as a large sequence of pairs of values; each pair contains an intensity value, dependent on the amount of the biomolecule found within the compound, and from a value of frequency or *D* factor shift depending on the molecular mass of the biomolecule. Both input and output SpADS files are in ASCII format.

3.4.2 Preprocessing

Data produced by the QCM—and usually by spectrometers of all kinds—however, are plagued by noise and errors due to different factors that are roughly compound preparation and distortion and noise introduced by analysis tools. Thus, preprocessing techniques are needed to avoid such kind of errors. Errors can be avoided by a better preparation of the compound, better extraction of the proteins and data processing. In any case, there are other imperfections due to distortion and peak broadening, saturation and distortion of the instrument, incorrect calibration of the instrument and various kinds of contamination. Data cleaning is performed in two different steps: better preparation of the compound and application of preprocessing algorithms to the data obtained by the spectrometer. For the purposes of this chapter, we will focus only on the stage of the implementation of algorithms preprocessing. Preprocessing algorithms provided by the dedicated section of the software sensors are normalization, smoothing, and

baseline subtraction. Normalization and noise reduction can be carried out as software tools applied to QCM output data. Each of these techniques aims at noise reduction. Baseline subtraction flattens the base profile of a spectrum while smoothing reduces the noise level in the whole spectrum. Each spectrum exhibits a level of intensity of the basis (the baseline) that varies spectra by spectra, this must be identified and subtracted.

3.4.2.1 Noise suppression: smoothing

Smoothing is a process by which a point is averaged with its neighbor in a time series of data. The purpose of this technique is to increase the ratio between signal and noise. The process behind this technique is very simple. The simplest is the process called moving average that is based on equidistant points. An array of raw data is converted into an array of "points smoothed" (smoothed points), in which each of these points is the average of $2n + 1$ consecutive points unpaired raw data. The number $2n + 1$ unpaired is generally called filtering window. Smoothing was done using LOESS function provided by R package and available from the R 2.0.1 version or later.

3.4.2.2 Data reduction: binning and intensity normalization

Binning procedure is one of the most used techniques in mass spectrometry data preprocessing analysis [33], and it could be useful in our problems to avoid samples with a huge number of data. Its aim is to preserve information from raw data performing a dimensional reduction before data processing. The data reduction takes place by grouping the data measured in *bins*. This procedure groups adjacent values by electing a representative one. Using a mass spectrometry example, this means collecting a pair dataset such as $[(I_1, MZ_1), (I_2, MZ_2), \ldots, (I_n, MZ_N)]$ and replace them with a single pair $[(I, mZ)]$, where I is given by an aggregate function on N intensity values of the data and the charged mass mZ is usually chosen among the original values mZ. These basic operations are conducted using a sliding window across the mZ spectrum axis. Therefore, main used parameters of this function are

(1) binning window width
(2) aggregate function used to calculate the I value
(3) function used to select the representative mZ

Dimensional data reduction makes data processing steps easier, allowing a reduction in the size of the problem and optimizing the overall performances. The approach used in this manuscript is the Gopalakrishnan approach [21], which groups multiple values *mZ*—in our case of *D* Factor shift—in a single representative value. This process groups *mZ* adjacent values and among them chooses a representative group member given by maximum, minimum, median, or average. The normalization process allows different samples' comparison when different values of absolute peak are not feasible. The purpose of normalization is to identify and delete sources of systematic variations between the spectra. Three types of normalization are allowed in this software sensor, and are the following:

(1) *Direct normalization*:

$$V_{\text{NORM}} = 1 - \left(\frac{V_{\max} - V_{\text{orig}}}{V_{\max} - V_{\min}} \right),$$

where V_{NORM} is the normalized intensity value, $V_{\max}$ and $V_{\min}$ are, respectively, the maximum and minimum intensity values, and V_{orig} is the intensity value to be normalized.

(2) *Inverse normalization*: Normalized intensity of each spectrum is obtained according to the following formula:

$$V_{\text{NORM}} = \left(\frac{V_{\max} - V_{\text{orig}}}{V_{\max} - V_{\min}} \right),$$

where V_{NORM} is the normalized intensity value, $V_{\max}$ and $V_{\min}$ are, respectively, the maximum and minimum intensity values, and V_{orig} is the intensity value to be normalized.

(3) *Canonical normalization according to the formula*:

$$V_{\text{NORM}} = \frac{V_i}{\sum_{i=1}^{n} V_i},$$

where V_{NORM} is the normalized intensity value and V_i is the intensity value to be normalized.

3.4.3 Processing

Semiautomatic algorithms—that require human intervention—are necessary for an easy, quick, and reproducible spectra processing.

Indeed, spectra often contain hundreds of thousands of peaks. Although usually some of these procedures can be made directly using the tools integrated in the spectrometer in the following sections some useful way to implement these procedures are shown. Indeed, for non-general-purpose systems, it could be useful to implement custom solutions to these procedures.

3.4.3.1 Peak extraction, peak alignment, and baseline subtraction

Peak extraction extracts the most significant peak values choosing real peaks among a huge amount of noisy peaks. In this software sensor core example, the peak extraction function was implemented using a sliding window for the *D* factor shift axes, and the intensity eligible representative value was selected as the maximum value. In other words, a binning function with a max function was applied. Once the real peaks are extracted, two other functions—for shape comparison purposes—are useful (Fig. 3.7):

- *Peak alignment*: It aligns the main peaks of the two (or more) compared spectra. Spectra of different acquisitions will show a left shift of their major peak. Indeed, for a nanogravimeter sensor, a weight gain on the quarts is transduced in a low frequency shift. In this example, a protein expression on the quartz means high weight and thus low frequency.
- *Baseline subtraction*: It deletes the baseline from spectra. Indeed, the spectra of different acquisitions usually differ in intensity, which is due to the different amount of biomolecules on the quartz.

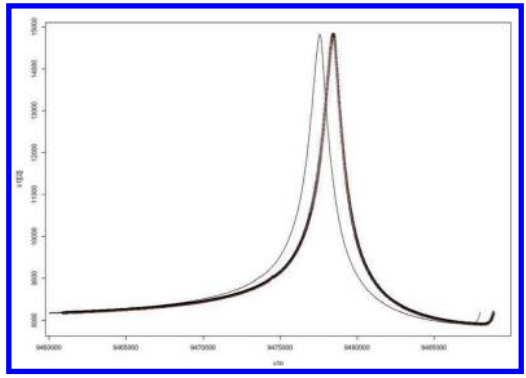

Figure 3.7 Spec alignment and baseline subtraction of two spectra: in black spectra 1, in red spectra 2, and in dotted black the shifted spectra 1.

3.4.4 Results: Normalized *D* Factor Calculation

D factor calculation results are presented in this section. These results are based on the definition given in Section 3.2.2.1.

3.4.5 Results: Michaelis–Menten Constant Calculation

As for the previous section, here we show some results obtained with the R routine for Michaelis–Menten kinetic parameters calculation for fructose. R routine is based on the algorithm explained in Section 3.2.2.2 and results are shown in the following. Input parameters of these routine are not only spectra files but enzyme concentration for K_{cat} calculation.

3.4.5.1 Spectra subtraction

Spectra subtraction processing function could be useful for spectra comparison (Fig. 3.8) since a master mix (MM) is used in protein expression for nanogravimetric NAPPA. This means that the spectra are not "pure protein spectra" and they contain even MM spectra. For further details on MM spectra, please see Chapter 11 (Spera et al.). Subtraction of two spectra retrieved from protein expression is given in Fig. 3.9 and 3.10.

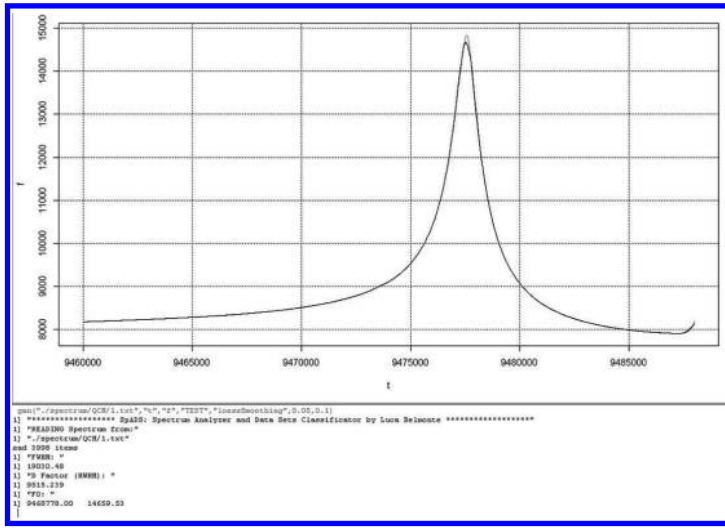

Figure 3.8 Normalized *D* Factor calculation on a quite Gaussian shape curve.

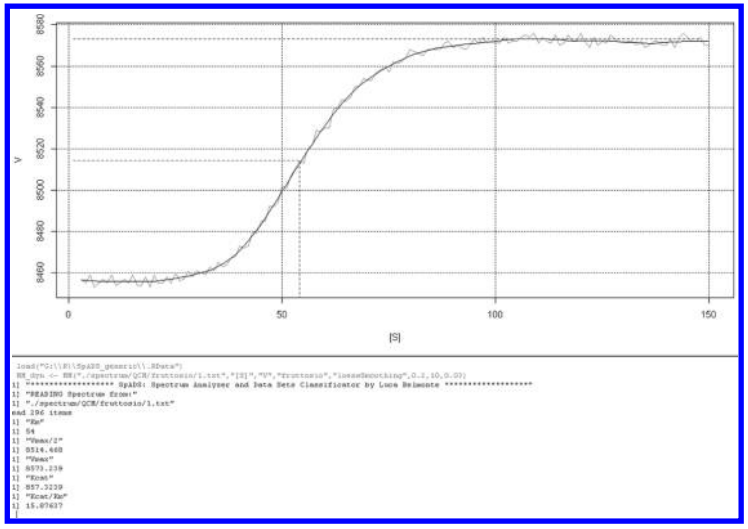

Figure 3.9 Michaelis-Menten constant calculation on a fructose spectra: plotting of the relative curves (top) and relative parameters calculation (bottom).

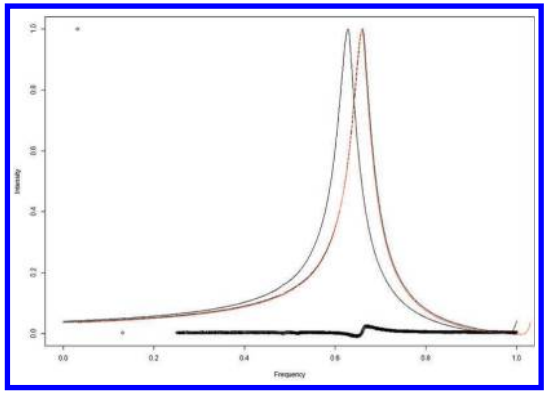

Figure 3.10 Peak alignment, base line subtraction and spectra subtraction. Spectra signals are from two blank quartzes.

3.4.5.2 3D spectra plotting

Another useful tool could be a 3D spectra plotting of processed data. In this type of chart, there are several spectra obtained at different times. Thus, three-axis systems are made up of frequency, impedance, and acquisition time. Parameters such as f_0 are then shown Fig. 3.11 and 3.12.

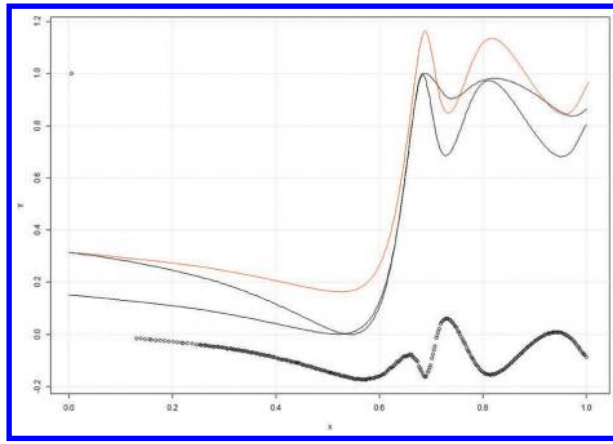

Figure 3.11 Spectra subtraction of two aligned spectra: The results of subtraction are shown as a black dotted resulting spectra.

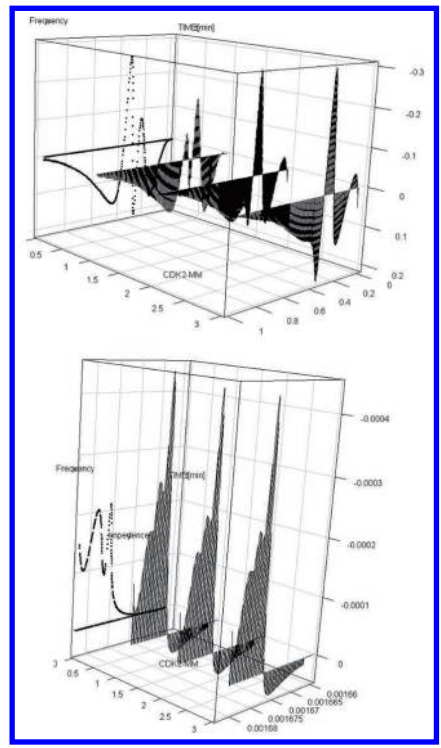

Figure 3.12 Three-dimensional plotting of spectra preprocessed with direct (top) and canonical (bottom) normalization. Subtraction of a spectra was applied, too.

Acknowledgment

SpADS and its modified version discussed in this chapter can be downloaded from the Web site http://www.ibf.unige.it/SPADS.

References

1. Weiser, M. (1991). The computer for the 21st century, *Sci*. *Am*., **265**, 94–104, doi:10.1038/scientificamerican0991-94.
2. Weiser, M., Gold, R., Brown, J.S. (1999). Origins of ubiquitous computing research at PARC in the late 1980s. IBM Systems Journal archive. **38**(4):693–696. doi: 10.1147/sj.384.069.
3. Weiser, M. (1993). *Hot Topics: Ubiquitous Computing*, *IEEE Computer*. **26**(10):71–72. ISSN: 0018-9162. DOI: 10.1109/2.237456.
4. York, J., Pendharkar, P. C. (2004). Human–computer interaction issues for mobile computing in a variable work context, *Int. J. Human-Computer Studies*, **60**, 771–797.
5. Hansmann, U. (2003). *Pervasive Computing: The Mobile World*. Springer. ISBN 3-540-00218-9.
6. Greenfield, A. (2006). *Everyware: The Dawning Age of Ubiquitous Computing*. New Riders. pp. 11–12. ISBN 0-321-38401-6.
7. Akyildiz, I. F., Su, W., Sankarasubramaniam, Y., Cayirci, E. (2002). Wireless sensors networks: a survey, *Computer Networks*, **38**, 393–422.
8. Spera, R., Labaer, J., Nicolini, C. (2011). MALDI-TOF characterization of NAPPA-generated proteins, *J. Mass Spectrometry*, **46**, 9, 960–965.
9. Cheruy, A. (1997). Software sensors in bioprocess engineering, *J. Biotechnol*., **52**, 193–199.
10. Nielsen, J., Molich, R. (1990). Heuristic evaluation of user interfaces, *CHI '90 Proceedings of the SIGCHI Conference on Human Factors in Computing Systems: Empowering People*, pp. 249–256, ISBN:0-201-50932-6, doi 10.1145/97243.97281.
11. Nielsen, J. (1994). *Usability Engineering*. Academic Press, an Imprint of Elsevier ISBN: 9780080520292.
12. Stephanopoulos, G., San, K. Y. (1984). Studies on on-line bioreactor identification. I. Theory (1984). *Biotechnol. Bioeng*., **26**, 10, 1176–1188.
13. Von Bastin, G., Dochain, D. (1991). On-line estimation and adaptive control of bioreactors, *Chem. Ingenieur Technik*, **63**(2), 148.

14. Chéruy, A., Flaus, J. M. (1994). Des Mesures Indirectes à l'estimation en Ligne. Capteur et mesures en Biotechnologie, Chapter 12. Ed. Technique et Documentation—Lavosier, Paris France.
15. Fox, J., Andersen, R. (2005). *Using the R Statistical Computing Environment to Teach Social Statistics Courses*. Department of Sociology, McMaster University. Available at http://www.unt.edu/rss/Teaching-with-R.pdf.
16. Vance, A. (2009). Data Analysts captivated by R's power. *New York Times*. Retrieved April 28, 2009.
17. Robert Gentleman's home page. http://myprofile.cos.com/rgentleman.
18. Free Software Foundation (FSF) Free Software Directory: GNU R. http://directory.fsf.org/wiki/GNU_R.
19. *What is R?*. http://www.r-project.org/about.html.
20. UML Forum. UML FAQ. http://www.umlforum.com/uml-faq/.
21. Gopalakrishnan, V., William, E., Ranganathan, S., Bowser, R., Cudkowic, M. E., Novelli, M., Lattazi, W., Gambotto, A., Day, B. W. (2004). Proteomic data mining challenges in identification of disease specific biomarkers from variable resolution mass spectra. In *Proceedings of SIAM Bioinformatics Workshop 2004*, pp. 1–10, Lake Buena Vista, FL, April 2004.
22. Lehninger, A. L., Nelson, D. L., Cox, M. M. (2005). *Lehninger Principles of Biochemistry*. W. H. Freeman. ISBN 978-0-7167-4339-2.
23. Chakraborty, S. (2009). *Microfluidics and Microfabrication*, 1st ed. Springer. ISBN 978-1-4419-1542-9.
24. Leskovac, V. (2003). *Comprehensive Enzyme Kinetics*. Kluwer Academic/Plenum Pub. ISBN 978-0-306-46712-7.
25. Greco, W.R., Hakala, M. T. (1979). Evaluation of methods for estimating the dissociation constant of tight binding enzyme inhibitors, *J. Biol. Chem.*, **254**(23), 12104–12109.
26. Hayakawa, K., Guo, L., Terentyeva, E. A., Li, X. K., Kimura, H., Hirano, M., Yoshikawa K., Nagamine T., et al. (2006). Determination of specific activities and kinetic constants of biotinidase and lipoamidase in LEW rat and Lactobacillus casei (Shirota). *J. Chromatogr. B Anal. Technol. Biomed. Life Sci.*, **844**(2), 240–250. doi:10.1016/j.jchromb.2006.07.006. PMID 16876490.
27. Segel, L. A., Slemrod, M. (1989). The quasi-steady-state assumption: A case study in perturbation. *Thermochim. Acta*, **31**(3), 446–477. doi:10.1137/1031091.
28. Menten, L., Michaelis, M. I. (1913). Die Kinetik der Invertinwirkung, *Biochemistry Z*, **49**, 333–369.

29. Nicolini, C., Adami, M., Dubrovsky, T., Erokhin, V., Facci, P., Paskievitch, P., Sartore, M. (1995). High sensitivity biosensor based on LB technology and on nanogravimetry, *Sens. Actuators B*, **24–25**, 121–128.
30. Adami, M., Sartore, M., Nicolini, C. (1996). Potentiometric and nanogravimetric biosensors for drug screening and pollutants detection, *Food Technol. Biotechnol. Rev.*, **34**(4), 125–130.
31. Sartore, M., Adami, M., Berzina, T., Nevernova, I., Petrigliano, A., Mascini, M., Nicolini, C. (1996). Validation of a new nanobalance system for the monitoring of molecule interactions, *Proceedings of the First National Conference on Sensors and Microsystems*, World Scientific Publishing Corp., Singapore.
32. Adami, M., Sallam, S., Eggenhoffner, R., Sartore, M., Hainsworth, E., LaBaer, J., Nicolini, C. (2010). Label-free NAPPA via nanogravimetry, in *Functional Proteomics and Nanotechnology-Based Microarrays* (ed. Nicolini, C., LaBaer, J.). Pan Stanford Series on Nanobiotechnology, London–New York– Singapore, vol. 2, Chapter 4, pp. 95–108.
33. Cannataro, M., Guzzi, P. H., Mazza, T., Veltri, P. *Proceedings of the 18th IEEE Symposium on Computer-Based Medical Systems (CBMS'05)*. 2005. doi: 1063-7125/05.
34. Ramachandran, N., Hainsworth, E., Bhullar, B., Eisenstein, S., Rosen, B., Lau, A. Y., Walter, J. C., LaBaer, J. (2004). Self-assembling protein microarrays, *Science*, **305**, 86.
35. Ramachandran, N., Raphael, J. V., Hainsworth, E., Demirkan, G., Fuentes, M. G., Rolfs, A., Hu, Y., LaBaer, J. (2008). Next-generation high-density self-assembling functional protein arrays, *Nat. Methods*, **5**, 535.
36. Keppler, A., Gendreizig, S., Gronemeyer, T., Pick, H., Vogel, H., Johnsson, K. (2003). A general method for the covalent labeling of fusion proteins with small molecules in vivo, *Nat. Biotechnol.*, **21**(1), 86–89.
37. Spera, R., Festa, F., Bragazzi, N. L., Pechkova, E., LaBaer, J., Nicolini, C. (2013). Conductometric monitoring of protein-protein interactions. *J Proteome Res*. 2013 Dec 6; **12**(12):5535–47.
38. Bragazzi N.L., Spera R., Pechkova E., Nicolini C. (2014). NAPPA-based nanobiosensors for the detection of proteins and of protein-protein interactions relevant to cancer. *J Carcinog & Mutagen,* **5**:166. doi: 10.4172/2157-2518.1000166.
39. Belmonte, L., Spera, R., Nicolini, C. (2013). SpADS: An R package for mass spectrometry data preprocessing before data mining, *J. Comput. Sci. Syst. Biol.*, **6**, 298–304.

Chapter 4

Nanotubes and Poly(o-Ethoxyaniline) Nanostructured Films for Sensor Development

Pierluigi Cossari,[a,c] Valter Bavastrello,[a] and Claudio Nicolini[a,b]

[a]*Laboratories of Biophysics and Nanobiotechnology, Department of Experimental Medicine, University of Genoa, Corso Europa 30, Genoa 16132, Italy*
[b]*Nanoworld Institute Fondazione ELBA Nicolini, Largo Redaelli 7, Pradalunga, Bergamo, Italy*
[c]*IGAG-CNR, Via Salaria Km 29.300, 00015 Monterotondo Scalo, Italy*

claudio.nicolini@unige.it

This chapter investigates the influence of different multi-walled carbon nanotubes (MWNTs) on the physical and chemical properties of poly(o-ethoxyaniline) (POEA) nanostructured films. The nanocomposites were synthesized by in situ chemical oxidative polymerization under identical conditions, and thin solid films were prepared by using the Langmuir–Schaefer (LS) technique. Different properties were measured and compared with POEA to find out whether the introduction of different MWNTs concentrations could affect the properties of POEA–MWNT composite materials. It was found that the presence of MWNTs in POEA enhances the interaction between the aromatic structure of the POEA and the basal plane of the MWNT graphitic surface via π-stacking,

Nanobiotechnology in Energy, Environment, and Electronics: Methods and Applications
Edited by Claudio Nicolini

ISBN 978-981-4463-96-6 (Hardcover), 978-981-4463-97-3 (eBook)
www.panstanford.com

affecting the vibrational modes of the polymer. Furthermore, an improvement in the thermal stability and surface morphology was also observed.

4.1 Introduction

Carbon nanotubes (CNTs) have gained great interest for their unique chemical and physical properties since their discovery by Iijima [1]. For this reason, CNTs, either single-walled carbon nanotubes (SWNTs) or MWNTs, enhance the mechanical, structural, and electronic properties of conducting polymers, even at very low quantity into the polymer matrix [2,3]. Thus, nanocomposites of CNTs with intrinsically conducting polymers, having a synergic effect on conduction properties, are used in many applications such as organic light-emitting diodes, photovoltaic cells, energy storage devices, and sensors [4–6].

Among conducting polymers, polyaniline derivatives have been widely studied in the past decades due to their electrical and optical properties associated with low costs, easy processability, environmental stability, and relatively simple method of synthesis [7–10]. In particular, Polyaniline (PANI) composites with CNTs have been receiving increasing attention from researchers due to charge transfer doping as well as site-selective interaction with the PANI chain [11–13].

Extensive effort has been made to fabricate PANI–CNTs composites based on the physical adsorption of PANI on the surface of CNTs or on grafting PANI onto CNTs by functionalization of nanotubes [14]. The synthesis of these nanocomposite materials, carried on by polymerizing the monomer in the presence of a dispersion of CNTs by sonication, is an effective approach for synthesizing homogenous polyaniline nanotube composites, where the polymer matrix is formed in the presence of nanotubes [15–17]. Furthermore, as recently reported, the presence of CNT dispersion during the syntheses affected the final products by acting as nucleation points for the growing polymer chains [18,22].

It is well known that the strong interaction between the aromatic rings of PANI and the graphitic structures of CNTs greatly enhances the charge transfer interaction between the two components [19]. This implies that the PANI–CNT composite nanostructured films with uniform structure would be advantageous

for improvements of the mechanical and electrical properties of the polyaniline.

Taking into account these considerations, the present work describes the synthesis and characterization of MWNTs and POEA nanocomposites in order to study the effect of different MWNTs concentrations on the properties of POEA nanostructured films. In particular, much attention is devoted to point out how large enough concentrations of CNTs may hinder some vibrational modes of the polymer chain.

This analysis may be useful for optimizing some physicochemical properties of POEA–MWNT composites with the aim of developing enhanced chemical sensors.

4.2 Experimental Section

4.2.1 Materials and Methods

Monomer of ortho-ethoxyaniline, ammonium persulfate [$(NH_4)_2S_2O_8$] as oxidizing agents and other reagents were purchased from Sigma and high purity MWNTs from Nanocs Inc, New York, USA. MWNTs had a diameter ranging 30–40 nm and length ranging 40–30 μm.

4.2.2 Synthesis of Pure Conducting Polymers and Related Nanocomposite Materials

The pure conducting polymer and nanocomposite materials were synthesized by in situ chemical oxidative polymerization under controlled conditions, maintaining the temperature within the range 0–4°C by means of an ice bath for 24 h. The medium of reaction was 200 mL of 1M HCl solution of monomer. For the synthesis of the nanocomposites we dispersed MWNTs with different contents of 10, 100, and 1000 wt% (weight percent with respect to aniline monomer) in the medium of reaction by sonication. We performed the sonication by means of SONIC 300 VT equipment, setting a 10% power for 1 min in order to only disperse CNTs without breaking processes. We used a monomer/oxidant molar ratio of 4/1, following previously performed methods of polymerization. Ammonium persulfate was slowly added dropwise into the suspension with constant mechanical stirring. The resulting

doped form (emeraldine salt form) was then filtered and treated with ammonium hydroxide for 2 h in order to obtain the solvent processable undoped form. We finally filtered and rinsed the undoped materials (EB form) with methanol and diethyl ether in order to eliminate the oligomers. For the synthesis of the pure polymer, we used the same steps carried out for the nanocomposites, save for the presence of either MWNT in the medium of reaction.

4.2.3 Fabrication of LS Films

We produced the Langmuir monolayers in a Langmuir–Blodgett trough (MDT corp., Russia), 240 mm × 100 mm in size and 300 mL in volume, having a compression speed of 1.67 mm/s (100 cm^2/min). The spreading solutions of POEA and nanocomposite materials were prepared by dissolving 5 mg of materials in 20 mL of chloroform. The LS films were deposited at the air–water interface, maintaining the surface pressure at 25 mN/m. We used distilled water as subphase for the deposition in order to obtain films of the material in the undoped form. We finally performed the doping process on the deposited films in the undoped form by dipping the substrate in 1M HCl aqueous solution for 1 h.

4.2.4 FTIR Spectroscopy

FTIR spectra of the pure conducting polymer and POEA/MWNT derivatives were obtained on a VARIAN 1000 of the SCIMITAR series (Quantum Analitics Inc, Foster City, CA, USA) within the wavenumber range of 4000–500 cm^{-1}. The samples were prepared in the pellet form by mixing the dry powder with potassium bromide (KBr) at ratio of 1:100 w/w.

4.2.5 UV-Vis Spectroscopy

The UV-vis spectra of the POEA and the nanocomposite materials, deposited in thin films on quartz substrate, in both the undoped and doped forms were recorded by using a UV-vis spectrophotometer Jasco model V530 with a spectral resolution of 2 nm.

4.2.6 Thermogravimetric Analysis

Thermogravimetric analysis (TGA) was carried out on a TGA, Q 600, TA Instruments (USA) by heating the POEA and its MWNT derivatives under N_2 gas atmosphere (100 mL/min) from 20 to 900°C at a heating rate of 10°C/min.

4.2.7 Morphological Analysis

The surface morphology of POEA and POEA–MWNT composites was determined using a scanning electron microscopy (SEM) FEI Quanta 400, USA. The samples in the undoped form were deposited in thin films on glass substrates (50 layers) and then were sputtered with a thin layer of gold prior to SEM analysis.

4.3 Results and Discussion

4.3.1 Synthesis and Characterization of Pure Conducting Polymer and Related Multi-Walled Carbon Nanotube Derivatives

We focused on the standardized oxidative polymerization, carried out for the synthesis of both POEA and its MWNT composite materials, in order to investigate whether the different content of MWNTs into the medium of reaction could affect the polymer chains oxidation ratio and the chemical structure in the final synthesis products.

For the polymer chains oxidation ratio, we studied the UV-vis to verify the amount of quinone–like structure per repeat unit. It is reported that in the UV-vis spectra the peak related to the π–π^* transition can give an estimation of the oxidation ratio, comparing the related absorbance to that of n–π^* [20].

Figures 4.1 and 4.2 show the UV-vis spectra of all materials in the undoped and doped form, respectively.

Figure 4.1a shows the characteristic absorption bands at 313 nm and 588 nm for the EB form of POEA. The band seen at 313 nm is due to (π–π^*) interband transition, whereas the observed peak at 588 nm is assigned to (n–π^*) transition band from the non-bonding nitrogen lone pair to the conduction band π^*.

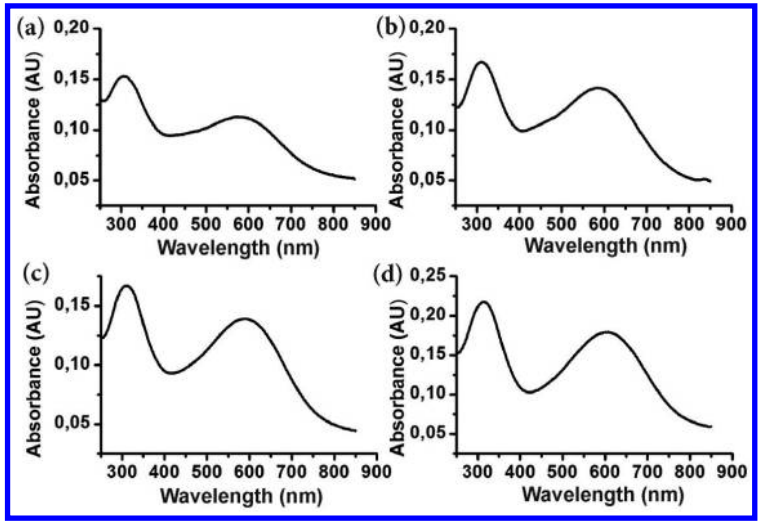

Figure 4.1 UV-vis spectra of materials in the undoped form: (a) poly(o-ethoxyaniline) (POEA), (b) POEA–MWNTs 1–10 w%, (c) POEA–MWNTs 1–100 w%, (d) POEA–MWNTs 1–1000 w%.

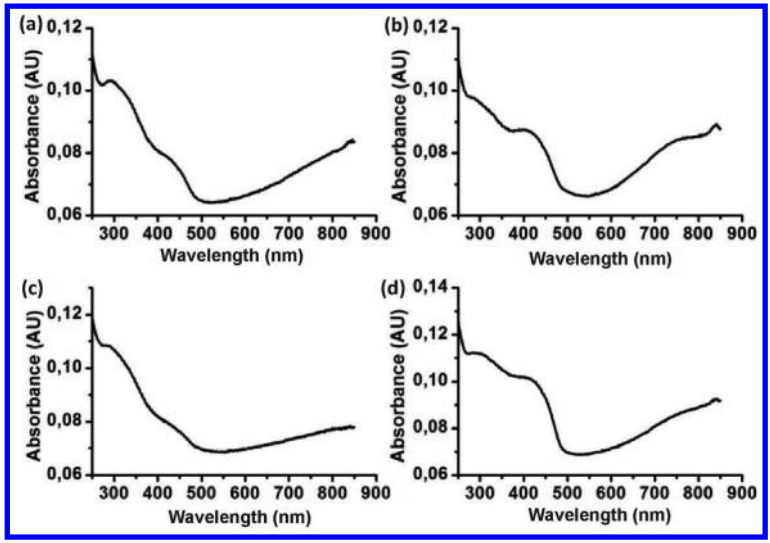

Figure 4.2 UV-vis spectra of materials in the doped form: (a) poly(o-ethoxyaniline)(POEA), (b) POEA–MWNTs 1–10 w%, (c) POEA–MWNTs 1–100 w%, (d) POEA–MWNTs 1–1000 w%.

In Table 4.1, the wavelengths of each band for all the synthesized undoped materials are illustrated.

Table 4.1 Wavelength of the peaks related to the π–π^* and n–π^* transitions for all materials in the undoped form

Material	π–$\pi^*_{undoped}$ (nm)	n–$\pi^*_{undoped}$ (nm)
POEA	313 ± 1	581 ± 1
POEA–MWNTs 1–10	313 ± 1	584 ± 1
POEA–MWNTs 1–100	313 ± 1	588 ± 1
POEA–MWNTs 1–1000	313 ± 1	596 ± 1

The introduction of MWNTs in POEA results in a decreased reduced/oxidized ratio (see Table 4.2) for all the nanocomposites. This suggests that the addition of different content of MWNTs associated to a higher quantity of quinoid units may establish an interaction between the aromatic structure of the POEA, especially through the quinoid ring, and the basal plane of the MWNT layer surface via π-stacking [21].

Table 4.2 Calculation of the reduced/oxidized ratio of the synthesized materials expressed as Abs (π–$\pi^*_{undoped}$)/Abs (n–$\pi^*_{undoped}$)

Material	Abs (π–$\pi^*_{undoped}$)	Abs (n–$\pi^*_{undoped}$)	Oxidation ratio Abs (π–$\pi^*_{undoped}$)/ Abs (n–$\pi^*_{undoped}$)
POEA	0.153 ± 0.001	0.113 ± 0.001	1.35 ± 0.001
POEA–MWNTs 1–10	0.166 ± 0.001	0.141 ± 0.001	1.17 ± 0.001
POEA–MWNTs 1–100	0.160 ± 0.001	0.139 ± 0.001	1.20 ± 0.001
POEA–MWNTs 1–1000	0.217 ± 0.001	0.179 ± 0.001	1.21 ± 0.001

In addition to this, the optical characterization revealed that the presence of MWNTs in the polymer matrix produced no change in the π–π^* transition. This result suggests that the polymer chains wrapped around CNTs with not-strong interactions [22]. Instead, the nanocomposite (n–π^*) transitions show a considerable blue shift of about 20 nm with respect to the corresponding pure conducting POEA.

The ES form of POEA (Fig. 4.2) shows characteristic absorption bands at 310, 415, and 810 nm associated with (π–π^*) interband transition, polaron-π^* and π-polaron transitions, respectively. It is

important to highlight that the position of the absorption peak at 420 nm assigned to polaron-π^* varies with the MWNT content in the nanocomposites, suggesting a possible interaction between the quinoid rings of the POEA and the planar layers of MWNTs.

The FTIR spectra of the MWNTs, POEA, and POEA–MWNTs composites are shown in Fig. 4.3. The FTIR spectra of synthesized POEA–MWNT composites with a weight ratio of 1:100 and 1:1000 reveal distinct peaks at 1596, 1510, 1245, and 810 cm^{-1}, which are all typical vibration modes of pure conducting polymer (POEA).

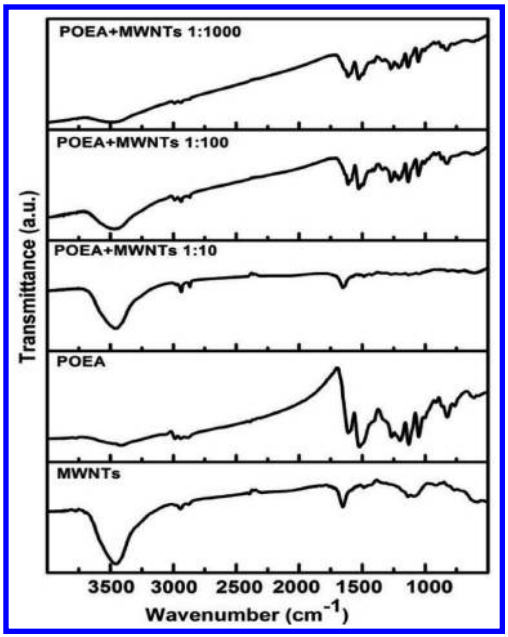

Figure 4.3 FTIR spectra of MWNTs, POEA and POEA–MWNTs with different weight ratio (1:10; 1:100; 1:1000).

Instead, the FTIR spectra of POEA–MWNT composites with a weight ratio of 1:10 show absorption peaks at 3440, 1630, 1470, 1110 cm^{-1}, which are all typical vibration modes of MWNTs. The band observed at around 1260 cm^{-1} is related to the C–N stretching vibration of the benzenoid ring while the peaks at 1034 and 810 cm^{-1} is due to the in-plane and out of plane C–H bending mode, respectively. The region between 1245 and 1030 cm^{-1}, respectively, assigned to symmetric and asymmetric stretching of the C_{ar}–O–C (ar = aromatic), is characteristic of ethoxy group.

The absorption peaks at 1595 and 1510 cm^{-1} are assigned to the quinoid and benzenoid phenyl ring stretching modes, respectively. It is commonly observed that the relative intensities of the two peaks give an estimation of the relative amount of each oxidation state in the polymer chains [23]. Moreover, it is reported that the quinoid peak is a measure of the degree of delocalization of the electrons and the increase in the quinone–like structure per repeat unit indicates an increase in the effective degree of electron dislocation [24]. For this reason, we studied the ratio of absorption intensities of the peaks related to the benzenoid and quinoid phenyl ring stretching frequency to verify the oxidation state of the polymer.

The spectra showed (see Fig. 4.3) the reversal of the relative intensity of these two bands in the POEA–MWNT composites (1:100 and 1:1000) compared to pure POEA and revealed that the POEA in these two multi-walled carbon nanocomposites is richer in the quinoid units than pure polymer. This also suggested that the chains of POEA are deposited on the surface of MWNTs through an interaction between the quinoid ring of polymer and the planar backbone of graphitic surface via π-stacking. POEA–MWNTs interaction could facilitate the charge transfer process between them and, in this way, influence the transport properties of composites.

As previously described, POEA and POEA–MWNT composites with a weight ratio of 1:100 and 1:1000 have approximately identical peak positions associated with the structure of the POEA, indicating the presence of the polymer over the layer on the MWNTs. On the contrary both the spectra of MWNTs and POEA–MWNT composite with a weight ratio of 1:10 show identical absorption peaks. A possible explanation is that the large content of CNTs strongly constraining the polymer chains hinders the vibrational modes of the latter.

MWNTs are very stable composites and the onset of the decomposition occurs over the temperature range 500–850°C (see Fig. 4.4, curve a).

POEA exhibits a three-step decomposition (curve b). The initial weight loss at around 40–150°C may be due to the loss of moisture and volatile matters. The second step for weight loss observed between 150–250°C is due to the loss of bound water or oligomers [25]. Then a strong weight loss occurs within the range 300–650°C due to the polymer chains degradation.

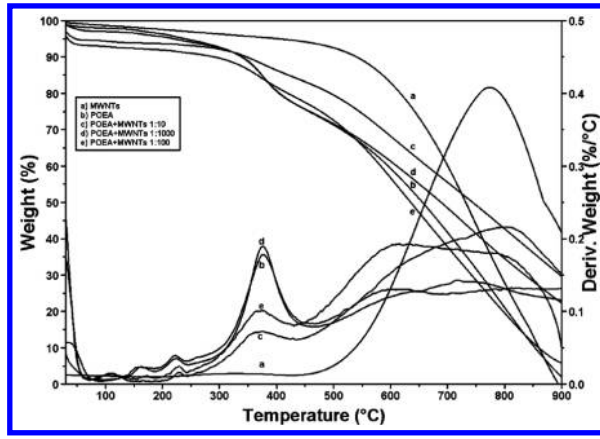

Figure 4.4 Weight loss (TGA) and derivative thermal gravimetric analysis (DTG) curves of (a) MWNTs, (b) poly(o-ethoxyaniline) (POEA), (c) POEA–MWNTs 1–10 w%, (d) POEA–MWNTs 1–1000 w%, (e) POEA–MWNTs 1–100 w%, upon heating treatment from room temperature (25°C) up to 900°C carried out under inert atmosphere (N_2).

These data indicate that the temperature of the thermal decomposition of POEA exhibits identical value (maximum decomposition at 375°C) with respect to POEA–MWNT composites and that the increased MWNT content enhances the thermal stability of the POEA.

As shown (see Fig. 4.4. curves b and d), we observed a higher weight loss (maximum derivative value) for POEA and POEA–MWNTs 1–1000, which indicates that too low content of MWNTs weakly affects the thermal stability of the polymer.

On the contrary, when the content of MWNTs increases (1:10, 1:100) in POEA composites, the decomposition pattern from 300 to 650°C is more similar to that of MWNTs. The results (curves c and e) reveal two weight losses in the range of 300–650°C. The decomposition of the polymer chains occurs with a first weight loss with a maximum (derivative value) at 375°C and then an additional fraction of weight loss emerges at about 590°C. The latter weight loss may be due to the decomposition of a thin layer of POEA deposited directly on the surface of the MWNTs [26].

From what one can see in scanning electron microscope (SEM) images, the films of POEA and POEA–MWNT composite appear very compact and homogenous, as shown in Fig. 4.5 (1:100 w% case).

These images highlight that POEA–MWNT composite thin films have a smaller number of defects and a more regular network-structure with respect to the POEA ones.

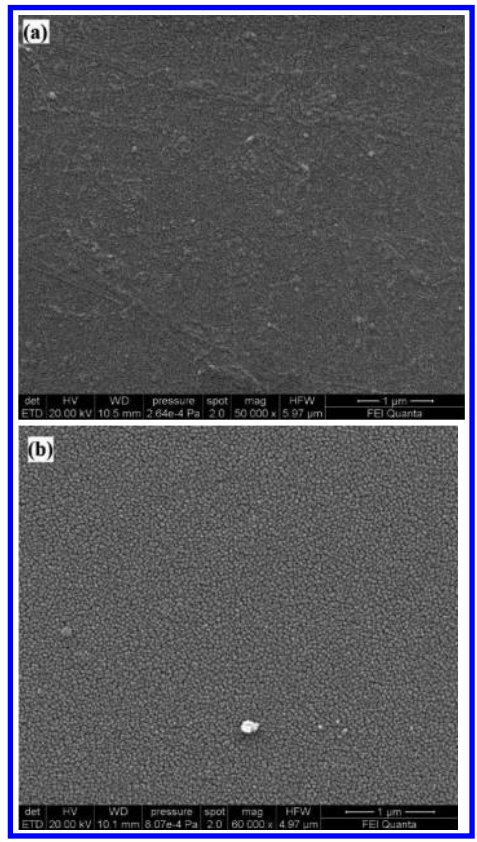

Figure 4.5 SEM images of poly(o-ethoxyaniline) (POEA) (a) and POEA–MWNTs 1–100 w% (b) deposited in thin films on glass substrate.

SEM images in Fig. 4.6 illustrate morphologies of small cracked areas of POEA (a, b) and POEA–MWNT composite (c, d) thin films. From these images appears the character of reinforcement of MWNTs on the structures of the polymer matrix with a better quality of the LS thin films.

Thus, Figs. 4.6a,b show typical SEM images of POEA synthesized by in situ chemical oxidative polymerization described by a fibrillar structure with agglomerates of irregular particulates and some

uneven surface morphology. In contrast, a more compact, dense, and networked structure is observed for the POEA–MWNT composites film (see Figs. 4.6c,d). In addition, no aggregation of multi-walled nanotubes is observed in either of the images indicating that the MWNTs are well dispersed within the polymer matrix.

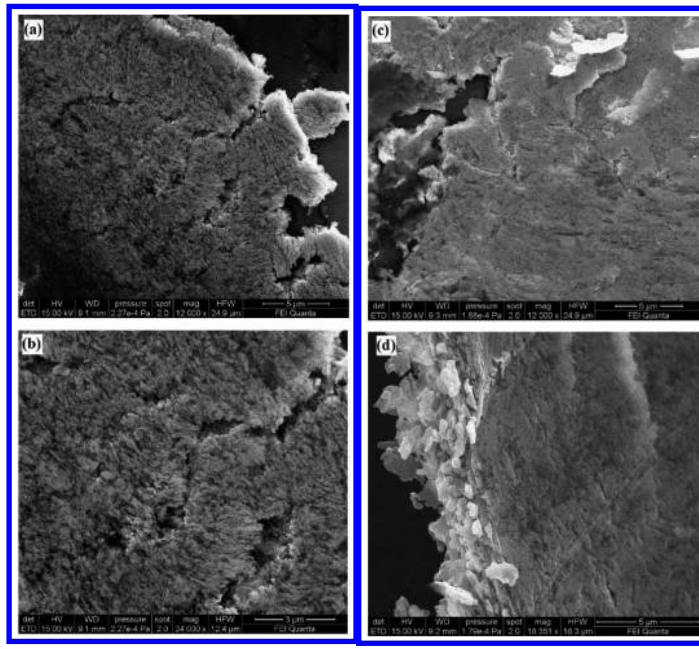

Figure 4.6 SEM images of cracked areas of poly(o-ethoxyaniline) (POEA) (a, b), and POEA–MWNTs 1–10 w% (c, d) thin films at different magnification.

4.4 Conclusions

Different concentrations of MWNTs inside the POEA matrix were studied. These nanocomposites were synthesized by oxidative polymerization and thin solid films were prepared in the undoped form by means of LS technique, and then doped by dipping the substrates in acidic solution (1M HCl). We found that the presence of MWNTs in these nanostructured films reveals an improvement in various chemical physical properties of PANI such as thermal

stability, charge carrier mobility, and surface morphology. The experimental results showed a predominant oxidized form for POEA–MWNT composites, revealing that POEA in these materials is richer in quinoid units. This enhances the interaction between the aromatic structure of the POEA, especially through the quinoid ring, and the basal plane of the MWNT graphitic surface via π-stacking. As a result, a more compact, dense, and networked structure is observed for the POEA–MWNT nanostructured films. This occurrence is confirmed by the FTIR spectral analysis, showing that the vibrational modes yielding the finger print of the POEA are hindered when a large enough amount of CNTs is employed.

Thus, optimized POEA–MWNT composites are expected to exhibit enhanced electrical properties, making these materials attractive for the development of effective chemical sensors. This possibility will be considered in a future research.

References

1. Iijima S. Helical microtubules of graphitic carbon. *Nature*, **354**, 56–58 (1991). DOI: 10.1038/354056a0.
2. Coleman J. N., Curran S., Dalton A. B., Davey A. P., McCarthy B., Blau W., Barklie R. C. Percolation-dominated conductivity in a conjugated-polymer-carbon-nanotube composite. *Phys. Rev. B*, **58**, 7492–7495 (1998). DOI: 10.1103/PhysRevB.58.R7492.
3. Bavastrello V., Ram M. K., Nicolini C. Synthesis of multiwalled carbon nanotubes and poly(o-anisidine) nanocomposite material: fabrication and characterization of its Langmuir Schaefer films. *Langmuir*, **18**, 1535–1541 (2002). DOI: 10.1021/la0104673.
4. Sivakkumar S. R., Kima W. J., Choi J. A., MacFarlane D. R., Forsyth M., Kima D. W. Electrochemical performance of polyaniline nanofibers and polyaniline/multi-walled carbon nanotube composite as an electrode material for aqueous redox supercapacitators. *J. Power Source*, **171**, 1062–1068 (2007). DOI: 10.1016/j.jpowsour.2007.05.103.
5. Bekyarova E., Davis M., Burch T., Itkis M. E., Zhao B., Sunshine S., Haddon R. C. Chemically functionalized single-walled carbon nanotubes as ammonia gas sensors. *J. Phys. Chem. B*, **108**, 19717–19720 (2004). DOI: 10.1021/jp0471857.

6. Ago H., Patritsch K, Shaffer M. S. P., Windle A. H., Friend R. H. Composites of carbon nanotubes and conjugated polymers for photovoltaic devices. *Adv*. *Mater*., **11**, 1281–1285 (2009). DOI: 10.1002/(SICI)1521-4095(199910)11:15<1281::AID-ADMA1281>3.0.CO;2–6.
7. MacDiarmid A. G., Chiang J. C., Halpen M., Huang W. S., Mu S. L., Nanaxaccara L. D., Wu S. W., Yaniger S. Y. Polyaniline: inter conversion of metallic and insulating forms. *Mol*. *Cryst*. *Liquid Cryst*., **121**, 173–180 (1985). DOI: 10.1080/00268948508074857.
8. Paul E. W., Ricco A. J., Wrighton M. S. Resistance of polyaniline films as a function of electrochemical potentialand the fabrication of polyaniline based microelectronic devices. *J*. *Phys*. *Chem*., **89**, 1441–1447 (1985). DOI: 10.1021/j100281a007.
9. Epstein A. J., MacDiarmid A. G. *Electronic Properties of Conjugated Polymer* (eds. Kuzmany H., Mehring M., Roth S), Springer-Verlag, Berlin, (1989).
10. Kobayashi T., Yoneyama H., Tamura H. J. Electrochemical reactions concerned with electrochromism of polyaniline film-coated electrodes. *J*. *Electronalytical Chem*. *Interfacial Electrochem*., **177**, 281–291 (1984). DOI: 10.1016/0022-0728(84)80229-6.
11. Cochet M., Maser W. K., Benito A. M., Callejas M. A., Martinez M. T., Benoit J. M., Schreiber J., Chauvet O. Synthesis of a new polyaniline/nano tube composite: in situ polymerization and charge transfer through site-selective interaction. *Chem*. *Commun*., **16**, 1450–1452 (2000) **DOI:** 10.1039/B104009J.
12. Deng J. D., Ding X. B., Zhang W. C., Peng Y. X., Wang J., Long X., Li P., Chan A. S. C. Carbon nanotube-polyaniline hybrid materials. *Eur*. *Polymer J*., **12**, 2497–2501 (2002). DOI: 10.1016/S0014-3057(02)00165-9.
13. Wu T. M., Lin Y. W. Preparation and characterization of polyaniline/multi-walled carbon nanotube composites. *Carbon*, **4**, 734–740 (2005). DOI: 10.1016/j.carbon.2004.10.043.
14. Zhao B., Hu H., Haddon R. C. Synthesis and properties of a water soluble single-walled carbon nanotube-poly(m-aminobenzene sulfonic acid) graft copolymer. *Adv*. *Funct*. *Mater*., **14**, 71–76 (2004). DOI: 10.1002/adfm.200304440.
15. Park S. J., Cho M. S., Lim S.T., Choi H. J., Jhon M. S. Synthesis and dispersion characteristics of multi-walled carbon nanotube composites with poly(methyl methacrylate) prepared by in situ bulk polymerization. *Macromol*. *Rapid Comun*., **24**, 1070–1073 (2003). DOI: 10.1002/marc.200300089.

16. Maser W. K., Benito A. M., Callejas M. A., Seeger T., Martinez S. T., Schreiber M. T., Muszynski J., Chauvet O., Osvàth Z., Koos A. A., Birò L. P. Synthesis and characterization of new polyaniline/nanotube composites. *Mater. Sci. Eng. C*, **23**, 87–91 (2003). DOI: 10.1016/S0928-4931(02)00235-7.

17. Park C., Ounaies Z., Watzon K. A., Crooks R. E., Smith J. J., Lowther S. E., Connell J. W., Siochi E. J., Harrison J. S., Clair T. L. S. Dispersion of single wall carbon nanotubes in situ polymerization under sonication. *Chem. Phys. Lett.*, **364**, 303–308 (2002). DOI: 10.1016/S0009-2614(02)01326-X.

18. Jimenez P., Castell P., Sainz R., Ansòn A., Martinez M. T., Benito A. M., Maser W. K. Carbon nanotube effect of polyaniline morphology in water dispersible composites. *J. Phys. Chem. B*, **114**, 1579–1585 (2010). DOI: 10.1021/jp909093e.

19. Li L., Qin Y., Liang X., Fan Q. Q., Lu Y. Q., Wu W. H., Zhu M. F. Facile fabrication of uniform core-shell structured carbon nanotube-polyaniline nanocomposites. *J. Phys. Chem. C*, **113**, 5502–5507 (2009). DOI: 10.1021/jp808582f.

20. Quillard S., Louarn G., Lefrant S., MacDiarmid A. G. Vibrational analysis of polyaniline: A comparative study of leucoemeraldine, emeraldine and pernigraline bases. *Phys. Rev. B*, **50**, 12496–12508 (1994). DOI: 10.1103/PhisRewB.50.12496.

21. Chen R. J., Zhang Y., Wang D., Dai H. Noncovalent sidewall functionalization of single-walled carbon nanotubes for protein immobilization. *J. Am. Chem. Soc.*, **123,** 3838–3839 (2001). **DOI:** 10.1021/ja010172b.

22. Bavastrello V., Terencio T., Nicolini C.. Synthesis and characterization of polyaniline derivatives and related carbon nanotube nanocomposites –Study of optical properties and band gap calculation, *Polymer*, **52**, 46–54 (2011). DOI: 10.1016/j.polymer.2010.10.022.

23. Li W., Hoa N. D., Cho Y., Kim D., Kim J. S. Nonofiber of conducting polymer for aromatic organic compound sensor. *Sens. Actuators B*, **143**, 132–138 (2009). DOI: 10.1016/jsnb.2009.09.006.

24. McCall R. P., Ginder J. M., Leng J. M., Ye H. J., Manohar S. K., Masters J. G., Asturias G. E., MacDiarmid A. G., Epstein A. J. Spectroscopy and defect states in polyaniline. *Phys. Rev. B*, **41**, 5202–5213 (1990). DOI: 10.1103/PhysRevB.41.5202.

25. Bhadra S., Chattopadhyay S., Singha N. K., Khastgir D. Effect of different reaction parameters on the conductivity and dielectric

properties of polyaniline synthesized electrochemically and modeling of conductivity against reaction parameters through regression analysis. *J. Polymer Sci*., **45**, 1763–1760 (2007). DOI: 10.1002/polb.21175.

26. YU Y., Che B., Si Z., Li L., Chen W., Xue G. Carbon nanotube/polyaniline core-shell nanowires prepared by in situ inverse microemulsion. *Synthetic Metals*, **150**, 271–277 (2005). DOI: 10.1016/j.synthmet.2005.02.011.

Chapter 5

Molecular Dynamics for Nanobiotechnology

Marine Bozdaganyan,[a,b] Nicola Bragazzi,[a,c] Eugenia Pechkova,[a,c] Philipp Orekhov,[b] Kostantin Shaitan,[b] and Claudio Nicolini[a,b,c,d]

[a]*Laboratories of Biophysics and Nanobiotechnology, Department of Medical Science, University of Genoa, Via Pastore 3, 16132 Genoa, Italy*
[b]*Lomonosov Moscow State University, Leninskie Gory, 1/19, Moscow 119991, Russia*
[c]*Nanoworld Institute, Fondazione ELBA Nicolini, Largo Redaelli 7, Pradalunga, Bergamo, Italy*
[d]*European Synchrotron Radiation Facility, Grenoble, 71 avenue des Martyrs, 38000 Grenoble, France*

claudio.nicolini@unige.it

5.1 Theory of Molecular Dynamics Simulations

5.1.1 Physical Basis of the Method

The computer simulation of dynamics in molecular systems is widely used in molecular physics, biotechnology, medicine, chemistry, and material sciences to predict physical and mechanical properties of new samples of matter.

In the molecular dynamics (MD) method, there is a polyatomic molecular system in which all atoms are interacting like material

Nanobiotechnology in Energy, Environment, and Electronics: Methods and Applications
Edited by Claudio Nicolini

ISBN 978-981-4463-96-6 (Hardcover), 978-981-4463-97-3 (eBook)
www.panstanford.com

points, and behavior of the atoms is described by the equations of classical mechanics. This method allows doing simulations of the system of the order of 10^6 atoms in the time range up to 1 microsecond. Despite some limitations, such approximation may describe the dynamics of macromolecules at the atomic level. However, this method does not consider the chemical reactions and the formation or breaking of chemical bonds. For these purposes, there are approaches that combine classical and quantum mechanics simulations.

The behavior of each atom can be described as Newton's equation of motion:

$$m_i \frac{d^2 \vec{r_i}(t)}{dt^2} = \vec{F_i} \tag{5.1}$$

$$\vec{F_i} = -\frac{dU(\vec{r_1},\ldots,\vec{r_n})}{d\vec{r_i}}, \tag{5.2}$$

where i is the atom number, n the amount of all atoms in the system, m_i the atom mass, $\vec{r}_i$ the atom radius vector, $\vec{F}_i$ the resultant force for each atom, and U the potential energy of the system.

Resultant force is the gradient of the potential, which includes the sum of all interactions of atoms in the system. For pairs of atoms there are different types of interactions: covalent and hydrogen bonds and Coulomb and van der Waals interactions. For triplets of atoms—the bond angles interactions, and for fours—torsion angles interactions (Fig. 5.1).

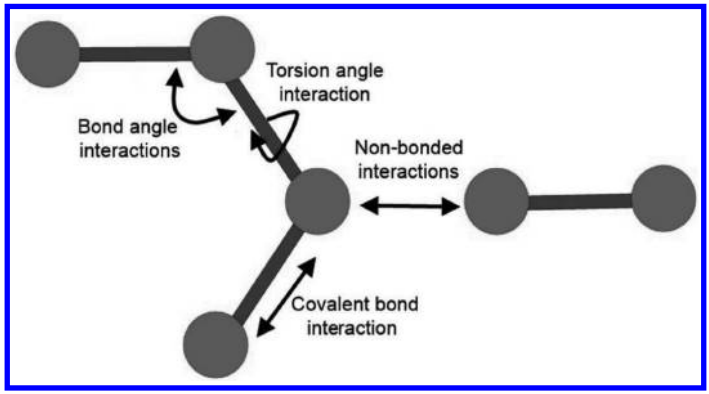

Figure 5.1 Types of interactions in molecular dynamics system.

New coordinates and velocities (Fig. 5.2) are calculated in every step with interval Δt (time step) with the following equations:

$$\vec{r}_i(t+\Delta t) = \vec{r}_i(t) + (\Delta t)\vec{v}_i(t) + \frac{1}{2}(\Delta t)^2 \frac{\vec{F}_i(t)}{m_i} \tag{5.3}$$

$$\vec{v}_i(t+\Delta t) = \vec{v}_i\left(t + \frac{\Delta t}{2}\right) + \frac{1}{2}(\Delta t)^2 \frac{\vec{F}_i(t+\Delta t)}{m_i} \tag{5.4}$$

The fundamental point of integration procedure is the choice of the value of the integration step Δt. The step should be less than the period of the fastest motions in the system. For organic molecules, the characteristic time of the valence oscillations of the C–H bond is 10 fs. Thus, for full-atom systems, we usually choose value of the integration step 1–2 fs. Initial velocities usually are randomly selected according to Maxwell distribution for a given temperature.

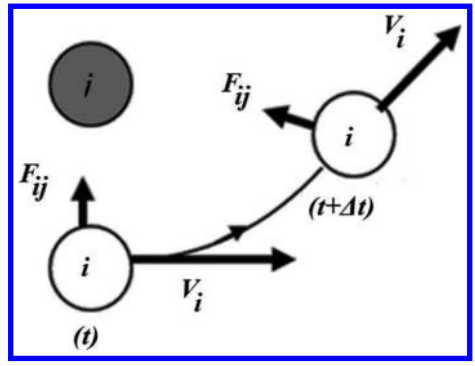

Figure 5.2 Algorithm of calculation of new coordinates and velocities.

5.1.2 Force Fields in MD Simulations

In the context of molecular modeling, a force field refers to the form and parameters of mathematical functions used to describe the potential energy of a system of particles (typically molecules and atoms). Force field functions and parameter sets are derived from both experimental work and high-level quantum mechanical calculations. "All-atom" force fields provide parameters for every type of atom in a system, including hydrogen, while "united-atom" force fields treat the hydrogen and carbon atoms in each terminal methyl and each methylene bridge as a single interaction center.

"Coarse-grained" force fields, which are frequently used in long-time simulations of proteins and membranes, provide even more crude representations for increased computational efficiency.

The potential energy in the different force fields is common; however, they may differ considerably by the calculation of individual contributions and parameterization.

In general, the potential energy of the system is represented as

$$\begin{aligned} U(r_1, r_2, \ldots, r_N) &= U_{\text{bond}} + U_{\text{n-b}} \\ &= \left[\sum_k U_k^{\text{bond}}(r_1, r_2) + \sum_k U_k^{\text{angle}}(r_1, r_2, r_3) + \sum_k U_k^{\text{torsional}}(r_1, r_2, r_3, r_4) \right] \\ &\quad + \left[\sum_k U_k^{\text{LJ}}(r_1, r_2) + \sum_k U_k^{\text{coulomb}}(r_1, r_2) \right], \end{aligned} \tag{5.5}$$

where U_{bond} is the potential of all covalent bonds interactions, $U_{\text{n–b}}$ the potential of all non-bonded interactions, U_k^{bond} the potential of covalent bond interaction, U_k^{angle} the potential of covalent bond interaction, $U_k^{\text{torsional}}$ the potential of torsion angle, U_k^{LJ} the potential of the van der Waals interaction, and U_k^{coulomb} the potential of electrostatic interaction.

The energy of the covalent bonds is approximated by a harmonic potential with stiffness k_{ij} and the bond length b_{ij}^0:

$$U_{ij}^{\text{bond}}(b_{ij}) = \frac{k_{ij}}{2}(b_{ij} - b_{ij}^0)^2, \tag{5.6}$$

where b_{ij} is the actual bond length.

The spring constant and the equilibrium bond length are chosen to reproduce the geometry and vibrational frequencies of simple model compounds. The main drawback of such representation of valence bonds is that at a great distance for two atoms, the bond does not break, and the energy of the system increases dramatically, which can lead to artifacts. Most software packages allow to fix valence bonds in the calculation using algorithms SHAKE [1] and LINKS [2]. This approach allows to increase the integration step to 4–5 fs.

The potential energy of the bond angles is also represented as harmonic potential:

$$U_{i,j,k}^{\text{angle}}(\theta_{i,j,k}) = \frac{k_{i,j,k}^{\theta}}{2}(\theta_{i,j,k} - \theta_{i,j,k}^0)^2, \tag{5.7}$$

where $k^{\theta}_{i,j,k}$ is the spring constant and $\theta_{i,j,k}$ and $\theta^{0}_{i,j,k}$ the actual and equilibrium angles, respectively.

Spring constant and the equilibrium value of the angle are selected the same like for bonds to reproduce the equilibrium geometry and vibrational frequency of simple molecules.

The torsion angle for the atoms *i*, *j*, *k*, and *l* is the dihedral angle between the planes, which are defined by atoms *ijk* and *jkl* (Fig. 5.3). The angle is 0° when molecule is in *cis*-conformation.

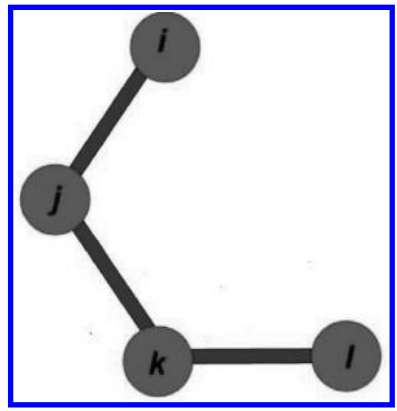

Figure 5.3 Torsion angle.

There are two common energy potentials for dihedral angles: periodic function and potential Ryckaerta-Bellemans.

For the first case, the potential energy is defined as follows:

$$U^{\text{torsional}}_{i,j,k,l}(\varphi_{i,j,k,l}) = k^{\varphi}_{i,j,k,l}[1+\cos(n\varphi-\varphi^{0})], \tag{5.8}$$

where the parameters are chosen so that energy of the *cis* and *trans* conformations was right.

The equation for the Ryckaerta-Bellemans potential is (Fig. 5.4):

$$U^{\varphi}_{i,j,k,l}(\varphi_{i,j,k,l}) = \sum_{0}^{5} C_n(\cos(\varphi-\pi))^{n}. \tag{5.9}$$

Both potentials can give an error in the case of aliphatic hydrocarbons where the transitions between the *cis* and *trans* conformations are sterically hindered. Therefore, for a more precise description of system behavior there, the non-bonded interactions (Coulomb and van der Waals forces) between the outermost atoms of the torsion

angle, so-called "1–4 interactions." In some force fields, there is potential for hydrogen bond energy, which is described with the following empirical equation:

$$U^{\text{H–bond}} = \varepsilon\left[A\left(\frac{r_0}{r}\right)^{12} - B\left(\frac{r_0}{r}\right)^{10}\right] \tag{5.10}$$

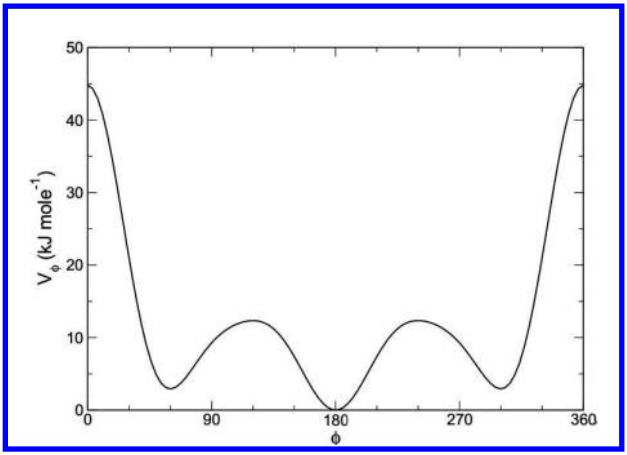

Figure 5.4 Ryckaert–Bellemans potential function.

In MD, atoms are material points and the existence of electrons is not taken into account. However, the electron density distribution in the molecule is unevenly and partial charge of each atom is used to describe the distribution of electron density in the force fields. Coulomb interaction energy between the atoms of the system is described by the following equation:

$$U_{i,j}^{\text{coulomb}}(r_{ij}) = \frac{q_i q_j}{4\pi\varepsilon\varepsilon_0 r_{ij}}, \tag{5.11}$$

where q_i and q_j are the partial charges on atoms, ε and ε_0 the permittivity of vacuum and medium, respectively, and r_{ij} the distance between atoms.

For non-bonded interactions, the potential energy is not calculated for each pair of atoms in the system but only for atoms located at a distance of less than a certain value—the cutoff radius.

In structured environments, such as lipid bilayers, using cutoff radius can lead to artifacts; so for these systems special

approximations are applied to take into account long-range Coulomb interactions.

The most common approach is calculating forces using the method of Ewald sums. In this method, the sum of all pair interactions is done in the reverse Fourier space. The computational complexity of the method is $O(N^2)$, where N is the amount of all atoms in the system. A modified method of Ewald sums—particle mesh Ewald (PME)—has complexity $O(N \cdot \log(N))$, and it is based on fast Fourier transforms in the summation in reciprocal space.

5.1.3 Physical Parameters for MD Simulations

5.1.3.1 Constant temperature: thermostats

The instantaneous value of temperature is related to the kinetic energy of the system by the following equation:

$$\sum_{i=1}^{N} \frac{\left|p_i^2\right|}{2m_i} = \frac{3Nk_B T}{2}, \tag{5.12}$$

where p_i is the momentum of the particle, m_i the particle mass, N the number of particles in the system, k_B the Boltzmann constant, and T the temperature.

During the MD simulation, atoms may be at too small distance to each other (in the forbidden region of the potential field) and at the next step the atom can receive the excess kinetic energy, which subsequently leads to the warming of the system. To avoid this situation, there are special algorithms—thermostats. Here, we discuss only two thermostats.

(1) Berendsen thermostat

For keeping the temperature of the system constant, it is heated externally with fixed temperature T_0. Velocity is scaled at each step, and the change in temperature is described by the following equation:

$$\frac{dT(t)}{dt} = \frac{1}{\tau}(T_0 - T(t)), \tag{5.13}$$

where τ is the parameter that defines the interaction between external and system heaters. Temperature change between two time steps in that case according to the following equation:

$$\Delta T = \frac{\delta t}{\tau}(T_0 - T(t)). \tag{5.14}$$

Then λ factor is

$$\lambda^2 = 1 + \frac{\delta t}{\tau}\left\{\frac{T_0}{T\left(t - \frac{\delta t}{2}\right)} - 1\right\}. \tag{5.15}$$

This thermostat has some drawbacks. It does not satisfy the canonical Gibbs distribution and does not take into account the law of equipartition of kinetic energy of the molecule degrees of freedom. In the computational experiments with small molecular systems it was observed pumping of energy from high to low frequency vibration modes.

(2) Nose–Hoover thermostat

The thermostat becomes an integral part of the system by adding an artificial variable s, coupled with "mass" $Q > 0$.

In this case, the Lagrangian of the system is

$$L_{\text{Nose}} = \sum_{i=1}^{N} \frac{m_i}{2} s^2 \dot{r}_i^2 - U(r^n) + \left(\frac{Q}{2}\right)\left(\frac{ds}{dt}\right)^2 - (f+1)k_B T \ln s, \tag{5.16}$$

where f is the number of degrees of freedom, T is temperature, and the third and fourth terms of the equation are, respectively, the kinetic and the potential energy of the system.

5.1.3.2 Constant pressure: barostats

Ensembles with constant pressure are often used in MD simulations. In particular this can be applied to systems where there are different phases (lipid–water systems as example). The most common barostats are Berendsen and Parrinello–Raman.

The pressure tensor **P** can be calculated using the virial theorem of Clausius:

$$\mathbf{P} = \frac{2}{V}(\mathbf{E}_{\text{kin}} - \Xi), \tag{5.17}$$

where V is the volume of the box, $\mathbf{E}_{\text{kin}}$ the kinetic energy, and virial is

$$\Xi = -\frac{1}{2}\sum_{i<j} r_{ij} \cdot F_{ij}. \tag{5.18}$$

5.1.4 Program Software

In this part of the chapter, we give a short overview of the existing software for MD simulations. All program software for molecular modeling can be divided by two groups:

(1) Molecule/topology builders and visualization

In this type of programs, there is a graphical interface that allows the visualization of different molecules and their editing, building of initial systems.
Following are some examples:

- *Automated Topology Builder (ATB)*[1]: automated molecular topology building service for small molecules
- *UCSF Chimera*[2]: 3D molecular viewer, amino acid rotamers and other building functions
- *Visual Molecular Dynamics (VMD)*[3]: 3D molecular viewer, molecule building, analysis of MD trajectories
- *PyMOL*[4]: python-based molecular viewer and editor, has a lot of additional plugins
- *RasMol*[5]: fast viewer of molecular systems
- Programs for running MD simulations
- *LAMMPS*[6]: has potentials for soft and solid-state materials and coarse-grain systems, uses spatial-decomposition

[1] http://compbio.biosci.uq.edu.au/atb.
[2] http://www.cgl.ucsf.edu/chimera/index.html.
[3] http://www.ks.uiuc.edu/Research/vmd/.
[4] http://www.pymol.org/.
[5] http://www.bernstein-plus-sons.com/software/rasmol/.
[6] http://lammps.sandia.gov/.

techniques to partition the simulation domain into small 3D sub-domains

- *GROMACS*[7]: has potentials for all types of biological systems, extremely fast due to algorithmic and processor-specific optimization, typically running 3–10 times faster than many simulation programs
- *NAMD*[8]: has potentials for biological molecules, written using the Charm++ parallel programming model, noted for its parallel efficiency and often used to simulate large systems (millions of atoms)
- *SCIGRESS*[9]: is molecular modeling, computational chemistry and materials science software suite, has MM2 and MM3 force fields, using DFT, semi-empirical methods, parallel MD, docking

5.1.5 How to Choose Parameters for MD Simulations

First is setting the main aim of simulation: which properties and characteristics are needed to get from the MD trajectories of certain object. The second is choosing the software and finally after all computational procedures—analysis of the results and conclusions.

Parameters for MD simulation are temperature, pressure, time step, duration of simulation, ensemble type, and force field, which fits the best for the chosen type of system.

The microcanonical ensemble maintains constant number of particles (N), constant volume (V), and constant total energy (E), so it is also known as the *NVE* ensemble. The canonical ensemble keeps a constant number of particles, constant volume, and constant temperature (T), so it is also called the *NVT* ensemble. The isothermal–isobaric ensemble keeps constant number of particles, constant pressure, and constant temperature, so it is also known as the *NPT* ensemble. The *NPT* ensemble is the most important in chemistry, because many chemical processes are performed under constant pressure and temperature.

Periodic boundary conditions are a set of boundary conditions that are often used to simulate a large system by modeling a small part that is far from its edge.

[7] http://www.gromacs.org/.
[8] http://www.ks.uiuc.edu/Research/namd/.
[9] http://www.scigress.com/.

Molecular dynamics is typically applied to small systems containing thousands of particles. Unless the behaviors near the walls (surface effects) are of interest, they can be eliminated and periodic boundary conditions are employed to simulate the bulk material. Particles are generated in a volume *V*, which is called the primary cell (see Fig. 5.5).

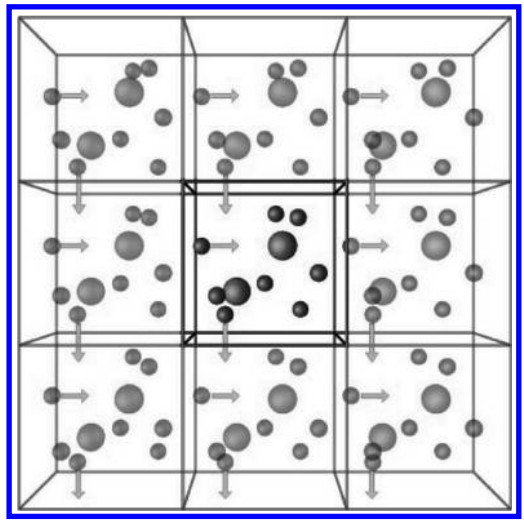

Figure 5.5 Schematic view of periodic boundary conditions for cubic box.

The bulk is assumed to be composed of the primary cell surrounded by its exact replicas to model a macroscopic sample. The image cells not only have the same size and shape as the primary one but also contain particles that are images of the particles in the primary cell. Cells are separated by open boundaries so particles can freely enter or leave any cell. When particles leave the cell, their images simultaneously enter the cell through the opposite face. Therefore, the shape of the cells must be space filling. The number of image cells needed depends on the range of intermolecular forces. When the forces are sufficiently short ranged (e.g., in truncated Lennard–Jones model), only image cells that adjoin the primary cell are needed (minimum image convention). For squares in two dimensions, there are eight adjacent image cells, whereas for cubes in three dimensions, the number of adjacent images is 26.

5.2 Applications of MD Simulation Method to Nanobiotechnology

5.2.1 Molecular Dynamics Method for Nanocrystallography

Atomic structure is an important information about a protein activity and function, since structure and function are known to be interconnected. This information can be obtained by X-ray, nuclear magnetic resonance (NMR), and other less used techniques in the field of crystallography. However, knowledge of all-atom structure represents only the first step toward a full complete understanding of proteins functionality. Bioinformatics, MD, and other computational procedures, coupling static structure with its dynamics and fluctuations study, could overcome the limitations of alone crystallography and provide useful structural and functional insights.

X-ray usually provides a protein modeling a static single conformation [3], even though indirect information about potential conformations, flexibility, and rigidity can be inferred from B-factor (isotropic and anisotropic), thermal motion parameters, and theoretical estimates. Nuclear magnetic resonance exploits the relaxation parameters [4]. Some advanced techniques—multi-start simulated annealing refinement [5], multi-copy refinement [6], multi-path simulated annealing refinement [7], time-averaging with multiple refinements [8], and dynamic-ensemble refinement [9]—have been proposed to study conformational back-bone and side-chain mobility, but MD remains fundamental in order to gain direct insights on protein motion and behavior. Protocols of simultaneous determination of protein native structure and its dynamics have been advocated as vital approaches to capture structural and functional variability [10].

MD has been used to better elucidate about potential thermodynamics (estimating enthalpy and entropy) [11], stability, folding, and unfolding disorders [12,13], structural variants of selected motifs and domains as well as mutated proteins [14–16], in order to foster advancement in the field of protein engineering, protein behavior in different environments, protein-protein interactions [17], from molecular docking [18] to the formation of macromolecular complexes [19], enzyme dynamics, binding [20]

and kinetics. MD has promising applications for new drugs design and discovery [21].

For these purposes, MD has been coupled with X-ray, NMR, atomic force microscopy (AFM), electron microscopy (EM), spectroscopy, and other experimental imaging procedures, or even integrating all of them in an ambitious multi-scale macromolecular simulation [22–28]. So far, little efforts have been made to investigate the advantages and the drawbacks of the crystallization techniques via MD [29].

Different crystallization techniques have been proposed during the decades, like classical vapor drop hanging and its variant sitting drop, dialysis, cryo-temperature, batch, and even in space (using techniques like free interface diffusion or FID, counter-ion diffusion, CID).

Recently a novel crystallization technique based on LB (Langmuir–Blodgett) has been proposed in order to improve crystal growth [30,31]. Using MD analysis, we show how LB-based crystals and space ones can be compared with classically grown crystals.

We took three different globular proteins: lysozyme, proteinase K, and thaumatin. Each protein was crystallized by different methods: classical HD method, LB-method, and also space-grown crystals. All proteins were put inside the box and solvated. After minimization and equilibration of the system production MD was run for 10 ns for each system at temperatures 300 and 500 K. Increasing the temperature of the simulated systems can help to understand the stability of proteins. Under higher temperature, protein can have much more conformations then at low temperatures, so we can study better for short time the potential energy surface of the protein.

A very important thing after each MD simulation approach is to understand which properties can be calculated. Following are examples of two functions that characterize the stability of the proteins and their conformation state.

The radius of gyration of an object describes its dimensions, calculated as the root mean square distance between its center of gravity and its ends. In analyzing proteins, the radius of gyration is indicative of the level of compaction in the structure, i.e., how folded or unfolded the polypeptide chain is

$$R_g = \left(\frac{\sum_i \mathbf{r}_i^2 m_i}{\sum_i m_i} \right)^{1/2} \tag{5.19}$$

In our case, the gyration radius should be normalized. In [32], for natural proteins under physiological conditions, the authors found a scaling law of $R_g \propto N^{2/5}$ by exploiting Protein Data Bank.

The root mean square deviation (RMSD) of certain atoms in a molecule with respect to a reference structure can be calculated by least-square fitting the structure to the reference structure ($t_2 = 0$) and subsequently calculating the RMSD:

$$\mathrm{RMSD}(t_1, t_2) = \left[\frac{1}{M} \sum_{i=1}^{N} m_i r_i(t_1) - r_i(t_2)^2 \right]^{1/2} \tag{5.20}$$

The normalized root-mean-square deviation or error (NRMSD or NRMSE) is the RMSD divided by the range of observed values or

$$\mathrm{NRMSD} = \frac{\mathrm{RMSD}}{x_{\max} - x_{\min}} \tag{5.21}$$

The value is often expressed as a percentage, where lower values indicate less residual variance.

We provide simulations of 15 different crystals at two temperatures—30 simulations with total time 300 ns. Figures 5.6 and 5.7 show the main results of MD simulations.

As can be seen, the structures of all proteins were very stable and the RMSD values remained almost constant around 1–1.3 Å at 300 K for all protein crystals, namely LB, classical and space. Such small changes in the structure are in line with those expected for a protein effectively transferred from a crystal to a solution environment. The RMSD increased more significantly after 2 ns when proteins in water were simulated at 500 K. Classical proteins exhibited higher RMSD values than LB and space: the difference is around 2–3 Å. The above results indicate that, compared with HD-proteins, LB and space proteins seems to be more stable at high temperature.

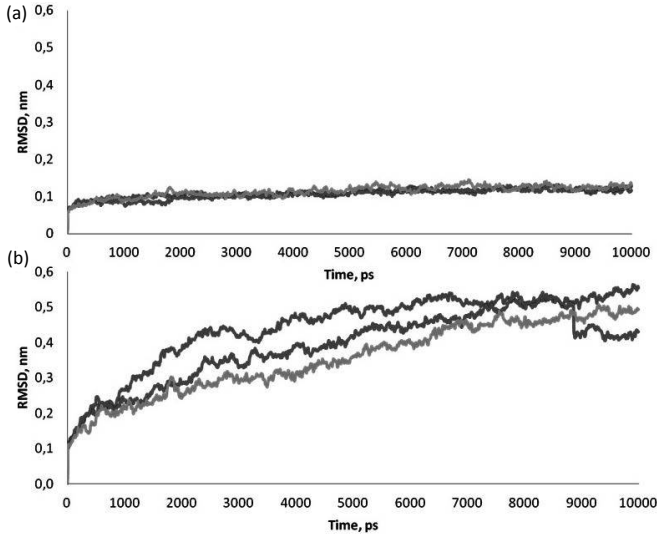

Figure 5.6 Averaged RMSD for all proteins at 300 K (a) and 500 K (b). Blue line denotes classically (HD) crystallized proteins, red line LB, and green line space-grown crystals.

Figure 5.7 shows the gyration radius at the different temperatures. As we can see, LB and space proteins have smaller meaning of R_g than the classical ones in both cases—for 300 and 500 K, indicating that the LB and space proteins are more compact than classical.

According to all data provided above, we can conclude that secondary and tertiary structures of the proteins are not destroyed during our simulation even at 500° K. Also, LB-crystals seem to be more compact and resistant to high temperatures.

Large-scale atomistic MD simulations can be applied to the study and modeling of proteins crystallized according to different crystallization techniques. According to RMSD-analysis, space-grown and LB proteins are more stable to unfolding at 500 K than classical ones (for LB structures our findings confirmed previous experimental results obtained with circular dichroism, microGISAXS and with bioinformatics and data mining). All these findings taken together prove that LB-proteins and space-grown ones are similar and LB-crystallography will pave the way for further discoveries in medicine.

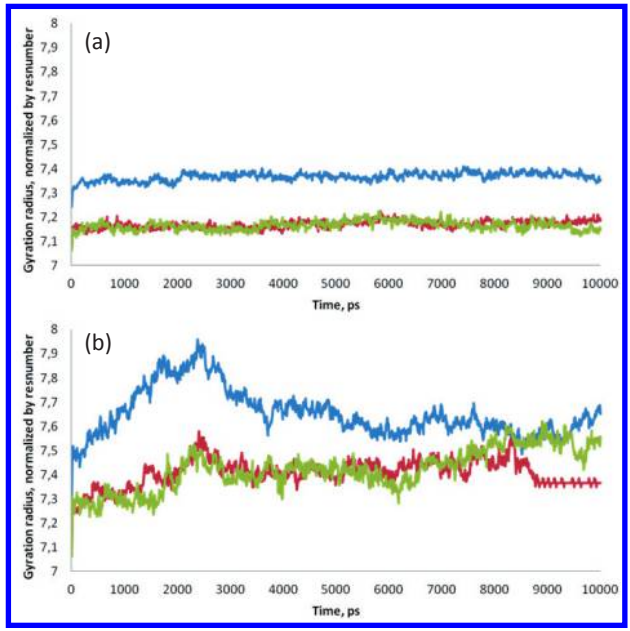

Figure 5.7 Normalized gyration radius of all proteins prepared by different techniques at 300 K (a) and 500 K (b). Blue line denotes classically (HD) crystallized proteins, red line LB, and green line space-grown crystals.

5.2.2 Molecular Dynamics Method for Nanomedicine

Nanomedicine is the medical application of nanotechnology. Nanomedicine ranges from the medical applications of nanomaterials, to nanoelectronic biosensors and possible future applications of molecular nanotechnology. Current problems for nanomedicine involve understanding the issues related to toxicity and environmental impact of nanoscale materials.

MD simulation method can be used in different fields of nanomedicine. Here we just overview nanotoxicology part: prediction of interaction of the fullerene and its derivative with biomembrane.

Nowadays, with increasing production of nanoparticles the problem of its toxicity is becoming more and more important. Fullerenes and its derivatives are being tested continuously to be used in different fields of nanomedicine [33]. As an object of our research, we have chosen fullerene C_{60} and its tris-malonic

derivative—radical scavenges—to test its interaction with biomembrane. These radical scavengers have shown to protect cell growth from various toxins that can induce apoptotic injuries in vitro [34,35] in different cell types such as neuronal cells [36], hepatoma cells [37], and epithelial cells [38].

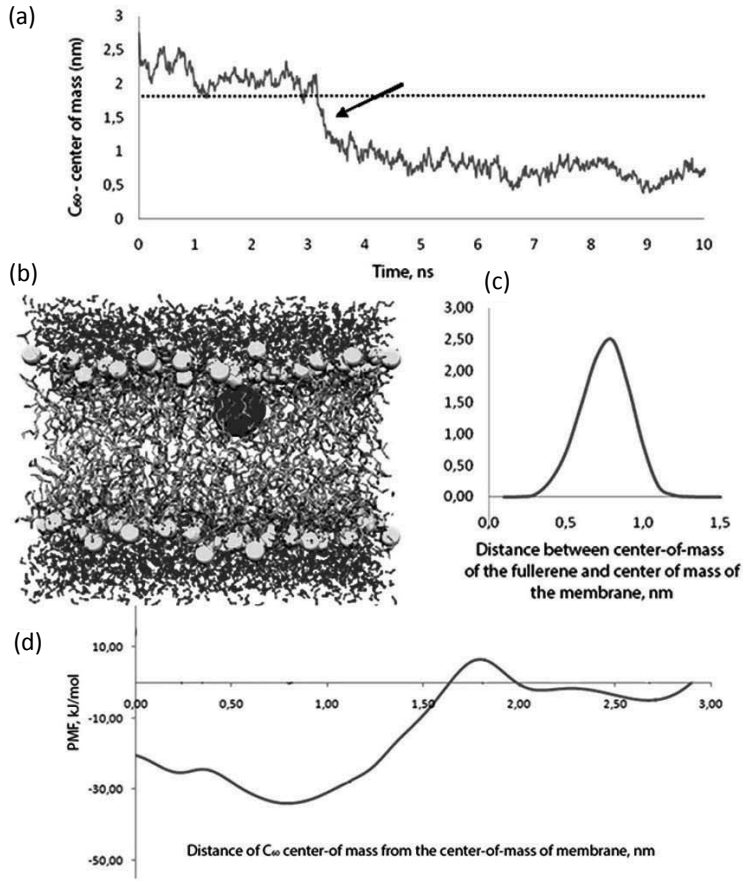

Figure 5.8 (a) Distance between center of mass of the fullerene and center of mass of the membrane during the simulation. On the third nanosecond, the fullerene spontaneously "jumps" into the membrane (shown with an arrow). (b) Snapshot of the system with the fullerene inside the membrane. (c) The probability distribution function of location of the fullerene at different distances from the center-of-mass of membrane. (d) Potential of mean force profile for fullerene and eukaryotic membrane.

Molecular dynamics simulations allow the study of the process of penetration of nanoparticles through biomembranes in all-atom computational models. For understanding the toxic properties of our molecules, we calculated the potential of mean force for the systems: fullerene and tris-malonic fullerene with biomembrane. This method allows the analysis of the interaction energy between molecules and membrane as function of the distance.

The analysis of the trajectories of the equilibrium MD shows that during the first nanoseconds of the simulation fullerene comes to be adsorbed onto the area of lipid heads. However, on the third nanosecond, it spontaneously jumps into the tail region (Fig. 5.8), which is consistent with [39]. The average speed of this jump is approximately 0.35 m/s.

In Fig. 5.8, one can see that fullerene in the beginning overcomes the energy barrier of 10 kJ/mol to pass the lipid heads. The energy minimum (–34 kJ/mol) is located at the distance of 0.75 nm from the center of the membrane. This means that being close to the membrane fullerene molecules got inside the membrane and stays in the region of hydrophobic tails.

Fullerenes, being hydrophobic molecules, in water solution aggregate in clusters. To study the permeability of the membrane for a fullerene cluster, we assembled a system, consisting of 10 fullerenes placed above the surface of the membrane (Figure 5.9). Initially, the fullerenes did not contact with each other or the membrane, but after a few nanoseconds, they aggregate and are absorbed in the head area. After 4 ns, one of the eight fullerenes in the aggregate penetrates the membrane, and the other seven latter follow it. As a result, after 100 ns, 9 of 10 fullerenes penetrate into the membrane.

The data from Table 5.1 show that the presence of the fullerene in the membrane does not significantly affect its basic physical properties. However, the membrane is deformed by the addition of a large number of fullerenes: It curves (Fig. 5.9), and the area per lipid head is reduced from 69 to 56 $Å^2$, while thickness is increased of 0.5 nm. In general, such changes upon the penetration of a large number of fullerenes into the membrane could preface further formation of a pore, a micelle, or a membrane rupture, which were not observed due to the limited simulation time and/or the restrained size of the system.

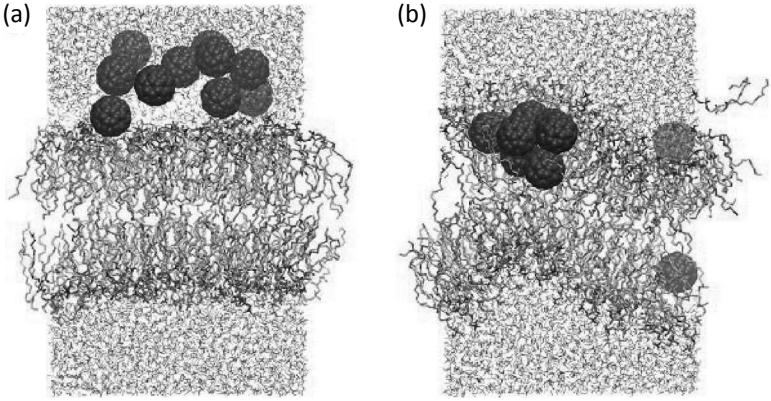

Figure 5.9 Snapshots of the membrane and ten fullerenes in the initial moment of time and after 100 ns of simulation.

Table 5.1 Properties of the DPPC membrane, DPPC membrane with one fullerene and DPPC membrane with ten fullerenes

Membrane property (averaged over the corresponding trajectory)	Pure DPPC	DPPC with one fullerene inside	DPPC with nine fullerenes inside
Thickness, nm	3.37	3.2	3.87
Lipid area per head group, Å^2	56	69	71
Lateral diffusion coefficient, 10^{-7} cm^2/s	0.98	1.3	0.99

In the simulation with C_3, it sorbed in the area of hydrophilic lipid heads on the first nanosecond and further preferably remained in this area, rather than in the bulk (Fig. 5.10). The calculations showed that the molecule of C_3 has a stable and well-structured hydration shell of 40 water molecules.

As can be seen from the plot of potential of mean force, the penetration of membrane appears to be energetically unfavorable for C_3 derivative—with decrease of the distance between C_3 and the membrane the repulsive force driving the fullerene away increases. Such a hindered penetration may occur because of a negative charge carried by C_3 as well as due to a high energetical cost of the water shell dissociation, which is essential for C_3 to pass through the membrane.

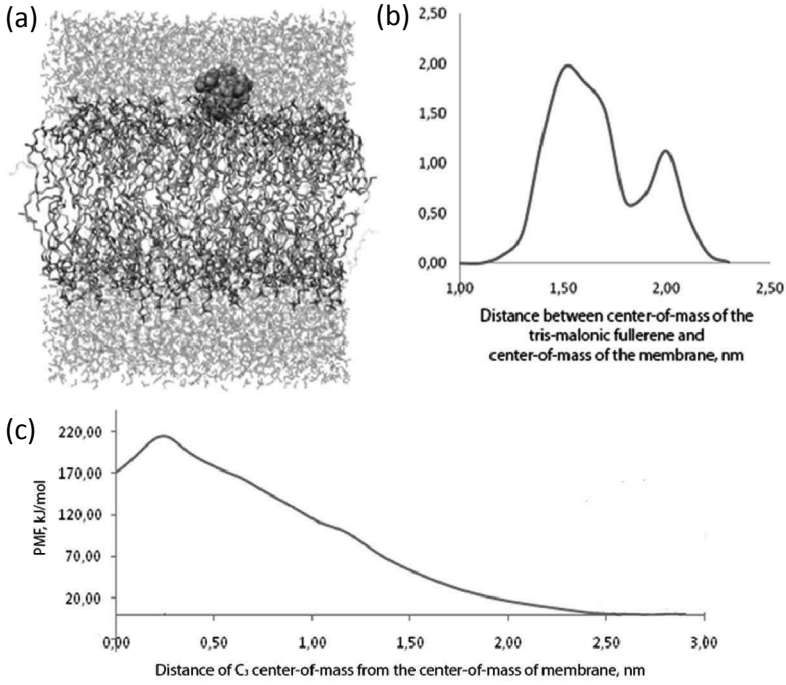

Figure 5.10 (a) Tris-malonic fullerene on the surface of the membrane (b). The probability distribution of location of the tris-malonic fullerene at different distances from the center-of-mass of membrane. (c) Potential of mean force profile for tris-malonic fullerene and eukaryotic membrane.

We conclude that MD simulations can be used for predictions of toxicity of different molecules to biological objects. The non-modified fullerene (a single molecule and a cluster of 10 molecules) spontaneously penetrate the membrane and remain there throughout the entire simulation time. After entry into the eukaryotic membrane, fullerenes remain at a distance of about 1 nm from the center of the membrane. Cluster of fullerenes deform membrane causing its curvature and changing of thickness. This fact means that C_{60} is potentially toxic molecule for eukaryotic cells. C_3 does not penetrate eukaryotic membranes and causes no changes in their structure—the toxicity of this molecule is lower than C_{60}.

5.3 QM/MM Methods: A Hybrid Approach

5.3.1 Theoretical Introduction

A quantum-mechanical description of molecular systems appears to be the most sophisticated and advanced computational approach allowing one to simulate accurately lots of processes, like breaking and formation of chemical bonds, electronic excitation, alteration of charge distribution, etc., untouchable with other techniques. The unpleasant undersides of this group of methods are their high computational cost, a limitation chiefly to relatively small molecules (up to several hundred atoms), and non-linear scaling of computational demands with the rise of number of atoms in a model system. Computational studying of biological molecules, such as DNA and proteins, requires simulations of huge systems containing thousands and even millions of atoms, what makes quantum chemical methods of limited usability in sense of application to this range of problems. On the other hand, a number of bimolecular phenomena have purely quantum nature (electron transfer, excitation, and relaxation of photoactive molecules, etc.) and, thus, should be treated at quantum level.

At the same time, MM methodology, being normally derived and parameterized from some basic quantum calculations, provides a possibility to calculate trajectories of MD for systems consisting of thousands of atoms at the timescale of up to microsecond employing modern supercomputer facilities. While allowing us, in fact, to span a very wide class of important problems, this classical approach is restrained by its principal assumption for molecular electronic structure, which is supposed to remain fixed and is modeled as a set of partial point charges set usually on the atoms.

The both of the computational techniques, QM and MM, have received notable popularity among researchers in the past decades as for biological applications [40,41], but their obvious limitations have been continuously stimulating seeking for some hybrid approaches, which can potentially combine the advantages of quantum and classical methods, i.e., which allow simulations of quantum processes (e.g., an enzymatic reaction) taking into

account the environment (e.g., a protein globe around the catalytic center) in sense of electrostatic influence, dielectric screening and mechanical restraining. One of the first formulations of such a scheme has been given in [42], but the earliest real applications of QM/MM appeared much more latter, when computational powers became sufficient for such tasks.

The central procedure of any QM/MM calculation is splitting of a system of interest (often referred as *real* or *entire*) up into few (usually, just two) *model* subsystems (Fig. 5.11), which are simulated at different levels of theory: QM (*high* or *inner*) and MM (*low* or *outer*). This partitioning leads to appearance of interface between the *high* and the *low* subsystems, which thus must be somehow described.

The first formulations of QM/MM have solved this interface in a fashion, which is known now as *energy additive* scheme. The general expression for the total energy of the *real* system, $E_{\text{real}}^{\text{QM/MM}}$, in this group of methods has a form of

$$E_{\text{real}}^{\text{QM/MM}} = E_{\text{high}}^{\text{QM}} + E_{\text{low}}^{\text{MM}} + E_{\text{boundary}} \tag{5.22}$$

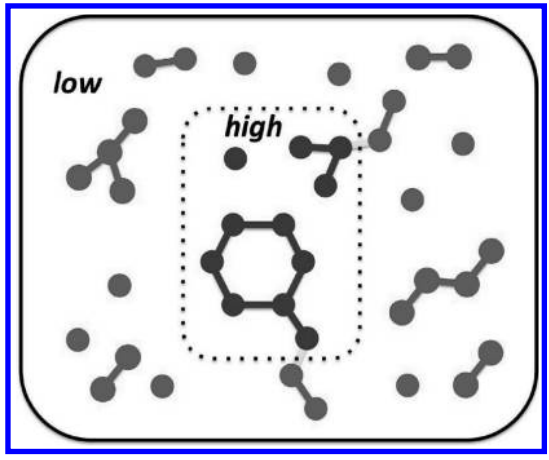

Figure 5.11 Scheme of partitioning of the real system of interest during QM/MM calculation. Red: particles of low or outer subsystem, simulated at MM level of theory; blue: particles of high or inner subsystem, modeled at QM level of theory; yellow sticks: bonds undergoing truncation during the division of the original real system into the two model subsystems.

Here, E_{high} is energy of the *high* model subsystem calculated on QM level, E_{low} corresponds to MM energy of the *low* model subsystem, while the addition of E_{boundary} accounts the interaction between the two subsystems. This interaction could be modeled in different ways. In *electronical embedding* schemes, the electrostatic interaction between the subsystems is included into E_{high} in a form of external potential of the MM partial atomic charges of the *low* subsystem acting on the *high* subsystem, so E_{boundary} should only contain terms corresponding to the van der Waals interactions of atomic centers of the subsystems and, if present, to covalent linkage between the subsystems. Alternatively, in so-called *mechanical embedding* scheme [43], electrostatic interactions are incorporated at MM level of theory through assignment of partial atomic charges to atoms of the *high* region. In general, electronical embedding schemes are deemed to be more accurate comparing to mechanical embedding, though the latter in many applications also show good accuracy providing at the same time more simple expressions for electrostatic interactions between the subsystems.

Another group of methods has got a name of *energy subtractive* schemes in literature [44]. The most widely spread method of this group, ONIOM, has been proposed in [45–47] by K. Morokuma with colleagues. The total energy of the real system in this approximation could be written as follows:

$$E_{\text{real}}^{\text{ONIOM}} = E_{\text{high}}^{\text{QM}} + E_{\text{real}}^{\text{MM}} - E_{\text{high}}^{\text{MM}} \tag{5.23}$$

As one can see, interactions between the two subsystems in ONIOM approach are included into the total energy, $E_{\text{real}}^{\text{ONIOM}}$, at the low level of theory through the calculation of the whole *real* system at MM level, $E_{\text{real}}^{\text{MM}}$. Subtraction of $E_{\text{high}}^{\text{MM}}$ is required here to avoid double counting of the energy of the *high* region. This implies that ONIOM is originally a formulation of a QM/MM scheme with mechanical embedding. However, in succeeding publications [48,49] the method has been extended to include the electronical embedding as well.

Among advantages of ONIOM, one could especially point out the possibility to broaden this formalism toward schemes with more than two layers; for instance, a three-layer scheme has been utilized [50,51].

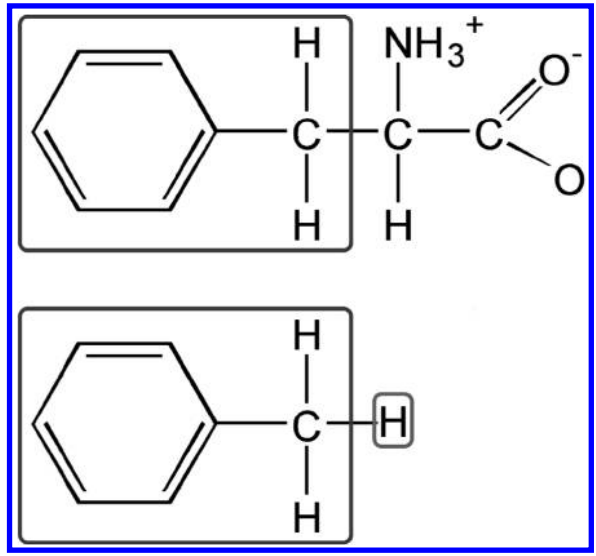

Figure 5.12 Application of link atom approach to treatment of truncation region in phenylalanine molecule divided between the QM region (in blue rectangle) and the MM region (the rest of molecule). Unsaturated valence, appearing during this partitioning process, is filled out with a link hydrogen atom (in red rectangle).

Another important aspect of any QM/MM scheme is the way in which the truncation of covalent bonds is dealt. Two major approaches exist. In the first of them, the appearing "dangling" bonds are treated filling the interface atoms with *link* (also known as *junction dummy*) atoms (see Fig. 5.12), usually hydrogen or pseudohalide atoms (mimicking properties of atoms or group of atoms, which they substitute). This approach particularly is implemented in ONIOM method of Gaussian 09 quantum chemistry package [52]. Alternatively, a *frozen orbital* approach described in [53] could be used.

5.3.2 Application of QM/MM to Prediction of Absorption Maximum Shifts of Bacteriorhodopsin Variants

Bacteriorhodopsin (bRh) is a small (24 kDa) membrane protein of halobacteria. Upon illumination, bacteriorhodopsin creates a

transmembrane proton gradient, which could be utilized for ATP synthesis as well as for other cell needs.

The functional element of bacteriorhodopsin is its chromophore—retinal—a conjugated polyene, which is covalently bound to Lys 216 of G helix of the protein via the Schiff base. In the dark adopted form retinal exists in thermodynamical equilibrium of all-*trans* and 13-*cis*,15-*syn* isomers, while when absorbing a light quantum, the all-*trans* form undergoes a process of photoisomerization, and the equilibrium shifts toward the abundance of 13-*cis*,15-*anti*.

An astonishing phenomenon characterizing bacteriorhodopsin along with other retinal-containing proteins is the so-called *spectral tuning*. It is known [54] that for free retinal in vacuum has an absorption maximum at 610 nm. However, in bacteriorhodopsin the maximum shifts into the blue region, down to 568 nm [55]. In other proteins containing retinal as the chromophore the values of absorption maxima differ from ca. 400 to 570 nm (see Fig. 5.13), what means that protein environment plays a crucial role in spectral tuning of retinal and, changing certain amino acids in protein sequence, one could virtually alter absorption maximum of retinal in protein.

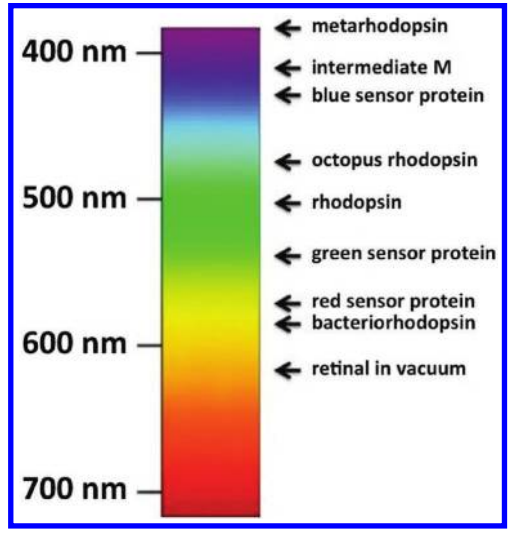

Figure 5.13 The spectral shift in the retinal-containing protein: adsorption maxima are shown for a number of proteins as well as for retinal in vacuum.

Understanding of molecular basis of the retinal spectral modulation by protein environment as well as ability to predict spectral characteristics of different proteins is necessary for solving applied tasks of nanotechnology connected with the construction on the basis of retinal-containing proteins nanoscale optical triggers applicable to data storage systems, holographic memory, information processing, etc. Particularly promising, these technologies might be in the field of digital information storage systems, which would allow increasing in tens folds the information recording density on such innovative storage devices. Such technical solutions are actively discussed in the literature [56,57]. In this sense, search for protein variants, which fulfill certain criterion such as photo- and thermostability, proper absorption maximum, high quantum yield of photoisomerization process, etc. (which is compulsory for these proteins to serve as the logical bits in hypothetical memory nanodevices), appears to be a very important task. This task could be addressed with modern computational techniques, including QM/MM methods.

Table 5.2 List of variants of bacteriorhodopsin used for computational prediction of spectral shifts with the experimentally measured absorption maxima

Protein variant	Experimental absorption maximum (nm)	Spectral shift (nm)
Wild type	568	0
13-*cis*, 15-*syn*	556	–12
Arg82-Gln	598	30
Asp85-Asn	617	49
Thr89-Val	455	–113
Asp96-Asn	569	1
Ser141-Cys	475	–93
Trp182-Phe	489	–79
Pro186-Leu	479	–89
Asp212-Ala	548	–20
Asp212-Asn	579	11

We have calculated absorption maxima for the wild type bRh as well as for its 8 mutants along with the structure containing 13-*cis*,15-*syn* isomer of retinal. For all of these variants, spectral shifts have been determined experimentally and are given in Table 5.2. ONIOM implementation (in electronical embedding form) of QM/MM method has been used as in Gaussian 09 program suite [52] for the optimization of structures (at DFTB:MM(Amber99) level of theory) and calculation of absorption maxima at DFT(TD-B3LYP:6-31G**):MM(Amber99) theory level, while Orca [58] has been used for semiempirical ZINDO/S calculations of absorption maxima.

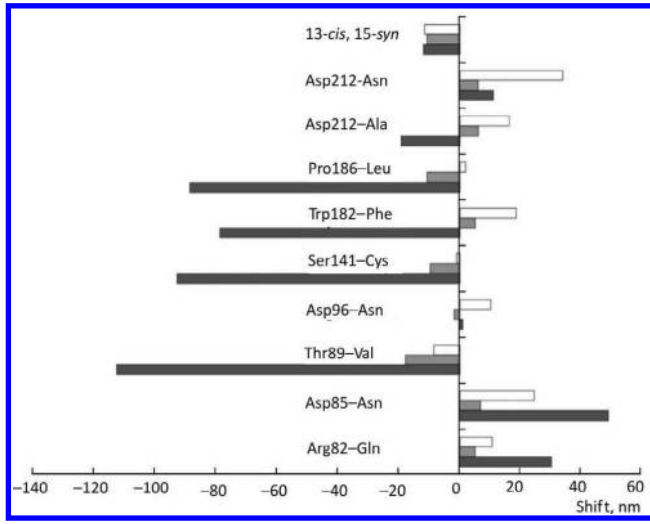

Figure 5.14 Predicted spectral shifts of the maximum of absorption spectrum for a set of bRh protein variants. For each protein form: upper bar, shift predicted by ZINDO/S method; middle, by TD-DFT; lower, experimental shift. ONIOM (TD-DFT:MM) is able to correctly predict the spectral shifts qualitatively in 8 out of 10 cases.

Computationally predicted spectral shifts are shown in Fig. 5.14. Of the two methods used for calculating the maximum of the optical spectra, the best result has been shown by TD-DFT, which has correctly predicted the spectral shifts qualitatively in 8 cases out of 10 and quantitatively in the two cases. The absolute error of the method in determining the value of spectral maximum

on average equals 40 nm, which is 6 nm less than the average absolute error of the semiempirical method ZINDO/S. In general, an approximate model, we have used in the present calculation, allows qualitative prediction of spectral shifts of bRh mutants despite a number of obvious assumptions, such as neglect of the polarization of the protein matrix by the strongly polarized dipole of retinal and ignoring of the dynamic correlations. According to [59,60], taking into account these factors may significantly improve the results of prediction.

References

1. Miyamoto, S., and Kollman, P. A., An analytical version of the SHAKE and RATTLE algorithm for rigid water models. *J. Comput. Chem*., 1992. **13**, 952–962.
2. Hess, B., Henk B., Berendsen, H. J. C., and Fraaije, J. G. E. M., A linear constrant solver for molecular simulation. *J. Comput. Chem*., 1997. **18**, 1463–1472.
3. DePristo, M. A., de Bakker, P. I., and Blundell, T. L., Heterogeneity and inaccuracy in protein structures solved by X-ray crystallography. *Structure*, 2004. **12**(5), 831–838.
4. Kay, L. E., Protein dynamics from NMR. *Nat. Struct. Biol*., 1998. **5 Suppl**, 513–517.
5. Rice, L. M., Shamoo, Y., and Brunger, A. T., Phase improvement by multi-start simulated annealing refinement and structure-factor averaging. *J. Appl. Crystallogr*., 1998. **31**, 798–805.
6. Burling, F. T., and Brunger, A. T., Thermal motion and conformational disorder in protein crystal-structures-comparison of multi-conformer and time-averaging models. *Israel J. Chem*., 1994. **34**(2), 165–175.
7. Liu, X. G., et al., Averaging tens to hundreds of icosahedral particle images to resolve protein secondary structure elements using a Multi-path Simulated Annealing optimization algorithm. *J. Struct. Biol*., 2007. **160**(1), 11–27.
8. Levin, E. J., et al., Ensemble refinement of protein crystal structures: Validation and application. *Structure*, 2007. **15**(9), 1040–1052.
9. Klepeis, J. L., et al., Long-timescale molecular dynamics simulations of protein structure and function. *Curr. Opin. Struct. Biol*., 2009. **19**(2), 120–127.

10. Karplus, M., and Kuriyan, J., Molecular dynamics and protein function. *Proc. Natl. Acad. Sci. U S A*, 2005. **102**(19), 6679–6685.

11. Levitt, M., et al., Potential-energy function and parameters for simulations of the molecular-dynamics of proteins and nucleic-acids in solution. *Comput. Phys. Commun.*, 1995. **91**(1–3), 215–231.

12. Beck, D. A., and Daggett, V., Methods for molecular dynamics simulations of protein folding/unfolding in solution. *Methods*, 2004. **34**(1), 112–120.

13. Day, R., and Daggett, V., All-atom simulations of protein folding and unfolding. *Adv. Protein Chem.*, 2003. **66**, 373–403.

14. Friedland, G. D., et al., A correspondence between solution-state dynamics of an individual protein and the sequence and conformational diversity of its family. *PLoS Comput. Biol.*, 2009. **5**(5), e1000393. doi:10.1371/journal.pcbi.1000393.

15. Kondrashov, D. A., et al., Protein structural variation in computational models and crystallographic data. *Structure*, 2007. **15**(2), 169–177.

16. Morrow, J. K., and Zhang, S. X., Computational prediction of protein hot spot residues. *Curr. Pharm. Des.*, 2012. **18**(9), 1255–1265.

17. Wass, M. N., David, A., and Sternberg, M. J. E., Challenges for the prediction of macromolecular interactions. *Curr. Opin. Struct. Biol.*, 2011. **21**(3), 382–390.

18. Ritchie, D. W., Recent progress and future directions in protein-protein docking. *Curr. Protein Pept. Sci.*, 2008. **9**(1), 1–15.

19. Terentiev, A. A., Moldogazieva, N. T., and Shaitan, K. V., Dynamic proteomics in modeling of the living cell. Protein-protein interactions. *Biochemistry* (*Mosc*), 2009. **74**(13), 1586–1607.

20. Aqvist, J., Luzhkov, V. B., and Brandsdal, B. O., Ligand binding affinities from MD simulations. *Acc. Chem. Res.*, 2002. **35**(6), 358–365.

21. Bienstock, R. J., Computational drug design targeting protein-protein interactions. *Curr. Pharm. Des.*, 2012. **18**(9), 1240–1254.

22. Kohn, J. E., et al., Evidence of functional protein dynamics from X-ray crystallographic ensembles. *PLoS Comput. Biol.*, 2010. **6**(8), e1000911. doi:10.1371/journal.pcbi.1000911.

23. Connelly, L., et al., Effects of point substitutions on the structure of toxic Alzheimer's beta-amyloid channels: Atomic force microscopy and molecular dynamics simulations. *Biochemistry*, 2012. **51**(14), 3031–3038.

24. Chan, K. Y., et al., Cryo-electron microscopy modeling by the molecular dynamics flexible fitting method. *Biopolymers*, 2012. **97**(**9**), 678–686.

25. Evans, J. E., and Browning, N. D., Enabling direct nanoscale observations of biological reactions with dynamic TEM. *J. Electron Microscop.*, 2013. **62**(1), 147–156.

26. Jana, S., et al., Study of microheterogeneous environment of protein human serum albumin by an extrinsic fluorescent reporter: A spectroscopic study in combination with molecular docking and molecular dynamics simulation. *J. Photochem. Photobiol. B-Biol.*, 2012. **112**, 48–58.

27. Lv, C. M., et al., Low folding cooperativity of Hp35 revealed by single-molecule force spectroscopy and molecular dynamics simulation. *Biophys. J.*, 2012. **102**(8), 1944–1951.

28. Frauenfelder, H., et al., A unified model of protein dynamics. *Proc. Natl. Acad. Sci. U S A*, 2009. **106**(13), 5129–5134.

29. Burnley, B. T., et al., Modelling dynamics in protein crystal structures by ensemble refinement. *Elife*, 2012. **1**, e00311.

30. Pechkova, E., and Nicolini, C., Protein nucleation and crystallization by homologous protein thin film template. *J. Cell. Biochem.*, 2002. **85**(2), 243–251.

31. Pechkova, E., and Nicolini, C., Protein nanocrystallography: A new approach to structural proteomics. *Trends Biotechnol.*, 2004. **22**(3), 117–122.

32. Hong, L., and Lei, J. Z., Scaling law for the radius of gyration of proteins and its dependence on hydrophobicity. *J. Polymer Sci. Part B-Polymer Phys.*, 2009. **47**(2), 207–214.

33. Bosi, S., et al., Fullerene derivatives: An attractive tool for biological applications. *Eur. J. Med. Chem.*, 2003. **38**(11–12), 913–923.

34. Lin, A. M. Y., et al., Carboxyfullerene prevents iron-induced oxidative stress in rat brain. *J. Neurochem.*, 1999. **72**(4), 1634–1640.

35. Lin, A. M. Y., et al., Local carboxyfullerene protects cortical infarction in rat brain. *Neurosci. Res.*, 2002. **43**(4), 317–321.

36. Dugan, L. L., et al., Carboxyfullerenes as neuroprotective agents. *Proc. Natl. Acad. Sci. U S A*, 1997. **94**(17), 9434–9439.

37. Huang, Y. L., et al., Blockage of apoptotic signaling of transforming growth factor-beta in human hepatoma cells by carboxyfullerene. *Eur. J. Biochem.*, 1998. **254**(1), 38–43.

38. Straface, E., et al., C3-fullero-tris-methanodicarboxylic acid protects epithelial cells from radiation-induced anoikia by influencing cell adhesion ability. *FEBS Lett.*, 1999. **454**(3), 335–340.
39. Qiao, R., et al., Translocation of C_{60} and its derivatives across a lipid bilayer. *Nano Lett.*, 2007. **7**(3), 614–619.
40. Karplus, M., and McCammon, J. A., Molecular dynamics simulations of biomolecules. *Nat. Struct. Mol. Biol.*, 2002. **9**(9), 646–652.
41. Friesner, R. A., and Beachy, M. D., Quantum mechanical calculations on biological systems. *Curr. Opin. Struct. Biol.*, 1998. **8**(2), 257–262.
42. Warshel, A., and Levitt, M., Theoretical studies of enzymic reactions: Dielectric, electrostatic and steric stabilization of the carbonium ion in the reaction of lysozyme. *J. Mol. Biol.*, 1976. **103**(2), 227–249.
43. Bakowies, D., and Thiel, W., Hybrid models for combined quantum mechanical and molecular mechanical approaches. *J. Phys. Chem.*, 1996. **100**(25), 10580–10594.
44. Young, D. C., *Computational Chemistry: A Practical Guide for Applying Techniques to Real-World Problems*. 2001: John Wiley & Sons, Inc.
45. Dapprich, S., et al., A new ONIOM implementation in Gaussian98. Part I. The calculation of energies, gradients, vibrational frequencies and electric field derivatives. *J. Mol. Struct.*: *THEOCHEM*, 1999. **461**, 1–21.
46. Svensson, M., et al., ONIOM: A multilayered integrated MO+ MM method for geometry optimizations and single point energy predictions. A test for Diels-Alder reactions and Pt(P(t-Bu)3)2^{+} H_2 oxidative addition. *J. Phys. Chem.*, 1996. **100**(50), 19357–19363.
47. Humbel, S., Sieber, S., and Morokuma, K., The IMOMO method: Integration of different levels of molecular orbital approximations for geometry optimization of large systems: Test for *n*-butane conformation and S_N2 reaction: $RCl^{+}Cl^{-}$. *J. Chem. Phys.*, 1996. **105**, 1959.
48. Vreven, T., et al., Combining quantum mechanics methods with molecular mechanics methods in ONIOM. *J. Chem. Theory Comput.*, 2006. **2**(3), 815–826.
49. Vreven, T., and Morokuma, K., Investigation of the S0-S1 excitation in bacteriorhodopsin with the ONIOM (MO: MM) hybrid method. *Theor. Chem. Acc.*, 2003. **109**(3), 125–132.

50. Froese, R. D. J., and Morokuma, K., Accurate calculations of bond-breaking energies in C_{60} using the three-layered ONIOM method. *Chem. Phys. Lett.*, 1999. **305**(5), 419–424.

51. Lundberg, M., et al., Case studies of ONIOM (DFT: DFTB) and ONIOM (DFT: DFTB: MM) for enzymes and enzyme mimics. *J. Chem. Theory Comput.*, 2010. **6**(4), 1413–1427.

52. Frisch, M., et al., *Gaussian 09*, *revision A. 1*. Gaussian Inc., Wallingford, 2009.

53. Kairys, V., and Jensen, J. H., QM/MM boundaries across covalent bonds: A frozen localized molecular orbital-based approach for the effective fragment potential method. *J. Phys. Chem. A*, 2000. **104**(28), 6656–6665.

54. Andersen, L. H., et al., Absorption of Schiff-base retinal chromophores in vacuo. *J. Am. Chem. Soc.*, 2005. **127**(35), 12347–12350.

55. Bogomolni, R. A., et al., Action spectrum and quantum efficiency for proton pumping in Halobacterium halobium. *Biochemistry*, 1980. **19**(10), 2152–2159.

56. Hampp, N., Bacteriorhodopsin as a photochromic retinal protein for optical memories. *Chem. Rev.*, 2000. **100**(5), 1755–1776.

57. Birge, R. R., et al., Biomolecular electronics: Protein-based associative processors and volumetric memories. *J. Phys. Chem. B*, 1999. **103**(49), 10746–10766.

58. Neese, F. Available from: http://www.thch.uni-bonn.de/tc/orca.

59. Wanko, M., et al., Computational photochemistry of retinal proteins. *J. Comput.-Aided Mol. Des.*, 2006. **20**(7–8), 511–518.

60. Wanko, M., et al., Calculating absorption shifts for retinal proteins: Computational challenges. *J. Phys. Chem. B*, 2005. **109**(8), 3606–3615.

Chapter 6

Nanomembranes for Biological Transmission Electron Microscopy

Daniel Rhinow

Max Planck Institute of Biophysics, Department of Structural Biology, Max-von-Laue-Str. 3, 60438 Frankfurt, Germany

daniel.rhinow@biophys.mpg.de

This chapter summarizes the preparation of nanomembrane and their subsequent characterization by transmission electron microscopy (TEM) utilizing new support materials such as metallic TiSi glasses, doped silicon carbide, and two-dimensional carbon materials such as carbon nanotube and grapheme.

6.1 Introduction: Transmission Electron Microscopy of Biological Specimens

Knowledge about the structure of proteins and macromolecular complexes is indispensable for understanding biological processes on the molecular level. The structure of biomolecules can be determined by X-ray crystallography, nuclear magnetic resonance

Nanobiotechnology in Energy, Environment, and Electronics: Methods and Applications
Edited by Claudio Nicolini

ISBN 978-981-4463-96-6 (Hardcover), 978-981-4463-97-3 (eBook)
www.panstanford.com

(NMR) spectroscopy, and TEM. Transmission electron microscopy is a powerful tool for structural biology as it covers the entire range of biological structures ranging from single molecules up to tomographic volumes of whole cells [1–3]. Moreover, TEM enables the structural analysis of non-periodic biological structures, whereas X-ray crystallography requires large, well-ordered three-dimensional crystals of biomolecules.

To preserve the structure of biomolecules in a near-native state, they are vitrified in a thin water layer by shock freezing in liquid ethane and analyzed at the temperature of liquid nitrogen or liquid helium. Cooling the specimen reduces the impact of radiation damage [4–6]. The goal of single-particle electron cryo-microscopy (cryoEM) is to unravel the structure of biomolecules at atomic or near-atomic resolution. Ultimately, the amino acid chain of a protein can be fitted into an electron density map obtained by TEM. The structure of several vitrified biomolecules has been solved at atomic or near-atomic resolution by cryoEM from two-dimensional crystals [7–11], helical arrays [12,13], and as single particles [14–19].

6.1.1 Electron Cryo-Microscopy of Ice-Embedded Specimens—Challenges

Many successful efforts have been made to improve instrumentation for TEM. Energy filters remove inelastically scattered electrons [20], correctors compensate for spherical and chromatic aberration [21,22], and physical phase plates are used to generate in-focus contrast for biological specimens [23–30], and CMOS detectors enable data acquisition with unprecedented signal-to-noise ratio [17,31,32]. Noteworthy, the resolution of modern aberration-corrected TEMs exceeds 0.5 Å in materials science applications [33]. Although theory predicts that atomic resolution should be routinely achieved with vitrified biomolecules [34], resolutions obtained with most ice-embedded specimens are considerably worse. The most critical factor in biological high-resolution cryoEM is the specimen itself.

For single-particle cryoEM, biomolecules are embedded in a thin layer of vitreous ice spanning the holes of a holey carbon film (Fig. 6.1).

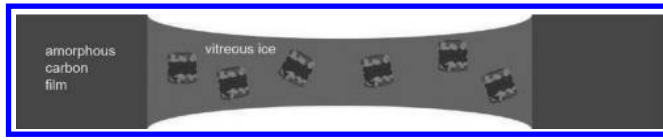

Figure 6.1 Vitrified biomolecules for structural analysis by cryogenic transmission electron microscopy (cryoEM). Biomolecules are suspended over the holes of a ~15 nm-thick holey support film consisting of amorphous carbon.

Amorphous carbon is a semiconductor, and therefore its conductivity decreases with decreasing temperature. This is of particular importance for cryoEM, where samples are studied at the temperature of liquid nitrogen or liquid helium. It has been shown that thin carbon films are electrically insulating [35]. Biomolecules are phase objects and image contrast is degraded by inelastic scattering of electrons, electrostatic charging, and beam-induced specimen movements [34]. Frozen-hydrated specimens tolerate an electron dose of ~20 $e^-/Å^2$ before high-resolution information is lost. Consequently, the low signal-to-noise ratio of EM images cannot be improved by merely increasing the electron dose.

Alternatively, thick continuous carbon films could be used instead of holey carbon films to enhance the mechanical stability of ice-embedded specimens. Glaeser et al. have shown that thick carbon support films (thickness > 30 nm) reduce beam-induced movements in cryoEM of two-dimensional crystals [36]. On the other hand, thick carbon support films considerably attenuate the signal from biological specimens, preventing their use for cryoEM of single particles.

Recently, direct electron detectors were developed, which enable video-rate acquisition of EM images with unprecedented signal-to-noise ratio [31,37], and thus facilitate removal of motion-induced image blurring by post-processing of the images [37,38]. Although this resembles a major technical achievement, specimen preparation for vitrified biomolecules should be optimized to exploit the full potential of cryoEM.

6.2 New Support Film Materials for Biological TEM

Considering the low electrical conductivity and low mechanical stability of amorphous carbon, it would be highly desirable to

develop new support film materials to improve specimen preparation for cryoEM of biological specimens.

Novel support films for cryoEM of biological specimens should meet the following requirements:

(1) Metallic conductivity, particularly at cryogenic temperatures
→ Mitigation of electrostatic charges
(2) Highly transparent
→ Minimizing inelastic scattering
(3) High mechanical stability
→ Reducing beam-induced movements
(4) Biocompatibility
→ Preservation of native protein structures

Scattering of electrons by the support film material sets an upper limit to the atomic number, the grain size, and the maximum thickness of the support film. This condition excludes metals such as gold, platinum, and tungsten, widely applied in the semiconductor industry. A variety of two-dimensional materials has been studied in the last years; the most prominent example of this new class of materials is grapheme [39,40]. Owing to their unique electrical and mechanical properties, semiconductor nanomembranes hold great promise for application in nanotechnology [41]. Furthermore, semiconductor nanomembranes are promising support film materials for cryoEM of biological specimens. In the following sections, we discuss a variety of nanomembranes, tested as support films for biological TEM.

6.2.1 Metallic Support Films

6.2.1.1 Metallic TiSi glasses

Owing to their high conductivity, amorphous alloys made from light metals are superior to amorphous carbon support films. We have studied metallic TiSi glasses as support films for cryoEM of biological specimens [42]. Alloys of titanium and silicon of $Ti_{88}Si_{12}$ stoichiometry are electrically conducting, have glass-like properties, and can be obtained in the form of thin amorphous films. The stoichiometry of the alloy is chosen to match the eutectic point of the TiSi phase diagram.

To test the properties of TiSi films under cryogenic conditions, we acquired EM images of TiSi films at 4 K. As contrast loss is

particularly noticeable at high tilt angles, images of TiSi support films were recorded at 45° tilt. The so-called Thon rings, visible in Fourier transforms of EM images of amorphous films, delineate the squared phase contrast transfer function. Beam-induced movements during image acquisition cause loss of phase contrast in EM images, which manifests in distorted Thon ring patterns. Figure 6.2 shows Fourier transforms calculated from EM images of TiSi compared to amorphous carbon. The success rate of recording images without contrast loss is ~50% higher for TiSi films than for amorphous carbon films.

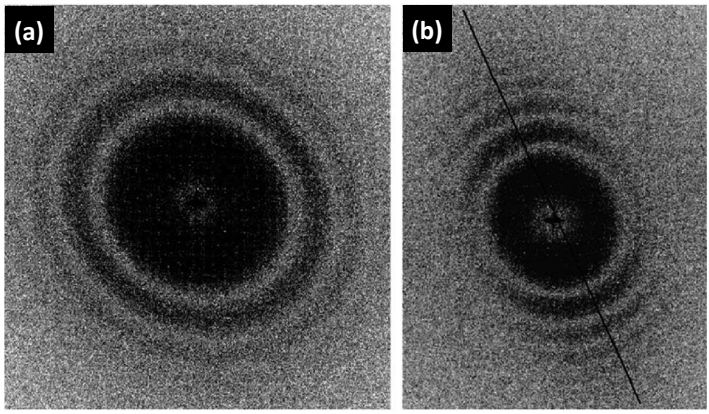

Figure 6.2 Fourier transform of representative images of bare support films taken at 4 K at a tilt angle of 45° relative to the optical axis. (a) TiSi support film. Thon rings are strong in all directions, indicating the absence of beam-induced movement of the support film. (b) Film of amorphous carbon. Thon rings are blurred in the direction perpendicular to the tilt axis (black line), indicating beam-induced movements, most likely normal to the plane of the support film. Modified with permission from [42].

Obviously, TiSi films at low temperatures reduce beam-induced movements, owing to their excellent conductivity. The high mechanical stability of metallic TiSi glasses probably will add additional stability to the sample. The support film material should be compatible with the biological specimens immobilized and vitrified on the support. It is worth noting that even amorphous carbon films can denature biological specimens severely unless age-related properties of the film are carefully controlled [7].

We used purple membranes (PM) from *Halobacterium salinarum* as test specimens, native two-dimensional (2D) crystals containing the integral membrane protein bacteriorhodopsin (BR) and lipids only [43–45]. The structure of BR has been extensively studied, particularly by cryoEM [7,46]. A projection map of PM at 4 Å resolution was calculated from images obtained from vitrified PM on TiSi support films (Fig. 6.3). The map reveals the well-known assembly of BR trimers, and thus demonstrates that TiSi is compatible with biological specimens.

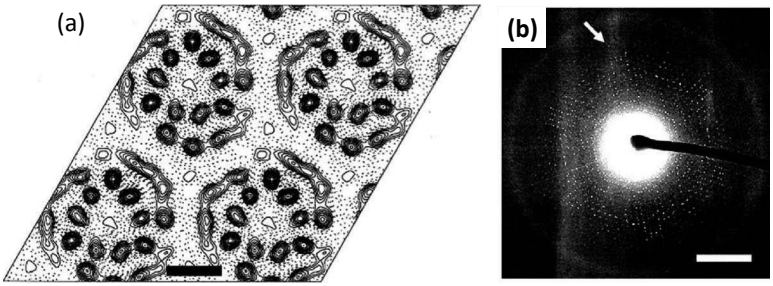

Figure 6.3 (a) Projection map of purple membrane on TiSi support film at 4 Å resolution, as calculated from amplitudes and phases of a spot-scan image. Scale bar: 20 Å. (b) Diffraction pattern of a PM multilayer on a TiSi film. Diffraction spots were observed to 2.9 Å resolution. Scale bar: 0.18 $Å^{-1}$. Modified from [42].

A diffraction pattern of PM on TiSi is shown in Fig. 6.3b. To fabricate atomically flat continuous support films the material is usually evaporated on freshly cleaved mica, subsequently floated off the mica substrate onto a water surface, and finally lowered onto an EM grid. This procedure is well established for hydrophobic materials such as amorphous carbon, which are easily released from mica. Adhesion forces between mica and metallic films are often stronger. We observed that acidification of the aqueous solution with 5% aqueous HCl is sufficient to lower the adhesion forces between mica and metallic films such as TiSi and gold.

6.2.1.2 Doped silicon carbide

Yoshioka et al. have tested Cryomesh grids, consisting of nanocrystalline conductive doped silicon carbide for application in single-particle cryoEM [47]. CryoEM images obtained from

specimens vitrified on Cryomesh grids showed less beam-induced movements compared to specimens vitrified on conventional holey carbon support films [47]. Similar to TiSi, doped silicon carbide films add mechanical stability to the sample and enable mitigation of electrostatic charges. Both factors reduce beam-induced movements of ice-embedded biological samples, and thus improve the achievable resolution.

6.2.2 Two-Dimensional Carbon Materials

Since the discovery of separated sheets of graphene [39,40], 2D carbon materials have been intensely studied [48]. 2D carbon materials are virtually transparent to the electron beam, making them promising substrates for application in biological TEM. The following sections give an overview of 2D carbon materials, which have been tested as support films for biological TEM. Ultrathin carbonaceous support films can be divided into two classes, electrically conductive and electrically insulating materials. Conductive support films are particularly suitable for structural analysis of ice-embedded biological specimens by cryoEM, which suffer from electrostatic charging. Insulating support films are suitable for TEM applications, which are not limited by electrostatic charging. We will discuss electrically insulating support film materials first, followed by the discussion of graphene as support film for biological TEM.

6.2.2.1 Carbon nanomembranes

Carbon nanomembranes (CNM) have been developed by the group of Armin Gölzhäuser at the University of Bielefeld, Germany [49,50]. First, thiolated biphenyl molecules form a densely packed self-assembled monolayer (SAM) on a gold substrate. Electron irradiation of the SAM causes cross-linking of biphenyl molecules [51]. After cross-linking, the gold substrate is dissolved and the 1 nm thin CNM is transferred to a TEM grid [52,53]. Alternatively, the cross-linked sheet can be converted to nanocrystalline graphene by pyrolysis [50,53]. Nanocrystalline graphene supports are discussed in Section 6.2.2.3.

The tensile strength of 1 nm thin CNM is high enough to span apertures as large as 250 μm [54]. In contrast, amorphous carbon films are unstable below a thickness of ~20 nm.

Figure 6.4a shows a TEM image of a CNM spanning the holes of a holey carbon substrate. In contrast to the ~15 nm carbon support film (Fig. 6.4b), ultrathin CNM contributes virtually no phase contrast to the image (Fig. 6.4c). A zero-loss energy-filtered TEM image of ferritin on a CNM support is shown in Fig. 6.4d. Ferritin is a ubiquitous iron storage protein, which consists of an iron core (6–8 nm diameter) surrounded by a protein shell. The ultrathin CNM support enhances the visibility of iron atom columns in the ferritin core.

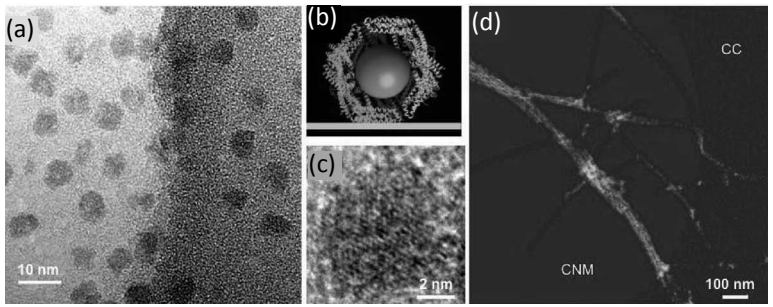

Figure 6.4 (a) Energy-filtered TEM image (zero-loss) of ferritin on CNM support film, including an area of conventional carbon. (b) Model of ferritin on CNM drawn to scale. (c) The ultrathin CNM support enhances the visibility of iron atom columns in the ferritin core. (d) Background-free elemental mapping on CNM, showing a uranium map of negatively stained tobacco mosaic virus (TMV).

Owing to their transparency, CNM supports are particularly suitable for energy-filtered TEM (EFTEM) applications, such as electron energy loss spectroscopy (EELS) and electron spectroscopic imaging (ESI) [55]. In contrast to zero-loss EFTEM, where only elastically scattered electrons contribute to the image, EFTEM uses inelastically scattered electrons to analyze the chemical composition and electronic structure of composite materials [56]. Figure 6.4g shows a uranium map of negatively stained tobacco mosaic virus (TMV) on a CNM support. Virtually background-free elemental maps can be obtained from stained and unstained biological specimens immobilized on CNM. This is important for EELS and ESI of biological materials, which are beam-sensitive and consist mainly of light elements. Depending on the biphenyl precursor used, the surface of CNM is either

hydrophilic or hydrophobic. To facilitate the immobilization of biomolecules from aqueous solution, the surface of hydrophobic CNM can be made hydrophilic by glow discharge.

6.2.2.2 Graphene oxide

Graphene oxide (GO) is a graphene-like material, obtained by oxidative splitting of graphite [57], consisting of carbon and oxygen functionalities including carboxyl, hydroxyl, and epoxy groups. The interest in GO support films for TEM stems from their transparency as well as their surface properties [58,59]. Owing to its high oxygen content, GO is a hydrophilic material, which facilitates adsorption of biological samples. Pantelic et al. have tested GO as support film for cryoEM of frozen-hydrated specimens [59]. Similar to CNM, pristine GO is electrically insulating, which might be a disadvantage for routine application of GO for cryoEM of vitrified biological specimens. However, it has been shown that the conductivity of GO can be significantly increased by heating to temperatures >200°C [60], due to loss of oxygen and partial restoration of the graphene.

6.2.2.3 Graphene

Graphene, a monolayer of sp^2-hybridized carbon, is the thinnest material, shows metallic conductivity, is mechanically robust, and can be obtained in the form of free-standing films [40,61]. Owing to its unique electrical and mechanical properties, graphene holds great promise for application as support film for TEM [62]. Application of graphene supports for TEM in materials science often requires a single graphene flake only [63]. Micron sized graphene sheets are obtained by mechanical or chemical exfoliation of graphite [64,65]. Reliable and scalable fabrication of extended sheets of graphene remains challenging. Recent approaches, such as growth on metal surfaces [66,67], can only partly meet the demand, because of difficulties with the production of homogeneous free-standing sheets, essential for application as support films in cryoEM. We have tested nanocrystalline graphene, obtained from pyrolysis of CNM (see Section 6.2.2.1), as support films for cryoEM. The electrical resistivity of annealed CNM, consisting of nanocrystalline graphene, is only one magnitude higher than the resistivity of pristine grapheme [53]. Purple membranes were analyzed on this substrate (Figs. 6.5a,b). Using TMV as a

test specimen (Figs. 6.5c,d) we demonstrated that nanocrystalline graphene supports reduce beam-induced movements considerably, due to their high conductivity and their excellent mechanical properties [68].

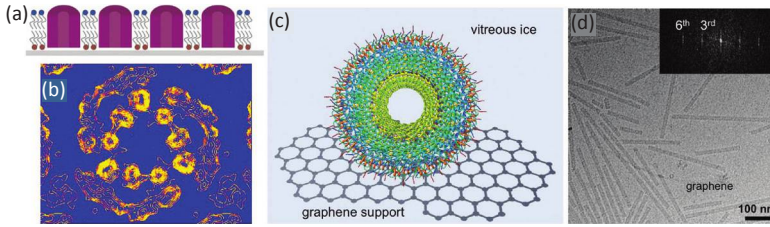

Figure 6.5 (a) Model of purple membranes (PM) from *Halobacterium salinarum* on CNM. (b) Projection map of PM on conductive CNM at 4 Å resolution. (c) Model of ice-embedded tobacco mosaic virus (TMV) on conductive CNM. (d) TEM image of ice-embedded TMV on conductive CNM. The inset shows the Fourier transform of a single TMV particle. Labels indicate the third and sixth layer lines.

Unfortunately, pristine graphene is very hydrophobic. We have observed that nanocrystalline graphene can be made hydrophilic by glow discharge. Owing to its low thickness, graphene is more sensitive toward ion bombardment and care must be taken to preserve the integrity of the support film. Pantelic et al. have shown that pristine graphene can be rendered hydrophilic by oxygen doping [69]. Alternatively, biomolecules can be transferred to graphene by microcontact printing (μCP), as demonstrated recently [70]. However, μCP of biological specimens on graphene is limited to specimens surviving the transfer procedure, which involves drying on a polydimethylsiloxane stamp.

6.3 Conclusions and Outlook

Amorphous carbon has been used for decades as support film material in biological TEM. Disadvantages of amorphous carbon films are their low electric conductivity and low mechanical stability. Table 6.1 summarizes new materials that have been tested as support film materials for biological TEM. Conductive support films are well suited for cryoEM of two-dimensional protein crystals or

single particles, which suffer from electrostatic charging. Graphene and graphene-like materials are virtually transparent to the electron beam and are therefore ideal substrates for energy-filtered TEM of biological specimens. In fact, ultrathin support films hold great promise for challenging applications such as DNA sequencing by TEM [70,71]. It is worth noting that TEM support films are among the first successful technological applications demonstrated for graphene and graphene-like materials.

Table 6.1 Materials used as support films for TEM

Support film	Material	Resistivity	Properties	References
Amorphous carbon	Disordered carbon	10 Ωm	Inert, easy to prepare	[72]
$Ti_{88}Si_{12}$	Metallic alloy	1.46×10^{-6} Ωm	High electric conductivity	[42]
Cryomesh	Doped silicon carbide	$2–4 \times 10^{-4}$ Ωm	High electric conductivity	[47]
Pristine graphene	2D crystal of carbon atoms	6 kΩ sq^{-1}	Ultrathin, high electric conductivity	[62,69, 73,74]
Graphene oxide	Graphene derivative	Insulator	Ultrathin, hydrophilic	[58,75]
Carbon nanomembrane	Cross-linked biphenyl SAM	Insulator	Ultrathin, large area sheets	[49,50,52, 55,76]
Pyrolized carbon nanomembrane	Nanocrystal-line graphene	100 kΩ sq^{-1}	Ultrathin, electrically conductive	[53,68, 77–79]

Note: Resistivity given as bulk resistivity (Ωm) or sheet resistivity (Ω sq^{-1}).

References

1. Cheng, Y., Walz, T., The advent of near-atomic resolution in single-particle electron microscopy. *Ann*. *Rev*. *Biochem*., **78**, 723 (2009).
2. Milne, J. L., Subramaniam, S., Cryo-electron tomography of bacteria: progress, challenges and future prospects. *Nat*. *Rev*. *Microbiol*., **7**, 666 (2009).

3. Lucic, V., Forster, F., Baumeister, W., Structural studies by electron tomography: from cells to molecules. *Ann. Rev. Biochem.*, **74**, 833 (2005).
4. Hayward, S. B., Glaeser, R. M., Radiation damage of purple membrane at low temperature. *Ultramicroscopy*, **04**, 201 (1979).
5. Stark, H., Zemlin, F., Boettcher, C., Electron radiation damage to protein crystals of bacteriorhodopsin at different temperatures. *Ultramicroscopy*, **63**, 75 (1996).
6. Bammes, B. E., Jakana, J., Schmid, M. F., Chiu, W., Radiation damage effects at four specimen temperatures from 4 to 100 K. *J Struct. Biol.*, **169**, 331 (2010).
7. Henderson, R., et al., Model for the structure of bacteriorhodopsin based on high-resolution electron cryomicroscopy. *J. Mol. Biol.*, **213**, 899 (1990).
8. Kuhlbrandt, W., Wang, D. N., Fujiyoshi, Y., Atomic model of plant light-harvesting complex by electron crystallography. *Nature*, **367**, 614 (1994).
9. Miyazawa, A., Fujiyoshi, Y., Unwin, N., Structure and gating mechanism of the acetylcholine receptor pore. *Nature*, **423**, 949 (2003).
10. Gonen, T., et al., Lipid-protein interactions in double-layered two-dimensional AQP0 crystals. *Nature*, **438**, 633 (2005).
11. Nogales, E., Wolf, S. G., Downing, K. H., Structure of the alpha beta tubulin dimer by electron crystallography. *Nature*, **391**, 199 (1998).
12. Sachse, C., et al., High-resolution electron microscopy of helical specimens: a fresh look at tobacco mosaic virus. *J. Mol. Biol.*, **371**, 812 (2007).
13. Ge, P., Zhou, Z. H., Hydrogen-bonding networks and RNA bases revealed by cryo electron microscopy suggest a triggering mechanism for calcium switches. *Pro. Natl. Acad. Sci. U S A*, **108**, 9637 (2011).
14. Ludtke, S. J., et al., De novo backbone trace of GroEL from single particle electron cryomicroscopy. *Structure*, **16**, 441 (2008).
15. Gipson, P., et al., Direct structural insight into the substrate-shuttling mechanism of yeast fatty acid synthase by electron cryomicroscopy. *Proc. Natl. Acad.Sci. U S A*, **107**, 9164 (2010).
16. Zhang, X., Jin, L., Fang, Q., Hui, W. H., Zhou, Z. H., 3.3 angstrom cryo-EM structure of a nonenveloped virus reveals a priming mechanism for cell entry. *Cell*, **141**, 472 (2010).

17. Bai, X. C., Fernandez, I. S., McMullan, G., Scheres, S. H., Ribosome structures to near-atomic resolution from thirty thousand cryo-EM particles. *eLife*, **2**, e00461 (2013).
18. Zhang, X., et al., Near-atomic resolution using electron cryomicroscopy and single-particle reconstruction. *Proc. Natl. Acad. Sci. U S A*, **105**, 1867 (2008).
19. Mills, D. J., Vitt, S., Strauss, M., Shima, S., Vonck, J., De novo modeling of the F420-reducing [NiFe]-hydrogenase from a methanogenic archaeon by cryo-electron microscopy. *eLife*, **2**, e00218 (2013).
20. Schroder, R. R., Hofmann, W., Menetret, J. F., Zero-loss energy filtering as improved imaging mode in cryoelectronmicroscopy of frozen-hydrated specimens. *J. Struct. Biol.*, **105**, 28 (1990).
21. Haider, M., et al., A spherical-aberration-corrected 200 kV transmission electron microscope. *Ultramicroscopy*, **75**, 53 (1998).
22. Evans, J. E., et al., Low-dose aberration corrected cryo-electron microscopy of organic specimens. *Ultramicroscopy*, **108**, 1636 (2008).
23. Danev, R., Nagayama, K., Transmission electron microscopy with Zernike phase plate. *Ultramicroscopy*, **88**, 243 (2001).
24. Majorovits, E., et al., Optimizing phase contrast in transmission electron microscopy with an electrostatic (Boersch) phase plate. *Ultramicroscopy*, **107**, 213 (2007).
25. Cambie, R., Downing, K. H., Typke, D., Glaeser, R. M., Jin, J., Design of a microfabricated, two-electrode phase-contrast element suitable for electron microscopy. *Ultramicroscopy*, **107**, 329 (2007).
26. Danev, R., Nagayama, K., Single particle analysis based on Zernike phase contrast transmission electron microscopy. *J. Struct. Biol.*, **161**, 211 (2008).
27. Schultheiss, K., et al., New electrostatic phase plate for phase-contrast transmission electron microscopy and its application for wave-function reconstruction. *Microsc. Microanal.*, **16**, 785 (2010).
28. Buijsse, B., et al., Design of a hybrid double-sideband/single-sideband (schlieren) objective aperture suitable for electron microscopy. *Ultramicroscopy*, **111**, 1688 (2011).
29. Barton, B., et al., In-focus electron microscopy of frozen-hydrated biological samples with a Boersch phase plate. *Ultramicroscopy*, **111**, 1696 (2011).
30. Walter, A., et al., Practical aspects of Boersch phase contrast electron microscopy of biological specimens. *Ultramicroscopy*, **116**, 62 (2012).

31. McMullan, G., et al., Experimental observation of the improvement in MTF from backthinning a CMOS direct electron detector. *Ultramicroscopy*, **109**, 1144 (2009).
32. Bammes, B. E., Rochat, R. H., Jakana, J., Chen, D. H., Chiu, W., Direct electron detection yields cryo-EM reconstructions at resolutions beyond 3/4 Nyquist frequency. *J. Struct. Biol.*, **177**, 589 (2012).
33. Erni, R., Rossell, M. D., Kisielowski, C., Dahmen, U., Atomic-resolution imaging with a sub-50-pm electron probe. *Phys. Rev. Lett.*, **102**, 096101 (2009).
34. Henderson, R., Image contrast in high-resolution electron microscopy of biological macromolecules: TMV in ice. *Ultramicroscopy*, **46**, 1 (1992).
35. Larson, D. M., Downing, K. H., Glaeser, R. M., The surface of evaporated carbon films is an insulating, high-bandgap material. *J. Struct. Biol.*, **174**, 420 (2011).
36. Glaeser, R. M., McMullan, G., Faruqi, A. R., Henderson, R., Images of paraffin monolayer crystals with perfect contrast: minimization of beam-induced specimen motion. *Ultramicroscopy*, **111**, 90 (2011).
37. Li, X., et al., Electron counting and beam-induced motion correction enable near-atomic-resolution single-particle cryo-EM. *Nat. Methods*, **10**, 584 (2013).
38. Brilot, A. F., et al., Beam-induced motion of vitrified specimen on holey carbon film. *J. Struct. Biol.*, **177**, 630 (2012).
39. Novoselov, K. S., et al., Electric field effect in atomically thin carbon films. *Science*, **306**, 666 (2004).
40. Novoselov, K. S., et al., Two-dimensional atomic crystals. *Proc. National Acad. Sci. U S A*, **102**, 10451 (2005).
41. Rogers, J. A., Lagally, M. G., Nuzzo, R. G., Synthesis, assembly and applications of semiconductor nanomembranes. *Nature*, **477**, 45 (2011).
42. Rhinow, D., Kuhlbrandt, W., Electron cryo-microscopy of biological specimens on conductive titanium-silicon metal glass films. *Ultramicroscopy*, **108**, 698 (2008).
43. Oesterhelt, D., Stoeckenius, W., Rhodopsin-like protein from the purple membrane of Halobacterium halobium. *Nat. New Biol.*, **233**, 149 (1971).
44. Haupts, U., Tittor, J., Oesterhelt, D., Closing in on bacteriorhodopsin: progress in understanding the molecule. *Ann. Rev. Biophys. Biomol. struct.*, **28**, 367 (1999).

45. Lanyi, J. K., Bacteriorhodopsin. *Annu. Rev. Physiol.*, **66**, 665 (2004).
46. Subramaniam, S., Henderson, R., Molecular mechanism of vectorial proton translocation by bacteriorhodopsin. *Nature*, **406**, 653 (2000).
47. Yoshioka, C., Carragher, B., Potter, C. S., Cryomesh: a new substrate for cryo-electron microscopy. *Microsc. microanal.*, **16**, 43 (2010).
48. Unarunotai, S., et al., Conjugated carbon monolayer membranes: methods for synthesis and integration. *Adv. Mater.*, **22**, 1072 (2010).
49. Eck, W., Küller, A., Grunze, M., Völkel, B., Gölzhäuser, A., Freestanding nanosheets from crosslinked biphenyl self-assembled monolayers. *Adv. Mater.*, **17**, 2583 (2005).
50. Turchanin, A., Golzhauser, A., Carbon nanomembranes from self-assembled monolayers: Functional surfaces without bulk. *Prog. Surf. Sci.*, **87**, 108 (2012).
51. Turchanin, A., et al., Molecular mechanisms of electron-induced cross-linking in aromatic SAMs. *Langmuir*, **25**, 7342 (2009).
52. Nottbohm, C. T., et al., Novel carbon nanosheets as support for ultrahigh-resolution structural analysis of nanoparticles. *Ultramicroscopy*, **108**, 885 (2008).
53. Turchanin, A., et al., One nanometer thin carbon nanosheets with tunable conductivity and stiffness. *Adv. Mater.*, **21**, 1233 (2009).
54. Nottbohm, C. T., Turchanin, A., Beyer, A., Golzhauser, A., Direct e-beam writing of 1 nm thin carbon nanoribbons. *J. Vac. Sci. Technol. B*, **27**, 3059 (2009).
55. Rhinow, D., et al., Energy-filtered transmission electron microscopy of biological samples on highly transparent carbon nanomembranes. *Ultramicroscopy*, **111**, 342 (2011).
56. Egerton, R. F., Electron energy-loss spectroscopy in the TEM. *Rep. Prog. Phys.*, **72**, (2009).
57. Hummers, W. S., Offeman, R. E., Preparation of graphitic oxide. *J. Am. Chem. Soc.*, **80**, 1339 (1958).
58. Wilson, N. R., et al., Graphene oxide: Structural analysis and application as a highly transparent support for electron microscopy. *ACS nano*, **3**, 2547 (2009).
59. Yuan, B., Zhang, Z. X., Zhou, K., Graphene oxide monolayers as supporting films for high resolution transmission electron microscopy. *Appl. Surf. Sci.*, **257**, 5754 (2011).
60. Jung, I., Dikin, D. A., Piner, R. D., Ruoff, R. S., Tunable electrical conductivity of individual graphene oxide sheets reduced at "low" Temperatures. *Nano Lett.*, **8**, 4283 (2008).

61. Meyer, J. C., et al., The structure of suspended graphene sheets. *Nature* **446**, 60 (Mar 1, 2007).
62. Pantelic, R. S., Meyer, J. C., Kaiser, U., Stahlberg, H., The application of graphene as a sample support in transmission electron microscopy. *Solid State Commun*., **152**, 1375 (2012).
63. Meyer, J. C., Girit, C. O., Crommie, M. F., Zettl, A., Imaging and dynamics of light atoms and molecules on graphene. *Nature*, **454**, 319 (2008).
64. Geim, A. K., Graphene: status and prospects. *Science*, **324**, 1530 (2009).
65. Hernandez, Y., et al., High-yield production of graphene by liquid-phase exfoliation of graphite. *Nat. Nanotechnol*., **3**, 563 (2008).
66. Reina, A., et al., Large area, few-layer graphene films on arbitrary substrates by chemical vapor deposition. *Nano Lett*., **9**, 30 (2009).
67. Li, X. S., et al., Large-area synthesis of high-quality and uniform graphene films on copper foils. *Science*, **324**, 1312 (2009).
68. Rhinow, D., Weber, N. E., Turchanin, A., Golzhauser, A., Kuhlbrandt, W., Single-walled carbon nanotubes and nanocrystalline graphene reduce beam-induced movements in high-resolution electron cryo-microscopy of ice-embedded biological samples. *Appl. Phys. Lett*., **99**, (2011).
69. Pantelic, R. S., Suk, J. W., Hao, Y., Ruoff, R. S., Stahlberg, H., Oxidative doping renders graphene hydrophilic, facilitating its use as a support in biological TEM. *Nano Lett*., **11**, 4319 (2011).
70. Cerf, A., Alava, T., Barton, R. A., Craighead, H. G., Transfer-printing of single DNA molecule arrays on graphene for high-resolution electron imaging and analysis. *Nano Lett*., **11**, 4232 (2011).
71. Bell, D. C., et al., DNA base identification by electron microscopy. *Microsc. Microanal*., **18**, 1049 (2012).
72. Robertson, J., Amorphous-carbon. *Adv. Phys*. **35**, 317 (1986).
73. Novoselov, K. S., et al., Two-dimensional gas of massless Dirac fermions in graphene. *Nature*, **438**, 197 (2005).
74. Pantelic, R. S., et al., Graphene: Substrate preparation and introduction. *J. Struct. Biol*., **174**, 234 (2011).
75. Pantelic, R. S., Meyer, J. C., Kaiser, U., Baumeister, W., Plitzko, J. M., Graphene oxide: a substrate for optimizing preparations of frozen-hydrated samples. *J. Struct. Biol*., **170**, 152 (2010).
76. Beyer, A., et al., Fully cross-linked and chemically patterned self-assembled monolayers. *Phys. Chem. Chem. Phys. PCCP*, **10**, 7233 (2008).

77. Rhinow, D., et al., Ultrathin conductive carbon nanomembranes as support films for structural analysis of biological specimens. *Phys. Chem. Chem. Phys. PCCP*, **12**, 4345 (2010).
78. Turchanin, A., et al., Conversion of self-assembled monolayers into nanocrystalline graphene: Structure and electric transport. *ACS nano*, **5**, 3896 (2011).
79. Rhinow, D., Weber, N. E., Turchanin, A., Atmospheric pressure, temperature-induced conversion of organic monolayers into nanocrystalline graphene. *J. Phys. Chem. C*, **116**, 12295 (2012).

Part B

Energy Applications

Chapter 7

Nanotechnology for Energy Devices

Enrico Stura,[a] Davide Nicolini,[b] and Claudio Nicolini[b]

[a]*Laboratories of Biophysics and Nanobiotechnology, Department of Experimental Medicine, University of Genoa, Via Pastore 3, Genoa 16132, Italy*
[b]*European Space Agency, Amsterdam*
[c]*Nanoworld Institute, Fondazione EL.B.A. Nicolini, Largo Redaelli 7, Pradalunga, Bergamo, Italy*

claudio.nicolini@unige.it

Energy-oriented components, as intended in this chapter, are elements designed in a power supply context, designed for the generation or the storage of energy in electrical form. Nanotechnology can help in the synthesis of materials with particular characteristics to make them suitable for the use in the energy field, particularly for the photovoltaic power generation and for the construction of parts of batteries, both object of this review.

The constant development of highly integrated electronic devices is leading circuits to very small dimensions. The power supply must provide enough energy for the proper functionality of these structures, so it should be based on materials with high energy efficiency to limit the weight and the volume of the device. For energy storage purposes, lithium-ion electrolytic cells for batteries are nowadays considered the best dealing with these

Nanobiotechnology in Energy, Environment, and Electronics: Methods and Applications
Edited by Claudio Nicolini

ISBN 978-981-4463-96-6 (Hardcover), 978-981-4463-97-3 (eBook)
www.panstanford.com

characteristics [1]. For what concerns energy conversion from renewable sources, solar systems based on non-standard construction techniques, like cadmium indium gallium (di)selenide (CIGS) cells or dye-sensitized solar cells (DSSCs) (also known as Gratzel cells) have gained interest also by an industrial point of view.

7.1 Lithium-Ion Batteries

A number of improvements of electrolytic lithium-ions cells for batteries (Figs. 7.1 and 7.2) were studied. An important characteristic considered while developing a lithium-ion battery is the cost of the materials involved, and it is one of the reasons for the use of polymers, spinels, and other low-cost materials. The demand for high performance of lithium-ion batteries generated strong incentives for the promotion of first-rate basic studies in different materials sciences (Fig. 7.3), surface science, crystallography, spectroscopy, microscopy, and electrochemistry.

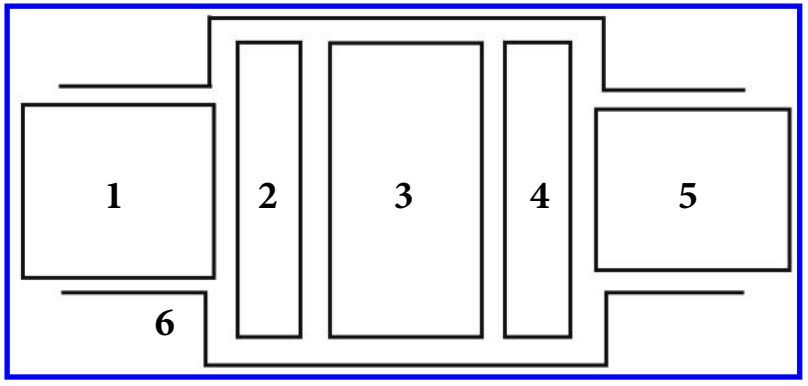

Figure 7.1 Physical layout of the cell: (1) Negative current collector (stainless steel); (2) cathode; (3) electrolytic solution (LP30-pregnated porous membrane); (4) anode (metallic lithium); (5) positive current collector (stainless steel); (6) hermetic plastic container.

Intensive efforts are now in progress in order to match the compatibility requirements of such devices, such as the development of new electrolyte solutions with non-flammable solvents [2] and to assure a safe operation, over charge protection [3].

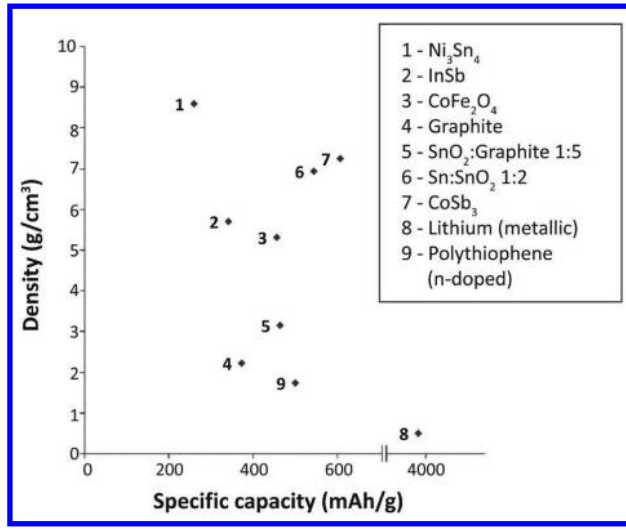

Figure 7.2 Comparison among different anode nanomaterials: density versus capacity (mAh g^{-1}).

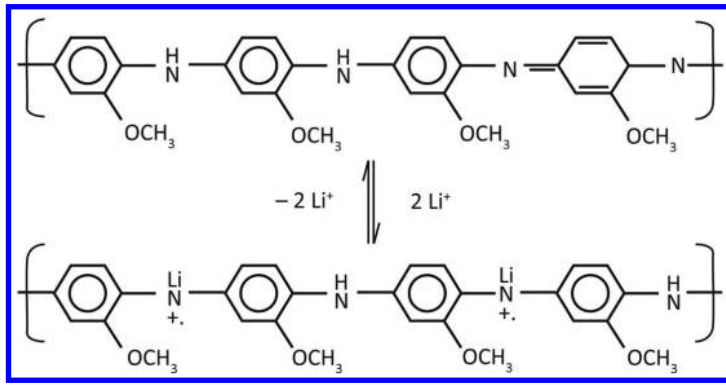

Figure 7.3 Chemical intercalation of the lithium ions in the polymer.

Many efforts are spent to develop new materials for separators [4] and new solid-state electrolytes, both polymeric [5] and ceramic [6]. There are also highly intensive efforts for the development of new cathode materials with high redox potential [7], including novel spinel compounds. The efficiency of different materials changes drastically between the raw form and the nanostructured form, the same molecules organized in different spatial position (pellets, nanoparticles, nanotubes, high-surface-ratio elements) can change their macroscopical behaviour and electrical characteristics,

because of their chemical and physical parameters (like surface energy). The correlation between these parameters and the electrochemical behaviour of electrode materials are still not completely defined.

The use of different analytical chemistry techniques such as neutron diffraction [8], X-ray absorption near edge structure [9], extended X-ray absorption fine structure [10], and in situ techniques like Raman spectroscopy [11], infrared spectroscopy [12], various kind of atomic force and tunnelling microscopies [13], X-ray diffraction [14] and mass spectroscopy [15] contribute to obtain clear relation between the chemical–morphological aspect and their behaviour. The use of electrochemical impedance spectroscopy is also an important tool for the characterisation of batteries and fuel cells. This technique yields quantitative information on a diverse range of processes including the analysis of state of charge, study of reaction mechanisms, film aestivation and corrosion processes.

7.1.1 Lithium-Ion Battery Elements

The studies oriented to the improvement of the efficiency in lithium-ion batteries are often carried out separately on each of the three most significative elements that compose the battery (cathode, anode and electrolyte). In this way, it is possible to define the parameters affecting the performances of the complete device by means of a methodical approach, using standard parts for the rest of the battery. Anyway, this way of operating not always grants the best results, particularly when different incompatible elements are joined (i.e. wet gel electrolytes with reactive cathodes), and introduces the risk of limiting the research to a purely scientific work, leaving the integration issues to the industrialization phase. For this reason, some research groups aim their efforts to the evaluation of the compatibility among different elements, trying to reduce the gap between the theoretical results and the scale-up processes.

7.1.1.1 The cathode

A considerable variety of cathode materials have been studied to develop efficient elements with high energy density: metallophosphate, lithium spinel materials. The overall effectiveness of different kinds of standard nanocomposite materials for

cathodes of batteries, intended as voltage versus lithium and specific capacity, is given in Table 7.1. Recently, innovative materials like metallophosphates with olivine-type structure lately attracted a noticeable attention as possible intercalation materials for the Li^+ ion [16–19]. This interest is focused mostly on the lithium iron phosphate ($LiFePO_4$) because of the high discharge voltage of 3.6 V versus metallic lithium and the environmental compatibility of iron. Delacourt et al. showed that the electrochemical deintercalation of the Li^+ ion from another interesting compound, $LiMnPO_4$, prepared by a new precipitation mean, leads to the disappearance of $LiMnPO_4$ and to the formation of the new material with the same structure, but with lower cell volume [20]. The reversibility of lithium intercalation and deintercalation from $LiCoPO_4$ was improved by an artificial method based on the precursor $NH_4CoPO_4{\cdot}H_2O$ [21], even if the cyclability of the material is not good. Diffraction patterns of Li_xCoPO_4 sample charged to $x = 0.05$ (from the electrochemical data) by refining a two-phase model were analyzed [22]. The difference in the cell volumes for both isostructural phases was found to be much lower in comparison with the data reported for manganese metallophosphate.

Table 7.1 Comparison of different nanostructured cathode materials used in lithium-ion batteries

Material	Voltage vs. Li/Li^+ (V)	Specific capacity
$LiNiO_2$	3.5	180 $mAhg^{-1}$
$LiCoO_2$	3.7	140 $mAhg^{-1}$
$LiFePO_4$	3.6	150 $mAhg^{-1}$
$LiMn_2O_4$	4.0	120 $mAhg^{-1}$
$Li_xNi_yMn_zCo_wO_2$	4.2	220 $mAhg^{-1}$

Another interesting material for batteries' cathodes is $LiMn_2O_4$, which attracted significant interest mostly because it has 4 V as voltage versus metallic lithium. Its reversible capacity (110–120 mAh g^{-1}) and its characteristics are similar to the ones of the currently used $LiCoC_2$. The manganese spinel material is cheaper and more environmentally compatible, and undergoes a phase transition at 290 K, transforming itself from a cubic phase (at high temperature) to a orthorhombic phase (at low temperature). This transition takes place for the critical concentration of Mn^{3+} ions

(Jahn–Teller ions). This is due to the presence of Mn^{3+} ions, and this transition is probably responsible of the limited cyclability [23,24].

Recent results in the cathode research introduced $LiNi_{0.5}Mn_{0.5}O_2$, providing over 30 cycles of charge/discharge with a capacity of 200 mAh g^{-1} [25]. Another useful material, $LiCo_{0.5}Mn_{0.5}O_2$, exhibits a first charge and discharge capacities of, respectively, 220 and 125 mAh g^{-1}, that makes it suitable for non rechargeable batteries too [26]. In the past 10 years, particular attention has been paid to TiO_2 nanoparticles and their electronic properties. This material can attract interest for the realization of low voltage batteries, since its discharge voltage is 1.8 V versus Li/Li^+. However, the insertion of 1 Li per TiO_2 unit corresponds to a capacity of 335 mAh g^{-1}. For the best results in the realization of cathodes for lithium batteries, 20 nm nanoparticles are normally used, since it has been reported that a sol–gel sample prepared starting with these nanoparticles undergoes an optimal partial phase transformation around 600°C that generates a favourable material with good electrochemical characteristics. The insertion coefficient in anatase (TiO_2) is usually close to 0.5 [27], making these nanoparticles interesting materials for batteries designed for particular purposes.

7.1.1.2 The anode

Carbon-based materials are currently commercially used as anode materials due to the flat charge and discharge plateau and excellent cycling stability. However, their theoretical maximum capacity is limited to 372 mAh g^{-1}, corresponding to the formation of LiC_6 [28]. Since the introduction of tin-based oxide composite by Fuji Photo Film Celltec in early 1997 [29], great interest has been turned to metal, intermetallic compounds and alloy anodes due to their extremely larger capacity compared to those of carbon-based materials. In the new battery technology, there is a renewed interest in metal alloys and intermetallic compounds for replacing graphitic carbon as the anode of choice in lithium-ion batteries.

The lithiation voltage of these materials is enough positive versus metallic lithium to minimize lithium plating problems (occurring in case of overcharge). Furthermore, these materials offer a higher volumetric capacity than graphite.

For example, the theoretical volumetric capacity of InSb is 1904 mAh cm^{-3} (assuming a constant electrode density of

5.6 g cm^{-3} throughout charge and discharge) compared with a theoretical 818 mAh cm^{-3} for graphite (ρ = 2.2 g cm^{-3}).

Although alloys have much higher capacities than that of graphite, they undergo severe volume expansion/contraction and pulverization. The effect of these events limits the life cycle of the anode and of the whole battery. The performance of an alloy anode can be improved if the active alloy is supported by inactive components, which provide structural stability during cycling [30,31]. Sn–Cu intermetallic compounds have been suggested as promising alternative anode materials [32–34]. Kim et al. [35] prepared nanosized Cu_6Sn_5 electrodes by chemical reduction and found that their cyclability was significantly enhanced as compared with the same material prepared by sintering or mechanical alloying. Even though, the above preparation methods are not suitable for large scale, where low-cost production of alloy electrode materials is of primary importance [36].

The main drawback of alloy compounds is the rapid capacity fade after repeated cycling, resulting from the large volume changes (expansion and compression) during the charge and discharge phases [37].

Among organic materials, dialkylimidazolium-based ionic liquids with the weakly complexing anions (e.g. PF_6^-, BF_4^- or $CF_3SO_3^-$, $(CF_3SO_2)_2N^-$) seem to be the most stable and conductive to date [38–41]. The 1-butyl-3-methylimidazole-based ionic liquids with PF_6^- [42] and $(CF_3SO_2)_2N^-$ [43] have high hydrophobicity besides other good properties [44]. These materials are particularly useful for the realization of anodes for specific applications like lithium/seawater batteries [45]. Figure 7.2 shows the comparison among the anode nanomaterials: density versus capacity (mAh g^{-1}). This figure gives an idea of how certain materials, universally considered "good" in reality need large volumes to reach few milligrams, while others considered "mediocre" need instead small volumes to obtain large masses.

7.1.1.3 The electrolyte

Currently most industrial electrolytes are mixtures of ethylenecarbonate, diethylcarbonate and dimethylcarbonate with lithium hexafluorophosphate ($LiPF_6$) as salt. This type of electrolyte permits a great number of charge–discharge cycles without noticeable loss in capacity but the search of new electrolytes with

higher thermal stability is of great importance [46–56]. Among polymeric electrolytes, poly(ethylene oxide)–lithium salt complexes are promising candidates as electrolytes for lithium polymer battery applications [57–60]. Large research efforts were spent for the development of poly(ethylene oxide) electrolyte solutions allowing to combine high conductivity, good interfacial stability with lithium metal anode and good mechanical properties [61–62]. A common approach is the use of a lithium salt having a very large counter-ion, able to interfere with the crystallization process of the polymer chains [63,64], promoting amorphous regions and increasing the lithium-ion transport across the polymeric electrolyte [65,66].

- Room temperature ionic liquids (RTIL) can also be used as safe electrolytes in electrochemical applications owing to their wide thermal stability, wide liquid-phase range, non-flammability and very low vapour pressure [67,68]. These RTIL are composed of a cation combined with a variety of large anions having a delocalized charge (PF_6^-, BF_4^-). All RTILs show a high viscosity and therefore a relatively low conductivity. In order to decrease the viscosity and increase the conductivity, aprotic dipolar organic solvent may be added to RTIL, experimental results obtained by Chagnes et al. [69] using butyrolactone confirm this. Recently, to avoid liquid electrolytes and the related hydraulic insulation issues, some efforts were spent in the research of solid state or gel electrolytes. Ion-conducting polymer electrolytes have contributed to the development of lithium battery technology by replacing the liquid electrolyte and thereby enabling the fabrication of flexible, compact and laminated solid-state structures free from leaks of the electrolyte [70]. However, their low ionic conductivities have been the reason for them not being used in practical applications in rechargeable lithium batteries that require a value of above 10^{-4} S cm^{-1} at room temperature [71]. It is only above the melting temperature of crystalline poly(ethylene oxide)-lithium salt complexes (60°C) that significative conductivity values ($\sigma > 10^{-4}$ S cm^{-1}) are measured [72]. An alternative strategy for creating polymer electrolyte systems with improved electrical and mechanical properties is through fabrication of polymer silicate nanocomposites. These materials are a

class of compounds in which nanoscale clay particles are molecularly dispersed within a polymeric matrix [73–76]. Recent commercial interest in these nanocomposites is derived from the fact that they show significant increases in tensile strength [77], heat resistance [78] and solvent resistance [79] as well as decreases in gas permeability when compared with the bulk polymer [80].

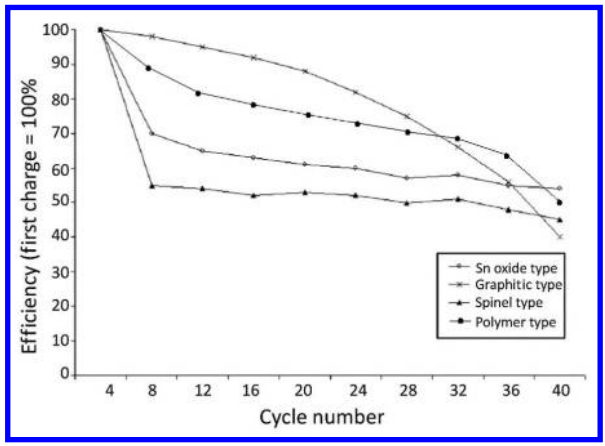

Figure 7.4 Cyclability of nanomaterials for lithium-ion batteries.

Hence, noteworthy is the development of

- new materials for batteries (Fig. 7.3)
- the unique cyclability of nanomaterials for lithium-ion batteries (Fig. 7.4) up to multiple cycles (Fig. 7.5)

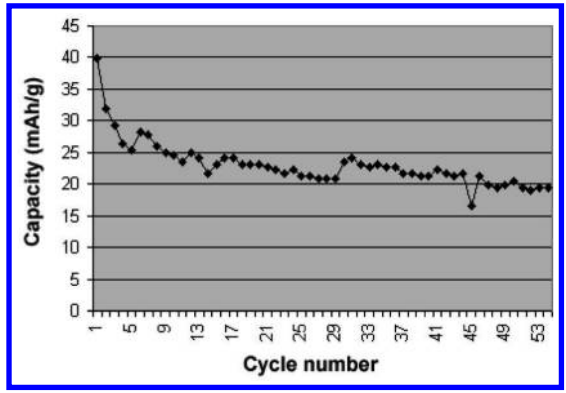

Figure 7.5 Multiple cycle analysis.

The overall effectiveness of different kinds of nanocomposite batteries is given in Table 7.2.

Table 7.2 Overall effectiveness of different kinds of nanocomposite batteries

Battery type	Energy density (Wh/kg)	Energy density (Wh/l)	Maximum charge/ discharge	Nominal voltage
Ni–Cd	34	80	~1000	1.2
Ni–H	54	64	~5000	1.2
Pb acid	38	78	~500	2.0
Li ion	152	305	~3000	3.3–4.0

7.2 Photovoltaic Systems

The continuously increasing demand for energy has been the main reason of the studies having as subject the conversion of energy from renewable sources in the last two decades. Particularly, solar power conversion has been one of the focal points in the energy-oriented nanotechnology research, mostly because of the open issues that are not yet solved using traditional silicon-based approaches. Since the first solar cell obtained by Czochralski in 1941, many improvements have been carried out, but to date the efficiency of conversion of the real commercial device is still far lower than 30% theoretically obtainable in state-of-the-art standard devices. Nevertheless, the recent efforts spent in the research of new techniques and materials already produced sufficiently encouraging results allowing thinking about a reasonable integration of photovoltaic modules in the overall energy production systems in the following decade.

Different technologies play different roles in the integration of solar power conversion devices (Figs. 7.6 and 7.7), according to the cost of production of the modules, their energy payback time and their optimal size to obtain the best efficiency (Fig. 7.8). Two main alternatives to the standard mono- and polycrystalline silicon devices, both based on thin-film technologies, are currently considered very interesting: CIGS cells and DSSCs. The first one, more industrially consolidated, is oriented to larger scale

applications such as solar plants; the second one is more interesting for local production of energy for low-power devices. The latter also requires far less precise and expensive instruments to be constructed, but the efficiency obtainable is currently lower with respect to the CIGS cells.

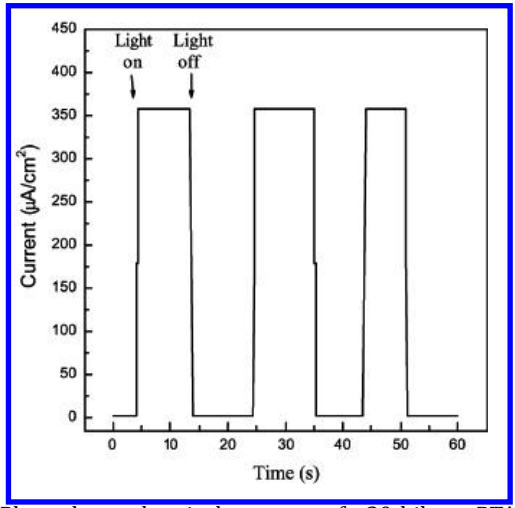

Figure 7.6 Photoelectrochemical response of a 20-bilayer PTAA/TiO_2 LBL film in an electrolyte of 0.1 mol dm23 NBu_4BF_4 acetonitrile solution. The potential of the working electrode was set at 0.0 V vs. the Pt counter electrode.

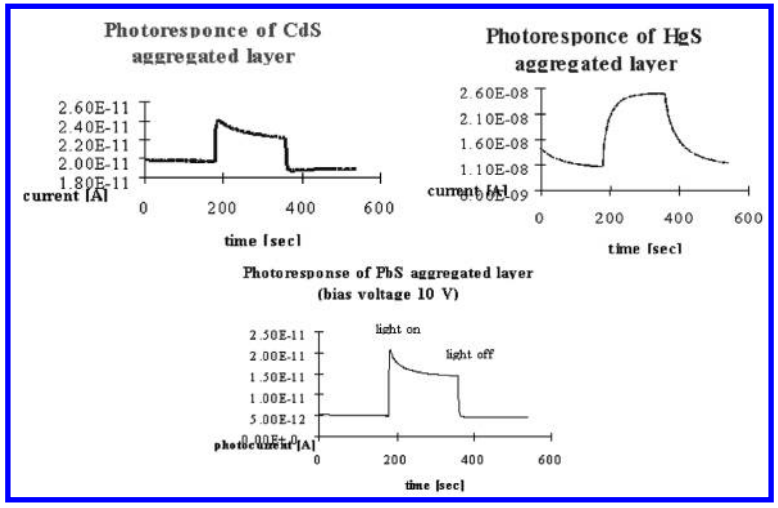

Figure 7.7 Photoresponse of aggregated nanoparticles.

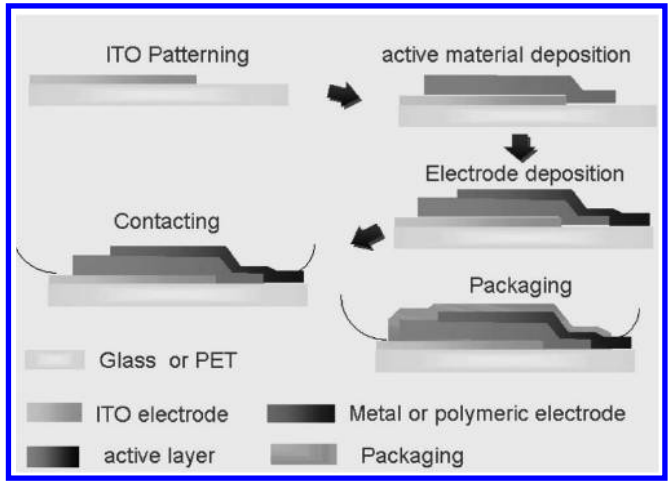

Figure 7.8 PV fabrication process.

7.2.1 Dye-Sensitized Solar Cells

Dye-sensitized solar cells were invented in 1991 by Michael Graetzel and Brian O'Regan [81] and represent one of the most interesting applications of the thin-film photovoltaic systems. The main difference with respect to the traditional silicon solar cells lies in the division of the roles of the semiconductor active material, whereas in standard photovoltaic cells, the silicon works both as a source of electrons and as a provider of electric field to move the charges. In DSSCs, the semiconductor is only used to transport the charge carriers. Electrons are obtained from a separate photosensitive dye, extracted from such molecule at the interface between dye, semiconductor and electrolyte.

7.2.2 DSSC Elements

The original and most typical DSSC design relies on titanium dioxide as semiconductor material, because of the wide bandgap of 3.0–3.2 eV and its relatively easy nanostructurability; fluorine-activated tin oxide as transparent conducting electrode; a liquid solution of triiodide–iodine ion as electrolyte; various ruthenium organometallic dyes as "light harvesting" molecule and a counter electrode of platinum, normally sputtered or evaporated over a glass substrate. All of these elements were widely studied in order

to find more efficient or cheaper alternatives. Nevertheless, the overall efficiency of the finite device is not significantly improved with respect to the original prototype by Michael Graetzel and Brian O'Regan, considering the worldwide research efforts spent in the last 19 years. The most important result in DSSC construction is the ability to build real-world devices, almost ready to face the market, starting from the original prototype consisting of the only proof of principle.

7.2.2.1 The semiconductor

Properties of the semiconductor (normally titanium dioxide) at the nanoscale affect the physical and energetic parameters of the DSSC. Such material is deposited in the best possible way to adsorb the maximum quantity of dye molecules on its surface, so high surface factors are desirable. Nanoparticles are often used to achieve highly efficiently surfaces; a study was carried out to investigate on their optimal diameter to achieve the maximum output voltage, showing that an increase of open-circuit voltage from 620 to 765 mV is observed with the increase of particle size from 8 to 48 nm [82]. This phenomenon was ascribed to different crystal qualities and to the vacancy of oxygen in scaffolds too small originating from excessively small nanoparticles. In the preparation of the colloid-containing titanium dioxide, hydrothermal temperature can influence the arrangement of the semiconductor over the transparent conducting electrode, it was found that an optimum temperature for films larger than 10 um is 240°C [83]. When using glancing angle deposition as alternative method for the structuring of titanium dioxide, using an electron beam equipment, the best results corresponding to the maximum adsorption of the dye on the semiconductor surface were obtained using an incident angle of 73° [84].

Instead of pure titanium dioxide, composite materials were tested to improve energy conversion efficiency. Interesting results were obtained using aluminium or tungsten impurities, that yielded higher open circuit voltages but lower short circuit current and vice versa, respectively; calcium-titanium oxide was also tested as additive, resulting in a thin layer over the titanium dioxide that improved the dye adsorption and consequently increased the efficiency conversion of 34% with respect to the undoped titanium dioxide [85]. Hybrid particles of gold (or silver) and titanium

dioxide were analysed, and some improvement in the efficiency of the cell was observed, probably due to plasmon resonance or Schottky barrier effects [86].

7.2.2.2 The electrolyte

The original design of DSSC used a liquid solution of triiodide–iodine to replace the electron lost from the dye molecule and injected in the semiconductor layer when light excites the light-harvesting molecule. Such liquid solution can be source of different problems both when temperature grows over the upper operating limit and when it falls under the lower operating limit. In the first case thermal expansion of the fluid results in stress on the sealing, inducing leaking of the electrolyte, in the second case the freezing leads to mechanical force making cracks of the entire system possible. Nevertheless liquid solutions grants the best availability of ionic charge carriers, diffusion of triiodide in the fluid according to temperature was studied [87] and it was found that an optimum temperature exists where a significant diffusion occurs but recombination phenomena are not yet significant.

Polymeric gel electrolytes are widely studied to achieve a good compromise between diffusion of charge carriers and mechanical properties, interesting results leading to efficiency values similar to the ones obtained with standard liquid solutions were achieved using 3-(iodohexyl)-1-(3-(triethoxysilyl)propylcarbamoyl)-1H-benzo[d]imidazol-3-ium iodide [88]. Simpler polymers like polyethylene oxide can be possible candidates as matrix for triiodide–iodine systems, probably for the coordination of the iodine cations to the ether group present in the polymer [89]. The same polymer, blended with poly vinylene fluoride, was used to investigate on the improvements obtainable adding hydroxyl rich small molecules (water and ethanol), resulting in enhanced ion mobility [90].

Solid and quasi-solid electrolyte systems were tested, aiming to build DSSC free from sealings and consequently more stable and to bypass the problem of the shrinkage of gel matrix due to evaporation of the solvent. Poly(vinylidenefluoride-co-hexafluoropropylene) was successfully used to obtain a solid electrolyte [91], but to avoid a reduction of the short circuit current particular attention must be paid to the physical structure of the cell.

7.2.2.3 The dye

Light-harvesting molecules studies were mostly carried out with focus on finding cheaper alternatives to the original ruthenium-based organometallic molecules, which significantly affected the final price of the device. Moreover, the reference dye N719 (cis-bis(isothiocyanato)-bis(2,2′-bipyridyl-4,4′-dicarboxylato)-ruthenium(II)) is a very good light absorber molecule in a wide but still not optimal range of frequency, so another target of many research works is to find a dye that covers the widest possible range of frequency emitted from the sun and reaching the earth's surface. Figure 7.9 compares the efficiency versus wavelength of three standard artificial dyes.

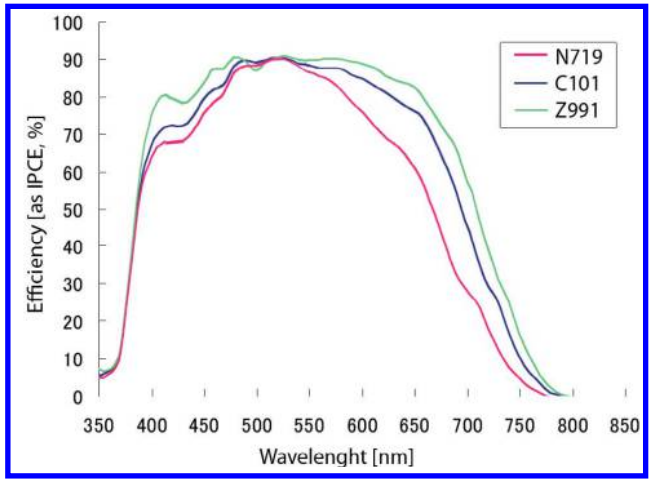

Figure 7.9 Comparison of three artificial dyes used in DSSCs.

The investigations on natural-based dyes focused on extracts from different plants, to exploit the biosynthesis processes and reducing the cost of production for the light harvesters. Among the tested species, a flowering plant belonging to the order of Commelinaceae named *Rhoeo spathacea* was used to obtain a pigment that yielded an efficiency of 1.49% [92], mixed extracts form Blue pea and Rosella, if extracted at 50°C, resulted in efficiency of 0.7% [93], chlorophyll obtained from Spinach and Ipomea converted energy with efficiency of 0.318% [94].

Such results obtained using natural dyes are very interesting from a scientific, ecological and economic point of view, but the

efficiencies listed are unsatisfactory for any application in real devices. For this reason, synthetic molecules have been constantly studied since the invention of the DSSC. Particularly, porphyrins have attracted the attention of many research groups, gathering interesting conversion efficiency of 4.2% for 4-*trans*-2′-(2′-(5′,10′,15′,20′-tetraphenylporphyrinato zinc(II)yl)ethen-1′-yl)-1-benzoic acid [95]. Good results were also obtained using coumarines modified to expand their PI-conjugation and therefore increasing their absorption in the visible frequencies, resulting in an overall efficiency of 6% [96].

Traditional ruthenium-based dyes are still of research interest, even if expensive, since they represent the most efficient light harvesters. Standard N3-based DSSCs were improved by adding a layer of polyacrylic acid and ethylenediamine linking the dye molecule to the titanium dioxide semiconductor, obtaining improvements both in the open circuit voltage and in the short circuit current [97]. A novel dye designated as CYC-B, still based on ruthenium complexed with an alkyl bithiophene group, is currently studied and shows improved short circuit current with respect to N3, and yields its best efficiency with semiconductor thickness of only 6 μm [98].

7.2.2.4 The counter electrode

The return path of electric charge to the electrolytic solution in DSSCs is mediated through a counter electrode interfacing the electrolyte to the end of the circuit fed by the electrical energy converted by the cell. Even if often not considered as a key element of DSSCs, the counter electrode is responsible for significant losses occurring in the complete path of energy, for this reason some studies are carried out to minimize such losses optimizing the conducting system in contact with the solution.

Normally, a sputtered layer of metallic platinum is used as standard counter electrode, because of its good conductivity and resistance to oxidation. Some improvement, particularly a higher short circuit current, is obtainable depositing platinum by means of more complex methods, like electrodeposition in mesoporous form in presence of a structure-directing non-ionic surfactant [99], producing a metallic layer with high specific surface and light reflection allowing better efficiency with respect to traditional sputtering methods.

Other non-metals were tested as replacement of platinum, including polymers. Polypyrrole layers with high surface factor were deposited starting from nanoparticles of diameter of 40–60 nm, resulting in a counter electrode with a conversion efficiency 11% higher than the same cell completed with a platinum counter electrode [100]. Polyaniline also showed good performances when used in layers with microporosity in the 100 nm range, exhibiting a higher electrocatalytic activity for the I^{3-}/I^{-} redox reaction than standard platinum counter electrode [101].

Carbon nanotubes attracted interest from various research groups, electric impedance spectroscopy showed that charge transfer is improved and series resistance is reduced with respect to graphite and platinum [102]. Hard carbon spherules also provided acceptable results when deposited to obtain a continuous layer as replacement to standard metallic counter electrodes [103].

7.2.2.5 Copper indium gallium diselenide cells

An attractive and innovative photovoltaic cell design is represented by copper indium gallium (di)selenide (CIGS) cells. Their working principle is similar to the traditional silicon photovoltaic devices, differing mainly because of the operation based on a heterojunction instead of a homojunction. The active part of the cell, constituted by the zinc oxide–CIGS junction, is normally present in the form of a thin film of few (2–4) μm. Often the junction is buffered by a thin layer of other components, like cadmium selenide, to optimize the overall efficiency. Because of the different doping level in the CIGS and zinc oxide regions, the space-charge region extends deeper in the first material with respect to the second, allowing the zinc oxide layer to be much thinner.

The energy conversion efficiency of the finite CIGS module reaches 15% in laboratory prototypes, and commercially available devices are rated up to 10% to date. Many research efforts are oriented to the improvement of both the materials involved in the device and the deposition techniques, allowing to obtain prototypal devices with laboratory efficiency reaching 19% [104].

The substrate upon which the active materials are deposited strongly affects the properties and the performances of the resulting device, particularly the thermal expansion parameters of such substrate, together with surface roughness, are proven to strongly influence growth and properties of the following layers.

The use of a flexible substrate, like polyimides, is very attractive for the construction of modules that are able to stand mechanical stress without loosing their functionality but require more complex techniques of fabrication like low temperature deposition processes [105].

To improve the surface efficiency of the CIGS material, additional treatments have been tested using liquid In-S aqueous solutions containing indium trichloride and thioacetamide, forming thin layers of copper-indium diselenide over the CIGS. This process enhanced the short circuit current density of the cell up to 36.1 mA/cm^{-3} [106]. Another process used to improve the CIGS surface has been carried on using indium sulphide deposited by evaporation, followed by annealing in presence of sulphur vapour [107], this process being attractive since no toxic hydrogen sulphide is involved for the sulphurization of the surface. As alternative to the traditional deposition methods of the CIGS layer, sintering process are currently studied, using pressureless techniques to obtain sputtering targets from raw powders of copper selenide, indium selenide and gallium selenide, properly balanced to meet the stoichiometry required in the final CIGS layer [108]. Also, organic solvent assisted deposition processes were studied, using hydrazine as matrix for the incorporation of metals and chalcogenides required for the formation of the CIGS layer. A precursor layer must be spin coated and a thermal treatment under 500°C of the solution has to take place in inert environment, in this way there is no need to post-treat the CIGS material with gaseous selenium or cyanide-based baths [109]. Also modern proofs of concepts have been experimented, including inkjet printing of colloidal chalcopyrite copper indium sulphide and copper indium gallium selenide nanocrystals ranging from 5 to 25 nm in diameter, obtained by precipitation [110]. Results are encouraging, opening the way to new possible experimentations, even if currently performances obtained by this method are still not comparable to more consolidated techniques.

Considering the complete photovoltaic device based on CIGS, also the transparent electrode has to be considered as an element that participates to the overall efficiency. Transparent conducting oxides, like indium tin oxide, are normally used in standard modules as current collectors. New alternatives are also studied, aiming to find a material that accomplishes the basic task of being

both conducting and transparent, but limiting the Joule losses and enhancing the compatibility with the rest of the system. Single wall carbon nanotubes, embedded in a matrix of insulating polymer, were deposited over the CIGS layer replacing the transparent conducting oxide layer, maintaining a high energy conversion efficiency of 13% and suggesting the use of such materials also in other applications benefiting from a p-type transparent conductor with high near-infrared transmission [111].

Table 7.3 Photovoltaic cells performances based on conventional and non-conventional materials

Material	Max. theoretical	Average specific power (W/m^2)	Average specific power (W/kg)	Flexibility
Silicon	18 (a)	190 (a)	32 (a)	No
Gallium arsenide	23 (a)	244 (a)	Up to 100 (a)	No
Indium phosphate	22 (a)	200 (a)	Up to 100 (a)	No
Light-sensitive proteins	25 (b)	250 (g)	2103 (f)	Excellent
Polymers	1.9 (c)	20 (g)	8103 (f)	Excellent
Fullerenes + polymers	5 (d)	50 (g)	104 (f)	Good
Aggregated particles	14.5 (e)	170 (g)	600 (f)	Good
Composite materials	6.5 (f)	70 (g)	104	Good

7.3 Conclusions

Starting from basic proof of principles using standard nonstructured materials, the evolution of nanotechnology led laboratory-scale energy devices [112–118] to significant performance improvements. Namely, worthy of notice are

- construction of organic/inorganic hybrid ultrathin films self-assembled from poly(thiophene-3-acetic acid) and TiC_{l4} [112]
- bacteriorhodopsin-based Langmuir–Schaefer films for solar energy capture targeted to space applications [113]
- hydrogen storage as stabilization for wind power: a completely clean system for insulated power generation [114] (Figs. 7.10 and 7.11)

- polyaniline nanocomposite materials for low-power long-life lithium [115]
- new materials for batteries [116]
- functionalization and photoelectrochemical characterization of poly[3-3(vinylcarbazole)] multi-walled carbon nanotube (PVK-MWNT) Langmuir–Schaefer films [117]
- nanostructured biofilms and biocrystals [118]

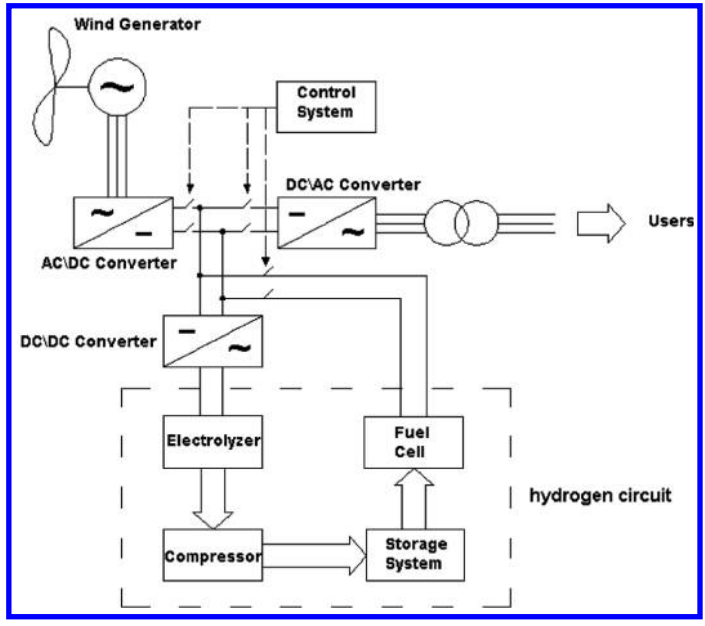

Figure 7.10 Layout of the system.

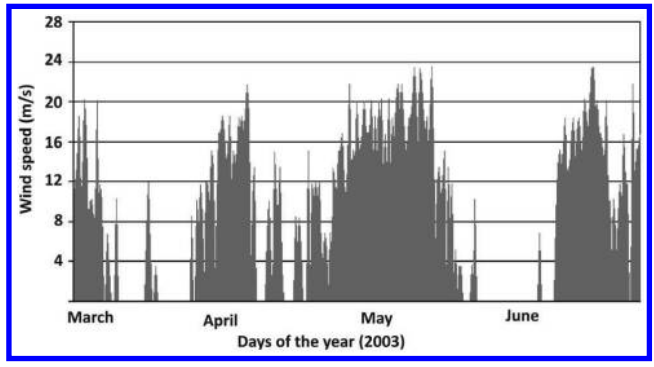

Figure 7.11 Wind activity as measured in the four months of acquisition.

By now, lithium-ion batteries are the most used devices in almost any kind of mobile devices, both for industrial and for commercial applications, overcoming most part of the issues typical of the previous technologies in batteries. In the past years, nanotechnologically engineered polymers (112,113) were implemented in the realization of lithium batteries (115,116), reducing the overall weight of the power supply element providing acceptable values of capacity. Most industries included in their next future research plans studies of better nanomaterials for the application in lithium-ion batteries. Particular attention is oriented nowadays to organic cathodes, not for their capacity values but for the low cost of production, ease of synthesis and good technological properties like material modelling and solubility in organic solvents.

A strong campaign for the use of renewable energy sources, particularly for distributed generation, is carried out considering the exhaustion of fossil fuels and the negative environmental impact of the indiscriminate use of carbon resources. Over the last two decades, solar power conversion efficiency of commercial devices rose significantly, and further improvements are the expectable consequence of laboratory success obtained worldwide in the last years. Novel materials and processes are constantly studied for the thin film–based photovoltaic systems, which are close to make obsolete the silicon-based first-generation devices. Energy payback of second and third generation solar cells can already justify the implementation of such devices in buildings and power plants; the awareness of this fact is proven by the birth of the first companies starting the business of mass production of thin film photovoltaic systems [113,117,118].

References

1. Winter, M., Brodd, J., *Chem. Rev.*, **104**, 4245–4269 (2004).
2. Zhang, A. S., Xu, K., Jow, T. R., *J. Power Sources*, **113**, 166 (2003).
3. Adachi, M., Tanaka, K., Sekai, K., *J. Electrochem. Soc.*, **146**, 1256 (1999).
4. Bohm, H., in *Handbook of Battery Materials*, Part III (Besenhard, J. O. B., ed.), Wiley/VCH, Weinheim/NY/Singapore, 1999, p. 565 (Chapter 11).

5. Scrosati, in *Advances in Lithium-Ion Batteries*, Kluwer Academic/Plenum Publishers (Van Schalkwijk, W. A., Scrosati, B., eds.), NY/Boston/London, 2002, p. 251 (Chapter 8).
6. Birke, P., Weppner, W., in *Handbook of Battery Materials*, Part III (Besenhard, J. O. B., ed.), Wiley/VCH, Weinheim/NY/Singapore, 1999, p. 525 (Chapter 9).
7. Wang, Z., Sun, Y., Chen, L., Huang, X., *J. Electrochem. Soc.*, **151**, A914 (2004).
8. Kim, J. M., Chung, H. I., *Electrochim. Acta*, **49**, 3573 (2004).
9. Jim, J. M., Chung, H. F., *Electrochim. Acta*, **49**, 937 (2004).
10. Okada, S., Sawa, S., Uebou, Y., Egashira, M., Yamaki, J., Tabushi, M., Kobayashi, H., Fukumi, K., Kageyama, H., *Electrochemistry*, **71**, 1136 (2003).
11. Dokko, K., Shi, Q. F., Stefan, I. C., Scherson, D. A., *J. Phys. Chem. B*, **107**, 12549 (2003).
12. Santner, H. J., Korepp, C., Winter, M., Besenhard, J. O. B., Moller, K. C., *Anal. Bioanal. Chem.*, **379**, 266 (2004).
13. Aurbach, D., Koltypin, M., Teller, H., *Langmuir*, **18**, 9000 (2002).
14. Hatchard, T. D., Dahn, J. R., *J. Electrochem. Soc.*, **151**, A838 (2004).
15. Lanz, M., Novak, P., *J. Power Sources*, **102**, 277 (2001).
16. Padhi, A. K., Nanjundaswamy, K. S., Goodenough, J. B., *J. Electrochem. Soc.*, **144**, 1188–1194 (1997).
17. Garśýa-Moreno, O., Alvares-Vega, M., Garśýa-Alvarado, F., Garsýa-Jaca, J., Gallardo-Amores, J. M., Sanjuán, M. L., Amador, U., *Chem. Mater.*, **13**, 1570–1576 (2001).
18. Yamada, A., Hosoya, M., Chung, S.-C., Kudo, Y., Hinokuma, K., Liu, K.-Y., Nishi, Y., *J. Power Sources*, **119–121**, 232 (2003).
19. Yamada, A., Chung, S.-C., Kudo, Y., Hinokuma, K., *J. Electrochem. Soc.*, **148**, A224 (2001).
20. Delacourt, C., Poisot, P., Morcrette, M., Tarascon, J. M., Masquelier, C., *Chem. Mater.*, **16**, 93 (2004).
21. Loris, J. M., Perez Vicente, C., Tirado, J. L., *Electrochem. Solid State Lett.*, **5**, A234 (2002).
22. Bramnik, N. N., Bramnik, K. G., Buhrmester, T., Baehtz, C., Ehrenberg, H., Fuess, H., *J. Solid State Electrochem.*, **8**, 558 (2004).
23. Tarascon, J. M., McKinnon, W. R., Coowar, F., Bowmer, T. N., Amatucci, G., Guyomard, D., *J. Electrochem. Soc.*, **141**, 1421 (1994).

24. Shimakawa, Y., Numata, T., Tabuchi, J., *J. Solid State Chem.*, **131**, 138 (1997).
25. Makimura, Y., Ohzuku, T., *J. Power Sources*, **119–121**, 156 (2003).
26. Tsuda, M., Arai, H., Takahashi, M., Ohtsuka, H., Sakurai, Y., Sumitomo, K., Kageshima, H., *J. Power Sources*, **144**, 183 (2005).
27. Kavan, L., Gratzel, M., Rathousky, J., Zukal, A., *J. Electrochem. Soc.*, **143**, 394 (1996).
28. Fong, R., Sacker, U. V., *J. Electrochem. Soc.*, **137**, 2009 (1990).
29. Idota, Y., Kubata, T., Matsufuji, A., Maekawa, Y., Miyasaka, T., *Science*, **276**, 1395 (1997).
30. Mao, O., Turner, R. L., Courtney, L. A., Fredericksen, B. D., Buckett, M. I., Krause, L. J., Dahnl, J. R., *Electrochem. Solid State Lett.*, **2**, 3 (1999).
31. Beaulieu, L. Y., Larcher, D., Dunlap, R. A., Dahn, J. R., *J. Electrochem. Soc.*, **147**, 3206 (2000).
32. Thackeray, M. M., Vaughey, J. T., Fransson, L. M. L., *JOM*, **54**, 20 (2002).
33. Mario, W., Besenhard, J. O., Martin, W., *J. Power Sources*, **94**, 189 (2001).
34. Martin, W., Besenhard, J. O., *Electrochim. Acta*, **45**, 31 (1999).
35. Kim, D. G., Kim, H., Sohn, H.-J., Kang, T., *J. Power Sources*, **104**, 221 (2002).
36. Pu, W., He, X., Ren, J., Wan, C., Jiang, C., *Electrochim. Acta*, **50**, 4140 (2005).
37. Xie, J., Zhao, X. B., Cao, G. S., Zhao, M. J., Su, S. F., *J. Power Sources*, **140**, 350 (2005).
38. Koel, M., *Proc. Estonian Acad. Sci. Chem.*, **49**(3), 145 (2000).
39. Hagiwara, R., Ito, Y., *J. Fluorine Chem.*, **105**, 221 (2000).
40. Bonhote, P., Dias, A.-P., Papageorgiou, N., *Inorg. Chem.*, **35**, 1168 (1996).
41. McFarlane, D. R., Sun, J., Golding, J. J., *Electrochim. Acta*, **45**, 1271 (2000).
42. Fuller, J., Breda, A. C., Carlin, R. T., *J. Electroanal. Chem.*, **459**, 29 (1998).
43. Zhang, Y., Urquidi-Macdonald, M., *J. Power Sources*, **144**, 191 (2005).
44. Botte, G. G., White, R. E., Zhang, Z., *J. Power Sources*, **97–98**, 570 (2001).
45. Zhang, Z., Fouchard, D., Rea, J. R., *J. Power Sources*, **70**, 16 (1998).
46. von Sacken, U., Nodwell, E., Sundher, A., Dahn, J. R., *Solid State Ionics*, **69**, 284 (1994).

47. Dahn, J. R., Fuller, E. W., Obravae, M., von Sacken, U., *Solid State Ionics*, **69**, 265 (1994).

48. Du Pasquier, A., Disma, F., Bowmer, T., Gozdz, A. S., Amatucci, G., Tarascon, J. M., *J. Electrochem. Soc.*, **145**, 472 (1998).

49. Gee, M. A., Laman, F. C., *J. Electrochem. Soc.*, **140**, L53 (1993).

50. Hong, J.-S., Maleki, H., Al Hallaj, S., Redey, L., Selman, J. R., *J. Electrochem. Soc.*, **145**, 1489 (1998).

51. Richard, M. N., Dahn, J. R., *J. Electrochem. Soc.*, **146**, 2068 (1999).

52. Ohta, A., Koshina, H., Okuno, H., Murai, H., *J. Power Sources*, **54**, 6 (1995).

53. Roth, E. P., in *The Electrochemical Society Meeting Abstracts*, Abstract 388, 99-2, Honolulu, HI, October 17–22 (1999).

54. Kumai, K., Miyashiro, H., Kobayashi, Y., Takei, K., Ishikawa, R., *J. Power Sources*, 81–82, 715 (1999).

55. Armand, M., Chabagno, J. M., Duclot, M. J., in *Fast Ion Transport in Solid* (Vashishita, P., Mundy, J. N., Shenoy, G. K., eds.), Elsevier, NY, 1989.

56. Gray, F. M., *Polymer Electrolytes*, Royal Society of Chemistry Monographs, Cambridge (1997).

57. Gray, F. M., Armand, M., in *Energy Storage System for Electronics* (Osaka, T., Datta, M., eds.), Gordon and Breach, Amsterdam (2000).

58. Lightfoot, P., Metha, M. A., Bruce, P. G., *Science*, **262**, 883 (1993).

59. Vincent, C., Scrosati, B., *Modern Batteries. An Introduction to Electrochemical Power Sources*, second ed., Arnold, London, 1993.

60. Wieczorek, W., Such, K., Wycislik, H., Plocharski, J., *Solid State Ionics*, **36**, 225 (1989).

61. Borghini, M. C., Mastragostino, M., Passerini, S., Scrosati, B., *J. Electrochem. Soc.*, **142**, 2118 (1995).

62. Appetecchi, G. B., Scaccia, S., Passerini, S., *J. Electrochem. Soc.*, **147**, 4448 (2000).

63. Appetecchi, G. B., Alessandrini, F., Duan, R. G., Arzu, A., Passerini, S., *J. Power Sources*, **1**, 4335 (2001).

64. Rossi Albertini, V., Appetecchi, G. B., Caminiti, R., Cillocco, F., Croce, F., Sadun, C., *J. Macromol. Sci. Phys.*, **B36**, 629 (1997).

65. Lascaud, S., Perrier, M., Valle, A., Besner, C., Prud'homme, J., Armand, M., *Macromolecules*, **27**, 7469 (1994).

66. Feuillade, G., Perche, P., *J. Appl. Electrochem.*, **5**, 63 (1975).

67. Hu, Y., Li, H., Huang, X., Chen, L., *Electrochem*. *Commun*., **6**, 28 (2004).
68. Ngo, H. L., LeCompte, K., Hargens, L., McEwen, A. B., *Thermochim*. *Acta*, **357–358**, 97 (2000).
69. Chagnes, A., Diaw, M., Carré, B., Willmann, P., Lemordant, D., *J*. *Power Sources*, **145**, 82 (2005).
70. Croce, F., Appetecchi, G. B., Persi, L., Scrosati, B., *Nature*, **394**, 456 (1998).
71. Jeona, J.-D., Chob, B.-W., Kwakc, S.-Y., *J*. *Power Sources*, **143**, 219 (2005).
72. Fauteux, D., Massucco, A., McLin, M., Vanburen, M., Shi, J., *Electrochim*. *Acta*, **40**, 2185 (1995).
73. Yano, K., Usuki, A., Okada, A., Kurauchi, T., Kamigaito, O., *J*. *Polym*. *Sci*. *Polym*. *Chem*., **31**, 2493 (1993).
74. Messersmith, P. B., Stupp, S. I., *J*. *Mater*. *Res*., **7**, 2599 (1992).
75. Kojima, Y., Usuki, A., Kawasumi, M., Okada, A., Kurauchi, T., Kamigaito, O., *J*. *Polym*. *Sci*. *Polym*. *Chem*., **31**, 983 (1993).
76. Krishnamoorti, R., Vaia, R. A., Giannelis, E. P., *Chem*. *Mater*., **8**, 1728 (1996).
77. Shi, H. Z., Lan, T., Pinnavaia, T. J., *Chem*. *Mater*., **8**, 1584 (1996).
78. Wang, Z., Pinnavaia, T. J., *Chem*. *Mater*., **10**, 3769 (1998).
79. Wang, Z., Pinnavaia, T. J., *Chem*. *Mater*., **10**, 1820 (1998).
80. Bumside, S. D., Giannelis, E. P., *Chem*. *Mater*., **7**, 1597 (1995).
81. O'Regan, B., Grätzel, M., *Nature*, **353**, 737 (1991).
82. Zhang, Y., Wu, L., Xie, E., Duan, H., Han, W., Zhao, J., *J*. *Power Sources*, **189**(2), 1256–1263 (2009).
83. Huang, C.-Y., Hsu, Y.-C., Chen, J.-G. Suryanarayanan, V. Lee, K.-M. Ho, K.-C., *Solar Energy Mater*. *Solar Cells*, **90**(15), 2391–2397 (2006).
84. Yang, H.-Y., Lee, M.-F., Huang, C.-H., Lo, Y.-S., Chen, Y.-J., Wong, M.-S., *Thin Solid Films*, **518**(5), 1590–1594 (2009).
85. Ko, K. H., Lee, Y. C., Jung, Y. J., *J*. *Colloid Interface Sci*., **283**(2), 482 (2005).
86. Chou, C.-S., Yang, R.-Y. Yeh, C.-K., Lin, Y.-J., *Powder Technology*, **194**(1–2), 95–105 (2009).
87. Kalaignan, G. P., Kang, M.-S., kang, Y. S., *Solid State Ionics*, **177**(11–12), 1091–1097 (2006).
88. Lee, J. P., Yoo, B., Suresh, T., Kang, M. S., Vital, R., Kim, K.-J., *Electrochim*. *Acta*, **54**(18), 4365–4370 (2009).

89. Kalaignan, G. P., Kang, M.-S., kang, Y. S., *Solid State Ionics*, **177**(11–12), 1091–1097 (2006).
90. Yang, Y., Zhou, C.-H., Xu, S., Hu, H., Chen, B.-L., Zhang, J., Wu, S.-J., Liu, W., Zhao, X.-Z., *J. Power Sources*, **185**(2), 1492–1498 (2008).
91. Asano, T., Kubo, T., Nishikitani, Y., *J. Photochem. Photobiol. A: Chem.*, **164**(1–3), 111–115 (2004).
92. Lai, W. H., Su, Y. H., Teoh, L. G., Hon, M. H., *J. Photochem. Photobiol. A: Chem.*, **195**(2–3), 307–313 (2008).
93. Wongcharee, K., Meeyoo, V., Chavadej, S., *Solar Energy Mater. Solar Cells*, **91**(7), 566–571 (2007).
94. Wub, H. M., Chenc, T. L., Huangd, K. D., Jwoe, C. S., Lo, Y. J., *J. Alloys Compounds*, **495**(2), 606–610 (2010).
95. Campbell, W. M., Burrell, A. K., Officer, D. L., Jolley, K. W., *Coordination Chem. Rev.*, **248**(13–14), 1363–1379 (2004).
96. Hara, K., Tachibana, Y., Ohga, Y., Shinpo, A., Suga, S., Sayama, K., Sugihara, H., Arakawa, H., *Solar Energy Mater. Solar Cells*, **77**(1), 89–103 (2003).
97. Jang, S.-R., Choi, M.-J., Vittal, R., Kim, K.-J., *Solar Energy Mater. Solar Cells*, **91**(13), 1209–1214 (2007).
98. Chen, J.-G., Chen, C.-Y., Wu, S.-J., Li, J.-Y., Wu, C.-G., Ho, K.-C., *Solar Energy Mater. Solar Cells*, **92**(12), 1723–1727 (2008).
99. Yoon, C. H., Vittal, R., Lee, J., Chae, W.-S., Kim, K.-J., *Electrochimica Acta*, **53**(6), 2890–2896 (2008).
100. Wu, J., Li, Q., Fan, L., Lan, Z., Li, P., Lin, J., *J. Power Sources*, **181**(1), 172–176 (2008).
101. Li, Q., Wu, J., Tang, Q., Lan, Z., Li, P., Lin, J., Fan, L., *Electrochem. Commun.*, **10**(9), 1299–1302 (2008).
102. Gagliardi, S., Giorgi, L., Giorgi, R., Lisi, N., Makris, T. D., Salernitano, E., Rufoloni, A., *Superlatt. Microstruct.*, **46**(1–2), 205–208 (2009).
103. Huang, Z., Liu, X., Li, K., Li, D., Luo, Y., Li, H., Song, W., Chen, L., Meng, V., *Electrochem. Commun.*, **9**(4), 596–598 (2007).
104. Ramanathan, K., Keane, J., Noufi, R., Properties of High-Efficiency CIGS Thin-Film Solar Cells. 31st IEEE Photovoltaics Specialists Conference and Exhibition, Lake Buena Vista, Florida, January 3–7 2005. Available online at http://www.nrel.gov/docs/fy05osti/37404.pdf.
105. Kessler, F., Rudmann, D., *Solar Energy*, **77**(6), 685–695 (2004).
106. Wada, T., Hashimoto, Y., Nishiwaki, S., Satoh, T., Hayashi, S., Negami, T., Miyake, H., *Solar Cells*, **67**(1–4), 305–310 (2001).

107. Ohashi, D., Nakada, T., Kunioka, A., *Solar Energy Mater*. *Solar Cells*, **67**(1–4), 261–265 (2001).

108. Zhang, N., Zhuang, D. M., Zhang, G., *Mater*. *Sci*. *Eng*. *B*, **166**(1), 34–40 (2010).

109. Mitzi, D. B., Yuan, M., Liu, W., A. J., Kellock, Chey, S. J., Gignac, L., Schrott, A. G., *Thin Solid Films*, **517**(7), 2158–2162 (2009).

110. Panthani, M. G., Akhavan, V., Goodfellow, B., Schmidtke, J. P., Dunn, L., Dodabalapur, A., Barbara, P. F., Korgel, B. A., *J*. *Am*. *Chem*. *Soc*., **130**(49), 16770–16777 (2008).

111. Contreras, M. A., Barnes, T., van de Lagemaat, J., Rumbles, G., Coutts, T. J. Weeks, C., Glatkowski, P., Levitsky, I., Peltola, J., Britz, D. A., *J*. *Phys*. *Chem*. *C*, **111**(38), 14045–14048 (2007).

112. Ding, H, Ram, M. K., Nicolini, C, *J*. *Mater*. *Chem*., **12**, 3585–3590 (2002).

113. Bertoncello, P., Nicolini, D., Paternolli, C., Bavastrello, V., Nicolini, C., *IEEE Trans*. *Nanobiosci*., **2**, 124–132 (2003).

114. Stura, E., Carrara, S., Bavastrello, V., Bertolotti, F., Nicolini, C., *Chem*. *Eng*. *Trans*., **4**, 317–323 (2004).

115. Stura, E., Carrara, S., Bavastrello, V., Nicolini, C., Polyaniline Derivative Nanocomposite Materials for Low Power Long Life Lithium Batteries. 2nd International Energy Conversion Engineering Conference. AIAA 2004–5766 (doi: 10.2514/6.2004-5766).

116. Stura, E., Nicolini, C., *Anal*. *Chim*. *Acta*, **568**, 57/64 (2006).

117. Bertoncello, P., Nicolini, C., *Nanotechnology*, **17**, 699 (2006).

118. Nicolini, C., Pechkova, E., *J*. *Nanosci*. *Nanotechnol*., **6**, 2209–2236 (2006).

Chapter 8

Matching Fungal Lipases Catalytic Activity for Biodiesel Production

Rosanna Spera[a] and Claudio Nicolini[a,b,c]

[a]*Laboratories of Biophysics and Nanobiotechnology, Department of Experimental Medicine, University of Genoa, Via Pastore 3, Genoa 16132, Italy*
[b]*Virginia G. Piper Center for Personalized Diagnostics, Biodesign Institute, Arizona State University, Tempe, AZ, USA*
[c]*Nanoworld Institute, Fondazione EL.B.A. Nicolini, Largo Redaelli 7, Pradalunga, Bergamo, Italy*

rosanna.spera@unige.it

This chapters analyzes the degradation of poly(ε-caprolactone) (PCL) by three fungal lipases from *Mucor miehei*, *Candida rugosa*, and *Rhizhopus arrizhus* in a solvent-free system. To evaluate the activity of the three lipases, we utilized olive oil as the substrate. *Mucor miehei* lipase proved to be the best biocatalyst for both substrates: The data presented suggest it has a better capability to hydrolyze triglycerides found in olive oil. This property is further enhanced when the enzyme is immobilized on a glass surface in monolayers ranging between 1 and 5. We analyzed the degradation of PCL by mass spectrometry discovering that only *Mucor miehei* lipase was able to completely degrade a PCL film. Moreover, mass spectrometry results evidenced the enzyme action of separating

Nanobiotechnology in Energy, Environment, and Electronics: Methods and Applications
Edited by Claudio Nicolini

ISBN 978-981-4463-96-6 (Hardcover), 978-981-4463-97-3 (eBook)
www.panstanford.com

plastic oligomers of PCL and of further hydrolyzing oligomers previously detached.

8.1 Introduction

8.1.1 Biodiesel

Biodiesel is an alternative fuel for diesel engines. Its primary advantages are that it is one of the renewable fuels currently available and is also non-toxic and biodegradable. It can also be used directly in most diesel engines without requiring extensive engine modifications.

Rudolf Diesel tested vegetable oil as fuel for his engine (Shay, 1993). With the advent of cheap petroleum, appropriate crude oil fractions were refined to serve as fuel and diesel fuels and diesel engines evolved together. In the 1930s and 1940s, vegetable oils were used as diesel fuels from time to time, but usually only in emergency situations. Recently, because of increases in crude oil prices, limited resources of fossil oil and environmental concerns there has been a renewed focus on vegetable oils and animal fats to make biodiesel fuels. Continued and increasing use of petroleum will intensify local air pollution and magnify the global warming problems caused by CO_2 (Shay, 1993). In a particular case, such as the emission of pollutants in he closed environments of underground mines, biodiesel fuel has the potential to reduce the level of pollutants and the level of potential or probable carcinogens (Krawczyk, 1996).

Fats and oils are primarily water-insoluble, hydrophobic substances in the plant and animal kingdom that are made up of one mole of glycerol and three moles of fatty acids and are commonly referred to as triglycerides (Sonntag, 1979a). Fatty acids vary in carbon chain length and in the number of unsaturated bonds (double bonds).

8.1.2 Lipases

Lipases (EC 3.1.1.3) are a class of enzymes that catalyze hydrolysis of triglycerides with the formation of fatty acids and glycerol (Gutiérrez–Ayesta et al., 2007) at lipid/water interface. The biochemical characteristics of several microbial lipases, fungal and

mammalian were extensively evaluated (Dominguez et al., 2006; Kovac et al., 1996; Sharma and Chisti, 2001). Their active site is composed of a "catalytic triad" of three amino acids (Ser-His-Asp/Glu) (Joseph et al., 1997; Ninia and Sardab, 2001; Varfolomeev et al., 2005) and when they are placed at lipid/water interface, an hydrophobic patch around the catalytic triad is creates (Kovac et al., 1996) allowing the enzyme's activation (Joseph et al., 1997; Ninia and Sardab, 2001; Varfolomeev et al., 2005). Lipases have an excellent catalytic activity and can also catalyze the reverse reaction, the esterification. These features make the use of lipases suitable in many biotechnological applications (Babu et al., 2007) as the synthesis of biopolymers and biodiesel (Bernardes et al., 2007; Salis et al., 2005; Zhao et al., 2007), and the production of pharmaceuticals, chemicals and soaps (Jaeger and Eggert, 2002).

In a previous study (Pastorino et al., 2004), we described the lipase-catalyzed degradation of PCL in organic solvent (toluene). Because of the high toxicity of many organic solvents used for the dissolution of plastic, this chapter compares the hydrolytic activity of three lipases from different fungal origin—*Mucor miehei*, *Candida rugosa*, and *Rhizhopus arrizhus*—in a solvent-free system with the aim of developing a new technological application based on innovative principles. In Sivozhelezov et al. (2009), we exploited the possibility of employing Langmuir–Blodgett (LB)-based protein structures to use in biocatalysis, exemplified by lipase with olive oil as substrate; we demonstrated that it was possible to form even more active lipase nanostructures by the LB technique at the air–water interface, proving that the Langmuir film provides a better catalytic effect in lipase than a mere oil–water boundary.

The goal of this study was to analyze the degradation in a solvent free system of PCL, which is a biodegradable aliphatic polyester, well known for its high mechanical compatibility with many polymers and good adhesion to a broad spectrum of substrates (Tsuji et al., 1996).

8.2 Materials and Methods

Lipases from *Mucor miehei* and *Candida rugosa* were purchased from Sigma–Aldrich (St. Louis, MO), lipase from *Rhizopus arrizhus* was obtained from Fluka (Milan, Italy). MilliQ (Millipore) water was used for preparation of enzyme solution. Lipase was utilized

without any further purification. Poly(ε-caprolactone) MW 80 kDa was from Sigma–Aldrich (St. Louis, MO). Olive oil and all the chemicals for enzymatic activity assay (sodium taurocholate, NaCl, and $CaCL_2$) were produced by Fluka (Milan, Italy). 2,5 Dihydroxybenzoic acid (DHB) (Bruker Daltonic, Leipzig, Germany) was used as matrix for matrix-assisted laser desorption ionization time-of-flight (MALDI-TOF) mass spectrometry. All the others chemicals (potassium phosphate, NaI, NaOH, TFA, and acetonitrile) were purchased from Sigma.

8.2.1 Measurement of the Enzymatic Activity of Lipase

Enzymatic activity of lipase was determined by modifying the standard test Sigma (N° 62300A2) (Worthington, 1988) using as substrate olive oil; 10 μL of enzyme from a stock solution (10 mg/mL) were added at the reaction mixture composed by potassium phosphate buffer 10 mM, Na taurocholate 1.5% NaCl 3M and $CaCl_2$ 75 mM. Subsequently, the pH was adjusted to 7.8 using NaOH 100 mM. The reaction mixture was magnetically stirred at 37°C for 30 min. The amount of fatty acids released was determined by titration with NaOH 100 mM.

8.2.2 Immobilization

The LB technique represents a "classical" tool for biofilm engineering. The biomolecules being placed at the air/water interface arrange themselves in such a way that their hydrophilic part penetrates water due to its electrostatic interactions with water molecules, which can be considered electric dipoles. The hydrophobic part (aliphatic chain) orients itself to air because it cannot penetrate water for entropy reasons. Therefore, few molecules placed at the water surface form a two-dimensional system at the air/water interface. Initially, the compression does not result in significant variations in surface pressure; molecules at the air/water interface are rather far from each other and do not interact. Further compression results in an increase in surface pressure: The molecules begin to interact. Continuation of the compression results in a sharp increase in surface pressure, even with small decrease in area per molecule: Dense packing of molecules in the monolayer is reached. Further compression results in the collapse of the monolayer (Nicolini and Pechkova, 2006).

Lipase LB films were obtained by an laboratory-developed trough (450 × 150 mm^2) [19]. The surface pressure was measured using a balance of Wilhelmy (having an accuracy of 0.2 mN m^{-1}). One hundred microliter of a 10 mg/mL stock solution of lipase was dispensed in the air/water interface. The subphase was pure water and the barriers compression speed was 20–30 mm/min. The surface pressure of deposition was 20 mN/m. The Langmuir–Schaefer (LS) technique (horizontal lifting) was adopted to transfer the enzyme film from the air/water interface to glass surface.

8.2.3 Process of Degradation

Ten microliter of lipase from a stock solution (10 mg/mL) was added in 10 mL Erlenmeyer flask containing 4 mL of potassium phosphate buffer 10 mM and 15 mg of PCL. The reaction was carried out in an incubator (Orbital Shaker OSI–502, Firstek Scientific) at 37°C under agitation. Every 24 h, the amount of PCL hydrolyzed by lipase was measured using a precision balance (Gibertini E42), and 300 μL of supernatant-containing oligomers were collected and stored at 4°C for subsequent mass spectrometry analysis.

Poly(ε-caprolactone) was taken off the solution, let to dry for 1 h at room temperature and after being weighed, it was placed back in the reaction mixture. Poly(ε-caprolactone) images are reported in Figs. 8.1 and 8.2 (taken using a scanner Canon N650).

8.2.4 Mass Spectrometry

According to Sato et al. (2003), to analyze PCL fragmentation by MALDI–TOF MS, a saturated solution of 2,5-dihydroxybenzoic acid (DHB; Bruker Daltonics) in TA (2/3 of 0.1% TFA and 1/3 of acetonitrile) was used as matrix; 1.5 μL of the PCL sample, prepared as described earlier in the text, was mixed with 1.5 μL of matrix solution. Prior to the sample/matrix co-crystal deposition, 2 μL of 1 mM sodium iodide solution in acetone was spotted onto a flat stainless steel MALDI target (Bruker Daltonics, Leipzig, Germany) and dried in air. Then 1.5 μL of the sample/matrix solution was deposited onto the thin NaI crystal layer, and dried in air. The analysis was performed on an Autoflex MALDI–TOF mass spectrometer (Bruker Daltonics, Leipzig, Germany) operated in the

linear and reflector mode. MALDI–TOF mass spectra were acquired with a pulsed nitrogen laser (337 nm) in positive ion mode. Laser beam intensity was empirically attenuated to just above the threshold values during the enzymatic degradation test of the PCL sample for analyte ionization. Internal calibration was performed using the DHB peaks.

8.3 Results

8.3.1 Enzymatic Activity Assay

The modifying hydrolytic activity test, using olive oil as substrate, showed that at the same concentrations, lipase from *Mucor miehei* has a better capability to hydrolyze triglycerides found in olive oil substrate. The activity of *Mucor miehei* lipase (10.07 μmol/mL) is, in fact, about thrice as strong as that of lipase from *Candida rugosa* (3.61 μmol/mL) and quadruple respect that of *Rhizopus arrizhus* (2.47 μmol/mL).

This property is further enhanced when the enzyme is immobilized on a glass surface. The data reported in Figure 8.1 (left) illustrates an evident increase in the specific activity on olive oil in monolayers ranging between 1 and 5 (46.77 μmol/mL), while the activity begins to decline in monolayer ranging between 5 and 10 (20 μmol/mL).

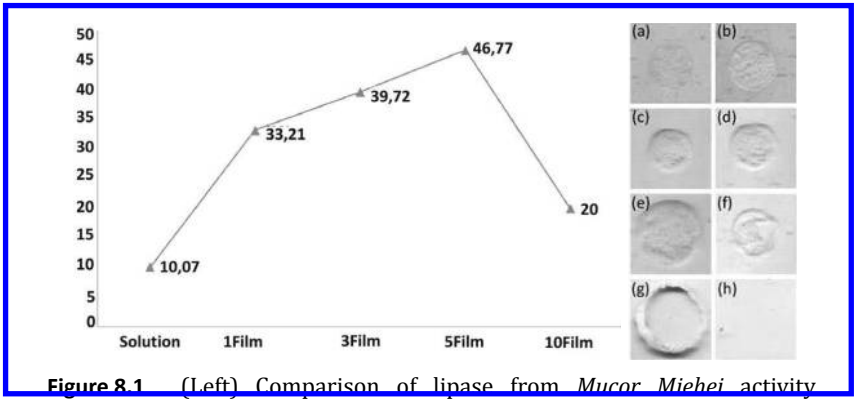

Figure 8.1 (Left) Comparison of lipase from *Mucor Miehei* activity dissolved in Milli Q water (solution) and immobilized in LB film when the reaction take place in Erlenmeyer flask. (Right) PCL degraded by lipase from *Mucor Miehe*i: (a) day 0, (b) day 1, (c) day 2, (d) day 3, (e) day 4, (f) day 5, (g) day 6, (h) day 7.

8.3.2 Degradation of PCL

Poly(ε-caprolactone) degradation was conducted in an Erlenmeyer flask at 37°C in agitation. The same quantities of three different lipases were added to the mixture. Every 24 h, the quantity of hydrolyzed PCL was measure by gravimetry assay. Lipase from *Mucor miehei* was the one able to degrade completely the PCL film (Fig. 8.1, right, Fig. 8.2).

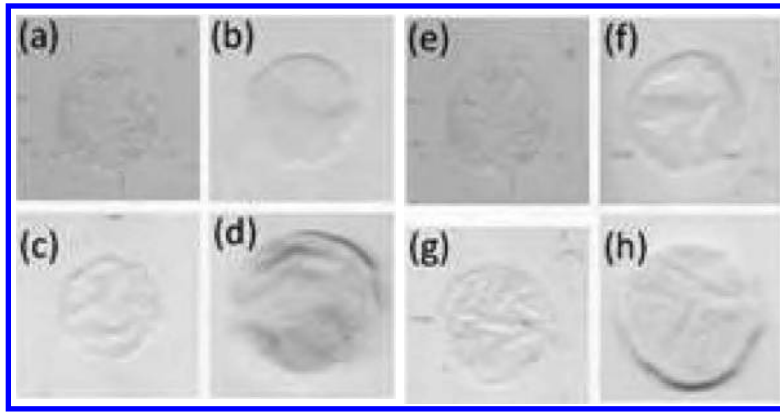

Figure 8.2 PCL degraded by lipase from *Candida Rugosa*: (a) day 0, (b) day 3, (c) day 4, (d) day 7. PCL degraded by lipase from *Rizopus Arrizus*: (e) day 0, (f) day 3, (g) day 4, (h) day 7.

Tests conducted with the other two enzymes show only a slight gravimetric variation. A functional characterization to evaluate the catalytic activity of lipase from *Mucor miehei* by monitoring the kinetics reaction at different concentrations of PCL followed these experiments. The enzymatic activity of lipase was assessed by monitoring the product formation over time. Kinetics of hydrolytic activity of free and immobilized lipase was investigated at various concentrations of olive oil (37°C, pH 7.7). These data were plotted according to the Lineweaver–Burke method:

$$\frac{1}{v} = \frac{K_m}{V_{max}} \frac{1}{s_0} + \frac{1}{V_{max}},$$

where v is the reaction rate, s_0 the substrate concentration, K_m the Michaelis–Menten constant, and V_{max} the maximum reaction rate. The data obtained are reported in Fig. 8.3. The kinetic parameters

K_m and V_{max} (K_m = 15625 μmol mL^{-1} and V_{max} = 6.8 μmol mL^{-1} min^{-1}), were extrapolated for the chart according to Lineweaver–Burke method. Figure 8.3 illustrates the substrate hydrolysis after replacing PCL in the same reaction mixture (a), and after the replacement in a new one (b); in the first 24 h, there was a high reduction of the PCL weight, and then this value decreased because the lipase acts both on the initial mass and on oligomers that had previously detached.

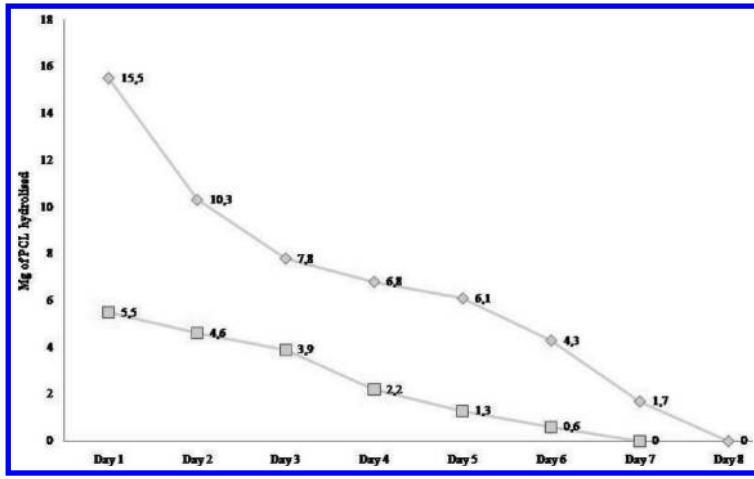

Figure 8.3 Degradation of PCL by the lipase. (a) PCL after being weighed is placed back in the same reaction mixture. (b) PCL after being weighed is replaced in a new reaction mixture.

8.3.3 Mass Spectrometry

After being taken off the solution, PCL was subjected to analysis and supernatant-containing oligomers were collected and analyzed by MALDI–TOF MS. The aim of this experiment was to monitor the process of plastic degradation day by day. Figure 8.4 illustrates the spectra related to the degradation of PCL by the lipase from *Mucor miehei* after 1 (a), 3 (b), and 5 days (c). In all spectra, there are peaks in the range 500–1300 m/z corresponding to the oligomers hydrolyzed by the enzyme. By the comparison of the three spectra, it is possible to note day by day a reduction of the peaks in the area between 900 and 1300 m/z. This data demonstrates the hydrolytic action of lipase on PCL oligomers previously detached.

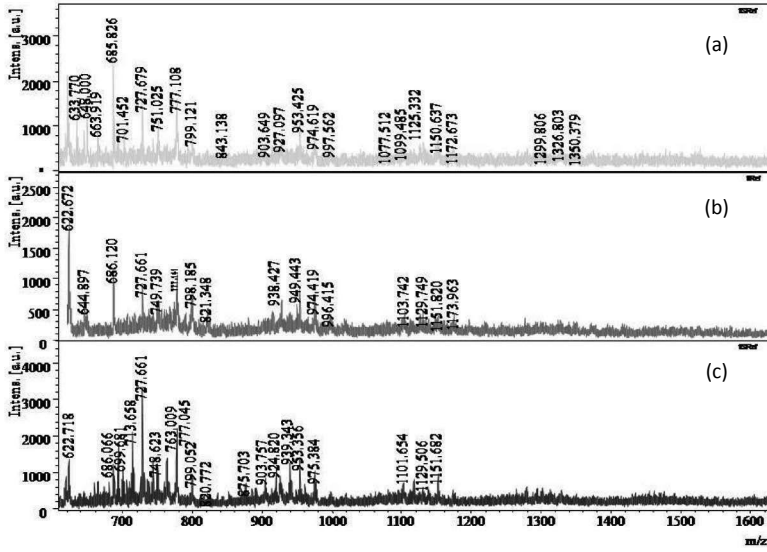

Figure 8.4 MALDI-TOF mass spectrum of the degradation of a sample of PCL after (a) 1 day, (b) 3 days, and (c) 5 days.

8.4 Conclusions

Comparative analysis of three lipases of different fungal origin showed that lipase from *Mucor miehei* had a better capability to hydrolyze olive oil. Another improvement was obtained when the enzyme was used and immobilized on glass support in a number monolayer ranging between 1 and 5. Regarding to PCL degradation in absence of organic solvent, lipase from *Mucor miehei* proved to be the only enzyme able to degrade completely the PCL plastic films. The gravimetric analysis related to mass spectrometry revealed the relative kinetics of PCL degradation. The presence of peaks corresponding to molecular weights between 900 and 1300 m/z showed that enzyme action was manifested first by separating plastic oligomers of PCL and then—as its action on plastic is continued—by hydrolyzing oligomers previously detached.

This result was shown by the progressive disappearance of peaks corresponding including between 900 and 1300 m/z (Figures 8.6b,c), accompanied by a decrease in the degradation grade.

References

Babu J., Ramteke P.W., Thomas G., Shrivastava N. (2007). Cold-active microbial lipases: A versatile tool for industrial applications. *Biotechnol. Mol. Biol. Stand. Rev.*, **2**, 039–048.

Bernardes O.L., Bevilaqua J.V., Leal MCMR, Freire D., Langone M. (2007). Biodiesel fuel production by the transesterification reaction of soybean oil using immobilized lipase. *Appl. Biochem. Biotechnol.*, **137**, 105–114.

Gutiérrez–Ayesta C., Carelli A., Ferriera M.L. (2007). Relation between lipase structures and their catalytic ability to hydrolyse triglycerides and phospholipids. *Enzyme Microb. Technol.*, **41**, 35–43.

Jaeger K.E., Eggert T. (2002). Lipases for biotechnology. *Curr. Opin. Biotechnol.* **13**, 390–397.

Joseph D., Cygler M., Cygler S. (1997). Lipases and α/β hydrolase fold. *Methods Enzymol.*, **284**, 85–107.

Kovac A., Stadler P., Haalck L., Spener F., Paltauf F. (1996). Hydrolysis and esterification of acylglycerols and analogs in aqueous medium catalyzed by microbial lipases. *Biochim. Biophys. Acta*, **1301**, 57–66.

Nicolini C., Pechkova E. (2006). Nanostructured biofilms and biocrystals. *J. Nanosci. Nanotechnol.*, **6**, 1–28.

Ninia L., Sardab L. (2001). Lipase-catalysed hydrolysis of short-chain substrates in solution and in emulsion: A kinetic study. *Biochim. Biophys. Acta (BBA)—Mol. Cell Biol. Lipids*, **1534**, 4–44.

Pastorino L., Pioli F., Zilli M., Converti A., Nicolini C. (2004). Lipase catalyzed degradation of polycaprolactone. *Enzyme Microb. Technol.*, **35**, 321–326.

Salis A., Pinna M., Monduzzi M., Solinas V. (2005). Biodiesel production from triole in and short chain alcohol through biocatalysis. *J. Biotechnol.*, **119**, 291–299.

Sato H., Kiyono Y., Ohtani H., Tsuge S., Aoi H., Aoi K. (2003). Evaluation of biodegradation behavior of poly(ocaprolactone) with controlled terminal structure by pyrolysis-gas chromatography and matrix assisted laser desorption/ionization mass spectrometry. *J. Anal. Appl. Pyrolysis*, **68**, 37–49.

Sharma R., Chisti Y. (2001). Production, purification, characterization, and applications of lipases. *Biotechnol. Adv.*, **19**, 627–662.

Sivozhelezov V., Bruzzese D., Pastorino L., Pechkova E., Nicolini C., (2009). Increase of catalytic activity of lipase towards olive oil by Langmuir film immobilization of lipase, *Enzyme Microb*. *Technol*., **44**, 72–76.

Tsuji H., Ikada Y. (1996). Blends of aliphatic polyesters. I. Physical properties and morphologies of solution-cast blends from poly(dl-lactide) and poly(ε-caprolactone), *J*. *Appl*. *Polymer Sci*., **60**, 2367–75.

Varfolomeev S.D., Gariev I.A., Uporov I.V. (2005). Catalytic sites of hydrolases: Structures and catalytic cycles, *Russ*. *Chem*. *Rev*., **74**, 61–76.

Worthington, C.C. (1988). In *Worthington Enzyme Manual* (Worthington, CC, ed), 212–214, Worthington Biochemical Corporation, Freehold, NJ.

Zhao X., El-Zahab B., Brosnahan R., Perry J., Ping P. (2007). An organic soluble lipase for water-free synthesis of biodiesel, *Appl*. *Biochem*. *Biotechnol*., **143**, 236–243.

Chapter 9

Prospects of Use of Megatechnologies for Development of the Earth's Interior

Alexey Alexandrovich Peshkov,[a] Natalia Arkadievna Matsko,[b] Alexander Gennadievich Mikhailov,[c] and Victor Igorevich Bragin[c]

[a]*Corresponding member of RAS*
[b]*Research Institute of Comprehensive Exploitation of Mineral Resources of the Russian Academy of Science*
[c]*Institute of Chemistry and Chemical Technology of the Siberian Branch of the Russian Academy of Science*

In this chapter, the authors analyze the tendencies for deterioration of geological conditions of mining and slowing down of rates of scientific and technical progress. New approaches to development of mineral deposits, based on their preliminary transformation, are proposed. For the realization of these approaches, the principles of construction of new megatechnologies are given. The general scheme of megatechnologies reduces to the technogenic initiation of directed geological processes, transformation of a deposit, and its subsequent mining. Examples of new megatechnologies for the development of technogenic and natural mineral deposits are given in this chapter. Megatechnologies are based on the application of analogues of infiltration and hydrothermal geological processes.

Nanobiotechnology in Energy, Environment, and Electronics: Methods and Applications
Edited by Claudio Nicolini

ISBN 978-981-4463-96-6 (Hardcover), 978-981-4463-97-3 (eBook)
www.panstanford.com

Possibilities of megatechnologies to restrict ecological damage are examined. The basic economic and ecological effects of application of such technologies are given.

9.1 Introduction

High growth rates of use of non-reproducible minerals, reached over the past 50 years (Fig. 9.1), have called into question not only an opportunity of further growth of a living standard but also an existence of life on the Earth.

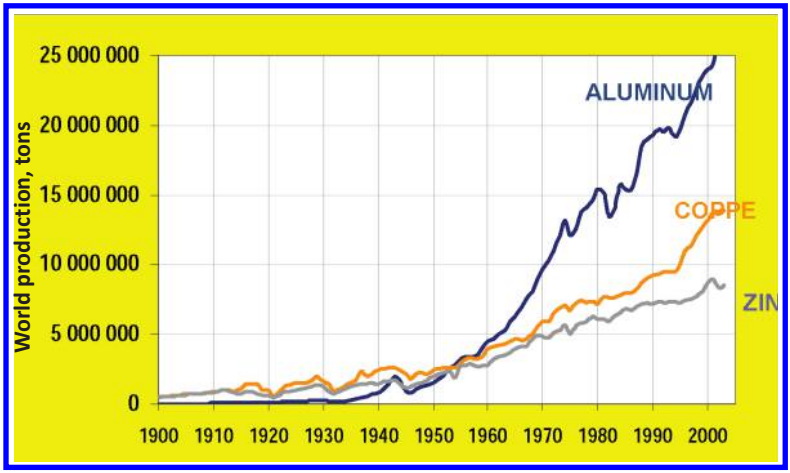

Figure 9.1 The trend in world production of non-ferrous metals.

For the first time, such fears have been stated in the report to Roman Club "Limits to Growth" (1972) [1]. In opinion of the authors of the report, in the near future, an industrial capital will reach such level when huge inflow of resources is required. Such inflow will quickly exhaust reserves of available raw material. With a rise in prices on minerals and with exhaustion of mineral deposits, more capital investments will be required for their prospecting and development, and, hence, less and less capital will be invested in the future growth. When capital investments cease to compensate an exhaustion of mineral resources, the industry will be destroyed. The authors of the report assumed mineral reserves are limited. They believed that the role of scientific and technical progress is in development of resource-saving technologies reducing rates of exhaustion of mineral deposits. They did not consider an opportunity

to expand mineral reserve base by means of drawing in mining the deposits with content of a useful component 2–5 times lower then today, keeping a level of mining profitability.

However, experience reflects precisely this tendency. Despite periodic discoveries of new deposits with high content of useful minerals, the average ore grade decreases over time. From 1925 to 1971, the average metal content in ores has decreased: for copper from 2.1% to 0.6%, lead from 2.7% to 0.6%, zinc from 4.6% to 4%, and tin from 1.2% to 0.4%. The average content of gold in all types of exploited reserves in Yakutia (Russia) has decreased 2 to 2.5 times during 1970–1990. Content of iron in ores extracted in Krivbass (mining region in Ukraine) in 1940 was about 62–67%, and in 1960, it averaged between 32% and 37% for all open pits of the basin. Cutoff grade of P_2O_5 has decreased from 18% in 1930 to 4% in 1980.

The fact that such reserves are drawing in mining testifies significant changes occurred in mining and processing technologies. Until now, rates of scientific and technical progress exceeded the rates of deterioration of geological conditions of mining. As a result, over the last century mining and processing operating cost annually decreased with average rate of 0.8%. However, over the last decades the rate has fallen to 0.15% a year. Now mining costs have stabilized at relatively low level (Fig. 9.2) [2].

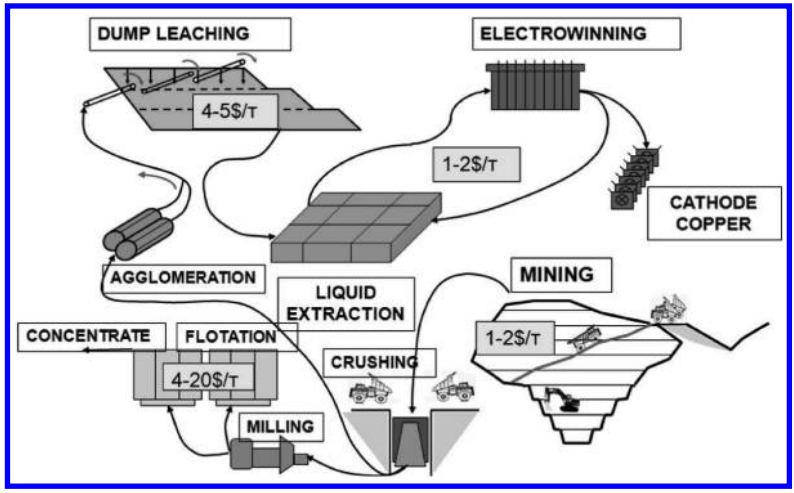

Figure 9.2 Traditional technologies of copper extraction and average cost for different operation [3].

Decrease of cost will continue to become slower in the future, having regard to exponential form of time-dependence of the rate of scientific and technical progress. The lower the content of useful components in ore and the worse the conditions of mining, the more difficult and the more expensive the development of new technologies will be. Such tendency has already caused serious statements about crisis in mining science.

Problems of development of mineral reserve base become aggravated under extreme environmental conditions, typical for many mining regions, such as adverse climatic conditions, remoteness from industrially developed areas and backwardness of an industrial and social infrastructure. Prime exploitation of the richest reserves and destruction of ecosystems are the characteristic features of mining. As known reserves of rich ores are depleted, mining, as a rule, moves to regions that are difficult to access, the efficiency of mineral production decreases, and the mechanism of slowing down of technical progress, described above, starts to work.

The basic features of development of mineral resources in such regions are summarized in the following three groups:

Economic: Both capital and operating costs of mining are essentially higher due to adverse climatic conditions and backwardness of an industrial, social, and transport infrastructure. An inevitable consequence of such state of affairs is drawing in mining only the most available mineral reserves.

Social: Adverse conditions for residing people are defined, first of all, by climatic conditions, environmental conditions of industrial region and, to a lesser degree, by a backwardness of infrastructure. The problem is partially solved using camp-type operation but it is not always possible.

Ecological: Both high level of concentration of manufacture and high sensitivity of primitive ecosystems to technogenic influences lead to a fast and complete destruction of ecosystem. Requirements to preservation of the environment become tougher. It leads to growth in mining costs, decrease in production efficiency, and cut-down of reserve base but does not lead to significant improvement of environment. In existing industrial regions, for example in Norilsk (one of the largest Siberian mining region), the degree of

technogenic change of landscapes is so high that it is possible to speak about practically utter annihilation of natural ecosystems.

It is known that the resolution of crises results from the change of existing paradigm (i.e., sets of implicitly specified regulative principles). In the field of development of natural resources, located on the surface of the Earth, the most significant system changes occurred, for example, at the transition from collecting to shifting agriculture and, further, to field agriculture. As to development of mineral resources, scale changes occurred only in the field of mining and metallurgical equipment and technology, depending on general technical progress (from manual instruments of work to mechanisms, from steam to electric engines). As a result, these changes have provided a growth of scales of development of the Earth's interior and the basis for extensive mining. As for the basic approach to development of the Earth's interior, it is still similar to collecting in agriculture. Besides, stagnation in decreasing of mining and processing costs, the outlined serious contradictions between extensive character of mining and toughening of requirements to preservation of environment may be thought of as precondition for a change of a paradigm.

Development in any areas of science, mining among them, includes two interacting and, partly opposite, tendencies: specialization, which is separation of the narrow directions for studying problems in details, and integration, which is synthesis both specialized and integrated scientific directions with use of methods and approaches of higher level of generality. By now, the turn in the Earth sciences from narrow specialization to integration has been outlined. Resolution of the crisis, mentioned above, would obviously occur on the basis of the synthetic tendency. Radical increase in efficiency and ecological safety of mining could be reached on the basis of essentially new approach, which is based on the following starting theses:

- Any form of the development of the Earth's interior represents technogenic geological processes, including both technological influence on geologic environment and natural geological processes initiated by technogenic action.
- Technogenically initiated geological processes are the main sources of ecological hazard resulting from development of the Earth's interior. Such processes involve potential resources

of the Earth's interior, which are not used in geotechnology now.

- Radical increase in efficiency and ecological safety of development of the Earth's interior is possible only with the proviso that the control over technogenically initiated geological processes is efficient and the most desirable form can be given to the processes for obtaining technological result. Under these circumstances, an efficiency of technogenically initiated processes is provided by substitution of expensive economic resources for potential resources of the Earth's interior, which are not commonly used now. Controllability and reduction of undesirable side effects of technogenically initiated geological processes provide an ecological safety.

In our opinion, new paradigm of the development of the Earth's interior, replacing the existing one, consists in transformation of the Earth's interior by means of initiation of natural geological processes with the use of potential energy of the Earth's interior as motive force for transformation and transfer of ore material. Figuratively speaking, it is a question of formation or "cultivation" of the deposits with parameters allowing the volumes of extracted and processed rock to be essentially lowered.

As it was already stated, the existing approach is based on "collecting," i.e., on extraction of mineral resources as they were created by the nature. In this case, transformation of the Earth's interior also takes place, but it is characterized by disturbance of the Earth's interior that, as a rule, leads to a negative influence on environment. The definition of a new paradigm also implies transformation of the Earth's interior; however, this transformation, by analogy with agriculture, could be named "cultivation of the Earth's interior." Unlike the existing approach, transformation of the interior of the Earth is carried out in this case, first, due to maximum attraction of additional resources of the Earth's interior (hydro-geological, chemical, geomorphological, thermodynamic) which are not commonly used in modern geotechnologies, and secondly, transformation is carried out by the processes similar to natural geological processes.

It is necessary to note that natural geological processes, even those that lead to formation of new deposits, proceed with various intensities nowadays. According to a new paradigm, transformation of the Earth's interior to a state appropriate for

further use should be carried out on the basis of highly intensive geological processes, which can be realized in a given area of the Earth's crust. Unlike natural geological processes, technogenic initiation and control are required for such processes. It can be said they are directed geological processes. Obviously, they are restrictedly controlled; therefore, the end result cannot be determined completely.

The change of a paradigm of development of the Earth's interior is connected with the change of a way of human activity, that is, with transition from surface technologies to volumetric ones. For the most part, modern technologies are connected with creation and use of new surfaces. For example, in mining, such surfaces are created in the form of working zones, surfaces of open pit or underground mine workings, holes, dumps, and tailing ponds. In comparison to volumes of geologic objects, the volumes that a person operates with, when extracting and processing mined rock (layer, bench, level, block), represent a chip removed from the Earth and stacked on the surface. Probably, the scaled process of explosive destruction of a massif is one of few exceptions. "Two-dimensionality" inherent in the majority of modern technologies is likely to be caused, firstly, by the habitat of a person, which represents a surface between an atmosphere and lithosphere, and, secondly, by the inability of a person to work with a thick of a chip comparable to the size of a deposit.

New paradigm assumes a turn from surface to volumetric technologies, as far as geological processes are basically volumetric. At the same time, even the directed geological processes are restrictedly controlled; therefore, the use of a volumetric geological process for satisfaction of a society demand for minerals is problematic without additional 2D technologies. The general scheme of coordination between 2D and 3D technologies is shown in Fig. 9.3b. The use of the results of a volumetric process, for example in the form of newly formed deposit, is obviously possible only with the help of traditional two-dimensional technologies. Besides, initiation of the directed three-dimensional geological process also requires an application of traditional two-dimensional technologies. In Fig. 9.3b technologies of this sort are represented by geotechnological holes, surfaces of a fluid fracturing. In the view of new paradigm, the general scheme of development of a part of the Earth's interior reduces to organization of 3D geological

process initiated by means of "sluice," which represents typical two-dimensional technology, and the "sluice" (also in the form of 2D technology) serving for consumption of the results of directed geological process.

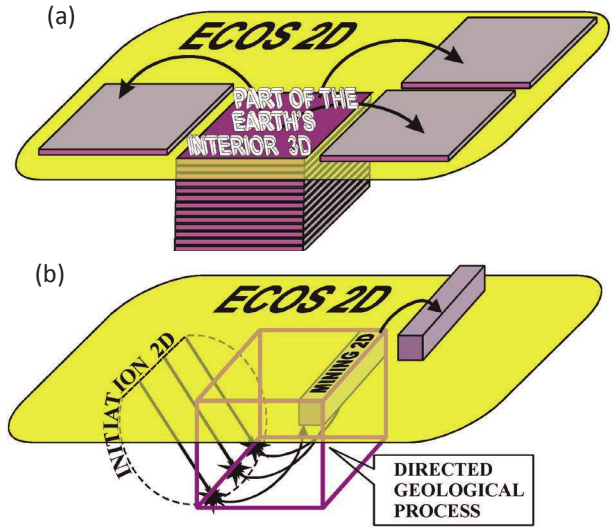

Figure 9.3 The scheme demonstrating transition from two-dimensional technologies to three-dimensional mining megatechnologies: (a) 2D technologies with layer-by-layer extraction of mined rock; (b) 3D megatechnology with use of the directed geological process.

Spatial boundaries of natural processes, proceeding in geologic environment, cannot be arbitrary narrowed. Use of these processes in geotechnologies will lead to the situation when mining starts operating with large volumes of the Earth's interior. However, until now, the man has not learned to predict and control the changes of environment resulted from mining. A necessary condition of new approach is an expansion of a zone of constructive control over technogenically changed interior of the Earth. Complex of "sluice" technologies and directed geological processes of transformation of the Earth's interior could be logically named a megatechnology. First, the complex includes a set of various technologies and methods and, secondly, the transformed volume of the Earth's interior essentially exceeds in size the massif involved in the traditional mining technologies.

As one of the examples of megatechnologies, we can take a look at the directed hydrochemical transformation of the technogenic objects, containing sulfides of nonferrous metals, for example, tailing ponds of processing plants. Chemical potential of a reaction of acidification of sulfides and potential energy of underground waters, defined by their hydraulic gradient, are the potential resources for realization of directed geological process. Process of acidification of sulfides, reprecipitation of nonferrous metals and oxidic iron on a geochemical barrier are steady geological process in this environment. Initiation of analogue of natural geological process consists in correction of underground water streams, giving them a direction to a geochemical barrier, creation of conditions for an easy access of air oxygen and, probably, initial acidification of a part of a massif or addition of necessary bacterial cultures. Research carried out for Maynsky copper tailing pond (0.2% Cu) has shown that development of this object with the use of such megatechnology is possible with efficiency four times as great as efficiency of traditional technology. It is necessary to note that in world and domestic practice the objects of this type are certainly considered unavailable for development not only by traditional technologies, but also with use of physico-chemical geotechnology.

In the industrial regions, such technologies of hydrochemical transformation of tailing ponds have significant prospects as methods of extraction of additional metal and as means of decreasing ecological pressure on landscapes. In the Norilsk industrial region, for example, products of oxidizing decomposition of technogenic products (tailings after processing of copper-nickel ores, stores of sub-economic ores, slags, and so forth) are the basic suppliers of pollution of surface and underground waters. Intensity of hypergenic processes, even in conditions of the Arctic climate, is appeared to be sufficient, first, for a deep acidification of the residual sulfides and transition of copper, nickel, iron, magnesium in a solution and, secondly, for formation of suspensions and colloids of hypergenic minerals. Content of useful minerals in interstitial solutions reaches hundreds of milligram per liter for nonferrous metals and grams per liter for iron and magnesium. These mineralized solutions mix up with surface and underground waters. During dry season, salted sulfates are formed on the surface. Thus, uncontrollable process of technogenic forming of the crust has involuntarily started on the area in tens and hundreds of square kilometers as a result of

activity of Norilsknickel Company. The process feeds on chemical potential of technogenic products. It is one of basic factors of ecological pressure on ecosystems of Norilsk tundra.

Under these conditions, a megatechnology, based on activation of homeostatic mechanisms of environment, becomes rational. Homeostatic mechanisms could be provided by organization of geochemical barriers of various types in directions to underground water and underground drain. The possibility of practically full clearing of waters from metals is established due to research carried out. At the same time deposits of technogenic ores with high content of useful components are formed on a barrier. Thus, realization of megatechnology provides an improvement in ecological situation in industrial region, protection of the Arctic basin against pollution and getting income from additional commodity output. It is necessary to note that fixing of pollution and creation of technogenic infiltration and evaporite formations at natural geochemical barriers spontaneously proceeds in Norilsk industrial region at the moment, without purposeful activity of a person. However, a positive effect from these processes is insignificant, as the degree of technogenic influence much more surpasses the power of homeostatic mechanisms of Arctic ecosystems.

The above example shows that geological processes, even being technogenically initiated, are difficult to control. At the same time, there are processes for which it is possible to predict a direction of their proceeding reliably enough. As a rule, these are the processes where hydraulic gradient or difference in heights is responsible for the direction of proceeding of the process.

For example, drainage, necessary for mining, creates a cone of influence in the Earth's interior around a deposit. Streams of underground waters are not disturbed below the surface of a cone of influence. Existence of a cone of influence is one of conditions for starting up and proceeding of the directed geological process. Existence of sub-economic mineral reserves nearby pit walls is the further condition. The possibility of transfer of a useful component in a solution and its subsequent sedimentation on a geochemical barrier is important condition of a volumetric geological process as well. Under the above conditions, the directed geological process can be initiated. The process uses the potential of the Earth's interior in the form of a hydraulic gradient of a slope of a cone of

influence. To initiate geological process and increase coefficient of filtration of a massif an explosive crushing is made in a zone of sub-economic reserves. Disintegration of a massif is sometimes one of the stages of natural geological process. In this case, the disintegration, carried out by technogenic ways (by the "sluice" in the form of two-dimensional technologies), initiates a geological process proceeding with use of the same mechanism of transport reactions as in the natural conditions, only realized artificially. Increase of coefficient of filtration leads to redistribution of water streams. They direct to the blasted area. The reagents initiating reactions of acidification of ore minerals are supplied to a zone of sub-economic reserves. The directed stream of underground waters with a solution of a useful component moves to a mined out area of a pit. In a pit, the solution moves through natural or technogenically created geochemical barrier where useful components are precipitated. In the given example, the 3D geological process of forming of a deposit on a geochemical barrier is an analogue of natural infiltration process of a deposit formation.

One more example is presented in Fig. 9.4. This is a process of hydrothermal transformation of a sulfidic deposit (a hydrothermal boiler) [4]. To create a zone of fracturing, the massif is blasted and filled with underground waters. Compressed air is injected into the area of initiation of hydrothermal process through the holes. It is obvious that the technology of initiation is a traditional 2D process. Under a pressure of tens of atmospheres, the exothermic reactions of acidification of sulfides of nonferrous metals and iron begin. Chemical potential of acidification of sulfides serves as source of energy for realization of the process. On our estimations, the temperature in a hot zone could reach 200–300°C, which corresponds to conditions of epithermal stage of hydrothermal process. Solutions, saturated with metals, rise from the hot zone to the top layers of a massif, giving them a heat. Under conditions of oxygen shortage, the metals from solutions are cemented on sulfides or precipitated in a solid phase as oxides. As sulfides are exhausted, the bottom part of a massif cools down. Process repeats in the top part. Thus, the hot layer is formed in a massif. It rises upward with some speed, processing and enriching ore substance. The process ends in the formation of a new deposit close to the surface of the Earth. The analogy with Korzhinzky metasomatosis,

i.e., a typical volumetric geological process, is seen in this example. After completion of the initiated geological process, the neogenic ore body, which is already located on a smaller depth, is mined by a traditional 2D technology, i.e., by open pit mining or physico-chemical methods. Temperature gradients, gradients of solution concentration, and solution density create circulation in a volume of the Earth's interior involved in hydrothermal transformation. This circulation provides transport of metals to geochemical barriers without use of additional pump equipment. Besides, surplus energy evolving at the acidification of sulfides could be utilized for industrial and household heating. This set of basic factors provides a high degree of substitution of economic resources for potential resources of the Earth's interior, which, in turn, provides high economic efficiency of mining.

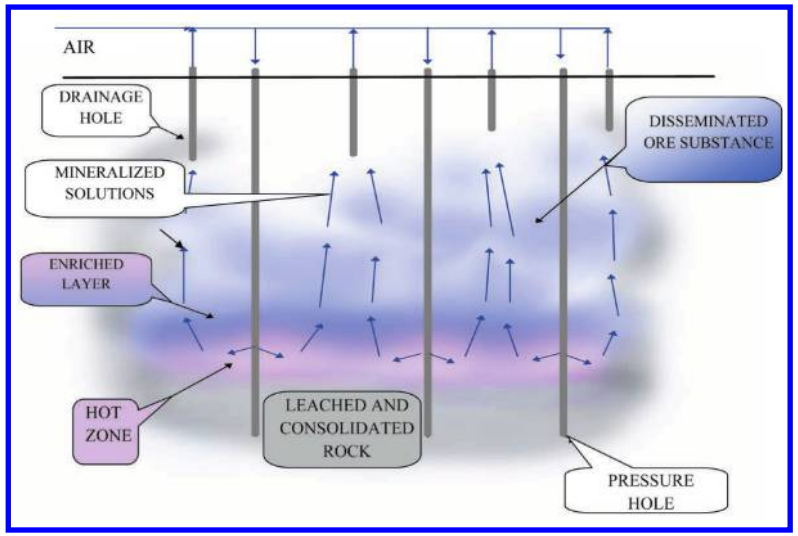

Figure 9.4 The scheme of infiltration re-structuring of sulfidic deposit ("the hydrothermal boiler").

In industrial regions, mining becomes deeper and deeper as reach available deposits are exhausted. Now mining industry faces the problem of drawing in mining rather poor ore deposits occurring at depth of 2–3 km. Ore-bearing bodies occurring at great depths are inaccessible for mining at the moment. Application of 3D megatechnologies and hydrothermal boiler, in particular, allows redeposition of ore substance of such deposits to the

depths accessible for traditional open pit and underground mining technologies.

Positive economic and ecological effects from application of megatechnologies are basically predetermined by use of volumetric geological processes and additional resources of the interior of the Earth that are not involved in traditional technological processes. The economic estimation shows that an effect from realization of megatechnologies is achieved due to reduction of extracted and processed volumes of mined rock (10–20 times), consumption of necessary economic resources (2–3 times), decrease of the depth of mining and improvement of quality of extracted raw material. On preliminary estimates, an effect from megatechnologies appears so significant that allows for increasing the scales of the development of the Earth's interior. Use of 3D megatechnologies provides a growth of amount of available mineral resources, even in conditions of inevitable decrease of ore grade. This is becomes possible due to drawing in mining not only reserves with low content of useful minerals, but also ore-bearing bodies, which are not considered today as deposits.

Application of megatechnologies enables the social problems, connected with mining in regions difficult of access, to be solved. The decrease of volumes of extracted and processed mined rock and partial substitution of 2D geotechnologies for 3D geotechnologies significantly reduce labor requirements of mining. The period of mining of neogenic deposit decreases. Finally, realization of a camp-type operation becomes easy, and quality of life in the North improves due to decline of total amount of workers.

The possibility of significant growth of scales of intervention in the Earth's interior raises the question on ecological consequences of the directed geological processes. There are two basic factors that not only limit possible negative ecological consequences but also reduce them in comparison with traditional technologies. The first factor is a volumetric character of geological processes. Traditional geotechnologies, as it has been shown earlier, transform a part of the Earth's interior to a chip placed in inhabitancy of a person. It predetermines an ecological hazard of traditional development of the interior of the Earth. In other words, the source of ecological hazard lies in the conflict between two-dimensionality of geotechnologies and three-dimensionality of the interior of the

Earth. Volumetric analogues of geological processes operate with the Earth's interior in situ, practically without influence on ecos. The second factor is that the directed geological processes, by definition, proceed with the intensity not falling outside the limits of possibilities of homeostatic mechanisms of the Earth's interior; therefore, the influence of these processes on ecos would be minimum. The additional ecological effect from megatechnologies lies in the possibility to enhance homeostatic mechanisms of ecos, for example due to creation of artificial geochemical barriers for protection of landscapes, as it has been described above.

Thus, the new paradigm of the development of the Earth's interior, based on organization and use of the directed geological processes, which transform the Earth's interior to a state appropriate for effective extraction of mineral resources, removes restrictions on limits to industrial growth and could resolve environmental problems, connected with mining, in the long term.

References

1. Meadows D. H. (1972). *Limits to Growth,* New York: University books. ISBN 0-87663-165-0.
2. Peshkov A. A., Matsko N. A. (2004). *Availability of Mineral Resources*. Moscow: Nauka. ISBN 5-02-032914-2.
3. Camm T. W. (1991). *Simplified Cost Model for Prefeasibility Mineral Evaluation*, Bureau of Mines Information Circular.
4. Peshkov A. A., Bragin V. I., Mikhailov A. G., Matsko N. A. (2007). *Geotechnological Preparation of Mineral Deposits for Mining*. Moscow: Nauka. ISBN 5-02-035306-X.

Part C

Environment Applications

Chapter 10

Anodic Porous Alumina and Nanosensors for Public Health and Vaccinology

Nicola Luigi Bragazzi, Manju Singh, and Claudio Nicolini

Nanobiotechnology and Biophysics Laboratories,
Department of Experimental Medicine, University of Genoa,
Via Antonio Pastore 3, Genoa, 16132, Italy

claudio.nicolini@unige.it

This chapter explores how nanobiotechnologies and nanostructured materials can be exploited in the field of medicine and public health, addressing several issues such as water and food safety and specifically the design and development of new vaccines. Water and food safety are two important and strongly interwoven topics in public health and represent big challenges to face due to increasing demand, population growth, climate change, and scarcity of the supplies. Nanotechnology and nanoscale devices can be a solution for these issues. In this chapter, we review potential application of anodic porous alumina (APA) in the field of public health: APA-enhanced water ultrafiltration seems to be a promising technique for having clean and fresh water, which is essential for human health, and APA-nanosensor seems to be

Nanobiotechnology in Energy, Environment, and Electronics: Methods and Applications
Edited by Claudio Nicolini

ISBN 978-981-4463-96-6 (Hardcover), 978-981-4463-97-3 (eBook)
www.panstanford.com

a useful tool to detect and remove pathogens both in food and in water. Moreover, we envisage and address the potential applications of APA in the field of vaccinology.

10.1 Introduction

In the past decades, medicine has undergone a deep and profound paradigm shift, turning from a reactive to a proactive approach toward diseases, thus becoming a preventive discipline and developing new techniques for defeating disorders. Vaccines are an example of an important tool for global health policy.

10.2 Nanomaterials for Public Health

Water and food safety are two important and strongly interwoven topics in public health and represent big challenges to face. Nanotechnology and nanoscale devices can be a solution to these problems (Barbosa-Cánovas et al., 2009; Chaudhry et al., 2010; Mamadou et al., 2009; Pray, 2009): APA-enhanced water ultrafiltration and desalination seems a promising technique for having clean and fresh water, which is essential for human health and whose scarcity is a threat for the entire mankind (White, 2012), and APA-nanosensor seems to be a useful tool to detect and remove pathogens both in food and in water.

Anodic porous alumina (also referred to as porous anodic alumina (PAA) or porous aluminum oxide (PAO) or self-ordered anodic aluminum oxide (AAO)) has a vast array of potential applications in the field of biomedicine. It can be used indeed in cellular biology as a medium for cultivating cells (Batista et al., 2012; Berthold et al., 2007; Brüggemann, 2013 and references therein; Dong et al., 2012; Ferraz et al., 2010; Graham et al., 2009; Hoess et al., 2012; Ingham et al., 2012b; Ishibashi et al., 2009; Kaji et al., 2010; Salerno et al., 2011; Salerno et al., 2013; Schlozen et al., 2009; Song et al., 2013; Swan et al., 2005; Tanvir et al., 2009; Thakur et al., 2012; Walpole et al., 2009; Yu et al., 2009), but there is also an increasing interest in APA as a material for application in the field of clinical medicine (for ocular implant, Lukáts et al., 2012; Zigiotti et al., 2012; Choi et al, 2011; Ramey et al., 2011; Goiato et al., 2010; for bone regeneration, Han et al., 2011, Boyer et al.,

2010; Mistry et al., 2010; Hamadouche et al., 2000; for human tissue engineering, Bukharova et al., 2009; Parkinson et al., 2009; for dentistry, Zhu et al., 2003; for infection prevention and as a collector around continuous ambulatory peritoneal dialysis catheter, Amano et al., 1990; for hemodialysis, Attaluri et al., 2009; Huang et al, 2007). In the pharmaceutical field, it has been exploited for drug delivery (Kwak et al., 2010).

Recently it has emerged as a smart biomaterial for public health (Narayan et al., 2010), due to the unique properties of anodic porous alumina (Nicolini et al., 2012) and there is an urgent need for solutions for providing and ensuring water and food safety.

The world is facing formidable challenges in meeting increasing demands of safe food and clean water as the available supplies of food and freshwater are decreasing (Cassardo and Jones, 2011; Chartres and Varma, 2010) due to

(i) climate changes causing droughts and famines (Carnicer et al., 2011; Gleick, 2010), which prompted the necessity of establishing ad hoc projects such as the 2010 Mid-Cycle Implementation Progress Report (MCIPR) for the 2003 strategy ("*Sustaining Water for All in a Changing Climate*") and a new plan is expected to be programmed and implemented in 2012 (World Bank, 2010, 2011);
(ii) exponential population growth (Burger et al., 2012), especially in Africa and in Asia with doubling population between 2020 and 2030;
(iii) competing demands from a variety of users (at industrial, public, and domestic level) (Grafton and Hussey, 2011).

In early 2012, the United Nations announced that the drinking-water target of the Millennium Development Goals (MDGs) had been reached in 2010 (WHO/UNICEF b 2012): In two decades, and five years ahead of schedule, the proportion of people without sustainable access to safe drinking-water had been halved (WHO/UNICEF a 2012), even if up to 100 million people are likely to lose access to drinking water in 2015 (Global Monitoring Report 2010). However, improved access to water does not mean necessarily that water is safe (Rob et al., 2012): According to some scholars (Onda et al., 2012), 1.8 billion people—28 percent of the population worldwide—were using unsafe water as of 2010.

According to some scholars (Mamadou et al., 2009), some points that are of extreme importance in water management are

(1) availability and source water protection;
(2) new water supplies;
(3) contaminant detection and selective decontamination/removal:
(4) pathogen deactivation and removal, possibly using ad hoc disinfection technologies;
(5) conservation and reuse, goals that can be attained for example by reducing waste amounts and improving efficiency of water management facilities;
(6) scalability, ramp-up, and technology diffusion (Norman et al., 2012). Weber (2002) has proposed the distributed optimal technology networks (DOT-NET) as an alternative to the "huge centralized" water treatment plant. The DOT-NET concept is predicated upon the "distribution and strategic placement of relatively small and highly efficient treatment systems at specific locations" in existing water supply networks. Such satellite water treatment systems would process relatively low flow rates and would use "off-the-shelf treatment technologies of the most advanced nature (e.g., supraselective foul-resistant membrane separations, customized polymeric adsorbents and molecular sieves, supercritical water oxidation, etc.)" to meet the water needs of population clusters such as housing subdivisions, apartment complexes, and commercial districts.

Nanotechnology can be useful in all the above-mentioned points.

Moreover, nanotechnology could reduce dramatically the enormous burden of water-borne diseases. According to the WHO, water-related diseases include those due to micro-organisms and chemicals in water people drink; diseases such as schistosomiasis, which have part of their lifecycle in water; diseases such as malaria with water-related vectors; drowning and some injuries; and others such as legionellosis carried by aerosols containing certain micro-organisms.

The total burden is estimated to be about 2 million annual deaths attributable to unsafe water, sanitation, and hygiene for diarrheal disease; more than 50 countries still report cholera to the WHO (Ali et al., 2012); millions are exposed to unsafe levels

of naturally occurring arsenic and fluoride and die or suffer from cancer and tooth/skeletal damage; an estimated 260 million are infected from schistosomiasis.

In conclusion, the WHO estimates that 4% of the global disease burden could be prevented by improving water supply, sanitation, and hygiene and specifically speaking of water-borne diseases in the developing countries the 80% of diseases.

The total global economic losses associated with inadequate water supply and sanitation were estimated at US$260 billion annually.

As far as food safety is concerned, it is estimated that in the United States, food-borne diseases result in 76 million illnesses, 325,000 hospitalizations, and 5,000 deaths each year and that the most widespread food pathogens in the United States are responsible for losses of over US$8 billion and 36,000 QALYs (Batz et al., 2012; Hoffmann et al., 2012).

10.2.1 APA-Enhanced Water Desalination

Desalination (or demineralization) is a kind of process and treatment that—removing dissolved salt and other minerals—enables to obtain fresh, potable, and clean drinking water from marine water, brackish groundwater, and other salty water samples. The employed technologies are high-temperature distillation, low-temperature distillation, mechanical and vacuum distillation (multi-stage flash distillation, multiple-effect distillation, vapor compression and its variant "co-generation," by adding waste heat, distillation/condensation), ion-exchange, solar desalination (solar humidification-dehumidification, multiple-effect desalination), geothermal desalination (geothermal energy and power driven desalination), methane hydrate crystallization, freezing desalination, and membrane-based desalination (electrodialysis reversal, reverse osmosis, membrane distillation, ultrafiltration/microfiltration/nanofiltration). Dealkalization softening can be considered a pre-treatment.

Classical membranes are made up of cellulose acetate, polyaromatic amide or similar polymeric materials. The new generation of membranes includes smart inorganic nanomaterials, such as APA, zeolite, crystal gravel, and amorphous molecular sieve silica (Duke et al., 2007).

Anodic porous alumina coupled with nanoporous organosilica membranes has proved to be an efficient tool in order to provide water desalination via membrane distillation (Chua et al., 2013). Together with mesoporous bentonite membranes, APA can perform reverse osmosis desalination (Li et al., 2004).

10.2.2 APA-Enhanced Water Ultrafiltration

Classical disinfection and decontamination technologies have a lot of limitations, which are indeed overcome by nanotechnological devices (Savage and Diallo, 2005; Smith, 2006). For example, conventional disinfectants such as free chlorine, chloramines, and ozone may interact with constituents of treated water to create carcinogenic disinfection by-products (Krasner et al., 2006).

Ultrafiltration is an important step in water management (Zeman and Zydney, 1996) and today can be achieved with nanoporous membranes (Peltier et al., 2003; Van der Bruggen et al., 2003), trying to minimize as much as possible membrane biofouling with a new-generation antimicrobial membranes (Park et al., 2005). Anodic porous alumina membranes can remove melamine (eye, skin, and lung irritant, it can cause cancer and has recently involved in some scandals of Chinese protein adulteration), arsenic (Kim et al., 2004) and other heavy metals (Hua et al., 2012). The maximum level of arsenic concentration in drinking water is 0.01 ppm (according to the USA EPA) and 10 μg/L (according to the European Union).

The first generation of nanoporous membranes-based filters were simply nanostructured, while the second generation have become nanoreactive.

Nanoporous membranes with anti-viral (Brown and Sobsey, 2009) and antimicrobial properties may be especially useful small-scale or point-of-use systems; distributed water systems may be especially useful for underdeveloped regions, remote locations and emergency situations (Haas, 2000). A-alumoxane nanoporous membranes have been used as filters (DeFriend et al., 2003), having the potential to capture and remove viral pathogens (Maguire-Boyle et al., 2012). They have been further functionalized with gold nanoparticles exploiting layer-by-layer deposition technique and were shown to be able to reduce 4-nitrophenol to 4-aminophenol (Dotzauer et al., 2006). Anodic porous alumina

and other porous materials have been shown to remove PAH (Lima et al., 2012).

10.2.3 APA-Enhanced Water Bioremediation

Anodic porous alumina has the potential to bioremediate water, removing micropollutants such as pharmaceuticals, like diclofenac sodium and carbamazepine (Wei et al., 2013).

10.2.4 APA-Based Food Detoxification

Anodic porous alumina-based high-sensitivity sensors have been recently developed in order to detect pathogens and pollutants in the food chain supply (Erdem et al., 2012; Farahi et al., 2012).

Some scholars built sensors for direct toxin detection in food, exploiting hydrophobically modified electrochemical impedance immunosensor (EII) technology (Chai et al., 2010; Chai and Takhistov, 2010).

An emerging topic in the field of biosensors is label-free technology, which appears capable to overcome labeled technology limitations (Nicolini et al., 2012). Anodic porous alumina surface, in fact, appears to allow a label-free analysis using electric impedance spectroscopy (EIS). It is known that with EIS it is possible to detect different amounts of organic materials deposited even indirectly over conducting surfaces (Nicolini et al., 2012).

Electric impedance spectroscopy sensor was designed by (Chai et al., 2010) to detect SEB (*Staphylococcus enterotoxin* B) toxin at the levels as low as 10 pg/mL in 15 min. SEB toxin is a superantigen protein with a mass of 28.4 kDa. It is considerably more stable in unphysiological conditions than other protein-based toxins such as ricin and botulinum neurotoxins. For example, SEB can survive in boiling water for several minutes, whereas ricin is all but inactivated after some 15 min at +80°C.

10.3 Nanosensors for Public Health

Since the introduction of the first biosensor by Clark and Lyons in 1962 (namely the glucose oxidase-based sensor, for the detection of glucose), biosensors have emerged as an extraordinarily versatile tool and device whose benefits and advantages have been

acknowledged in many areas of biomedical and analytical sciences, from research to development, being now routinely used in many laboratories and firms, for many applications.

Biosensors play a key role in the clinical and industrial areas. Many scholars have suggested that clinical biosensors, besides enabling an earlier diagnosis of the disease, a control of its progression and a reduction in the complications rate, could improve patient self-monitoring and self-management. This would result in an empowerment of the patient, enhancing compliance and adherence to the treatment and favoring therapy adjustments toward an optimal strategy choice. Also, the industrial field can widely benefit from biosensors applications, which are, for example, an important option in the agricultural and food sectors to control the entire chain of production processes (from the initial manipulation and separation, to fermentation and supply) and can ensure high food quality, acceptability and safety standards by reliable, quick and cost effective procedures, by testing residue and contaminant concentration. Biosensors are promising alternatives to conventional analytical tools since they offer advantages in size, cost, specificity, rapid response, precision and sensitivity or they can be integrated with them as complementary approaches.

Biosensors are biological or chemical sensors with high selectivity and sensitivity to biologically active materials. They can be considered the combination of a bioreceptor, which is the biological or organic component, and a transducer, which is able to transform and amplify the signal resulting from the interaction of the analyte with the biological element into a distinct signal, that can be more easily measured and quantified. The interaction of sensing and query molecules, in fact, leads to changes in the mass, electric charge, magnetic or optical properties of the immobilized molecules, which can be detected, for example, by fluorescence, nanogravimetric transducers, potentiometric, amperometric, and/or spectrophotometric/polarimetric ones.

Label-free biosensors instead do not require the use of reporter elements (fluorescent, luminescent, radiometric, or colorimetric) for the measurement of the signal. In fact, a receptor molecule is connected to a transducer that produces an electrical signal in real time. Therefore, label-free techniques can provide direct and straightforward information on analyte binding to target molecules

typically in the form of mass addition or depletion from the surface of a sensor substrate or via changes in a physical bulk property of a sample.

In the protein-based sensors field, engineered protein-based biosensors—i.e. biosensors realized immobilizing engineered proteins in order to improve determinate characteristics—provide a sensible improvement offering advantages such as high sensitivity (by specifically binding and identifying chemical substrates or other molecules), thermostability, and reusability. The use of native proteins for this purpose cannot adequately embrace the limits of detection and level of stability required for a usable sensor, since they cannot be easily obtained, manipulated and modified until they meet with the desired properties. The most desirable biological molecules features for the construction of a biosensor are intrinsic signal-transduction functions easily measurable by a robust and miniaturizable instrumentation and a readily accessible, and highly diverse collection of binding sites. In protein engineering for the electrochemical biosensor implementation, three main strategies are used to modify aspects of stability, sensitivity, selectivity, surface tethering, and signal transduction; they are rational protein design, directed evolution (by situ-directed mutagenesis) and de novo protein design.

10.3.1 APA-Based Nanosensors

Anodic porous alumina is a versatile smart nanomaterial that has been used also for the design of point-of-care (POC) systems, such as lab-on-chips, biochips, microarrays (Kim et al., 2007; Lee et al., 2006; Piao and Kim, 2009) and biosensors. Because of their unique properties, nanoporous thin films based on alumina have been used for the electrochemical detection of a vast array of molecules and substances.

Anodic porous alumina can be used for a variety of purposes, implementing optical, interferometric (Kumeria and Losic, 2012; Dronov et al., 2011), and polarimetric (Álvarez et al., 2013) sensors or label-free (Alvarez et al., 2009; Ko et al., 2009; Nicolini et al., 2012), SERS (Das et al., 2012; Huang et al., 2011; Lee et al., 2009), SPR (Saito et al., 2012) sensors.

Binding kinetics can be studied observing the changes in resistance, impedance, and capacitance of the film. The sensing

potential of APA can be understood using the constant phase element (CPE) theory instead of the too simplified resistor–capacitor (RC)-layer model, because APA is a heterogeneous material and this can explain the distribution of capacitance values (Nguyen et al., 2012).

Nguyen and collaborators have put forward the following equation:

$$Z_{CPE} = 1/(Q(j\omega)^n),$$

where Z_{CPE} is the impedance of the CPE, ω is the angular frequency, Q is the capacitance, j is the imaginary unit, n is a parameter that if assuming the value of 1 makes the CPE behave exactly as a pure capacitor and in this case the equation simplifies to a normal RC equation.

10.3.2 APA-Based Nanosensors for Proteins and Genes Studies

Another use of APA is the detection of DNA and nucleotides (Guo et al., 2010; Ke et al., 2009; Li et al., 2010; Ma and Yeung, 2010; Matsumoto et al., 2004; Yamashita et al., 2009; Wu et al., 2004) (Fig. 10.1).

Anodic porous alumina–based sensors can also be used to investigate proteins, since they are specifically and selectively captured by the nanochannel structure: Chen et al. term this phenomenon protein entrapment in the nanotubes, in so that APA layout can be thought of as a "protein-trapping device" (Chen et al., 2012). They implemented an APA thermal nanoimprint lithography (NIL) sensor for investigating proteins like the immunoglobulin. They found that LOD was 1.0 ng/mL. Dhathathreyan used APA sensor for studying enzyme activity (namely, invertase) (Dhathathreyan, 2011). Not only from an electrochemical point of view but also optically speaking, APA sensors can be used as nanoporous-waveguide sensors (NPWG), performing better than SPR biosensors (Hotta et al., 2012). They succeeded in showing that a careful manipulation of parameters such as porosity, pore density, thickness, and refractive index resulted in optimal adsorption and kinetics of bovine serum albumin (BSA). Also, Shen and collaborators immobilized BSA on functionalized APA (Shen et al., 2004). Jernshøj and collaborators used APA to adsorb rhodamine

and study it with SERS approach (Jernshøj et al., 2011). Kim and collaborators coupled localized SPR (LSPR) with interferometry to study thrombin and aptamer III (LOD 1nM) (Kim et al., 2008).

10.3.3 APA-Based Nanosensors for Drugs Monitoring

Anodic porous alumina sensors can quantitatively monitor drugs such as penicillin G (Takhistov, 2004), retinoic acid (Yu et al., 2009), valinomycin (Kepplinger et al., 2009), 5-fluoro-uracil (Hiep et al., 2010). Hiep and collaborators created an interesting biosensor termed ILSPR (interference localized surface plasmon resonance), a photonic thin-film multilayers of APA coated with gold nanoparticles.

10.3.4 APA-Based Nanosensors for Disease Biomarkers

Specific APA-designed biosensors can monitor cancer biomarker such as Galectin-1 and Galectin-9 (van Hattum et al., 2013), CA-15.3 (De La Escosura-Muñiz and Merkoçi, 2011). Kumeria and collaborators implemented a label-free APA-based reflectometric sensor for monitoring circulating tumor cells (Kumeria et al., 2012).

Other clinically relevant biosensors can detect cardiovascular markers and inflammatory markers (CRP, C-reactive protein, Yeom et al., 2011), endocrinological ones (such as 5 alpha-androstane-3 alpha, 17 beta-diol, performed by Pailler et al., 1985) or others (Barabino et al., 1978, for alpha-amylase detection).

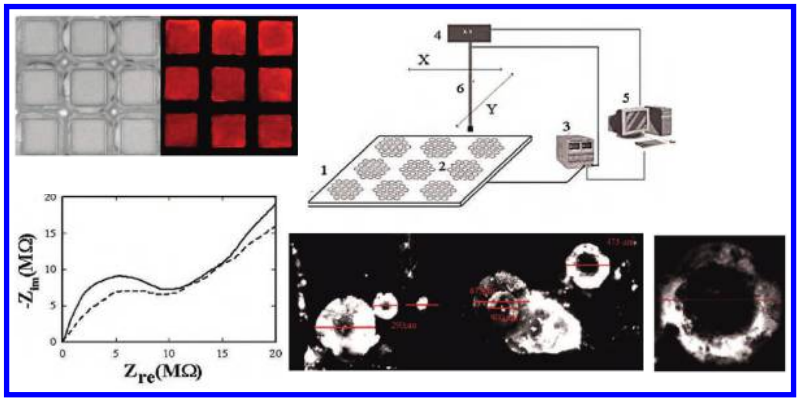

Figure 10.1 Anodic Porous Alumina (APA) application for gene microarrays.

10.3.5 APA-Based Enzymatic Nanosensors

Anodic porous alumina has proved to be an excellent substrate and materials for the implementations of enzymatic biosensors (Heilmann et al., 2003). Specifically, it has enables the design of glucose oxidase (Ansari et al., 2008; Claussen et al., 2011; Ekanayake et al., 2007; Koh et al., 2007; Myler et al., 2002; Xian et al., 2007), catalase (Vasudevan and Thakur, 1994), alliinase (Milka et al., 2000), tyrosinase (for the detection of phenols, Liu et al., 2000; for the detection of dopamine and other neurotransmitters, Kisner et al., 2012; for the detection of phenolic compounds, Zejli et al., 2008), urease (Yang et al., 2007) and cytochrome P450scc (Stura et al., 2007) sensors.

P450scc (P450 side chain cleavage) belongs to the large super family of heme-thiolate proteins of cytochromes P450 and plays a major role in the catalysis of several biochemical reactions such as the monooxygenase reactions. These reactions imply the insertion of one atom of oxygen into substrate while the other oxygen atom is reduced to water, according the following general reaction:

$$RH + O_2 + H^+ + 2e^- \rightarrow ROH + H_2O,$$

where RH is the enzyme substrate such as the cholesterol. The enzyme catalyzes the cholesterol side chain cleavage reaction, which is the key initial step in steroid hormone biosynthesis. The mechanism of the reaction is complex: initially the enzyme binds cholesterol; during this process, the Fe^{3+} ion of the heme group undergoes a low spin to high-spin transition. The Fe^{3+} is then reduced to Fe^{2+} by $NADPH^+$, via andrenodoxin reductase and at least further four electrons are transferred to convert the cholesterol to pregnenolone. Many steps in the biosynthesis of steroid hormones are catalyzed by cytochrome P450 enzymes and the reactions depend on the electrons transfer of from NADPH to P450 via electron transfer proteins adrenodoxin reductase and adrenodoxin in the mitochondria, and cytochrome P450 reductase in the endoplasmic reticulum.

This redox reaction between an enzyme and an analyte can be transduced to an electrical signal via subsequent direct electron transfer between the enzyme and the electrode.

Cytochrome P450sccK201E clone was produced via the recombinant genetic engineering. After the production of APA, the

APA layer was deposited on a rhodium–graphite screen-printed electrode by an adhesive conductive Ag paste, in order to create a functionalized modified working electrode. The rhodium–graphite s.p.e. was used also as a reference electrode as well as working electrode (Fig. 10.2).

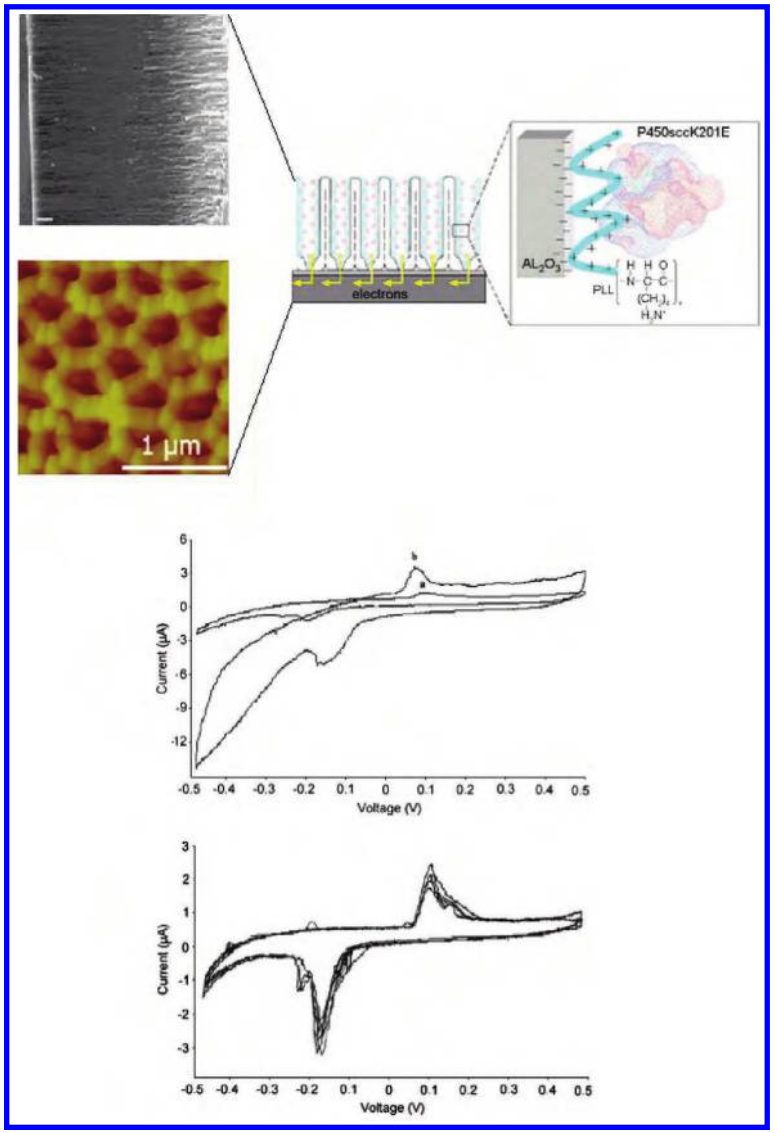

Figure 10.2 APA application for biosensors.

The immobilized P450scc cytochrome was used to characterize process of electroactive species on electrode surface. The measures were carried out using a final concentration range of substrate from 0.5 to 1.6 mg/mL, considering that the physiological total serum level of LDL-cholesterol corresponds to 1.1 mg/mL. The sensor proved highly sensitive and time-stable.

10.3.6 APA-Based Nanosensors for Microbiological Applications

Anodic porous alumina sensors for microbiological detection are a further promising potential. Anodic porous alumina permits germs culture and testing assays (Ferrari et al., 2005; Ingham et al., 2005, 2007), as well as sensing. Ingham and collaborators used APA for microcolony based antibiotic susceptibility to study *Candida* spp. (Inhgam et al., 2012a), while other scholars have studied the *Enterobacteriaceae* and methicillin-resistant *Staphylococcus aureus* (Ingham et al., 2006; Liu et al., 2012; Tsou et al., 2010), *Mycobacterium tuberculosis* (den Hertog et al., 2010; Ingham et al., 2008), *Klebsiella pneumoniae* and *Mycobacterium smegmatis* (Liu et al., 2012).

Bacteria can be used in particular for studying biochemical oxygen demand (BOD) values (Chen et al., 2002).

APA-based sensors can detect viruses such as Dengue virus (Nguyen et al., 2012). Anodic porous alumina-biosensor coated with specific IgG immunoglobulins can be represented as being made up of two components: the insulating porous membrane layer and the electrode conductive layer. The virus is captured by the nanochannels, which can be modeled using non-Faradaic components comprising a channel resistance in parallel with a CPE that represents the channel capacitance. The pore resistance is proportional to the Dengue Denv2 antigen concentration, linearity of the dynamic response has been found from 1 to 900 PFU/mL, and this correlation can be theoretically explained using the Freundlich–Langmuir isotherm model.

Another investigated virus is the West Nile virus (Nguyen et al., 2009). In addition, these nanoporous films and membranes when coupled to cyclic voltammetry (CV), differential pulse voltammetry (DPV) or EIS methods are highly useful for DNA hybridization detection (Li et al., 2010) and bacteria sensing such

as *Staphylococcus aureus* and *Escherichia coli* O157:H7 (Tan et al., 2011).

Generally, these detection methods rely on the interaction of the target species at the electrode/electrolyte interface or within the nanoporous channels of the alumina layer.

Basu and collaborators have designed an APA-based biosensor for a specific clinical purpose: monitoring kidney infectious diseases (Basu et al., 2004). This sensor, based on the enzyme-linked immunosorbent assay (ELISA) system, is able to determine bacteria in clinical concentrations via electrochemical and optical techniques.

10.3.7 APA-Based Nanosensors for Environmental Applications

Another promising field of sensor applications is given by the environmental sensors. Anodic porous alumina has been used for sensing ammonia gas (Markovics and Kovács, 2013) using a reflectometric optical approach, for oxygen (Lu et al., 2010), for peroxide compounds (Chang et al., 2009) and for volatile sulfur compounds (Kumeria et al., 2011) using interferometric technique. Yao and collaborators designed a humidity sensors based on APA films, prepared via stable high-field anodization and subsequent isotropic chemical etching (Yao et al., 2009).

10.4 APA for Vaccinology

In the last decades, vaccinology has emerged as a complex interdisciplinary science, especially because of the contributions of the new OMICS disciplines, such as vaccine bioinformatics (advocated by Rappuoli) (Donati and Rappuoli, 2013), immunogenomics (pioneered by Poland) (Klein and Poland, 2013; Poland et al., 2011), and vaccinomics (developed and fostered by Ozdemir) (Ozdemir et al., 2011a, 2011b). Moreover, the study of proteins interactions and networks has further advanced and accelerated thanks to the new developments in the field of functional proteomics. Immunoproteomics indeed represents a crucial discipline for vaccine discovery and design (Falisse-Poirrier et al., 2006). Protein interactions can now be assessed using

nucleic acid programmable protein array (NAPPA), and, in its turn, NAPPA can be coupled with label-free approaches and technologies.

The label-free NAPPA and SNAP technologies, in combination with APA along with cell-free expression system, appear converging into a single approach capable to more effectively address the numerous problems still open in medical diagnosis and vaccine implementation. These tecnologies can be a useful platform for screening and tests of vaccine immunogenicity, in the frame of design and development of new vaccines.

Results

Preliminary proofs of principle appear promising and encouraging for monitoring immune response to antigen exposure, also in the framework of a personalized vaccine discovery and design.

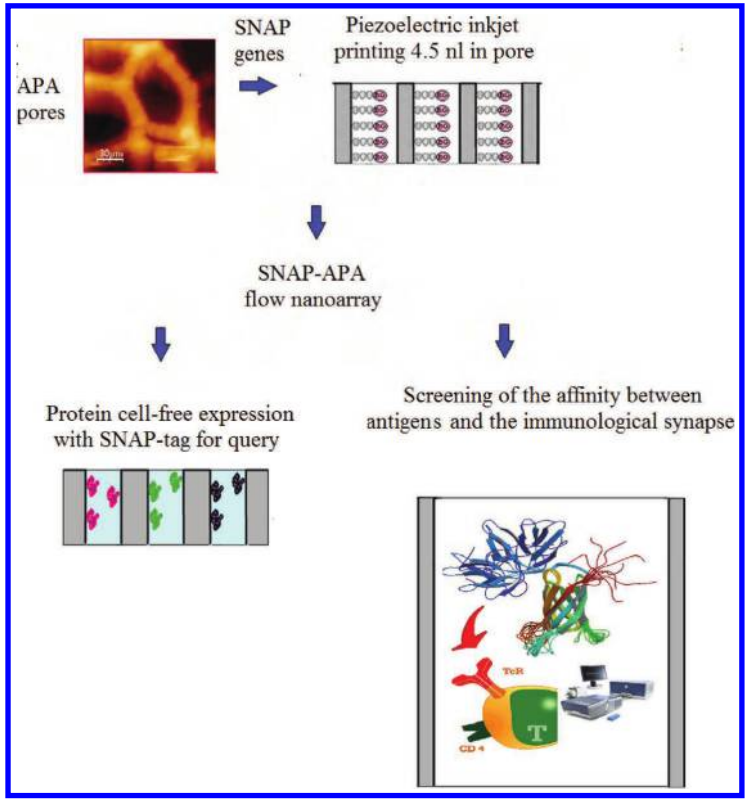

Conclusions

Among the avenues being currently explored, NAPPA-based vaccine identification appears to represent an additional promising future perspective in the frame of the new OMICS-based public health. Only recently were protein arrays used to discover new antigenic determinants for vaccine development. Nucleic acid programmable protein array–based sensors could be used for screening the affinity between the identified proteins and the immunological synapse (CD4, TCR, MHC complex). Affinity kinetics can be evaluated also using classical techniques, or new efforts to evaluate it via atomic force microscopy (AFM) and surface plasmon resonance (SPR) (Bragazzi and Nicolini, 2013).

References

Ali M, Lopez AL, Ae You Y, Eun Kim Y, Sah B, Maskery B, Clemens J. The global burden of cholera. *Bull World Health Organ*., 2012, **90**, 209–218A.

Alvarez SD, Li CP, Chiang CE, Schuller IK, Sailor MJ. A label-free porous alumina interferometric immunosensor. *ACS Nano*., 2009, **3**(10), 3301–3307.

Álvarez J, Serrano C, Hill D, Martínez-Pastor J. Real-time polarimetric optical sensor using macroporous alumina membranes. *Opt. Lett*., 2013, **38**(7), 1058–1060.

Amano I, Katoh T, Inagaki Y. Clinical experience with alumina ceramic transcutaneous connector to prevent skin-exit infection around CAPD catheter. *Adv. Perit. Dial*., 1990, **6**, 150–154.

Ansari SG, Ansari ZA, Wahab R, Kim YS, Khang G, Shin HS. Glucose sensor based on nano-baskets of tin oxide templated in porous alumina by plasma enhanced CVD. *Biosens. Bioelectron*, 2008, **23**(12), 1838–1842.

Attaluri AC, Huang Z, Belwalkar A, Van Geertruyden W, Gao D, Misiolek W. Evaluation of nano-porous alumina membranes for hemodialysis application. *ASAIO J*., 2009, **55**(3), 217–223.

Bain RES, Gundry SW, Wright JA, Yang H, Pedley S, Bartram JK. Accounting for water quality in monitoring access to safe drinking-water as part of the Millennium Development Goals: Lessons from five countries. *Bull World Health Organ*., 2012, **90**, 228–235A.

Barabino RC, Gray DN, Keyes MH. Coupled reactions of immobilized enzymes and immobilized substrates: Clinical application as exemplified by amylase assay. *Clin. Chem*., 1978, **24**(8), 1393–1398.

Barbosa-Cánovas GV, Mortimer A, Lineback D. Spiess, Buckle, Colonna (Editors). Release Date: 22 Jul 2009. Print Book ISBN :9780123741240 eBook ISBN :9780080920818 Pages: 520.

Basu M, Seggerson S, Henshaw J, Jiang J, del A Cordona R, Lefave C, Boyle PJ, Miller A, Pugia M, Basu S. Nano-biosensor development for bacterial detection during human kidney infection: Use of glycoconjugate-specific antibody-bound gold nanowire arrays (GNWA). *Glycoconj J*., 2004, **21**(8–9), 487–496.

Batista PS, Rodrigues MA, Silva DM, Morgado PI, Henriques JP, Almeida MO, Silva AP, Correia IJ. Characterization of the mechanical and biological properties of a new alumina scaffold. *J. Appl. Biomater. Funct. Mater*., 2012, doi: 10.5301/JABFM.2012.9264. [Epub ahead of print].

Batz, MB, Hoffmann, S, Morris Jr, Glenn J. Ranking the disease burden of 14 pathogens in food sources in the United States using attribution data from outbreak investigations and expert elicitation. *J. Food. Prot*., 2012, **75**(7), 1278–1291.

Berthold A, Haibel A, Brandes N, Kroh L, Gross U, Uharek L, Schubert H. Biocompatible porous ceramics for the cultivation of hematopoietic cells. *J. Mater. Sci. Mater. Med*., 2007, **18**(7), 1333–1338.

Boyer P, Huten D, Loriaut P, Lestrat V, Jeanrot C, Massin P. Is alumina-on-alumina ceramic bearings total hip replacement the right choice in patients younger than 50 years of age? A 7- to 15-year follow-up study. *Orthop. Traumatol. Surg. Res*., 2010, **96**(6), 616–622.

Bragazzi N, Nicolini C. Nanovaccinology: Nanogenomics, nanoproteomics and nanosensors for vaccine design. *Critical Rev. Eukaryotic Gene Expression*, 2014, submitted.

Brown J, Sobsey MD. Ceramic media amended with metal oxide for the capture of viruses in drinking water. *Environ. Technol*., 2009, **30**(4), 379–391.

Brüggemann D. Nanoporous aluminium oxide membranes as cell interfaces. *J. Nanomater*., 2013 (2013), Article ID 460870, 18 pages http://dx.doi.org/10.1155/2013/460870.

Bukharova TB, Fatkhudinov TKh, Tsedik LV, Ilyushchenko AF, Goldshtein DV. Tissue engineering construction from 3D porous ceramic carriers and multipotent stromal cells for the repair of bone tissue defects. *Bull Exp. Biol. Med*., 2009, **147**(1), 147–155.

Burger JR, Allen CD, Brown JH, Burnside WR, Davidson AD, Fristoe TS, Hamilton MJ, Norman M-S, Nekola JC, Okie, JG, Zuo W. The macroecology of sustainability. *PLoS Biol*., 2012, **10**(6), e1001345.

Carnicer J, Coll M, Ninyerola M, Pons X, Sánchez G, Peñuelas J. Widespread crown condition decline, food web disruption, and amplified tree mortality with increased climate change-type drought. *Proc. Natl. Acad. Sci. U S A*., 2011, **108**, 1474–1478.

Cassardo C, Jones JAA. Managing water in a changing world. *Water,* 2011, **3**, 618–628.

Chai C, Lee J, Takhistov P. Direct detection of the biological toxin in acidic environment by electrochemical impedimetric immunosensor. *Sensors (Basel)*., 2010, **10**(12), 11414–11427.

Chai C, Takhistov P. Label-free toxin detection by means of time-resolved electrochemical impedance spectroscopy. *Sensors (Basel)*., 2010, **10**(1), 655–669.

Chang S, Ko H, Singamaneni S, Gunawidjaja R, Tsukruk VV. Nanoporous membranes with mixed nanoclusters for Raman-based label-free monitoring of peroxide compounds. *Anal. Chem*., 2009, **81**(14), 5740–5748.

Chartres, C, Varma, S. *Out of water*. *From Abundance to Scarcity and How to Solve the World's Water Problems*, FT Press (USA), 2010.

Chaudhry Q, Castle L, Watkins R. *Nanotechnologies in Food*. RSC Nanoscience & Nanotechnology. The Royal Society of Chemistry. 2010, 244 pp.

Chen W, Jin B, Hu YL, Lu Y, Xia XH. Entrapment of protein in nanotubes formed by a nanochannel and ion-channel hybrid structure of anodic alumina. *Small*., 2012, **8**(7), 1001–1005.

Chen D, Cao Y, Liu B, Kong J. A BOD biosensor based on a microorganism immobilized on an Al_2O_3 sol-gel matrix. *Anal. Bioanal. Chem*., 2002, **372**(5–6), 737–739.

Choi S, Lee SJ, Shin JH, Cheong Y, Lee HJ, Paek JH, Kim JS, Jin KH, Park HK. Ultrastructural investigation of intact orbital implant surfaces using atomic force microscopy. *Scanning*., 2011, **33**(4), 211–221.

Chua YT, Lin CX, Kleitz F, Zhao XS, Smart S. Nanoporous organosilica membrane for water desalination. *Chem. Commun. (Camb)*., 2013, **49**(40), 4534–4536.

Claussen JC, Wickner MM, Fisher TS, Porterfield DM. Transforming the fabrication and biofunctionalization of gold nanoelectrode arrays into versatile electrochemical glucose biosensors. *ACS Appl. Mater. Interfaces*., 2011, **3**(5), 1765–1770.

Das G, Patra N, Gopalakrishnan A, Zaccaria RP, Toma A, Thorat S, Di Fabrizio E, Diaspro A, Salerno M. Fabrication of large-area ordered and reproducible nanostructures for SERS biosensor application. *Analyst*., 2012, **137**(8), 1785–1792.

Donati C, Rappuoli R. Reverse vaccinology in the 21st century: Improvements over the original design. *Ann N Y Acad Sci*., 2013, doi: 10.1111/nyas.12046 [Epub ahead of print].

DeFriend KA, Wiesner MR, Barron AR. Alumina and aluminate ultrafiltration membranes derived from alumina nanoparticles. *J. Membr. Sci*., 2003, **224**(1–2), 11–28.

de la Escosura-Muñiz A, Merkoçi A. A nanochannel/nanoparticle-based filtering and sensing platform for direct detection of a cancer biomarker in blood. *Small*, 2011, **7**(5), 675–682.

den Hertog AL, Visser DW, Ingham CJ, Fey FHAG, Klatser PR, Anthony RM. Simplified automated image analysis for detection and phenotyping of *Mycobacterium tuberculosis* on porous supports by monitoring growing microcolonies. *PLoS One*., 2010, **5**, e11008.

Dhathathreyan A. Real-time monitoring of invertase activity immobilized in nanoporous aluminum oxide. *J. Phys. Chem. B*., 2011, **115**(20), 6678–6782.

Dong Z, Wu Y, Wang Q, Xie C, Ren Y, Clark RL. Reinforcement of electrospun membranes using nanoscale Al_2O_3 whiskers for improved tissue scaffolds. *J. Biomed. Mater. Res. A*., 2012, **100**(4), 903–910.

Dotzauer DM, Dai J, Sun L, Bruening ML. Catalytic membranes prepared using layer-by-layer adsorption of polyelectrolyte/metal nanoparticle films in porous supports. *Nano. Lett*., 2006, **6**(10), 2268–2272.

Dronov R, Jane A, Shapter JG, Hodges A, Voelcker NH. Nanoporous alumina-based interferometric transducers ennobled. *Nanoscale*, 2011, **3**(8), 3109–3114.

Duke MC, Mee S, da Costa JC. Performance of porous inorganic membranes in non-osmotic desalination. *Water Res*., 2007, **41**(17), 3998–4004.

Ekanayake EM, Preethichandra DM, Kaneto K. Polypyrrole nanotube array sensor for enhanced adsorption of glucose oxidase in glucose biosensors. *Biosens. Bioelectron*, 2007, **23**(1), 107–113.

Erdem A, Muti M, Karadeniz H, Congur G, Canavar E. Electrochemical biosensors for screening of toxins and pathogens. *Portable Chemical Sensors*, NATO Science for Peace and Security Series A: Chemistry and Biology, 2012, 323–334.

Falisse-Poirrier N, Ruelle V, ElMoualij B, Zorzi D, Pierard O, Heinen E, De Pauw E, Zorzi W. Advances in immunoproteomics for serological characterization of microbial antigens. *J. Microbiol. Methods*., 2006, **67**(3), 593–596.

Farahi RH, Passian A, Tetard L, Thundat T. Critical issues in sensor science to aid food and water safety. *ACS Nano*., 2012, **6**(6), 4548–4556.

Ferrari BC, Binnerup SJ, Gillings M. Microcolony cultivation on a soil substrate membrane system selects for previously uncultured soil bacteria. *Appl. Environ. Microbiol*., 2005, **71**, 8714–8720.

Ferraz N, Hong J, Santin M, Karlsson Ott M. Nanoporosity of alumina surfaces induces different patterns of activation in adhering monocytes/macrophages. *Int. J. Biomater*., 2010, 402715.

Gleick PH. Climate change, exponential curves, water resources, and unprecedented threats to humanity. *Climatic. Change*., 2010, **100**(1) 125–129.

Goiato MC, Haddad MF, dos Santos DM, Pesqueira AA, Ribeiro Pdo P, Moreno A. Orbital implants insertion to improve ocular prostheses motility. *J. Craniofac. Surg*., 2010, **21**(3), 870–875.

Grafton QR, Hussey K. *Water Resources Planning and Management*. New York: Cambridge University Press. 2011.

Graham AH, Bowen CR, Taylor J, Robbins J. Neuronal cell biocompatibility and adhesion to modified CMOS electrodes. *Biomed Microdevices*., 2009, **11**(5), 1091–1101.

Guo M, Lv W, Zhang S, Jin FM, Wang Q, Ling GW, Yang QH. Ultrathin carbon nanotube-DNA hybrid membrane formation by simple physical adsorption onto a thin alumina substrate. *Nanotechnology*., 2010, **21**(28), 285601.

Haas CN. Disinfection in the twenty-first century. *J. Am. Water Works Assoc*., 2000, **92**, 72–73.

Hamadouche M, Meunier A, Greenspan DC, et al., Bioactivity of sol-gel bioactive glass coated alumina implants. *J. Biomed. Mater. Res.,* 2000, **52**, 422–429.

Han M, Kim JM, Choi SH, Lee FY, Son JS, Oh D. Bone regeneration of tibial segmental defect using isotropic-pore structures hydroxyapatite/alumina bi-layered scaffold: In vivo pilot study. *J. Long Term Eff. Med. Implants*, 2011, **21**(2), 159–167.

Heilmann A, Teuscher N, Kiesow A, Janasek D, Spohn U. Nanoporous aluminum oxide as a novel support material for enzyme biosensors, *J. Nanosci. Nanotechnol*., 2003, **3**(5), 375–379.

Hiep HM, Yoshikawa H, Tamiya E. Interference localized surface plasmon resonance nanosensor tailored for the detection of specific biomolecular interactions. *Anal. Chem*., 2010, **82**(4), 1221–1227.

Hoess A, Thormann A, Friedmann A, Heilmann A. Self-supporting nanoporous alumina membranes as substrates for hepatic cell cultures. *J. Biomed. Mater. Res. A*., 2012, **100**(9), 2230–2238.

Hoffmann S, Batz, Michael B, Morris J, Glenn J. Annual cost of illness and quality-adjusted life year losses in the United States due to 14 foodborne pathogens. *J. Food. Prot*., 2012, **75**(7), 1292–1302.

Hotta K, Yamaguchi A, Teramae N. Nanoporous waveguide sensor with optimized nanoarchitectures for highly sensitive label-free biosensing. *ACS Nano*., 2012, **6**(2), 1541–1547.

Hua M, Zhang S, Pan B, Zhang W, Lv L, Zhang Q. Heavy metal removal from water/wastewater by nanosized metal oxides: a review. *J. Hazard. Mater*., 2012, **211–212**, 317–331.

Huang CH, Lin HY, Chen S, Liu CY, Chui HC, Tzeng Y. Electrochemically fabricated self-aligned 2-D silver/alumina arrays as reliable SERS sensors. *Opt. Express*., 2011, **19**(12), 11441–11450.

Huang Z, Zhang W, Yu J, Gao D. Nanoporous alumina membranes for enhancing hemodialysis. *J. Med. Devices*, 2007, **1**(1), 79–83.

Ingham CJ, Ayad AB, Nolsen K, Mulder B. Rapid drug susceptibility testing of mycobacteria by culture on a highly porous ceramic support. *Int. J. Tuberc. Lung. Dis*., 2008, **12**(6), 645–650.

Ingham CJ, Boonstra S, Levels S, de Lange M, Meis JF, Schneeberger PM. Rapid susceptibility testing and microcolony analysis of *Candida* spp. cultured and imaged on porous aluminum oxide. *PLoS One*, 2012, **7**(3), e33818.

Ingham CJ, Sprenkels A, Bomer J, Molenaar D, van den Berg A, van Hylckama Vlieg, et al. The micro-Petri dish, a million well growth chip for the culture and highthroughput screening of microorganisms. *Proc. Natl. Acad. Sci. USA*, 2007, **13**, 18217–18222.

Ingham CJ, ter Maat J, de Vos WM. Where bio meets nano: The many uses for nanoporous aluminum oxide in biotechnology. *Biotechnol. Adv*., 2012, **30**(5), 1089–1099.

Ingham CJ, van den Ende M, Pijnenburg D, Wever PC, Schneeberger PM. Growth and multiplexed analysis of microorganisms on a subdivided highly porous, inorganic chip manufactured from Anopore. *Appl. Environ. Microbiol*., 2005, **71**, 8978–8981.

Ingham CJ, van den Ende M, Wever PC, Schneeberger PM. Rapid antibiotic sensitivity testing and trimethoprim-mediated filamentation of clinical isolates of the *Enterobacteriaceae* assayed on a novel porous culture support. *J. Med. Microbiol*., 2006, **55**, 1511–1519.

Ishibashi T, Hoshino Y, Kaji H, Kanzaki M, Sato M, Nishizawa M. Localized electrical stimulation to C_2C_{12} myotubes cultured on a porous membrane-based substrate. *Biomed. Microdevices*, 2009, **11**(2), 413–419.

Jernshøj KD, Hassing S, Hansen RS, Krohne-Nielsen P. Experimental study on polarized surface enhanced resonance Raman scattering of rhodamine 6G adsorbed on porous Al_2O_3 substrates. *J. Chem. Phys*., 2011, **135**(12), 124514.

Kaji H, Ishibashi T, Nagamine K, Kanzaki M, Nishizawa M. Electrically induced contraction of C_2C_{12} myotubes cultured on a porous membrane-based substrate with muscle tissue-like stiffness. *Biomaterials*, 2010, **31**(27), 6981–6986.

Ke XB, Shao RF, Zhu HY, Yuan Y, Yang DJ, Ratinac KR, Gao XP. Ceramic membranes for separation of proteins and DNA through in situ growth of alumina nanofibres inside porous substrates. *Chem. Commun.* (*Camb*)., 2009, **10**, 1264–1266.

Kepplinger C, Höfer I, Steinem C. Impedance analysis of valinomycin activity in nano-BLMs. *Chem. Phys. Lipids*., 2009, **160**(2), 109–113.

Kim DK, Kerman K, Hiep HM, Saito M, Yamamura S, Takamura Y, Kwon YS, Tamiya E. Label-free optical detection of aptamer–protein interactions using gold-capped oxide nanostructures. *Anal. Biochem*., 2008, **379**(1), 1–7.

Kim DK, Kerman K, Saito M, Sathuluri RR, Endo T, Yamamura S, Kwon YS, Tamiya E. Label-free DNA biosensor based on localized surface plasmon resonance coupled with interferometry. *Anal. Chem*., 2007, **79**(5), 1855–1864.

Kim Y, Kim C, Choi I, Rengaraj S, Yi J. Arsenic removal using mesoporous alumina prepared via a templating method. *Environ. Sci. Technol*., 2004, **38**(3), 924–931.

Kisner A, Stockmann R, Jansen M, Yegin U, Offenhäusser A, Kubota LT, Mourzina Y. Sensing small neurotransmitter-enzyme interaction with nanoporous gated ion-sensitive field effect transistors. *Biosens. Bioelectron*, 2012, **1**(1), 157–163.

Klein SL, Poland GA. Personalized vaccinology: One size and dose might not fit both sexes. *Vaccine*, 2013, doi:pii: S0264-410X(13)00366-6. 10.1016/j.vaccine.2013.02.070 [Epub ahead of print].

Ko H, Chang S, Tsukruk VV. Porous substrates for label-free molecular level detection of nonresonant organic molecules. *ACS Nano*., 2009, **3**(1), 181–188.

Krasner SW, Weinberg HS, Richardson SD, Pastor SJ, Chinn R, Sclimenti MJ, Onstad GD, Thruston AD, Jr. Occurrence of a new generation of disinfection byproducts. *Environ. Sci. Technol*., 2006, **40**, 7175–7185.

Kumeria T, Kurkuri MD, Diener KR, Parkinson L, Losic D. Label-free reflectometric interference microchip biosensor based on nanoporous alumina for detection of circulating tumour cells. *Biosens. Bioelectron*, 2012, **35**(1), 167–173.

Kumeria T, Losic D. Controlling interferometric properties of nanoporous anodic aluminium oxide. *Nanoscale Res. Lett*., 2012, **7**(1), 88.

Kumeria T, Parkinson L, Losic D. A nanoporous interferometric micro-sensor for biomedical detection of volatile sulphur compounds. *Nanoscale Res. Lett*., 2011, **6**(1), 634.

Kwak DH, Yoo JB, Kim DJ. Drug release behavior from nanoporous anodic aluminum oxide. *J. Nanosci. Nanotechnol*., 2010, **10**(1), 345–348.

Lee W, Ji R, Ross CA, Gösele U, Nielsch K. Wafer-scale Ni imprint stamps for porous alumina membranes based on interference lithography. *Small*, 2006, **2**(8–9), 978–982.

Lee HO, Kim EM, Yu H, Jung JS, Chae WS. Advanced porous gold nanofibers for highly efficient and stable molecular sensing platforms. *Nanotechnology*, 2009, **20**(32), 325604.

Li L, Dong J, Lee R. Preparation of alpha-alumina-supported mesoporous bentonite membranes for reverse osmosis desalination of aqueous solutions. *J. Colloid. Interface Sci*., 2004, **273**(2), 540–546.

Li SJ, Li J, Wang K, Wang C, Xu JJ, Chen HY, Xia XH, Huo Q. A nanochannel array-based electrochemical device for quantitative label-free DNA analysis. *ACS Nano*., 2010, **4**(11), 6417–6424.

Lima AT, Ottosen LM, Heister K, Loch JP. Assessing PAH removal from clayey soil by means of electro-osmosis and electrodialysis. *Sci. Total. Environ*., 2012, 1–6, 435–436.

Liu TY, Chen Y, Wang HH, Huang YL, Chao YC, Tsai KT, Cheng WC, Chuang CY, Tsai YH, Huang CY, Wang DW, Lin CH, Wang JK, Wang YL. Differentiation of bacteria cell wall using Raman scattering enhanced by nanoparticle array. *J. Nanosci. Nanotechnol*., 2012, **12**(6), 5004–5008.

Liu Z, Liu B, Kong J, Deng J. Probing trace phenols based on mediator-free alumina sol–gel-derived tyrosinase biosensor. *Anal. Chem*., 2000, **72**(19), 4707–4712.

Lu CC, Huang YS, Huang JW, Chang CK, Wu SP. A macroporous TiO_2 oxygen sensor fabricated using anodic aluminium oxide as an etching mask. *Sensors (Basel)*., 2010, **10**(1), 670–683.

Lukáts O, Bujtár P, Sándor GK, Barabás J. Porous hydroxyapatite and aluminium-oxide ceramic orbital implant evaluation using CBCT scanning: A method for in vivo porous structure evaluation and monitoring. *J. Int. J. Biomater*., 2012, 764749.

Ma C, Yeung ES. Entrapment of individual DNA molecules and nanoparticles in porous alumina membranes. *Anal. Chem*., 2010, **82**(2), 654–657.

Maguire-Boyle SJ, Liga MV, Li Q, Barron AR. Alumoxane/ferroxane nanoparticles for the removal of viral pathogens: The importance of surface functionality to nanoparticle activity. *Nanoscale*, 2012, **4**(18), 5627–5632.

Mamadou D, Duncan JS, Savage N, Street A, Sustich RC (eds). *Nanotechnology Applications for Clean Water*. Micro and Nano Technologies Series. William Andrew Inc., New York, 2009.

Markovics A, Kovács B. Fabrication of optical chemical ammonia sensors using anodized alumina supports and sol-gel method. *Talanta*, 2013, 109, 101–106.

Matsumoto F, Nishio K, Masuda H. Flow-through-type DNA array based on ideally ordered anodic porous alumina substrate. *Adv. Mater*., 2004, **16**, 23–24.

Milka P, Krest I, Keusgen M. Immobilization of alliinase on porous alumium oxide. *Biotechnol. Bioeng*., 2000, **69**, 344–348.

Mistry AS, Pham QP, Schouten C, Yeh T, Christenson EM, Mikos AG, Jansen JA. In vivo bone biocompatibility and degradation of porous fumarate-based polymer/alumoxane nanocomposites for bone tissue engineering. *J. Biomed. Mater. Res. A*., 2010, **92**(2), 451–462.

Myler S, Collyer SD, Bridge KA, Higson SP. Ultra-thin-polysiloxane-film-composite membranes for the optimisation of amperometric oxidase enzyme electrodes. *Biosens. Bioelectron*, 2002, **17**(1–2), 35–43.

Narayan RJ, Adiga SP, Pellin MJ, Curtiss LA, Hryn AJ, Stafslien S, Chisholm B, Shih C, Shih C, Lin S, Su Y, Jin C, Zhang J, Monteiro-Riviere NA Elam JW. Atomic layer deposition-based functionalization of materials for medical and environmental health applications. *Philos. Trans. R. Soc. A. Math. Phys. Eng. Sci*., 2010, **368**(1917), 2033–2064.

BT, Koh G, Lim HS, Chua AJ, Ng MM, Toh CS. Membrane-based electrochemical nanobiosensor for the detection of virus. *Anal. Chem*., 2009, **81**(17), 7226–7234.

Nguyen BT, Peh AE, Chee CY, Fink K, Chow VT, Ng MM, Toh CS. Electrochemical impedance spectroscopy characterization of nanoporous alumina dengue virus biosensor. *Bioelectrochemistry*, 2012, **88**, 15–21.

Nicolini C, Bragazzi N, Pechkova E. Nanoproteomics enabling personalized nanomedicine. *Adv. Drug. Deliv. Rev*., 2012, **64**(13), 1522–1531.

Norman ES, Bakker K, Cook C. Water governance and the politics of scale: How thinking critically about scale can help create better water governance Discussion Paper No. 1226. Global Water Forum, Canberra, Australia. 2012.

Onda K, LoBuglio J, Bartram J. Global access to safe water: Accounting for water quality and the resulting impact on MDG progress. *Int. J. Environ. Res. Public. Health*, 2012, **9**(3), 880–894.

Ozdemir V, Faraj SA, Knoppers BM, Steering vaccinomics innovations with anticipatory governance and participatory foresight. *OMICS*, 2011, **15**(9), 637–646.

Ozdemir V, Pang T, Knoppers BM, Avard D, Faraj SA, Zawati MH, Kolker E, Vaccines of the 21st century and vaccinomics: data-enabled science meets global health to spark collective action for vaccine innovation. *OMICS*, 2011, **15**(9), 523–527.

Pailler FM, Patricot MC, Giroud-Argoud M, Revol A. Urinary 5 alpha-androstane-3 alpha, 17 beta-diol (5-Ad) determination in healthy children and adults. *J. Endocrinol. Invest.*, 1985, **8**(3), 265–268.

Park N, Kwon B, Kim IS, Cho J. Biofouling potential of various NF membranes with respect to bacteria and their soluble microbial products (SMP): Characterizations, flux decline, and transport parameters. *J. Membr. Sci*., 2005, **258**, 43–54.

Parkinson LG, Giles NL, Adcroft KF, Fear MW, Wood FM, Poinern GE. The potential of nanoporous anodic aluminium oxide membranes to influence skin wound repair. *Tissue Eng. A*., 2009, **15**, 3753–3763.

Peltier S, Cotte E, Gatel D, Herremans L, Cavard J. Nanofiltration improvements of water quality in a large distribution system. *Water Sci. Tech. Water Supply*., 2003, **3**, 193–200.

Piao Y, Kim H. Fabrication of nanostructured materials using porous alumina template and their applications for sensing and electrocatalysis. *J. Nanosci. Nanotechnol*., 2009, **9**(4), 2215–2233.

Poland GA, Kennedy RB, Ovsyannikova IG. Vaccinomics and personalized vaccinology: Is science leading us toward a new path of directed vaccine development and discovery? *PLoS Pathog*., 2011, **7**(12), e1002344.

Pray LA. *Nanotechnology in Food Products: Workshop Summary*. *IOM* (*Institute of Medicine*). Washington DC. The National Academies Press. 2009.

Ramey N, Gupta D, Price K, Husain A, Richard M, Woodward J. Comparison of complication rates of porous anophthalmic orbital implants. *Ophthalmic Surg. Laser. Imaging*., 2011, **42**(5), 434–440.

Saito M, Kitamura A, Murahashi M, Yamanaka K, Hoa le Q, Yamaguchi Y, Tamiya E. Novel gold-capped nanopillars imprinted on a polymer film for highly sensitive plasmonic biosensing. *Anal. Chem*., 2012, **84**(13), 5494–5500.

Salerno M, Caneva-Soumetz F, Pastorino L, Patra N, Diaspro A, Ruggiero C. Adhesion and proliferation of osteoblast-like cells on anodic porous alumina substrates with different morphology. *IEEE Trans. Nanobiosci*., 2013, **12**(2), 106–111.

Salerno M, Giacomelli L, Larosa C. Biomaterials for the programming of cell growth in oral tissues: The possible role of APA. *Bioinformation*, 2011, **5**(7), 291–293.

Savage N, Diallo MS. Nanomaterials and water purification: Opportunities and challenges. *J. Nanoparticle Res*., 2005, **7**, 331–342.

Schlozen A, Mittag D, Rogerson SJ, Cooke BM, Plebanski M. Plasmodium falciparum mediated induction of human CD25hiFoxp3hi CD4 T cells is independent of direct TCR stimulation and requires IL-2, IL-10 and TGFβ. *PLoS Pathog*., 2009, **8**, e1000543.

Shen Y, Jia RP, Luo HQ, Chen XG, Xue DS, Hu ZD. Enhanced photoluminescence of morin-bovine serum albumin on porous anodized aluminum oxide. *Spectroch. Acta. A. Mol. Biomol. Spectrosc*., 2004, **60**(5), 1007–1011.

Smith, A. Opinion: Nanotech—the way forward for clean water? *Filtr. Separat*., 2006, **43**, 32–33.

Song Y, Ju Y, Morita Y, Song G. Effect of the nanostructure of porous alumina on growth behavior of MG63 osteoblast-like cells. *J. Biosci. Bioeng*., 2013 May 2. doi:pii: S1389-1723(13)00128-X. 10.1016/j.jbiosc.2013.04.007 [Epub ahead of print].

Stura E, Bruzzese D, Valerio F, Grasso V, Perlo P, Nicolini C. Anodic porous alumina as mechanical stability enhancer for LDL-cholesterol sensitive electrodes. *Biosens. Bioelectron,* 2007, **23**(5), 655–660.

Swan EE, Popat KC, Grimes CA, Desai TA. Fabrication and evaluation of nanoporous alumina membranes for osteoblast culture. *J. Biomed. Mater. Res. A*., 2005, **72**(3), 288–295.

Takhistov P. Electrochemical synthesis and impedance characterization of nano-patterned biosensor substrate. *Biosens. Bioelectron*, 2004, **19**(11), 1445–1456.

Tan F, Leung PHM, Liu Z-B, et al., A PDMS microfluidic impedance immunosensor for *E. coli* O157:H7 and *Staphylococcus aureus* detection via antibody-immobilized nanoporous membrane, *Sens. Actuators*., 2011, **159**(1), 328–335.

Tanvir S, Morandat S, Frederic N, Adenier H, Pulvin S, Activity of immobilised rat hepatic microsomal CYP2E1 using alumina membrane as a support. *N. Biotechnol*., 2009, **26**(5), 222–228.

Thakur S, Massou S, Benoliel AM, Bongrand P, Hanbucken M, Sengupta K. Depth matters: cells grown on nano-porous anodic alumina respond to pore depth. *Nanotechnology*, 2012, **23**(25), 255101.

Tsou P-H, Sreenivasappa H, Hong S, Yasuike M, Miyamoto H, et al. Rapid antibiotic efficiency screening with aluminium oxide nanoporous membrane filter-chip and optical detection system. *Biosens. Bioelectron*, 2010, **26**, 289–294.

van Hattum H, Martin NI, Ruijtenbeek R, Pieters RJ. Development of a microarray detection method for galectin cancer proteins based on ligand binding. *Anal. Biochem*., 2013, **434**(1), 99–104.

Vasudevan PT, Thakur DS. Soluble and immobilized catalase. Effect of pressure and inhibition on kinetics and deactivation. *Appl. Biochem. Biotechnol*., 1994, **49**(3), 173–189.

Walpole AR, Xia Z, Wilson CW, Triffitt JT, Wilshaw PR. A novel nano-porous alumina biomaterial with potential for loading with bioactive materials. *J. Biomed. Mater. Res. A*., 2009, **90**(1), 46–54.

Weber WJ Jr. Distributed optimal technology networks: A concept and strategy for potable water sustainability. *Water Sci. Technol*., 2002, **46**(6–7), 241–246.

Wei H, Deng S, Huang Q, Nie Y, Wang B, Huang J, Yu G. Regenerable granular carbon nanotubes/alumina hybrid adsorbents for diclofenac sodium and carbamazepine removal from aqueous solution. *Water Res*., 2013. doi:pii: S0043-1354(13)00185-1. 10.1016/j.watres.2012.11.062 [Epub ahead of print].

White, C. Global Water Forum, Canberra, Australia. 2012. Understanding water scarcity: Definitions and measurements Discussion Paper No. 1217.

WHO/UNICEF a (2012), Progress on sanitation and drinking-water: 2012 update. Geneva: World Health Organization Press.

WHO/UNICEF b (May 2012). Global costs and benefits of drinking-water supply and sanitation interventions to reach the MDG target and universal coverage. WHO/HSE/WSH/12.01.

World Bank. 2010. *Global Monitoring Report 2010: The MDGs after the Crisis*. A Joint Report of the Staffs of the World Bank and the International Monetary Fund. Washington DC: The World Bank.

World Bank 2011 Annual Report (July 2012). Strengthen secure sustain. Paper 72028.

Wu Y, de Kievit P, Vahlkamp L, Pijnenburg D, Smit M, Dankers M, Melchers D, Stax M, Boender PJ, Ingham C, Bastiaensen N, de Wijn R, van Alewijk D, van Damme H, Raap AK, Chan AB, van Beuningen R. Quantitative assessment of a novel flow-through porous microarray for the rapid analysis of gene expression profiles. *Nucleic. Acids. Res*., 2004, **32**(15), e123.

Xian Y, Hu Y, Liu F, Xian Y, Feng L, Jin L. Template synthesis of highly ordered Prussian blue array and its application to the glucose biosensing. *Biosens. Bioelectron*, 2007, **22**(12), 2827–2833.

Yamashita T, Kodama S, Kemmei T, Ohto M, Nakayama E, Muramoto T, Yamaguchi A, Teramae N, Takayanagi N. Separation of adenine, adenosine-5′-monophosphate and adenosine-5′-triphosphate by fluidic chip with nanometre-order diameter columns inside porous anodic alumina using an aqueous mobile phase. *Lab. Chip*., 2009, **9**(10), 1337–1339.

Yang Z, Si S, Dai H, Zhang C. Piezoelectric urea biosensor based on immobilization of urease onto nanoporous alumina membranes. *Biosens. Bioelectron*, 2007, **22**(12), 3283–3287.

Yao L, Zheng M, Li H, Ma L, Shen W. High-performance humidity sensors based on high-field anodized porous alumina films. *Nanotechnology*, 2009, **20**(39), 395501.

Yeom SH, Kim OG, Kang BH, Kim KJ, Yuan H, Kwon DH, Kim HR, Kang SW. Highly sensitive nano-porous lattice biosensor based on localized surface plasmon resonance and interference. *Opt. Express*., 2011, **19**(23), 22882–22891.

Yu J, Liu Z, Mak A. Nanoporous membrane-based cell chip for the study of anti-cancer drug effect of retinoic acid with impedence spectroscopy. *Talanta,* 2009, **80**, 189–194.

Zejli H, Hidalgo-Hidalgo de Cisneros JL, Naranjo-Rodriguez I, Liu B, Temsamani KR, Marty JL. Phenol biosensor based on Sonogel-Carbon transducer with tyrosinase alumina sol-gel immobilization. *Anal. Chim. Acta*., 2008, **612**(2), 198–203.

Zeman LJ, Zydney AL. *Microfiltration and Ultrafiltration*. 1996, New York: Marcel Dekker principles and applications.

Zhu Q, de With G, Dortmans LJ, Feenstra F. Subcritical crack growth behavior of Al_2O_3-glass dental composites. *J. Biomed. Mater. Res. B. Appl. Biomater*., 2003, **65**(2), 233–238.

Zigiotti GL, Cavarretta S, Morara M, Nam SM, Ranno S, Pichi F, Lembo A, Lupo S, Nucci P, Meduri A. Standard enucleation with aluminium oxide implant (bioceramic) covered with patient's sclera. *Sci, World J*., 2012, 481584.

Chapter 11

Mass Spectrometry and Protein Array for Environment

Rosanna Spera,[a] Luca Belmonte,[a] Fernanda Festa,[b] Eugenia Pechkova,[a,c] Shaorong Chong,[d] Joshua LaBaer,[b] and Claudio Nicolini[a,b,c]

[a]*Laboratories of Biophysics and Nanobiotechnology, Department of Experimental Medicine, University of Genova, Via Pastore 3, Genova, 16132, Italy*
[b]*Virginia G. Piper Center for Personalized Diagnostics, Biodesign Institute, Arizona State University, Tempe, AZ, USA*
[c]*Nanoworld Institute, Fondazione ELBA Nicolini, Largo Redaelli 7, Pradalunga, Bergamo, Italy*
[d]*New England Biolabs, Inc, 240 County Road, Ipswich, MA 01938, USA*

rosanna.spera@unige.it

This chapter highlights the versatility of mass spectrometry (MS) in environmental applications when coupled with other very innovative proteomic techniques such as the nucleic acid programmable protein arrays (NAPPA) and fluorescence microscope analysis. We summarize the results obtained through the labeled and label-free detection of NAPPA—investigated by different mass spectrometry techniques. Two kinds of NAPPA arrays have been analyzed, GST-NAPPA and SNAP-NAPPA, the latter specifically designed for MS analysis.

Nanobiotechnology in Energy, Environment, and Electronics: Methods and Applications
Edited by Claudio Nicolini

ISBN 978-981-4463-96-6 (Hardcover), 978-981-4463-97-3 (eBook)
www.panstanford.com

11.1 Introduction

11.1.1 Mass Spectrometry for Environment Monitoring

The use of mass spectrometry for the measurement of organic contaminants in environmental samples is one of its largest areas of application. In waste reduction activities and treatment and remediation of contaminated sites, compounds such as polyaromatic hydrocarbons (PAHs), polychlorinated biphenyls (PCBs), dioxins, and volatile organic compounds (VOCs) are measured using routine MS methods. Recent developments in environmental mass spectrometry have focused on the determination of possible new chemical pollutants (e.g., pharmaceuticals, natural and synthetic estrogens and water disinfection by-products) and on the development of new methods for on-line/on-site measurements minimizing environmental pollution, energy and raw material usage (Ketola et al., 2002). Natural and synthetic estrogens and their metabolites have been detected in sewage treatment plant effluents at nanogram/liter concentrations that are similar to those at which both total sex reversal and intersex is induced in fish exposed to these compounds in laboratory experiments. The development of techniques for the analysis of natural and synthetic estrogens in biological fluids (i.e., serum and urine) has been a priority in the biomedical field. However, the recent recognition that estrogen hormones are contaminants in the environment that may contribute to endocrine disruption has focused attention on the need for highly sensitive and specific techniques that are applicable for trace analysis in complex environmental matrices (Croley et al., 2000). In literature, there are several examples of mass spectrometry applications developed for the determination and quantification of steroid hormones in environmental matrices (Croley et al., 2000) and advantages and disadvantages of each method are presented. In particular, analysis by LC/MS-SIM was quick and facile; however, the limits of detection were higher than desirable. GC/MS/MS in a quadrupole ion trap is a proven technique for environmental analysis that reliably gives low limits of quantification. However, the sample preparation for this method was found to be unreliable. The LC/MS/MS method has shown the most promise, but it also requires a sample preparation step before the analysis (Croley et al., 2000).

11.1.2 Protein Array Applications

Traditional environmental monitoring approaches are based on discrete sampling methods followed by laboratory analysis and protein arrays are rapidly becoming established as a powerful means in this field, allowing for proteins detection, monitoring their expression levels, and investigating their interactions and functions (Nagl and Schaeferling, 2005). They are seeing an explosive progress and interest at the moment and have become one of the most active areas emerging in biotechnology today. Protein arrays make possible the parallel multiplex screening of thousands of interactions, encompassing protein–antibody, protein–protein, protein–ligand or protein–drug, enzyme-substrate screening and multianalyte diagnostic assays. Such determinations can be carried out with minimum use of materials while generating large amounts of data. Moreover, since most proteins are made by recombinant methods, there is direct connectivity between results on protein arrays and DNA sequence information. (Jongsma and Litjens, 2006; Keppler, et al., 2003; Sakanyan, 2005; Stoevesandt, 2009).

At present, protein arrays are poised to become a central proteomics technology. Proteomic analysis by 2D gel electrophoresis and mass spectrometry has great advantages but also some limitations; in particular, it may miss low-abundance proteins and is unsuited to diagnostic applications. Since the low-abundance proteins are often those of the greatest interest, there is an acknowledged need for other highly sensitive, specific, and accessible high-throughput technologies for protein detection, quantification and differential expression analysis in health and environment. For this reason, protein arrays are generating enormous interest at the research and biotechnology levels especially if coupled to mass spectrometry as label-free detecting technique. (Koopmann and Blackburn, 2003; Stoevesandt, 2009).

Label-free analysis does not require the use of reporter elements (fluorescent, luminescent, radiometric, or colorimetric) to facilitate measurements. It can provide direct information on analyte binding to array molecules typically in the form of mass addition or depletion from the array surface (Adami et al. 2010; Spera and Nicolini, 2008; Spera et al., 2013a). The unquestionable advantages of such approach with respect to the fluorescence

one are many, in particular the possibility to overcome labeling methods' limitations, particularly in the context of measuring naturally occurring ligands, such as in clinical studies where it is not possible to produce fusion proteins: namely the need to obtain a capture antibody for each analyzed protein, and the concern that a labeling molecule may alter the properties of the query protein (Nicolini et al., 2013; Ray et al., 2010; Spera et al., 2011). Among the label-free detection methods, mass spectrometry has the unique advantage of being able to determine not only the presence but also the identity of a given ligand without the introduction of extraneous molecules (Nedelkov and Nelson, 2003). If the mass spectrometry technology can be successfully introduced into the detection of protein arrays, the need for labeled proteins in protein array would be reduced and the range of applications broadened greatly (Spera et al., 2010).

11.1.2.1 NAPPA

The NAPPA method allows for functional proteins to be synthesized in situ directly from printed cDNAs just in time for assay (Ramachandran et al., 2004, Ramachandran et al., 2005). Building upon the successful use of in vitro translated protein in standard scale applications, Ramachandran et al. substituted the use of purified proteins with the use of cDNAs encoding the target proteins for the microarray. The proteins are translated using a T7-coupled rabbit reticulocyte lysate in vitro transcription-translation (IVTT) system. The addition of a C-terminal tag (glutathione S-transferase, GST, or SNAP) to each protein enabled its capture to the array through an anti-tag antibody printed simultaneously with the expression plasmid (Ramachandran et al., 2004, Spera et al., 2011, Spera et al., 2013) (Fig. 11.1).

Common protein microarrays are generated by separately spotting purified protein on the arrays with linkage chemistries. However, due to the sensitivity and heterogeneity of proteins, it is difficult to store large-scale protein arrays in a functional state for long periods of time. In contrast, DNA is a highly stable molecule capable of long-term storage. Therefore, an interesting concept is to make protein arrays directly from DNA, either co-distributed or pre-arrayed, using cell-free protein expression systems, to create the proteins on the arrays on demand as and when required. Moreover, since the proteins are made and immobilized simultaneously in

a single step on the chip surface, the laborious and often costly processes of separate protein purification and DNA cloning are avoided. Thus, in situ methods address three issues in protein array technology: (i) efficient global protein expression and availability; (ii) functional protein immobilization and purification; and (iii) stability over time. The nucleic acid programmable protein array method is based on this approach; it substituted the use of purified proteins with the use of cDNAs encoding the target proteins for the microarray. The proteins are translated using a IVTT system. The addition of a tag to each protein enabled its capture to the array through an anti-tag antibody printed simultaneously with the expression plasmid (Nicolini et al., 2013; Spera et al., 2011).

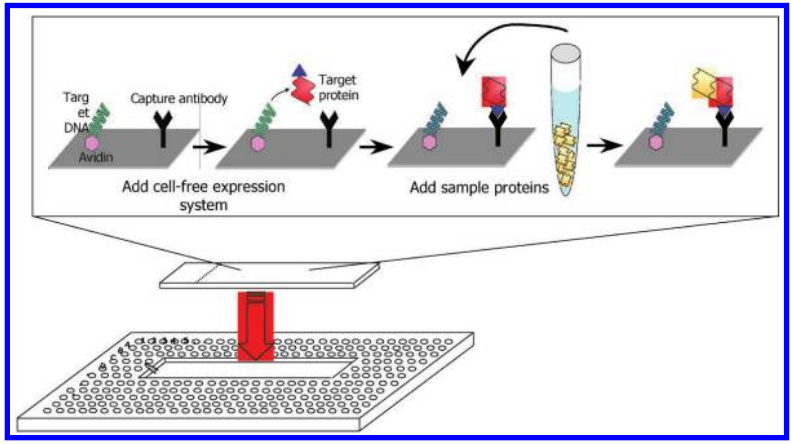

Figure 11.1 (Top) NAPPA chemistry and technology. (Bottom) MALDI-TOF target adapted to carry the NAPPA slide.

One of the challenges in evaluating the mass spectra obtained from NAPPA was the extra-biological material present on the NAPPA together with the target proteins, such as the BSA protein. This also required interpreting the spectra of synthesized proteins in the context of the additional peptide chain, the GST tag, and the anti-GST antibody (Matsuura, et al., 2009). Fortunately, these proteins are present in all features of the array and represent a "common background." In this study, then, we used bioinformatic tools to better interpret the obtained results. Namely, we developed a matching algorithm to identify those peaks corresponding to the "background peaks." All these background NAPPA components,

including capture antibody and amino-PEG thiols, have been chosen after long experimentation (Espina et al., 2004; Ramachandran et al., 2004; Ramachandran et al., 2008) to guarantee the maximum performances of the array in terms of protein yield and stability. Our aim is now to use mass spectrometry to detect proteins in NAPPA applications to medicine as they have already been developed. It will also be conceivable to develop new NAPPA based protocols better suited to mass spectrometry, but these are likely to be slower to develop given the complexities of finding methods for robust protein expression and capture as it applies to thousands of proteins. The current chemistry allows us to validate label-free technology even in clinical settings through the correlation with the tremendous amount of fluorescence data already acquired over the years (LaBaer et al., 2005; Nicolini et al., 2013; Sivozhelezov et al., 2010; Spera et al., 2013).

11.2 Experimental Setup

In our research (Belmonte et al., 2013; Nicolini et al., 2013; Spera and Nicolini 2008; Spera et al., 2010; Spera et al., 2011), we employed mass spectrometry–matrix-assisted laser desorption ionization time-of-flight mass spectrometry (MALDI-TOF MS) and in some cases liquid chromatography–electrospray ionization mass spectrometry (LC-ESI-MS/MS), NAPPA technology, and bioinformatics analysis for the detection of the proteins translated from the cDNA on the surface of NAPPA. We decided to employ both MALDI-TOF and LC-ESI MS since one of the main challenges in evaluating the mass spectra obtained from NAPPA would be the biological material present on the NAPPA together with the target proteins. A chromatographic step, before MS analysis, could reduce the complexity of the sample, thus providing better results.

However, the development of a MALDI-TOF MS–compatible protein microarray is complex since existing methods for forming protein microarrays do not transfer readily into a MALDI target. For use with laser desorption/ionization mass spectrometry, a support having an electroconductive target surface was essential. For this study the NAPPA was produced on a standard microscope glass covered with a thin layer of gold and mounted on an adapter obtained by modifying a standard MS target (Spera et al., 2010; Spera et al., 2011) (Fig. 11.1).

The analyses were performed using three different MALDI-TOF mass spectrometers, a Voyager-DE STR (Applied Biosystems, Framingham, MA, USA) and an Ultraflex III and an Autoflex (Bruker Daltonics, Leipzig, Germany), and a LC-ESI MS using an HPLC Ultimate 3000 (DIONEX, Sunnyvale, CA, USA) connected on line with a linear ion trap (LTQ, ThermoElectron, San Jose, CA, USA) (see Fig. 11.2).

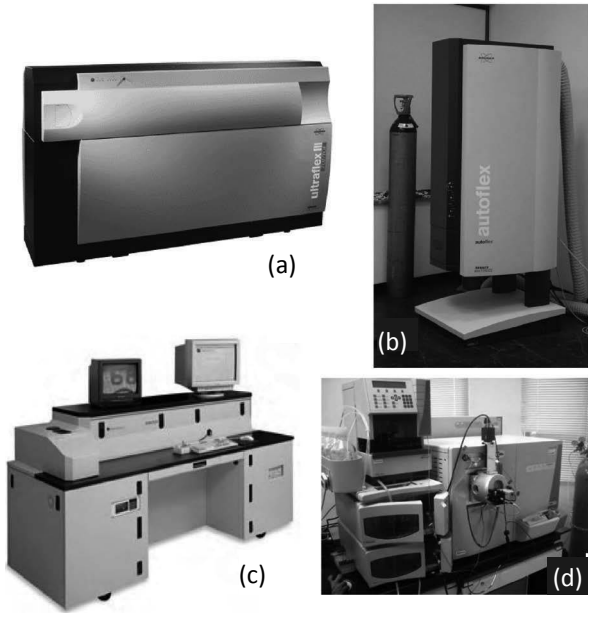

Figure 11.2 NAPPAs were analyzed by LC-ESI and MALDI-TOF MS. We utilized three MALDI-TOF MSs: a Bruker Ultraflex III (a), a Bruker Autoflex (b), and a Voyager (c) MS. LC-ESI MS was composed by an HPLC Ultimate 3000 connected on line with a linear ion trap.

11.2.1 GST-NAPPA

The microarray was produced on a standard size microscope glass slide covered with a thin layer of gold (Fig. 11.3). The gold surface was then functionalized by amino-PEG-thiols generating a homogeneous self-assembled monolayer onto the gold surface.

Target plasmid DNAs encoding C-terminal GST fusion proteins (MW 26 kDa) in pANT7_cGST were immobilized

onto the slide. The spotting of the array was realized in a new special geometry getting protein samples with higher density to obtain an amount of protein appropriate for MS fingerprinting. The array was divided in 12 boxes of 4 × 4 spots (each spot in a box is of the same gene) of 300 microns (space of 750 microns, center to center). The average protein yield is 9 fmol per spot (4–13 fmol, 10th percentile to 90th percentile) (Spera et al., 2011). After expression, then, about 0.15 pmol of proteins are immobilized on each box.

The corresponding 12 samples (from HIP human plasmid collection) spotted on the array surface are reported hereafter.

The first four samples were

(i) P53_Human: gene 1182 bp and corresponding protein of 43.653 kDa;
(ii) Jun_Human: gene of 996 bp and corresponding protein of 35.676 kDa;
(iii) CdK2_Human: gene of 897 bp and corresponding protein of 33.930 kDa;
(iv) CdKN1A_Human: gene of 495 bp and corresponding protein of 18.119 kDa.

The second quartet of samples is composed of the same genes of the first quartet but they are spotted in a blinded order and labeled with the letters A, B, C, and D. The last four samples are two unknown genes (unknown 1 and unknown 2) and two copies of the plasmid vector.

This configuration allowed us to test the capability to identify proteins gradually: The first step was to identify the samples named A, B, C, and D (named "blinded samples") simply matching their experimental mass lists with those of the known four samples (P53, Jun, CdK2, and CdKN1A). Once correctly identified, it was possible to proceed to their peptide mass fingerprint (through data bank search) to further confirm the results. The last step was the identification by peptide mass fingerprint of the unknown proteins.

For the MS analysis, the NAPPA was mounted on an adapter for the mass spectrometer (Fig. 11.1). The adapter was generated by modifying a standard MALDI-TOF MS target with lodging realized on a standard Bruker Scout Target (Bruker Daltonics, Leipzig, Germany) (Spera et al., 2010; Spera et al., 2011).

11.2.1.1 GST-NAPPA expression

To express proteins, we adopted the protocol described here as modified from Ramachandran et al. (2005). For blocking the arrays, slides were absorbed in 30 mL of SuperBlock (in a pipette box) and shaken for 1 h at room temperature. After rinsed with milli-Q water and dried with nitrogen, a HybriWell gasket was applied to the slides. 400 μL of IVT lysate mix was prepared mixing 16 μL of TNT buffer, 8 μL of T7 polymerase, 4 μL of –Met, 4 μL of –Leu, 8 μL of RNaseOUT, 160 μL of DEPC water and 200 μL of reticulocyte lysate. The IVT lysate mix was added to three slides (130 μL per slide): It was spread out to cover all of the area of the array by gently massaging the HybriWell. The slides were placed on a bioassay dish inside the incubator and incubated for 1.5 h at 30°C and then 30 min at 15°C. The HybriWells were removed and each slide was immediately immersed in water, washed for three times and dried with nitrogen.

To confirm protein expression and immobilization, we led parallel experiments by fluorescence microscopy (Sivozhelezov et al., 2010), atomic force microscopy (Nicolini et al., 2012), and nanogravimetry QCM (Adami et al., 2010; Spera et al., 2012, 2013) on the same kind of NAPPA.

To proceed to MALDI-TOF MS analysis, each box (of 16 spots) was overlaid with 2.5 μL of sinapinic acid saturated solution (in 0.1% TFA/acetonitrile (2:1)) and was left to dry.

11.2.2 SNAP NAPPA

Shimizu and coworkers first developed a protein-synthesizing system reconstituted from recombinant tagged protein factors purified to homogeneity. The system was able to produce protein at a rate of about 160 μg/mL/h in a batch mode without the need for any supplementary apparatus. Moreover, omission of a release factor allowed efficient incorporation of an unnatural amino acid using suppressor transfer RNA (tRNA). The system was termed the "protein synthesis using recombinant elements" (PURE) system (Shimizu et al., 2001; Shimizu et al., 2005). The reconstruction of an *E. coli*-based in vitro translation system using protein components, highly purified on an individual basis, showed that 36 enzymes and ribosomes are sufficient to carry out protein translation (Shimizu et al., 2005). These minimal protein components

include the ribosomal proteins; initiation, elongation, and release factors; aminoacyl-tRNA synthetases; and enzymes involved in energy regeneration. In addition, many studies have characterized the properties of such individual proteins in detail, for example, by kinetic analysis and three-dimensional structural determination and to quantify the interactions among the components constituting the system (Matsuura et al., 2005).

The drawback of any extract-based systems is that they often contain nonspecific nucleases and proteases that adversely affect protein synthesis. In addition, the cell extract is like a "black box" in which numerous uncharacterized activities may modify or interfere with the downstream assays (Pechkova et al., 2010). Except for the ribosomes and tRNAs, which are highly purified from *E. coli*, the PURE system reconstitutes the *E. coli* translation machinery with fully recombinant proteins. These include 10 translation factors (IF1, IF2, IF3, EF-Tu, EF-Ts, EF-G, RF1, RF2, RF3, RRF), 20 aminoacyl-tRNA synthetases and several enzymes for energy regeneration (see Table 11.1). In addition, recombinant T7 RNA polymerase is used to couple transcription to translation (Asahara and Chong, 2010; Zhou et al., 2012).

Table 11.1 PURExpress® (Nen England Biolabs) components

Recombinant proteins			
IF1	RF3	GlnRS	AspS
IF2	RRF	TrpRS	AlaRS
IF3	ArgRS	TyrRS	GlyRS
Methionyl-tRNA formyltransferase	CysRS	HisRS	PheRS α2β2
EF-Tu	IleRS	ProRS	Creatine kinase
EF-Ts	LeuRS	ThrRS	Nucleotide diphosphate Kinase
EF-G	MetRS	SerRS	Myokinase
RF1	ValRS	LysRS	Inorganic pyrophos-phatase
RF2	GluRS	AsnRS	T7 RNA polymerase

Ribosomal proteins			
30S ribosomal subunit protein S1	50S ribosomal subunit protein L17	50S ribosomal subunit protein L5	30S ribosomal subunit protein S17
30S ribosomal subunit protein S2	50S ribosomal subunit protein L18	50S ribosomal subunit protein L6	30S ribosomal subunit protein S18
30S ribosomal subunit protein S3	50S ribosomal subunit protein L19	50S ribosomal subunit protein L7/L12	30S ribosomal subunit protein S19
30S ribosomal subunit protein S4	50S ribosomal subunit protein L20	50S ribosomal subunit protein L9	30S ribosomal subunit protein S20
30S ribosomal subunit protein S5	50S ribosomal subunit protein L21	50S ribosomal subunit protein L10	30S ribosomal subunit protein S21
30S ribosomal subunit protein S6	50S ribosomal subunit protein L22	50S ribosomal subunit protein L11	30S ribosomal subunit protein S22
30S ribosomal subunit protein S7	50S ribosomal subunit protein L23	50S ribosomal subunit protein L13	50S ribosomal subunit protein L1
30S ribosomal subunit protein S8	50S ribosomal subunit protein L24	50S ribosomal subunit protein L14	50S ribosomal subunit protein L2
30S ribosomal subunit protein S9	50S ribosomal subunit protein L25	50S ribosomal subunit protein L15	50S ribosomal subunit protein L3
30S ribosomal subunit protein S10	50S ribosomal subunit protein L27	50S ribosomal subunit protein L16	50S ribosomal subunit protein L4
30S ribosomal subunit protein S11	50S ribosomal subunit protein L28	50S ribosomal subunit protein L32	30S ribosomal subunit protein S13
30S ribosomal subunit protein S12	50S ribosomal subunit protein L29	50S ribosomal subunit protein L33	30S ribosomal subunit protein S14

(*Continued*)

Table 11.1 (*Continued*)

Ribosomal proteins			
50S ribosomal subunit protein L35	50S ribosomal subunit protein L30	50S ribosomal subunit protein L34	30S ribosomal subunit protein S15
50S ribosomal subunit protein L36	50S ribosomal subunit protein L31	30S ribosomal subunit protein S16	
Ribosomal RNAs			
23S rRNA	**5S rRNA**	**16S rRNA**	
Bulk tRNAs			
tRNAalaT	tRNAmetT	tRNAglyX	tRNAglnX
tRNAalaU	tRNAmetU	tRNAglyY	tRNAgltT
tRNAalaV	tRNAmetV	tRNAhisR	tRNAgltU
tRNAalaW	tRNAmetW	tRNAileT	tRNAgltV
tRNAalaX	tRNAmetY	tRNAileU	tRNAgltW
tRNAargQ	tRNAmetZ	tRNAileV	tRNAglyT
tRNAargU	tRNApheU	tRNAileX	tRNAtyrU
tRNAargV	tRNApheV	tRNAileY	tRNAtyrV
tRNAargW	tRNAproK	tRNAleuP	tRNAvalT
tRNAargX	tRNAproL	tRNAleuQ	tRNAvalU
tRNAargY	tRNAproM	tRNAleuT	tRNAvalV
tRNAargZ	tRNAsec	tRNAleuU	tRNAvalW
tRNAasnT	tRNAserT	tRNAleuV	tRNAvalY
tRNAasnU	tRNAserU	tRNAleuW	tRNAvalZ
tRNAasnV	tRNAserV	tRNAleuX	tRNAglyU
tRNAasnW	tRNAserW	tRNAleuZ	tRNAglyV
tRNAaspT	tRNAserX	tRNAlysQ	tRNAglyW
tRNAaspU	tRNAthrT	tRNAlysT	tRNAglnV
tRNAaspV	tRNAthrU	tRNAlysV	tRNAglnW
tRNAcysT	tRNAthrV	tRNAlysW	tRNAtrpT
tRNAglnU	tRNAthrW	tRNAlysY	tRNAtyrT
tRNAlysZ	tRNAvalX		

11.2.2.1 SNAP-NAPPA production

For MS analysis, the array printing was realized in a special geometry. The spots of 300 microns were printed in 12 boxes of 7 × 7 or 10 × 10 (spaced of 350 microns, center to center). The spots in a box were of the same gene, and in particular one box apiece was reserved to the sample genes (p53, CDK2, Src-SH2 and PTPNII-SH2), two boxes were printed with master mix (MM) as negative control and reference samples, and six boxes, labeled with the letters from A to F, were printed with the sample genes in an order blinded to the researcher who made MS analysis. This configuration allowed us to test the capability to identify proteins gradually: The first step was to identify the samples named A, B, C, D, E, and F ("blinded samples") matching their experimental mass lists with those of the known samples (p53, CDK2, Src-SH2 and PTPNII-SH2) and of the MM (Fig. 11.3) (Nicolini et al., 2013). Once we correctly identified them, we would proceed to their peptide mass fingerprint (through data bank search) to further confirm the results.

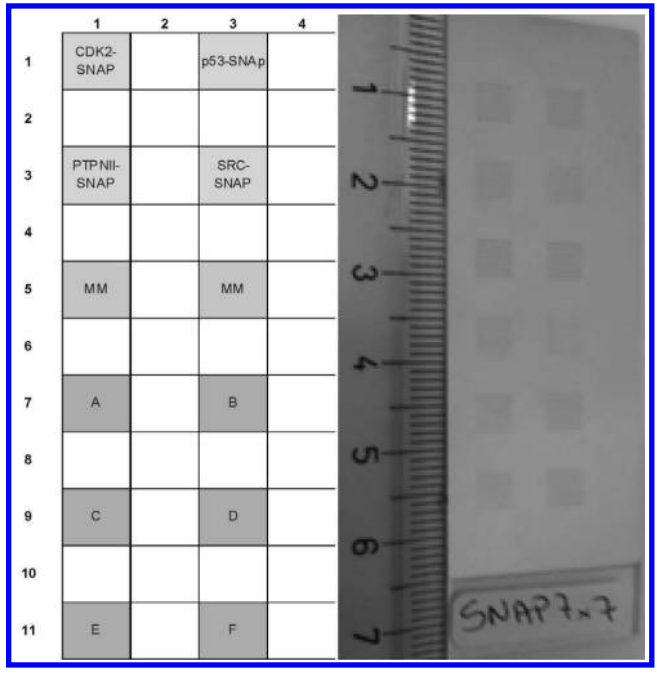

Figure 11.3 Scheme and image of SNAP-NAPPA sample.

11.2.2.2 SNAP-NAPPA expression

The printed slides were expressed using a reconstituted *E. coli* coupled cell-free expression system (*E. coli* IVTT) (Nicolini et al., 2013) or 1-Step Human Coupled IVT (Human IVTT) (Thermo Scientific, Rockford, IL, USA), as described previously (Spera et al., 2013; Festa et al., 2013). Briefly, slides were blocked in SuperBlock (Thermo Scientific, Rockford, IL, USA) for 1 h at room temperature with constant agitation and dried with filtered air. HybriWells were applied on the top of the slide and 160 μL of Human IVTT or *E. coli* IVTT, prepared according to the manufacturers' instructions, was added. Slides were incubated for 90 min at 30°C and 30 min at 15°C, followed by 1 h of blocking/washing with PBSTM (1X PBS supplemented with 0.2% Tween 20 and 5% Milk). The levels of protein expression were assayed with anti-SNAP antibody (New England Biolabs, Ipswich, MA, USA) or anti-p53 antibody (Santa Cruz Biotechnology, Inc.; Santa Cruz, CA, USA), followed by secondary antibodies labeled with cy3 (Jackson Immuno Research Laboratories, Inc., West Grove, PA, USA). All antibodies incubations were performed in a 1:300 dilution in PBSTM at RT, with agitation for 1 h.

11.2.3 Fluorescence Analysis

NAPPA microarrays were employed in several distinct applications including functional assays to detect protein–protein interactions (Miersch and LaBaer, 2011) and biomarker discovery for breast cancer (Anderson et al., 2010), arthritis (Wright et al., 2012) and *Pseudomonas aeruginosa* infection (Montor et al., 2009). Since the proteins on the array are in principle in a native state, these arrays should allow the parallel detection of protein activity (Miersch and LaBaer, 2011; Qiu and LaBaer, 2011).

Cancer patients spontaneously generate autoantibodies (AAb) to tumor-derived proteins. To detect AAb, it has probed a novel high-density custom protein microarray (NAPPA) expressing 4988 candidate tumor antigens with sera from patients with early-stage breast cancer (IBC), and bound IgG was measured. Twenty-eight antigens were identified as potential biomarkers for the early detection of breast cancer (Anderson et al., 2010). To determine whether plasma from patients with Ankylosing spondylitis, an autoimmune rheumatic diseases, contained autoantibodies and,

if so, characterize and quantify this response in comparison to patients with rheumatoid arthritis (RA) and healthy controls, two high-density nucleic acid programmable protein arrays expressing a total of 3498 proteins were screened with plasma from patients and healthy controls. Thus, patients with AS show evidence of systemic humoral autoimmunity and multispecific autoantibody production. Nucleic acid programmable protein arrays constitute a powerful tool to study autoimmune diseases (Wright et al., 2012).

Slide images were obtained with PowerScanner (Tecan Group Ltd., Männedorf, Switzerland) and the signal intensity was quantified using the Array-ProAnalyzer 6.3 (Tecan Group Ltd., Männedorf, Switzerland), using the default settings. The median intensity across the quadruplicates was measured and the background was corrected through the subtraction of the median value of the negative control with a matching anti-tag antibody concentration.

11.2.4 MS Analysis of NAPPA

11.2.4.1 MALDI-TOF analysis of GST-NAPPA

The proteins synthesized on the NAPPA were trypsin digested: each box (of 16 spots) was overlaid with 5 μL of 0.01 mg/mL trypsin in 25 mM ammonium bicarbonate (pH 7.5) and incubated in a humid chamber at 37°C for 4 h. At the end of the digestion, the solvent was evaporated under nitrogen. Each box was, then, overlaid with 2.5 μL of a-cyano-4-hydroxy-cinnamic acid (HCCA) saturated solution (in 0.1% TFA/acetonitrile (2:1)) and let it dry.

Analysis of native proteins was performed in the linear detection mode, whereas tryptic digests were analyzed in reflectron mode for increased mass accuracy; the resulting mass accuracy for protein was <300 ppm and for peptides was <20 ppm. MALDI-TOF mass spectra were acquired with a pulsed nitrogen laser (337 nm) in positive ion mode.

Peaks in the mass range of m/z 600–2300 were used for the peptide mass fingerprint. For data bank search, we utilized Biotools software v2.2 (Bruker Daltonics, Leipzig, Germany), which allowed an automated protein identification via library search with fully integrated MASCOT software v2.2.06 (Matrix Sciences, Ltd., London, UK), which searches against the Swiss-Prot/TrEMBL database. Identification was accepted based on significant MASCOT Mowse scores ($p < 0.05$).

11.2.4.2 MALDI-TOF analysis of SNAP-NAPPA

The analyses were performed using two different MALDI-TOF mass spectrometers: an Ultraflex III (Bruker Daltonics, Leipzig, Germany) and a Voyager-DE STR (Applied Biosystems, Framingham, MA, USA) TOF MS.

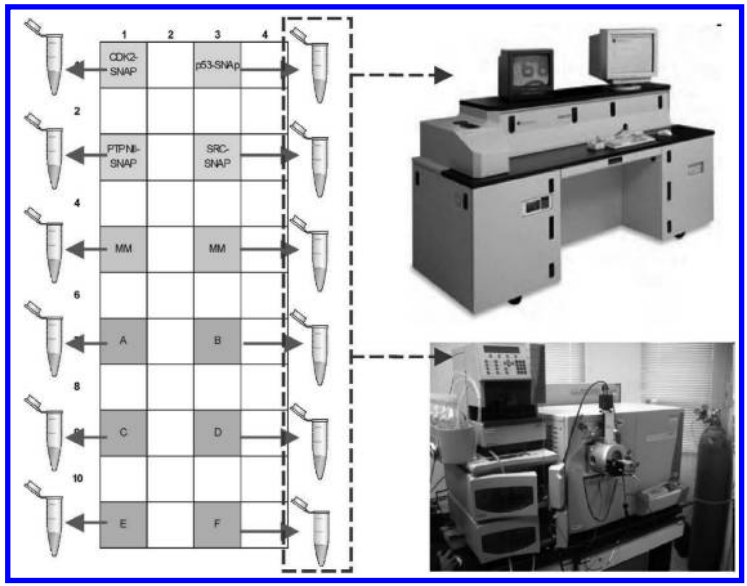

Figure 11.4 For LC-ESI MS and Voyager MS analysis the sample were collected at the end of trypsin digestion and stored liquid in Eppendorf tubes since the analysis.

For MS analysis, after the incubation, the slides were washed with PBS NaCl (1X PBS with 500 mM NaCl) three times and dried with nitrogen. The proteins synthesized on the NAPPA were trypsin digested: Each box (of 16 spots) was overlaid with 5 μL of 0.01 mg/mL trypsin (Trypsin Gold, Mass Spectrometry Grade, Promega, Madison, WI, USA) in 25 mM ammonium bicarbonate (pH 7.5) and incubated in a humid chamber at 37°C for 4 h (Koopmann and Blackburn, 2003; Finnskog et al., 2004). At the end of the digestion the tryptic digested solutions were collected and stored in Eppendorf tubes at 4°C for the LC-ESI and Voyager MALDI-TOF MS analysis or the solvent was let evaporating at RT and the slides were stored at 4°C for Ultraflex III MALDI-TOF MS analysis. For Voyager MALDI-TOF MS analysis, 1 μL of sample (collected from

the array surface) was spotted on a standard Voyager target. Then 1 μL of HCCA (Bruker Daltonics Leipzig, Germany) saturated solution in 0.1% trifluoroacetic acid/acetonitrile (2:1) (matrix solution) was added and finally this solution was let to dry (Fig. 11.4).

The instrument operated in the delayed extraction mode. Peptides were measured in the mass range from 750 to 4000 Da. Proteins were unambiguously identified by searching a comprehensive non-redundant protein database (Swiss Prot) using the program Mascot (www.matrixscience.com).

For Ultraflex III MALDI-TOF MS each box was overlaid with 2.5 μL of HCCA matrix solution and let it dry. To calibrate the spectra, we spotted on the array surface 1 μL of peptide calibration standard solution (Bruker Daltonics, Leipzig, Germany) in HCCA matrix solution (Fig. 11.5).

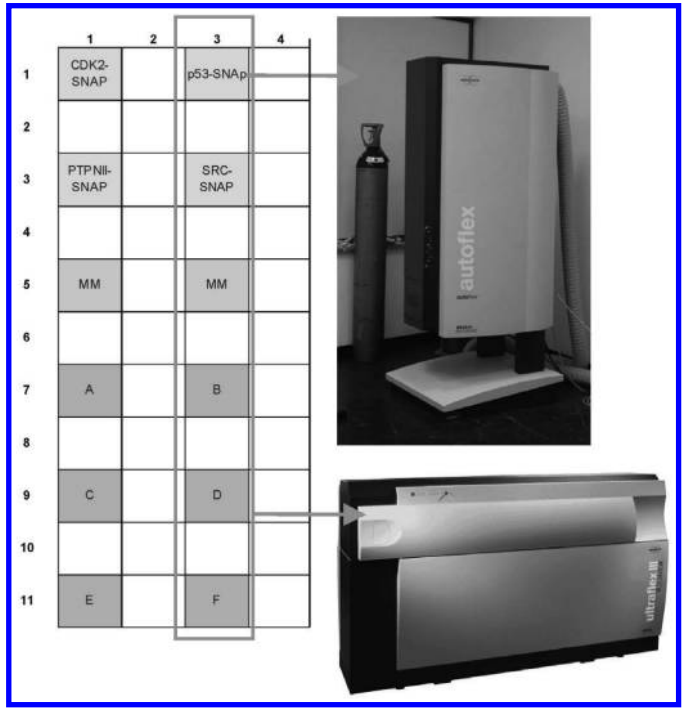

Figure 11.5 For Bruker MS (either Ultraflex or Autoflex) analysis the matrix was mixed with the trypsin digested fragment solutions directly on the slides and let to dry before the analysis.

The MALDI-TOF measures were performed in reflectron mode; the resulting mass accuracy for protein was <50 ppm. MALDI-TOF mass spectra were acquired with a pulsed nitrogen laser (337 nm) in positive ion mode. The algorithm used for spectrum annotation was SNAP (Sophisticated Numerical Annotation Procedure).

Peaks in the mass range of m/z 600–3000 were used for the peptide mass fingerprint. For MASCOT data bank search, we utilized Biotools software v2.2 (Bruker Daltonics, Leipzig, Germany), which allowed automated protein identification via library search with fully integrated MASCOT software v2.2.06 (Matrix Sciences, Ltd., London, UK), which searches against the Swiss-Prot/TrEMBL database. Identification was accepted based on significant MASCOT Mowse scores ($p < 0.05$).

11.2.4.3 LC-ESI analysis of SNAP-NAPPA

For LC-ESI MS analysis, Peptide mixtures were analyzed by nanoflow reversed-phase liquid chromatography tandem mass spectrometry (RP-LC-MS/MS) using an HPLC Ultimate 3000 (DIONEX, Sunnyvale, CA, USA) connected on line with a linear ion trap (LTQ, ThermoElectron, San Jose, CA). Full MS spectra ranging from m/z 400 to 2000 Da were acquired in the LTQ mass spectrometer operating in a data-dependent mode in which each full MS scan was followed by five MS/MS scans where the five most abundant molecular ions were dynamically selected and fragmented by collision-induced dissociation (CID) using a normalized collision energy of 35%. Target ions already fragmented were dynamically excluded for 30 s. Tandem mass spectra were matched against Swiss Prot database and through SEQUEST algorithm (Ytes et al., 1995) Incorporated in Bioworks software (version 3.3, Thermo Electron) using fully tryptic cleavage constraints with the possibility to have one miss cleavage permitted, static carbamidomethylation on cysteine residues and methionine oxidation as variable modification. Data were searched with 1.5 and 1 Da tolerance, respectively, for precursor and fragment ions.

11.2.5 Matching Algorithm

In order to identify the blinded proteins (A, B, C, D, E, and F), we implemented an algorithm utilizing, initially C language (freely

downloadable compiler from Embarcadero Developer Network) (Spera et al., 2011), and in a second moment an in-house R script (Belmonte et al., 2013; Nicolini et al., 2013). The experimental mass lists of the blinded panel were matched with those of the known samples. The same algorithm was used to subtract MM peaks to the other spectra in order to obtain a mass list containing only the peaks obtained from protein digestion.

The first version of the algorithm was used to identify "background peaks" that are the peaks common—or quasi—to all spots and corresponding not to the synthesized protein but to the other molecules immobilized on the NAPPA, present in all the samples. The first step of the program was to compare all the input peak-lists—within a given tolerance threshold—identify the background peaks, save them in an output file and delete them from each peak-list.

Then the program carried out the proper matching between known samples and blinded samples assessing the number of matched peaks—within a given tolerance threshold.

To match two mass lists, the algorithm calculated for each couple of masses the value: $D = |m_{\text{known}} - m_{\text{unknown}}|$; and assumes equal two masses for which $\Delta D \leq 1$. For each mass list—after the subtractions of the background peaks—the algorithm calculated the percentage of matched peaks as:

Percentage of matched peaks for two mass lists = (number of matching masses/number of peaks in the unknown sample mass list) × 100.

The final identification was made considering the match with the best score (Spera et al., 2011).

11.3 Results

11.3.1 Fluorescence

11.3.1.1 SNAP NAPPA

Slide images were obtained with PowerScanner (Tecan Group Ltd., Männedorf, Switzerland) and the signal intensity was quantified using the Array-ProAnalyzer 6.3 (Tecan Group Ltd., Männedorf, Switzerland), using the default settings. The median intensity across the quadruplicates was measured and the background

was corrected through the subtraction of the median value of the negative control with a matching SNAP concentration.

SNAP-NAPPA has been preliminary analyzed by fluorescence microscopy. SNAP-cDNAs were spotted on microscope glass using increasing SNAP concentrations. Proteins were synthesized by an IVTT system extracted from human cells (1-Step Human Coupled IVT, HCIVT, Thermo Scientific) and by *E. coli* IVTT.

Figure 11.6 reports the images of three SNAP-NAPPA slides after proteins expression fluorescence acquired. Two slides were expressed with HCIVT and a third with *E. coli* IVTT; the level of protein displayed on the array was measured using, respectively, anti-SNAP antibody or anti –p53 antibody, followed by a cy3-labeled secondary antibody.

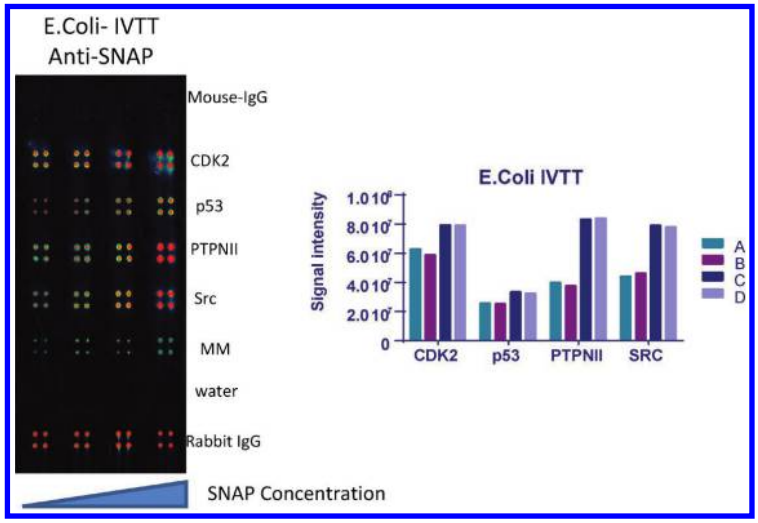

Figure 11.6 Fluorescence analysis of SNAP-NAPPA array.

The results obtained confirmed the proper protein expression and capture on the array surface and demonstrated that *E. coli* IVTT systems ensured a higher protein yield respect HCIVT (Nicolini et al., 2013).

11.3.1.2 Traditional NAPPA

NAPPA is well suited to the detection of protein–protein interactions because both the target proteins (bound to the array) and the query

protein (used to probe the array) can be transcribed and translated in the same extract. As validation, the query protein Jun was tagged with a hemagglutinin (HA) epitope and coexpressed with the target proteins (Fig. 11.7b) (Ramachandran et al., 2008).

The interaction was visualized with an antibody to HA, which revealed that Jun query protein bound to the Fos target. To determine if binding selectivity is preserved, we tested the Cdk inhibitor p16, which binds selectively to Cdk4 and Cdk6 but not the closely related Cdk2. As shown in Fig. 11.7c, this specificity was recapitulated with NAPPA (Ramachandran et al., 2008).

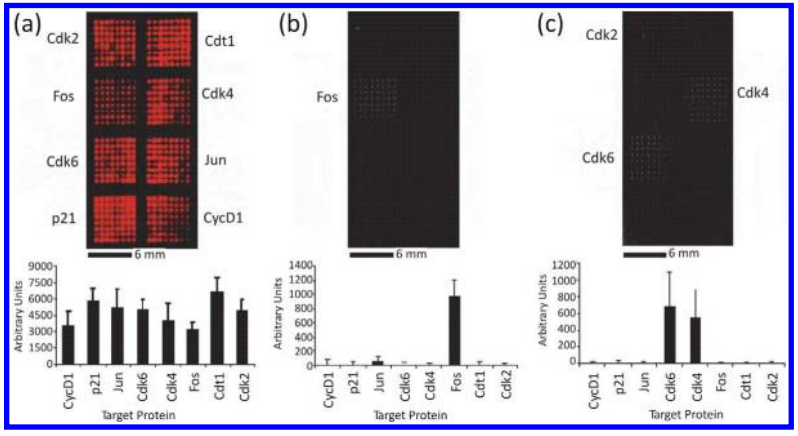

Figure 11.7 Expression of target proteins and detection of protein interactions on a NAPPA microarray format.

Sequence-verified human genes for 29 proteins involved in DNA replication initiation (in addition to Fos and Jun as positive controls) were immobilized and expressed on NAPPA (Fig. 11.7a). Signals were readily detected for all of the target proteins, showed high reproducibility between duplicates, and ranged from 270 pg (4 fmol) to 2600 pg (29 fmol), a sevenfold range that falls well within the range observed in protein-spotting protein microarrays (10 to 950 pg (8)). Each of the 29 DNA replication proteins was used as a query to probe a pair of duplicate arrays to generate a 29 × 29 protein interaction matrix. Examples of the interaction data are shown in Fig. 11.7b,c (Ramachandran et al., 2008).

11.3.2 Mass Spectrometry Analysis

11.3.2.1 GST-NAPPA Intact protein analysis and blinded samples identification

The analysis of the mass spectra of the intact proteins gave us some fundamental information about the contamination of the samples and the complexity of the analysis after trypsin digestion. These spectra, in fact, are practically identical among the different samples because in the samples analyzed many protein species inherent to the NAPPA procedures are abundant. For example, in the spectrum of Fig. 11.8 the 65 kDa protein could be either BSA, for which molecular weights from 65 to 69 kDa were reported, or the one of the subunits of the eif2b translation factor present in rabbit reticulocyte lysate. Both proteins are always used in the NAPPA technology.

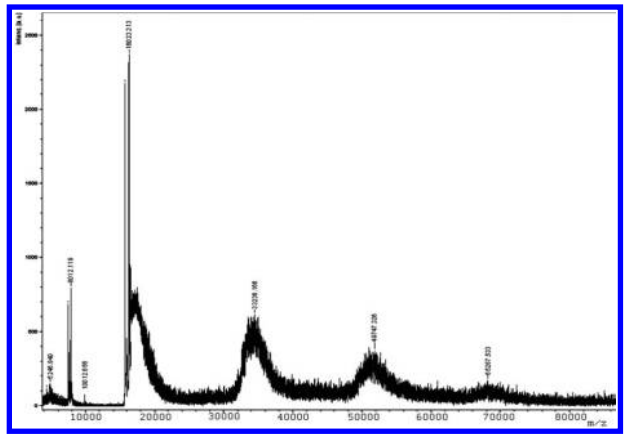

Figure 11.8 MALDI TOF spectra of P53 NAPPA spot after protein synthesis (no digestion), 5–90 kDa ranges. The peak at m/z = 65.3 kDa peak could correspond either to bovine serum albumin, or to one of the subunits of the eif2b translation factor present in rabbit reticulocyte lysate.

In order to identify the blinded samples (A, B, C, and D) we matched their experimental mass lists with those of the known samples (P53, Jun, CdK2, CdKN1A). Considering that the correct match are those with the highest percentage the results, we expect the following: *A* = P53, *B* = CdK2, *C* = Jun, *D* = CdKN1A (Spera et al., 2011).

11.3.2.2 GST-NAPPA fingerprinting results

We submitted the experimental mass list obtained for the known samples to a data bank search. The MASCOT searching engine uses the Mowse scoring algorithm to determine the significance of the peptide fingerprint result. Protein score is –10*Log(P), where P is the probability that the observed match is a random event. Protein scores greater than 64 are significant ($p < 0.05$). In our analysis, the scores obtained did not appear to have a highly significant identification, mostly due to the large number of masses not identified.

We have been able to match the four proteins known to be spotted, even in the blinded order, with an optimum probability, but to identify our single protein spectra in the overall protein spectra present on the Internet databases turned out to be a difficult task. In our spectra, there are too many peaks that do not correspond to any theoretical peak in comparison to the few peaks matching the theoretical ones (Spera et al., 2011).

The proteins immobilized on the NAPPA are synthesized as chimera with a GST tag that could also contribute to the difficulty in matching spectra with databases that are based on tryptic digests of natural proteins. It was then useful to consider strategies that compensate for this (Ponomarenko et al., 2008; Spera et al., 2011).

We have, then, modified the sequence of our proteins, adding the tag sequence (obtained from the sequence of the vector pANT7_cGST). We used this modified sequence to perform a new fingerprint: the theoretical mass lists of the chimeras P53, Jun, CdK2, and CdKN1A proteins plus the GST tag—after trypsin digestion by means of the software SequenceEditor included into the Biotools package. We matched the experimental mass lists by our algorithm (considering the masses in the range 360–2300 Da) with these theoretical mass lists. We calculated the percentage of experimental masses identified (before and after the background peaks subtraction) and the sequence coverage—calculated as number of identified residues to number of protein residues ratio. The percentages of experimental masses that match the theoretical mass lists of the native protein and of the chimera proteins made evident that accounting for the tag improved the results (Spera et al., 2011).

The percentage of experimental masses matching the theoretical mass list increased from values between 6% and 23%

(after the background subtraction) to values between 16% and 36% (after the background subtraction). For these chimera proteins, searches of the standard databank cannot estimate the quality of the identifications, so we calculated the percentage of sequence coverage—obtained as the ratio between the number of residues matched and the total number of protein residues. We obtained percentages between 20% and 40%, which may be satisfactory if we consider the large number of different molecular species analyzed simultaneously and the effect of ions suppression that occurs in these cases (Spera et al., 2011; Xu and Freitas, 2007).

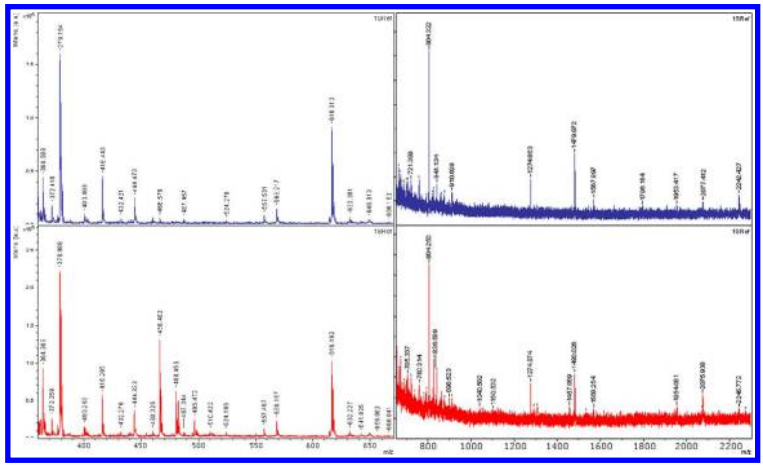

Figure 11.9 MALDI-TOF spectra of GST-NAPPA samples, in red B and in blue CDK2.

11.3.2.3 SNAP-NAPPA fingerprinting results

We submitted the experimental mass list obtained for the known samples (p53, CDK2, Src-SH2 and PTPNII-SH2) obtained by both MALTI-TOF mass spectrometers to MASCOT data bank search to verify if it is possible to identify a protein synthesized on a NAPPA spot through the standard process of fingerprinting. The results obtained by both the MALDI-TOF mass spectrometers were the same; the only proteins identified with a significant score were found matching the results in Bacteria database (Nicolini et al., 2013).

Also, in this case, the problems may be caused from the tags, which now are SNAP and FLAG tags; this could also contribute to the difficulty in matching spectra with databases.

We modified the sequence of sample proteins present in the reference database, adding the tags. We used these modified sequences to perform a new fingerprint: The theoretical mass lists of the chimeras after in silico trypsin digestion were obtained by means of the software Sequence Editor. We matched the experimental mass lists with these theoretical mass lists. The sequence coverage was calculated as the ratio between the number of residues matched and the total number of protein residues. For SRC-SH2 and PTPNII-SH2 samples, no fragments were identified, whereas for CDK2, we obtained a percentage of sequence coverage of 22% and of 6% for p53 (Nicolini et al., 2013).

11.3.2.4 LC-ESI MS

The matching of the results in human database allowed us to identify with a good score only albumin (ALBU_HUMAN Serum albumin), presumably due to some peptides that are common also to BSA. No other human proteins were identified. We performed a search also against bacterial database; for all the samples, we identified approximately the same proteins (from NAPPA chemistry and from bacterial lysate).

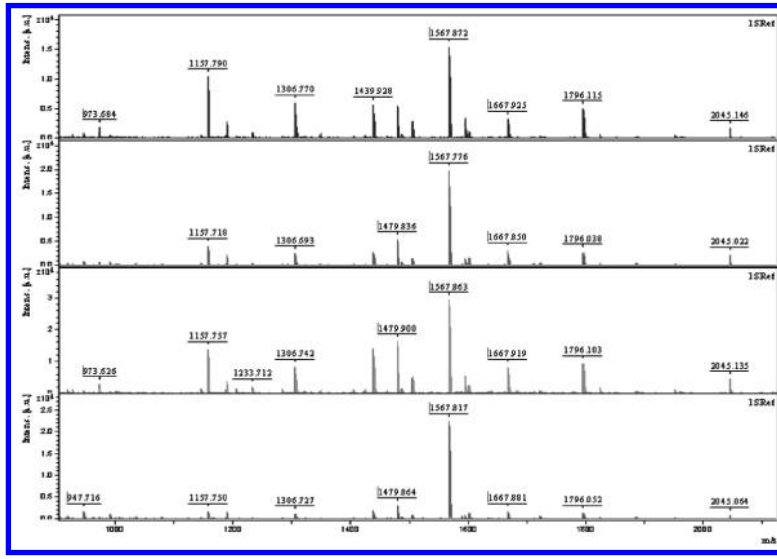

Figure 11.10 MALDI-TOF spectra of SNAP-NAPPA samples, from the bottom Src-SH2, PTPNII-SH2, p53 and CDK2.

11.3.2.5 SPADS matching algorithm

Cluster analysis based on different specimen of same proteins was performed using two different software tools. The former tool is here first introduced as SPADS, and it is able to perform preprocessing on spectra data. The latter is a K Means clustering software by Peeples (Peeples, 2011) used to cluster previously preprocessed data. It is very hard to discriminate different kinds of proteins, and this is mainly due to spectra expression of master mix. Noise reduction, i.e., alignment and subtraction of master mix spectrum from each protein spectra; results are improved, as shown in Table 11.2. The master mix effect is to spread out on the chart protein spectra, forming different distinct clusters but with a minor selection power (Belmonte et al., 2013; Nicolini et al., 2013).

Table 11.2 Cluster assignment for each known protein sample on a specimen of 23 spectra in the ROI 1000/1200 with a binning window of 500 m/z

Cluster number	1	2	3	4
P53 (p)	2	3	1	—
PTPN11-SH2 (pt)	3	—	—	3
Src-SH2 (s)	3	1	1	—
CDK2 (c)	—	1	2	3

Note: Statistics are based on the SpADS results coupled with K Means clustering given in Fig. 11.9.

Table 11.3 Cluster assignment for each known protein sample on a specimen of 56 spectra

Cluster number	1	2	3	4
P53 (p)	1	1	4 (66%)	—
PTPN11-SH2 (pt)	3	3 (50%)	—	—
Src-SH2 (s)	—	3	1	1 (20%)
CDK2 (c)	2 (33%)	1	3	—
A = Src–SH2*	1	2	—	3 (50%)
B = CDK2	2 (40%)	2	—	1
C = p53	4	—	1(20%)	—

D = PTPN11-SH2	1	2 (20%)	2	—
E = PTPN11-SH2	—	4 (100%)	—	—
F = PTPN11-SH2	2	4 (50)	1	1

Note: Statistics are based on the SpADS results coupled with K Means clustering given in Fig. 11.10. Assignment of clusters by human interpretation of cluster results. Highlighted with *: Striking recognition.

The results obtained through the bioinformatic processing, although not striking, it is a good result if associated with the results of the database search. In the former case (i.e., of the dataset "only proteins"), thanks to an ad hoc ROI algorithm it is possible to divide the dataset to obtain an almost absolute identification of proteins. Indeed, while using the data obtained without a well-suited ROI there is no way to uniquely identify the couple protein-cluster, whereas in the second case, it is possible to associate three of the proteins to three cluster and thus belonging to these latter (Belmonte et al., 2013; Nicolini et al., 2013).

11.3.2.6 Background databank

One of the main reasons why we choose PURE Express as the IVTT system is that each component is well characterized. For this reason, we are reconstructing a theoretical background database by digesting in silico each lysate molecules. Hereafter an example.

Table 11.4 Theoretical mass list of 50S ribosomal protein L25

Mass (Da)	Peptide
1461.055	K
1490.51	M
1741.117	R
2031.27	GK
2871.957	LR
3021.954	GVK
3401.859	GHK
3562.424	LPK
3621.802	TDK
3742.165	VEK

(*Continued*)

Table 11.4 (*Continued*)

Mass (Da)	Peptide
3742.165	VEK
3892.023	GASR
4432.969	RLR
5272.34	HEDK
5453.034	GASRR
5472.966	TDKGK
5482.377	DMQR
5743.187	GKGASR
5771.868	DADEE
6963.919	VEKGHK
7084.283	HQAILK
7684.283	HPYKPK
7964.192	LRHEDK
8365.232	KHQAILK
9865.648	GVELVELTK
10285.4	LTHLDFQR
12386.55	HQAILKDMQR
12986.55	DMQRHPYKPK
13247.97	LPKGVELVELTK
13757.1	AELDFNIQATVR
13847.46	LTHLDFQRVEK
15067.5	MAELDFNIQATVR
15937.75	GEDHDQAVVSITAPR
17198.79	AELDFNIQATVRTDK
17789.58	R.HPYKPKLTHLDFQR.V
18479.89	LHTNLPLHFLNETTAK
18509.2	MAELDFNIQATVRTDK
19499.81	GEDHDQAVVSITAPRVEK
20158.81	EETEEDTVAPGDVPAENSK
21321.74	LHTNLPLHFLNETTAKGVK
21691.43	EEGGVVVHHVNDVEITVLPK
21701.65	GHKLHTNLPLHFLNETTAK

21751.69	VPAILYGGQGEPIALALDHNK
23720.87	R.VEKEETEEDTVAPGDVPAENSK.D
24533.28	GVKEEGGVVVHHVNDVEITVLPK
25621.74	VNNMADYEAFYSHIVTLEFDGK
25623.29	GVELVELTKGEDHDQAVVSITAPR
25750.57	EETEEDTVAPGDVPAENSKDADEE
26843.92	HEDKVPAILYGGQGEPIALALDHNK
26902.69	VNNMADYEAFYSHIVTLEFDGKK
27974.27	DLPEYLEVDIAELSVGDTIHLTDLK
31356.59	DLPEYLEVDIAELSVGDTIHLTDLKLPK
47193.32	VPAILYGGQGEPIALALDHNKVNNMADYEAFYSHIVTLEFDGK
49485.6	EEGGVVVHHVNDVEITVLPKDLPEYLEVDIAELSVGDTIHLTDLK

11.4 Discussion

Label-free detection of NAPPA microarrays is an arduous task because the NAPPA technology involves a lot of molecules, many of which may end up deposited on the NAPPA slides together with the target proteins. We revised our feasibility studies of a label-free detection method using MALDI-TOF MS for NAPPA analysis. Some issues were resolved such as obtaining arrays with a particular geometry to make the query protein amount sufficient for the MS analysis.

As expected, the MS analysis after trypsin digestion produced complex spectra. There were background peaks to be removed and other signals to be interpreted. For GST-NAPPA with the aid of a matching algorithm, we subtracted the background signals and we identified the four test samples by matching them to the first four known samples, with a high probability but not absolute certainty. Using tryptic fingerprinting, we obtain many peaks that are recognized neither as background nor as the analyzed protein. Reasons for this are not clear though they can be thought to result from either interactions of analyzed proteins with other proteins present in the NAPPA slides (for example, antibodies), or from the expression mix itself. For example, if we want to identify samples by peptide mass fingerprint, the issue is more complex, leaving room for improvement.

We obtained better results considering the matching between the experimental mass lists and the theoretical mass lists obtained from the in silico digestion of the chimera proteins formed by the native proteins plus the GST tag. For GST-NAPPA the percentage of experimental masses matching the theoretical mass list increased from values between 6% and 23% to values between 16% and 36%. For these chimera proteins, searches of the standard databank cannot estimate the quality of the identifications; so we calculated the percentage of sequence coverage. We obtained percentages between 20% and 40%, which may be satisfactory if we consider the large number of different molecular species analyzed simultaneously and the effect of ions suppression that occurs in these cases (Spera et al., 2011).

The preparation of NAPPA slides surface involves large amounts of biological material, especially proteins. These include primarily the complex of BSA and cross-linker, and especially the antiGST antibody and the GST tag itself, which is fused with the target proteins. In addition, IVTT inherent in the NAPPA technology includes many proteins some of which could remain on the NAPPA slides even after washing. For transcription, those could be subunits of the T7 RNA polymerase and for translation, those include subunits of the ribosome, translation factors, and chaperone proteins. All this material could generate series of background signals more or less common to all the spectra.

We have then analyzed SNAP-NAPPA, an improved version of GST-NAPPA, expressed with an IVTT system reconstituted from the purified components necessary for *E. coli* translation, and analyzed by MALDI-TOF and LC-ESI-MS. Again, the results were very complex and a bioinformatics tool has been developed ad hoc to their analysis.

The fluorescence analysis carried out as preliminary test demonstrated not only the proper SNAP-NAPPA behavior but also that *E. coli* IVTT systems ensured higher protein yield than HCIVT.

The samples were printed in 12 boxes: four for sample genes (p53, CDK2, SH2-Src and SH2-PTPN11), two for negative controls (MM) and reference samples, and six boxes for blinded samples (sample genes in an order blinded to the researcher who made MS analysis).

Also, in this case, we conducted two parallel identifications: the first through the matching algorithm comparing blinded and

known samples experimental mass lists and the second submitting experimental mass lists to databank search.

The databank search of samples experimental mass lists obtained by MALDI-TOF or LC-ESI-MS provided the identification, with significative scores, of molecules of MM or *E. coli* lysate. Then different strategies have been addressed to overcome the presence of these "background" molecules that represented the main obstacle to the samples identification. Experimental and theoretical master mix plus *E. coli* lysate mass lists have been subtracted to samples experimental mass lists and the results have been submitted to MASCOT databank search. Unfortunately, neither strategy gave statistically significative results.

Considering that samples were synthesized with a SNAP tag, which could also contribute to the difficulty in matching spectra, we examined the proteins modified sequences to perform a new fingerprint.

The results obtained seem worse if compared with those relative to the GST-NAPPA. Considering the chimeras sequences, we obtained for GST-NAPPA percentages of coverage between 20% and 40%. On the contrary, for SNAP-NAPPA, no unknown protein identification has been obtained. Moreover, the coverage percentages obtained considering chimeras have been 0% for SRC-SH2 and PTPN11-SH2 samples and the maximum obtained was 22% for CDK2 sample (Nicolini et al., 2013; Spera et al., 2011). Coupling SpADS to K Means Cluster algorithm allows to identify some proteins and partially fixed the trouble of the blinded proteins, although not every protein. This deficiency is most likely due to a lack of sufficient number of spectra for each sample that do not admit to conduct reliable statistic; a conservative rule of thumb would require at least hundred times more MS spectra of the unknown protein (a minimum of hundred rather than 1 as was in the limiting worst case and rather than 8 in the best case) (Nicolini et al., 2013; Spera et al., 2011). The results obtained by bioinformatics, however, are encouraging even with a low number of spectra because they partially fix the trouble and show the way to go in future development of this emerging technique. Finally, the authors consider that the elements of the specimen were chosen for human intervention. Therefore, there is the need to implement heuristics to allow determining a priori which data are suitable for the purposes of processing.

11.5 Conclusions

By running a test in which the known query proteins following in blinded order were successfully identified, we have shown that mass spectrometry based label-free detection of NAPPA slides is possible. We have shown that the method can be improved by introducing special enzymatic preprocessing of NAPPA slides, and by performing in-depth bioinformatic studies linking the unmatched peaks to the proteins inherent in the NAPPA technology other than the target and query proteins. On the whole, considering the abundance of protein material different from target and query protein, the results are very encouraging, showing the potential to couple the NAPPA technology with the MALDI-TOF MS facility for a label-free investigation of protein samples.

The technique needs more effort to improve the protocols in order to reduce the abundance of background species, and also, the bioinformatic analysis can clarify the emerging issues by better interpreting the MS spectra.

We can then conservatively conclude that the chemistry and the algorithms progressively implemented prove for the first time that mass spectrometry facilitates the characterization of proteins immobilized on nucleic acid programmable protein arrays, pointing that with further development, this label-free procedure will be fully reduced to practice in correlation with the fluorescence NAPPA work that has already seen significant clinical applications in the last decade. With more stringent post-synthetic rinsing/purification to reduce the abundance of background protein/peptide ions and more sophisticated bioinformatics algorithms to subtract background species, the results here presented suggest that mass spectrometry serves as an important tool to characterize label-free NAPPA arrays.

References

Adami M., Eggenhöffner R., Sartore M., Hainsworth E., LaBaer J., Nicolini C., *Label Free NAPPA Via Nanogravimetry* (ed. Nicolini C., LaBaer J.), Pan Stanford Series on Nanobiotechnology—Volume 2, Chapter 2, pp. 79–93, 2010, Singapore.

Anderson K. S., Sibani S., Wallstrom G., Qiu J., Mendoza E. A., Raphael J., Hainsworth E., Montor W. R., Wong J., Park J. G., Lokko N., Logvinenko

T., Ramachandran N., Godwin A. K., Marks J., Engstrom P., Labaer J., Protein microarray signature of autoantibody biomarkers for the early detection of breast cancer. *J. Proteome Res.,* 2011, **10**(1), 85–96.

Asahara, H., Chong, S., In vitro genetic reconstruction of bacterial transcription initiation by coupled synthesis and detection of RNA polymerase holoenzyme. *Nucleic Acids Res.,* 2010, **38**, e141.

Belmonte L., Spera R., Nicolini C. SpADS: An R package for mass spectrometry data preprocessing before data mining. *J. Comput. Sci. Syst. Biol*., 2013 (in press).

Croley T. R., Hughes R. J., Koenig B. G., Metcalfe C. D., March, R. E., Mass spectrometry applied to the analysis of estrogens in the environment. *Rapid Commun. Mass Spectrom.,* 2000, **14**, 1087–1093.

Espina V., et al., Protein microarray detection strategies: focus on direct detection technologies. *J. Immunol. Methods.,* 2004, **290**(1–2), 121–133.

Festa F., Rollins S. M., Vattem K., Hathaway M., Lorenz P., Mendoza E.A., Yu X., Qiu J., Kilmer G., Jensen P., Webb B., Ryan E. D., LaBaer J., Robust microarray production of freshly expressed proteins in a human milieu. *Proteomics Clin. Appl*., 2013, **7**(5–6), 372–377.

Finnskog D., Ressine A., Laurell T., Marko-Varga G., Integrated protein microchip assay with dual fluorescent and MALDI read-out. *J. Proteome Res.,* 2004, **3**, 988.

Jongsma, M. A., Litjens R.H., Self-assembling protein arrays on DNA chips by auto-labeling fusion proteins with a single DNA address. *Proteomics,* 2006, **6**(9), 2650–2655.

Keppler A., et al., A general method for the covalent labeling of fusion proteins with small molecules in vivo. *Nat. Biotechnol.*, 2003, **21**(1), 86–89.

Ketola R. A., Kotiaho T., Cisper M. E., Allen T. M., Environmental applications of membrane introduction mass spectrometry. *J. Mass Spectrom.,* 2002, **37**, 457–476.

Koopmann J. O., Blackburn J., High affinity capture surface for matrix-assisted laser desorption/ionisation compatible protein microarrays. *Rapid Commun. Mass Spectrom.,* 2003, **17**, 455.

LaBaer J., Ramachandran N., Protein microarrays as tools for functional proteomics. *Curr. Opin. Chem. Biol.,* 2005, 9(1), 14–19.

Language R., Platform StatSoft http://www.statsoft.com/Solutions/Cross-Industry/R-Integration/.

Matsuura T., et al., Quantifying epistatic interactions among the components constituting the protein translation system. *Mol. Syst. Biol.,* 2009, **5**, 297.

Miersch S., LaBaer J., Nucleic acid programmable protein arrays: Versatile tools for array-based functional protein studies. *Curr. Protoc. Protein Sci*. 2011, Chapter 27, Unit27 2, doi: 10.1002/0471140864.ps2702s64.

Montor W. R., Huang J., Hu Y., Hainsworth E., Lynch S., Kronish J. W., Ordonez C. L., Logvinenko T., Lory S., LaBaer J., Genome-wide study of Pseudomonas aeruginosa outer membrane protein immunogenicity using self-assembling protein microarrays. *Infect Immun*., 2009, **77**(11), 4877–4886.

Nagl S., Schaeferling M., Wolfbeis O. S., Fluorescence analysis in microarray technology. *Microchim. Acta.,* 2005, **151**, 1.

Nedelkov D., Nelson R. W., Delineating protein-protein interactions via biomolecular interaction analysis-mass spectrometry. *J. Mol. Recognit.,* 2003, **16**(1), 9–14.

Nicolini C., Correia T. B., Stura E., Laarosa C., Spera R., Pechkova E., Atomic force microscopy and anodic porous allumina of nucleic acid programmable protein arrays. *Recent. Pat. Biotechnol.,* 2013, **7**, 112–121.

Nicolini C., Spera R., Festa F., Belmonte L., Chong S., Labaer J., Pechkova E., (2013) Mass spectrometry and florescence analysis of SNAP-NAPPA arrays expressed using *E. coli* cell free expression system. *J. Nanomed. Nanotechnol*., In press

Pappin D. J., Hojrup P., Bleasby A. J., Rapid identification of proteins by peptide-mass fingerprinting. *Curr. Biol.,* 1993, **3**, 327.

Pechkova E., Chong S., Tripathi S., Nicolini C., Cell free expression and APA for NAPPA and protein crystallography, in *Functional Proteomics and Nanotechnology-Based Microarrays* (eds. Nicolini C., LaBaer J.), Pan Stanford Series on Nanobiotechnology Volume 2, Chapter 7, pp. 121–147, London–New York–Singapore, 2010.

Peeples, M. A., R script for K-means cluster analysis. [online]. Available: http://www.mattpeeples.net/kmeans.html (November 21, 2012).

Ponomarenko J., Bui H. H., Li W., Fusseder N., Bourne P. E., Sette A., Peters B., ElliPro: A new structure-based tool for the prediction of antibody epitopes. *BMC Bioinformatics.,* 2008, **9**, 514.

Qiu J., LaBaer, J., Nucleic acid programmable protein array a just-in-time multiplexed protein expression and purification platform. *Methods Enzymol.,* 2011, **500**, 151–163.

Ramachandran N., Hainsworth E., Bhullar B., Eisenstein S., Rosen B., Lau A. Y., Walter J. C., LaBaer J., Self-assembling protein microarrays. *Science*, 2004, **305**, 86.

Ramachandran N., Larson D. N., Stark P. R., Hainsworth E., LaBaer J., Emerging tools for real-time label-free detection of interactions on functional protein microarrays. *FEBS J.,* 2005, **272**, 5412.

Ramachandran N., Raphael J.V., Hainsworth E., Demirkan G., Fuentes M.G., Rolfs A., Hu Y., LaBaer J., Next-generation high-density self-assembling functional protein arrays. *Nat. Methods*, 2008, **5**, 535.

Ray S., Mehta G., Srivastava S., Label-free detection techniques for protein microarrays: Prospects, merits and challenges. *Proteomics,* 2010, **10**(4), 731–748.

Sakanyan V., High throughput and multiplexed protein array technology: protein-DNA and protein-protein interactions. *Journal of Chromatography B.,* 2005, **815**, 77.

Shimizu Y., et al., Cell-free translation reconstituted with purified components. *Nat. Biotechnol.,* 2001, **19**(8), 751–755.

Shimizu Y., Kanamori T., Ueda T., Protein synthesis by pure translation systems. *Methods*, 2005, **36**(3), 299–304.

Sivozhelezov V., Spera R., Giacomelli L., Hainsworth E., LaBaer J., Bragazzi N.L., Nicolini C., Bioinformatics and fluorescence DNASER for NAPPA studies on cell transformation and cell cycle, in *Functional Proteomics and Nanotechnology-Based Microarrays* (eds. Nicolini C., LaBaer J.), Pan Stanford Series on Nanobiotechnology Volume 2, Chapter 2, pp. 31–59, 2010, Singapore.

Spera R., Badino F., Hainsworth E., Fuentes M., Srivastava, S., LaBaer J., Nicolini C., Label-free detection of NAPPA via mass spectrometry, in *Functional Proteomics and Nanotechnology-Based Microarrays* (eds. Nicolini C., LaBaer J.), Pan Stanford Series on Nanobiotechnology Volume 2, Chapter 3, pp. 61–78, 2010, Singapore.

Spera R., Bezzerra T., Nicolini C., NAPPA based nanogravimetric biosensor: Preliminary characterization. *Sens. Actuators B.,* 2013, **182**, 682–688.

Spera R., Festa F., Bragazzi N., Pechkova E., LaBaer J., Nicolini C., Conductometric monitoring Of protein-protein interactions. *J. Proteome Res.,* 2013, **12**(12), 5535–5547. Article ASAP.

Spera R., LaBaer J., Nicolini C., Mass spectrometry detection of nucleic acid programmable protein array. *J. Mass Spectrom*. 2011, **46**, 960–965,

Spera R., Nicolini C., NAPPA microarrays and mass spectrometry: New trends and challenges. Nano Article—Taylor & Francis/CRC Press 2008.

Stoevesandt O, Taussig M. J., He M. Protein microarrays: High-throughput tools for proteomics (Review). *Expert Rev. Proteomics,* 2009, **6**, 145–157.

Wright C., Sibani S., Trudgian D., Fischer R., Kessler B., LaBaer J., Bowness P., Detection of multiple autoantibodies in patients with ankylosing spondylitis using nucleic acid programmable protein arrays. *Mol. Cell Proteomics,* 2012, **11**(2), M9 00384.

Xu H., Freitas M. A., A mass accuracy sensitive probability based scoring algorithm for database searching of tandem mass spectrometry data, *BMC Bioinformatics*, 2007, **8**, 133.

Zhou Y., Asahara H., Gaucher E. A., Chong S., Reconstitution of translation from Thermus thermophilus reveals a minimal set of components sufficient for protein synthesis at high temperatures and functional conservation of modern and ancient translation components. *Nucleic Acids Res*, 2012, **40**, 7932–7945.

Part D

Electronic Applications

Chapter 12

Conductive Polymers and Gas Sensors

Valter Bavastrello,[a] Tercio Terencio Correia Bezzerra,[a] and Claudio Nicolini[a,b,c]

[a]*Nanobiotechnology and Biophysics Laboratories, Department of Experimental Medicine (DIMES), University of Genoa, Via Antonio Pastore 3, Genoa, 16132, Italy*
[b]*Virginia G. Piper Center for Personalized Diagnostics, Biodesign Institute, Arizona State University, Tempe, AZ USA*
[c]*Nanoworld Institute, Fondazione ELBA Nicolini, Largo Redaelli 7, Pradalunga, Bergamo, Italy*

claudio.nicolini@unige.it

Poly(o-methylaniline) (POTO) and nanocomposites based on both multi-walled carbon nanotubes (MWNTs) and single-walled carbon nanotubes (SWNTs) embedded in this conducting polymer, were synthesized by oxidative polymerization. Langmuir–Schaefer (LS) films were fabricated at the air–water interface. Experimental data showed that the synthesized materials were able to detect carbon dioxide (CO_2) via nanogravimetric method. The aim of this work is to investigate the behavior of POTO and related nanocomposites in presence of CO_2. For this reason, nanogravimetric measurements were performed in a dedicated chamber filled with dioxide flux. Single acquisitions were performed and tests carried out demonstrate that these materials are suitable for applications as sensors for dioxide.

Nanobiotechnology in Energy, Environment, and Electronics: Methods and Applications
Edited by Claudio Nicolini

ISBN 978-981-4463-96-6 (Hardcover), 978-981-4463-97-3 (eBook)
www.panstanford.com

12.1 Introduction

In recent years, two classes of organic materials such as conducting polymers and carbon nanotubes (CNTs) have gained great interest for their unique physical chemistry properties [1–4]. The embedding of little quantity of CNTs, either SWNTs or MWNTs, inside the polymer matrix of conducting polymers for the fabrication of nanocomposites may pave the way to interesting application of these materials [5,6]. This method of synthesis, carried on by polymerizing the monomer in the presence of a dispersion of CNTs, is very simple. Polyaniline derivatives have been deeply studied among conducting polymers in the last decades for their good electrical properties, easy methods of synthesis and high environmental stability [7–10]. The chemistry of polyanilines is generally more complex with respect to other conducting polymers, due to their dependence on both the pH value and the oxidation states, described by three different forms known as leucoemeraldine base (fully reduced form), emeraldine base (EB) (50% oxidized form), and pernigraniline base (fully oxidized form). The most important is the EB form and its protonation by means of H^+ ions, generated from protic acids, issues the emeraldine salt form, responsible of the strong increment of the conducting properties [11]. This process is reversible and it is possible for the presence of imine group basic sites located along the conducting polymer backbone [12,13]. The doping process of polyanilines is always associated to conformational modifications of the polymer chains, due to the local distortions created by the addition of H^+ ions to the basic sites [14]. These distortions are even able to affect the morphology of the deposited films by varying their organization and play an important role in the electrical properties of the conducting polymer [15]. The number and kind of substituents along the aromatic rings along with the possible presence of CNTs in the medium of reaction were proved to affect both the chemical structure and the final physical and chemical properties of synthesized materials [16]. The conformation of the polymers backbone seems also to affect the molecular rearrangement occurring during the doping process, and in some cases, the sterical hindrance generated by “too close” substituents to the aromatic ring is responsible of the spontaneous undoping process [17]. Taking into account these considerations, the aim

of the present study was to investigate the possible application of these materials as sensors for the detection of environmental carbon dioxide.

12.2 Experimental Section

12.2.1 Materials

Monomers of ortho-methylaniline, ortho-methoxyaniline, 2,5-dimethylaniline, ammonium persulfate [$(NH_4)_2S_2O_8$] as oxidizing agents and other reagents were obtained from Sigma. We purchased high-purity MWNTs from NANOCS Inc, New York, USA. Multi-walled carbon nanotubes had a diameter ranging between 30 and 40 nm and length between 40 and 50 micron.

12.2.2 Synthesis of Nanocomposite Materials

The standardized synthesis of nanocomposite materials was carried out by oxidative polymerization under controlled conditions, maintaining the temperature at 0–4°C by means of an ice bath for 24 h. The medium of reaction was 200 mL of 1 M HCl solution of the monomers. For the synthesis of the nanocomposites, we dispersed 100 mg CNTs in the medium of reaction by sonication. We performed the sonication by means of SONIC 300 VT equipment, setting a 10% power for 1 min in order to only disperse CNTs without braking processes. We used a monomer/MWNTs weight ratio of 100/1 and a monomer/oxidant molar ratio of 4/1, following methods of polymerization previously performed [16,18]. Figure 12.1 resumes the amounts of reagents used for the synthesis. Particular care was taken on adding the oxidizing agent to have the most reproducible conditions at the very begin of the polymerization. In order to obtain the solvent processable undoped form, we filtered and subsequently treated the crude materials in the doped form (emeraldine salt form) with ammonium hydroxide for 2 h. We finally filtered the undoped materials (EB form) and performed a treatment with methanol and diethyl ether in order to eliminate the oligomers, followed by the evaporation of the residue solvents by vacuum. The final products, in the EB forms, were completely soluble in chloroform. Figure 12.1 illustrates the scheme of synthesis.

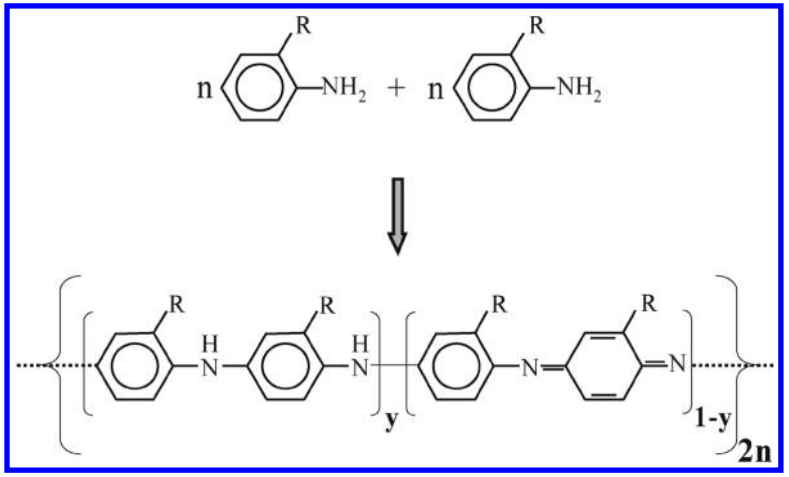

Figure 12.1 Scheme of the synthesis leading to the formation of a repeat unit starting from monomers. Basing on the fraction of imine nitrogen groups per repeat unit it is possible to obtain different reduced/oxidized polymer chains as following: Fully reduced form (leucoemeraldine base) for $y = 1$; fully oxidized form (pernigraniline base) for $y = 0$; half oxidized form (emeraldine base) for $y = 0.5$.

12.2.3 Fabrication of LS Films

We fabricated the Langmuir monolayers in a Langmuir–Blodgett trough (MDTcorp., Russia), 240 mm × 100 mm in size and 300 mL in volume, having a compression speed of 1.67 mm/s (100 cm^2/min). The spreading solutions of nanocomposites were prepared by dissolving 5 mg of materials in 20 mL of chloroform. The LS films were deposited at air–water interface, maintaining the surface pressure at 25 mN/m [15–18]. We used distilled water as subphase for the deposition in order to obtain films of the materials in the undoped form.

12.2.4 Setup of the Sensing Apparatus

In order to test the sensing properties of the synthesized materials, we set up a homemade glass chamber of 340 mL volume. The homemade chamber (Figs. 12.2 and 12.3) is provided of four input socket for quartzes, a gas valve in, and a gas valve out.

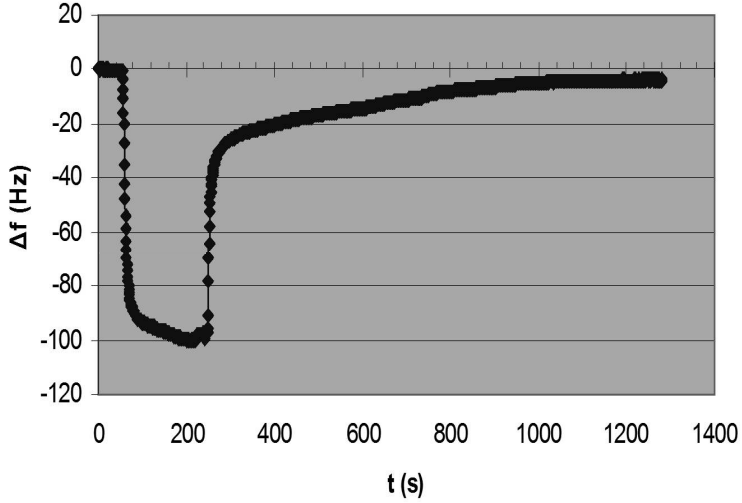

Figure 12.2 Quartz reference: Variation in the quartz frequency.

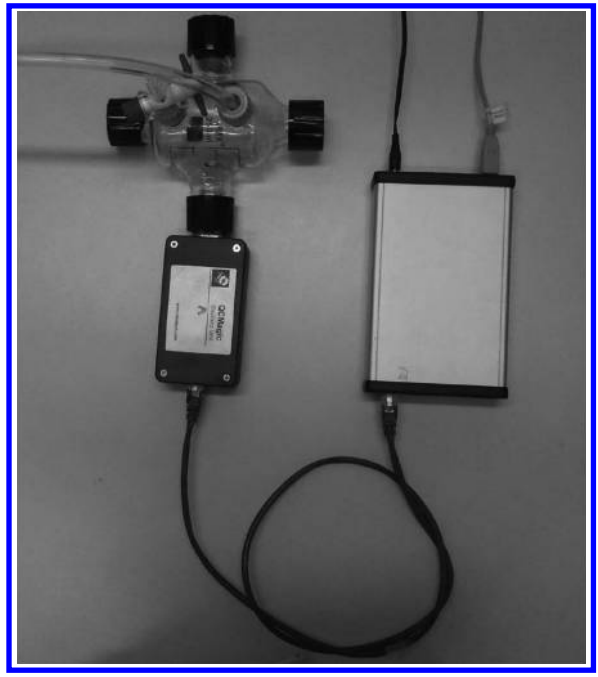

Figure 12.3 Setup, homemade chamber, and nanogravimeter.

In this chamber, an acquisition of four different quartzes per time could be performed; anyway, in this particular setup, only a quartz per time was used for acquisition, due to different times. Quartzes were used with the following characteristics: diameter 0.550 cm, electrode diameter 0.295 cm, electrode material Cr + AU, fundamental frequency 9.5 MHz. Quartzes are directly connected to a nanogravimeter Elbatech QCMagic R3. This last one is linked to a PC with an acquisition USB card provided with the same nanogravimeter. On the PC, dedicated software called QCMagic R3 was run to acquire nanogramitric signals. A flux of dioxide with 1 bar pressure was used during these acquisitions.

12.3 Results and Discussion

The synthesized materials were deposited on quartz. To carry out measurements, a single quartz per time was introduced in the chamber. After an initial period of adjustment, the quartz signal acquisition begun and then a flux of CO_2 was pumped in the chamber. The first acquisition was called "adjustment" with the vacuum quartz, to carry out the frequency variation in presence of a CO_2 flux. This acquisition was necessary to avoid affecting the data and to evaluate the effect of pressure exerted by the gas entering the chamber needed to have cognizance of the effects of this flux pressure on the final results. According to the equation,

$$\Delta s = -k \times \Delta f,$$

where Δs is the mass variation, k the instrument sensitivity constant, and Δf the frequency variation, the value of the oscillations of the quartz vacuum, i.e., without the deposition of the polymer, must be less than that obtained with the polymer deposited on quartz (Fig. 12.2). In each of the graphs, it is possible to see the entrance of the gas flow inside the chamber in conjunction with the negative peak of the curve. As soon as the gas flow is interrupted, and thus opens the gas out valve of the chamber, the quartz tends to re-establish the initial condition. In order to assess whether the dioxide interacts with the polymers, it is necessary

to compare the results of subsequent acquisitions with the adjustment value.

12.4 Conclusions

Chloroform processable pure POTO and related nanocomposites were synthesized by oxidative polymerization. Thin solid films were prepared for all the materials in the undoped form by means of LS technique. Tests were carried out in order to determine whether these materials were suitable for application as sensors for CO_2.

Experimental data highlights different behavior of chloroform processable pure POTO, depending on the nanocomposites deposited on the quartz surface. Nanogravimetric analysis demonstrates that these materials are suitable for applications as sensors for carbon dioxide. From the experimental results obtained, the highest peak of oscillation is obtained in the presence of O-methylaniline (Fig. 12.4), which shows the best behavior with dioxide respect single-walled nanotube (SWNT) of O-methylaniline (Fig. 12.5) and multi-walled nanotube (MWNT) of O-methylaniline (Fig. 12.6).

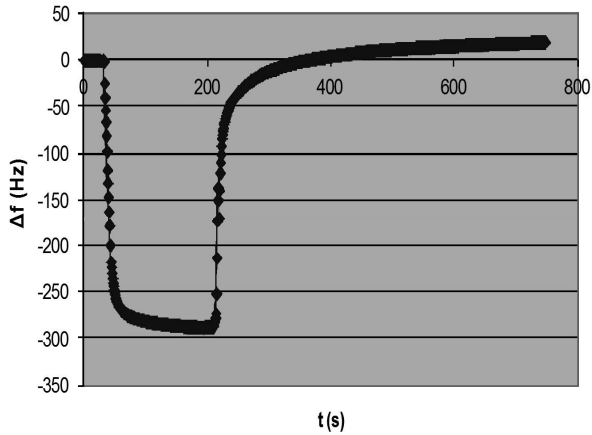

Figure 12.4 Quartz frequency variation recorded with O-methylaniline superposed on the quartz.

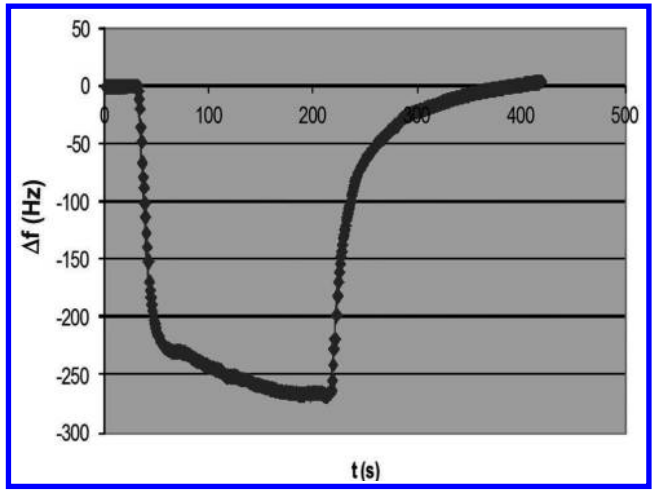

Figure 12.5 Quartz frequency variation recorded with single-walled nanotube (SWNT) of O-methylaniline superposed on the quartz.

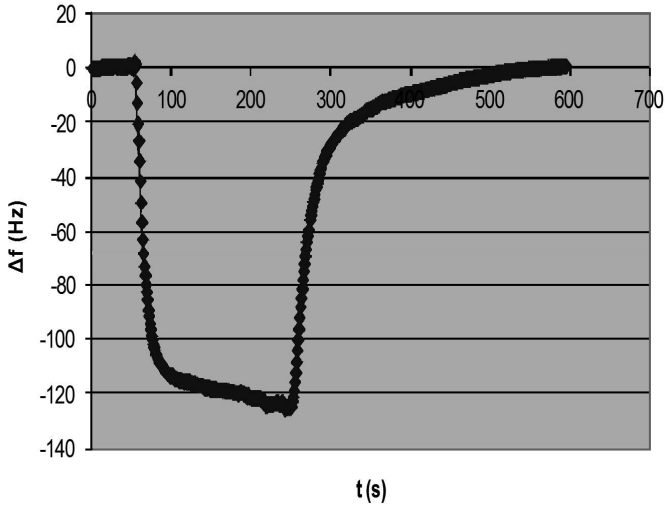

Figure 12.6 Quartz frequency variation recorded with multi-walled nanotube (MWNT) of O-methylaniline superposed on the quartz.

Work is in progress to evaluate and optimize both the selectivity with respect to a different gas and the sensitivity with respect to gas concentration.

References

1. MacDiarmid A.G., Yang L.S., Huang W.S., Humphrey B.D. *Synth. Met*., 1987, **18**, 393.
2. Iijima S. *Nature*, 1991, **56**, 354.
3. Dresselhaus M.S., Dresselhaus G., Eklund P.C. *Science of Fullerenes and Carbon Nanotubes*. New York: Academic Press; 1996.
4. Iijima S., Brabec C., Maiti A., Bernholc J.J. *Chem. Phys*., 1996, **5**, 2089.
5. Coleman J.N., Curran S., Dalton A.B., Davey A.P., McCarthy B., Blau W., et al., *Phys. Rev. B*., 1998, **58**, 7492.
6. Bavastrello V., Ram M.K., Nicolini C. *Langmuir*, 2002, **20**, 1535.
7. MacDiarmid A.G., Chiang J.C., Halpen M., Huang W.S., Mu S.L., Somasiri N.L.D., et al. *Mol. Cryst. Liq. Cryst.,* 1985, **121**, 173.
8. Paul E.W., Ricco A.J., Wrighton M.S.J. *Phys. Chem*., 1985, **89**, 1441.
9. Epstein A.J., MacDiarmid A.G. In: (Kuzmany H, Mehring M, Roth S, ed). *Electronic Properties of Conjugated Polymer*. Berlin: Springer-Verlag; 1989.
10. Kobayashi T., Yoneyama H., Tamura H.J., *Electroanal. Chem*., 1984, **177**, 281.
11. Chiang J.C., MacDiarmid A.G. *Synth Met.,* 1986, **13**, 193.
12. Epstein A.J., Ginder J.M., Zuo F., Bigelow R.W., Woo H.S., Tanner D.B., et al. *Synth. Met.,* 1987, **18**, 303.
13. Genies E.M., Labkowski M.J. *Electroanal. Chem*., 1987, **236**, 199.
14. de Oliveira Jr Z.T., dos Santos M.C. *Solid State Commun*., 2000, **114**, 49.
15. Bavastrello V., Erokhin V., Carrara S., Sbrana F., Ricci D., Nicolini C., *Thin Solid Films*. 2004, **468**, 17.
16. Bavastrello V., et al. *Polymer*. 2011, **52**, 46.
17. Bavastrello V., Stura E., Carrara S., Erokhin V., Nicolini C. *Sens. Actuators B*., 2004, **98**, 247.
18. Bavastrello V., Carrara S., Ram M.K., Nicolini C. *Langmuir,* 2004, **20**, 969.

Chapter 13

Hardware Implementation of New Sensors for Health and Environment

Manuela Adami,[a] Marco Sartore,[a] and Claudio Nicolini[a,b]

[a]*University of Genova, Via Antonio Pastore 3, Genoa, 16132, Italy*
[b]*Nanoworld Institute, Fondazione ELBA Nicolini, Largo Redaelli 7, Pradalunga, Bergamo, Italy*

claudio.nicolini@unige.it

This chapter describes the hardware design and development and its optimal implementation for realizing three newly conceived sensors for both health and environmental applications, exploiting a wide range of detection methods and complex nanocomposites. The first one is inorganic and based on matrices of calcium oxide (CaO), the second is based on protein arrays, and the third one is based on Langmuir–Blodgett (LB) laccase multi-layers.

13.1 Gas Sensor for CO_2 Detection

Sensors for CO_2 detection can be used in order to reveal the increased emissions of gases from fossil fuel combustion, industrial processes, and agriculture associated to deforestation and habitat destruction.

Nanobiotechnology in Energy, Environment, and Electronics: Methods and Applications
Edited by Claudio Nicolini

ISBN 978-981-4463-96-6 (Hardcover), 978-981-4463-97-3 (eBook)
www.panstanford.com

The instruments generally employed consist of infrared (IR) detectors performing a continuous plotting in the site with a good degree of accuracy, but are expensive and time consuming. Long-term sampling devices such as diffusive sampling techniques are the cheapest and easiest way.

An alternative long-term sampling method for the determination of environmental CO_2 accumulation takes advantages of the properties of CaO to be carbonated by this gas, according to the following equation (see also Fig. 13.1):

$$CaO + CO_2 \leftrightarrow CaCO_3$$

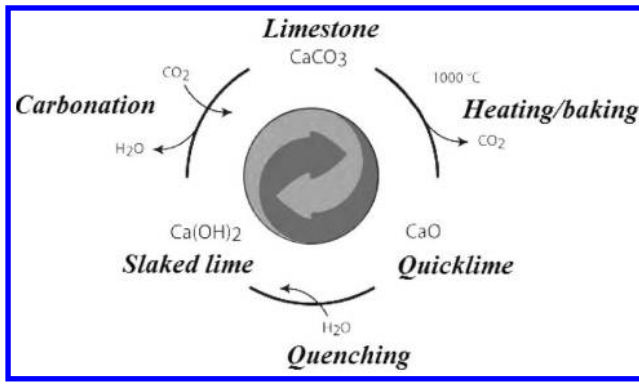

Figure 13.1 The carbonation cycle of CaO.

We carried out preliminary tests to assess the best concentration of CaO in the composite, individuated in the CaO/PEG weight ratio of 1/4. We tested the sensing properties of the composite materials via a nanogravimetric method by using a homemade glass chamber of 340 mL in volume.

As transducers, quartz crystals were used (International Crystal Manufacturing Co., Inc., ICM, Oklahoma City, OK, USA), as shown in Fig. 13.2 and Table 13.1.

Table 13.1 Transducers features

AT-cut quartz crystal
Native fundamental frequency: 9.5 MHz
Crystal diameter: 0.550″
Superficial roughness: ~3 μm
Electrode diameter: 0.295″
Electrode composition: 100 Å Cr and 1000 Å Au

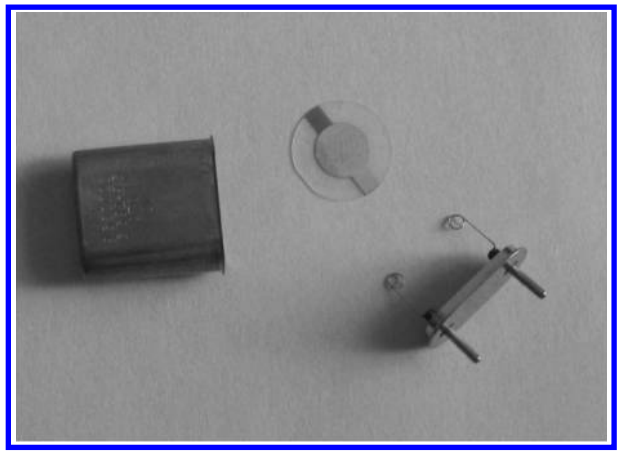

Figure 13.2 The transducers used for the nanogravimetric sensor.

This homemade chamber was provided with four input sockets and inlet and outlet valves to feed and empty the gas (Fig. 13.3).

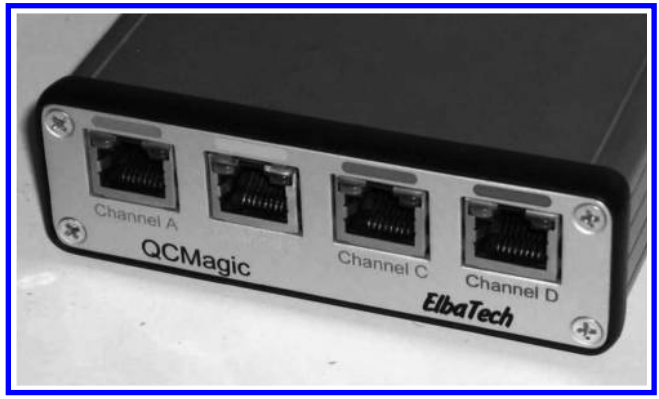

Figure 13.3 Nanogravimetric base-unit, able to drive up to four oscillating units.

The composite material showed a linear absorption of CO_2 as a function of the gas concentration inside the atmosphere-controlled chamber, thus paving the way for the possible use of these matrices for applications in the field of sensor devices for long-term evaluation of accumulated environmental CO_2.

The preliminary results were extremely encouraging and allowed us to design and realize a dosimeter for the long-term analysis of the carbon dioxide.

We used the same transducers but they were inserted in a homemade and ad hoc designed and built Plexiglas measuring chamber, divided into two parts: the upper one, with a funnel opening, allowed the exchange of the sensing matrix with the environment and the lower one that allowed the housing of the transducer (Fig. 13.4).

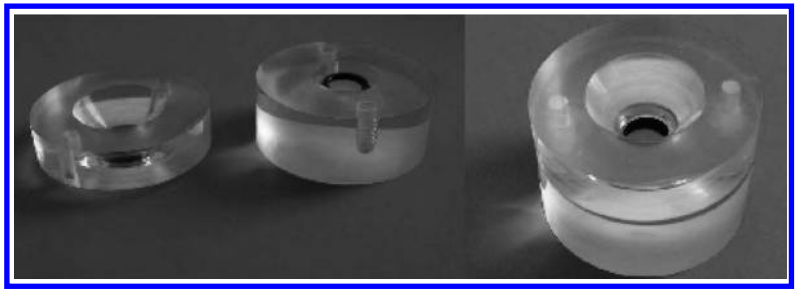

Figure 13.4 The Plexiglas chamber of the sensor.

The nanogravimetric instrument used for relating CO_2 concentrations with mass variations consisted of a base unit, interfaced to a PC via USB port and able to drive up to four oscillator units. The base unit embedded the interface circuitry to/from the USB port, a digital signal controller, and a fast programmable logic device containing an accurate four-channel counter, plus the four interfaces to the oscillator units. The counter logic was fully parallel, this meaning that the four input signals were acquired and counted-up simultaneously at a gate interval selectable from fractions of a second to 10 s. The base unit was powered by means of an external pluggable +12 V power supply, which sustained input AC voltages from 90 to 240 VAC (Fig. 13.3). The choice to have the oscillators outside the base unit allows the maximum flexibility when building an experimental setup. The noise immunity was preserved and guaranteed by the oscillator design, which was based on a precision internal reference crystal, used as a timebase comparator for the working quartz crystal. Only the mixed, lower frequency signal was then transmitted to the base unit by dedicated twisted pair lines on the cable. The oscillator units were connected to the base unit by means of standard Ethernet class V cables (see Fig. 13.5).

Figure 13.5 The oscillator unit of the sensor.

The properties of the sensor are summarized in Table 13.2.

Table 13.2 Sensor properties and features

Features	Values
Maximum resolution (gate-dependent)	±0.05 Hz
Gate range	0.01 to 10 s
Frequency stability	100 ppm/°C
Counting logics	32 bit
Interface	USB
Output signal	Δf (proportional to mass absorbed onto electrode surface)
Biochemical signal	Analyte concentration
Transducer	AT-cut quartz crystal, 9.5 MHz
Oscillator units	1
Physical dimensions	Base unit: 165 mm × 35 mm × 105 mm (L × H × W) Oscillator unit: 115 mm × 35 mm × 65 mm (L × H × W)
Working temperature	0–55°C
Power supply	+12 VDC

13.2 Biosensor for Antidepressant Sensing

A LB thin film of recombinant laccase from *Rigidoporus lignosus*, obtained by means of genetic engineering, was prepared using a highly concentrated sample of enzyme.

The topology of the LB thin film of laccase was investigated via atomic force microscopy (AFM). The roughness of the film was found to be 8.22 nm and the compressibility coefficient about 37.5 m/N. The enzyme was deposited onto the electrode via Langmuir-Schaefer (LS) technique and a protocol of immobilization overnight was followed; after depositing the film, the electrodes (Fig. 13.6) were kept at 4°C up to a maximum of 16 h. The employed electrodes were ruthenium and graphite ones, while the counter-electrode was of silver.

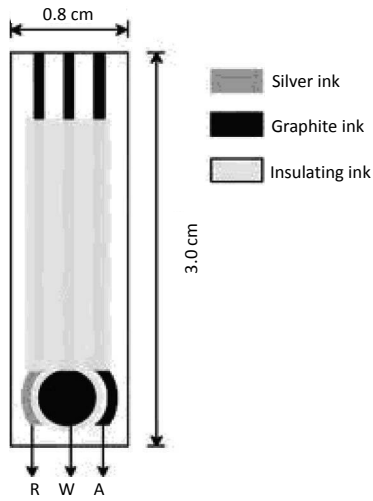

Figure 13.6 Printed electrode of the biosensor for antidepressant sensing.

The area of the electrode was about 0.75 mm per 1 mm. The properties of the used electrodes are summarized in Table 13.3.

Table 13.3 Used ink-printed electrodes for the biosensor for antidepressant monitoring and sensing

Working electrode:	graphite/ruthenium
Reference electrode:	silver
Counter-electrode:	graphite

Note: Kindly provided by Università degli Studi di Firenze, Department of Chemistry, Florence (Italy).

The amperometric technique was used to polarize the electrochemical couple and to obtain a current discharge related

to the amount of the investigated drug, namely clomipramine, with an EG&G PARC model 263A potentiometer, equipped with dedicated software.

Clomipramine, a drug belonging to the tricylic tertiary amine antidepressants class, is widely used for the therapy of depressive and obsessive disorders. Because of its clinical importance many analytical methods have been developed to monitor its levels, above all chromatographic techniques (gas chromatography, high performance liquid chromatography), eventually coupled with tandem mass spectrometry, but all these techniques are time-consuming and laborious. Moreover, the AGNP-TDM panel of experts has emphasized the importance of therapeutic drug monitoring. In our experiment, clomipramine was added at varying concentrations in the micromolar range. The therapeutic dose is from 75 to 200 mg/day; the pharmacokinetics among patients is extremely variable. Generally, the therapeutic concentration in the human blood of psychiatric patients is usually in the low micromolar range. The side effects of the drugs, especially in case of overdose, are seizures, hematological, cardiological, and neurological adverse effects up to the coma (tricyclic antidepressant syndrome). Experiments carried out with cyclic voltammetry highlighted excellent reproducibility and linearity of the peaks of oxidation and reduction, related to the presence of the drug in several biological fluids (in particular in whole blood).

These results allowed the design and the creation of a prototype of a biological sensor for antidepressants (Fig. 13.7).

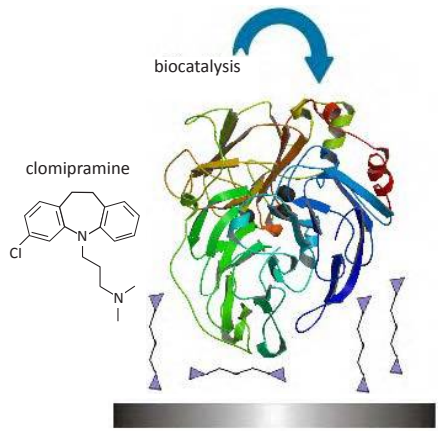

Figure 13.7 Surface chemistry of the biosensor for antidepressant sensing.

The instrument consisted of a central unit, able to bias the working electrode on which the enzyme was deposited and to detect the current generated as a result of the interaction of the enzyme with the analyte containing the drug of interest. By a multiple selector, the user can choose the fluid to be analyzed and, through the proper calibration parameters, on the display, the proper drug concentration will be provided (Fig. 13.8).

Figure 13.8 A picture of the display, providing the user with the proper drug concentration.

The instrument was powered by two 9 V batteries, in order to avoid noise from the main voltage.

Use of commercial laccase, screen-printed electrodes technique and a portable device appear to provide an emerging instrument suitable for investigation in biological fluids as well as for other medical applications. The same enzyme and the same proposed device could be used also in many different fields, such as in degradation of polyaromatic hydrocarbons, in textile industry, in food industry and in waste detoxification. Laccase-based sensors for detection of clomipramine in breast milk, saliva, and semen were less sensitive than the others, while sensors for the monitoring of the drug level in urine and blood had better pronounced and separated peaks.

The Plexiglas homemade chamber for the measurements is shown in Fig. 13.9.

Figure 13.9 The Plexiglas homemade chamber.

The features and the properties of the biosensor are summarized in Table 13.4.

Table 13.4 The feature and the properties of the biosensor for antidepressant sensing

Features	**Values**
Output signal/biochemical signal	Drug concentration
Working range	Micromolar
Transducer	Printed electrode
Kind of measurement	Static
Physical dimensions	165 mm × 35 mm × 105 mm (L × H × W)
Working temperatures	0–55°C
Power supply	+12 VDC

13.3 QCM_D-Based Biosensor

The QCM_D results were calibrated for both frequency and D factor shifts using fructose. We monitored by QCM_D the viscoelastic behavior of the quartzes during the NAPPA expression process, recording the impedance curves in correspondence with the main steps of the expression process. Moreover, we monitored by QCM-F the variation in the mass adsorbed on the surface of the sensors (corresponding to a decrease of the resonance frequency).

The protocol we used is the following (see Fig. 13.10):

- at the beginning of the expression process, i.e., before reticulocyte lysate addition;
- 120 min after reticulocyte lysate addition (i.e., after 90 min at 30°C for gene expression and protein synthesis plus 30 min at 15°C for protein immobilization) and after washing process, at 22°C;
- after the addition of a MDM2 50 μM solution.

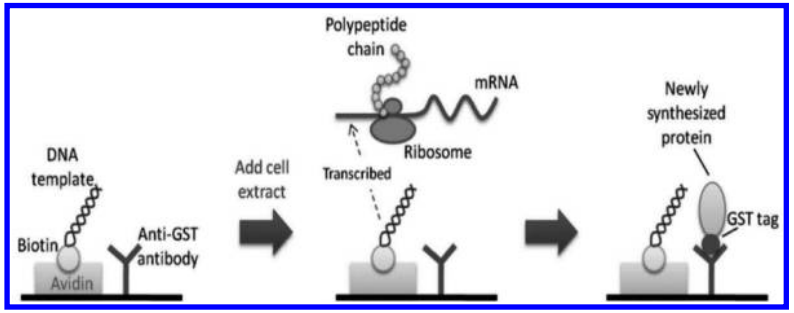

Figure 13.10 Protocol of NAPPA expression.

In order to investigate the biosensor response to protein–protein interaction the p53 quartz, once expressed the proteins, was positioned in the flux chamber, connected with the pump, and a MDM2 solution was flowed on the quartz surface: 2 mL of 50 μM MDM2 solution in PBS was injected in the pump. The corresponding frequency decrease was recorded.

In order to properly set up the QCM_D for routine measurements, we immobilize the NAPPA on the given reference quartzes provided by the manufacturer. Then, in order to eliminate the background signal, we carry out the measurements starting from the crystal native frequency subtracted of 15 kHz and using

a step of 1.0 Hz for collecting whole impedance plots. For this reason, we have used a dsPIC (Microchip Technology, Inc., Chandler, AZ, USA) featuring at the same time good computational power and sufficient memory space. This represents a PC-driven prototype to establish the proof of principle (as shown in Fig. 13.11).

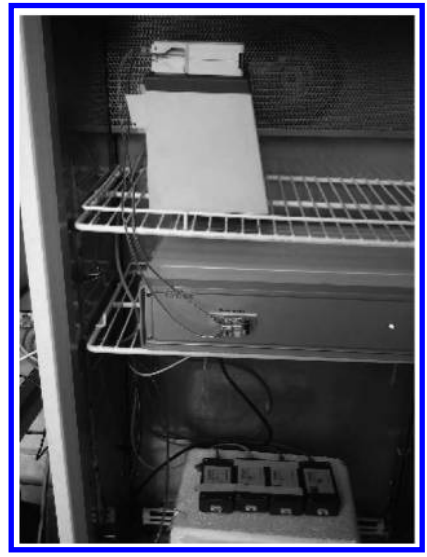

Figure 13.11 The PC-driven NAPPA-QCM_D sensor.

The properties of the biosensor are summarized in Table 13.5.

Table 13.5 Feature and properties of the sensor

Features	Values
Maximum resolution	14 Hz
Counting logics	… bit
Interface	USB
Output signal	Impedance curve
Biochemical signal	Variation of the quartz quality factor
Transducer	AT-cut quartz crystal, 9.5 MHz
Oscillating unit	1
Physical dimensions	… mm (L × H × W)
Working temperatures	0–55°C
Power supply	+12 VDC

Chapter 14

Role of π–π Interactions in the Charged Species Stabilizations of Conjugated Polymers for Nanoelectronics

Riccardo Narizzano[a] and Claudio Nicolini[a,b]

[a]*Eminent Biophysics Chair, University of Genoa*
[b]*Fondazione Nanoworld Institute ELBA Nicolini, Pradalunga, Bergamo, Italy*

claudio.nicolini@unige.it

The interchain interactions of poly(2,6-pyridinylenevinylene)-*co*-[(2,5-dioctyloxy-*p*-phenylene)vinylene] (PPyPV), are investigated by UV-Vis absorption spectroscopy. The PPyPV is a Lewis base and can be doped by strong and weak Lewis acids. The interchain interactions seem to play a fundamental role only in charged states. The basicity strength of the PPyPV depends on the polymer interchain interactions, as the polymer concentration is increased, a K_b increment is observed, reversal a decrease of polymer concentration lowers the K_b of the PPyPV.

14.1 Introduction

Materials based on π-conjugated polymers have attracted interest because of their unusual electronic and mechanical properties

Nanobiotechnology in Energy, Environment, and Electronics: Methods and Applications
Edited by Claudio Nicolini

ISBN 978-981-4463-96-6 (Hardcover), 978-981-4463-97-3 (eBook)
www.panstanford.com

(1) leading to an entire set of devices (2–4) such as light-emitting diodes (5), field-effect transistors (6) and photovoltaics (7). A better control of the electronic properties and devices performances are expected in this material due to the electronic interactions between the polymer and/or the nanoscopic structural organization of the polymer chains (8,9).

Recent studies have shown that interchain interactions play a fundamental role in the excited states of conjugated polymers allowing the delocalization of the charge over different chains (10–11).

In this work, we prepared a metalinked PPV derivative, PPyPV. The interactions between the polymeric chains were studied using absorption spectroscopy. The addition of a positive charge by chemical means on the polymer chains, which is the doping process, was investigated using strong and very weak Lewis acids. We found that the basic character of the PPyPV is a function of the polymer concentration proving that the organization of the polymer chains plays a fundamental role in the doping process.

These experimental results are very important because, until this work, all the experimental evidence has been deduced mainly through photoluminescence and photo-induced absorption data. As far as we know there has been no experimental data based on UV-Vis absorption spectroscopy that shows evidence for the stabilization of the charged species due to the interchain interaction reported in literature. We report the spectroscopic evidence based on UV-Vis absorption of this phenomena.

14.1.1 Experimental Section

General Information. Chemicals were purchased from Aldrich and used as received. Solvents were dried, distilled, and stored under argon. Melting points (mp) were determined on an electrothermal melting point apparatus and are uncorrected. Proton and carbon nuclear magnetic resonance spectra (^{1}H-NMR and ^{13}C-NMR) were recorded on a Bruker 500 MHz at 25°C, using the deuterated solvent as a lock and the residual solvent as an internal standard. Electron Impact Ionization Mass Spectrometry (EI-MS) was performed on an AUTO-SPEC instrument. Elemental analyses were performed by Quantitative Technologies Inc. Molecular weights of

the polymers were determined by using a Dynamax solvent delivery module system, Styragel HR3 column, and a Dynamax PDA-2 diode array detector, at a flow rate of 1.0 mL/min. The molecular weight was measured against polystyrene standards in THF.

Synthesis. **1,4-Bis(octyloxy)benzene** (2). A solution of 1,4-dihydroquinone (1) (6.5 g, 59 mmol), K_2CO_3 (32.6 g, 236 mmol), and 1-chlorooctane (20 mL, 118 mmol) in DMF (240 mL) was heated for 5 days at 90°C. The product was isolated by extraction with light petroleum, washed with H_2O, dried over Na_2SO_4, and evaporated to obtain 2 as a white solid (14 g, 71%). M.p. 56–57°C (light petroleum); ^{1}H NMR (360 MHz, $CDCl_3$): δ = 6.82 (s, 1H), 3.89 (t, J = 6.6 Hz, 2H), 1.75 (p, J = 6.7 Hz, 2H), 1.44 (p, J = 6.7 Hz, 2H), 1.31 to 1.28 (m, 8H), 0.88 (t, J = 6.6 Hz, 3H); ^{13}C NMR (90 MHz, $CDCl_3$): δ = 153.2, 115.4, 68.7, 31.8, 29.4, 29.2, 26.0, 22.6, 14.1.

2,5-Bis(chloromethyl)-1,4-bis(octyloxy)benzene (3). 1,4-Bis(octyloxy)benzene (2) (9.5 g, 28 mmol) was added to a mixture of dioxane (80 mL), 37% aqueous formaldehyde solution (17 mL) and conc. hydrochloric acid (12 mL), saturated with hydrogen chloride. The mixture was heated at 60–70°C with continuous introduction of HCl for 9 h. After cooling, ice/water (300 mL) was added and the precipitate was filtered. Crystallization from light petroleum yielded 1,4-bis(chloromethyl)-2,5-dioctyloxybenzene (3) as colorless needles (9.4 g, 77%). M.p. 80°C; ^{1}H NMR (360 MHz, $CDCl_3$): δ = 6.91 (s, 1H), 4.63 (s, 2H), 3.98 (t, J = 6.5 Hz, 2H), 1.80 (p, J = 6.5 Hz, 2H), 1.48 (p, J = 6.5 Hz, 2H), 1.35 to 1.29 (m, 8H), 0.89 (t, J = 6.5 Hz, 3H); ^{13}C NMR (90 MHz, $CDCl_3$): δ = 150.6, 127.0, 114.3, 69.1, 41.3, 31.8, 29.3, 26.0, 22.6, 14.1; EI-MS: 430.2 to 432.2 $[M]^+$; calculated for $C_{24}H_{40}Cl_2O_2$ (431.5): C 66.81, H 9.34; found: C 66.73, H 9.56.

2,5-Bis(methyl triphenylphosphonium chloride)-1,4-bis(octyloxy)benzene (4). A mixture of 1,4-bis(chloromethyl)-2,5-dioctyloxybenzene (3) (1.45 g, 3.36 mmol) and triphenylphosphine (2.69 g, 10 mmol) in anhydrous DMF (20 mL) was heated under reflux for 3 days. The resulting solution was added dropwise into Et_2O (100 mL) to precipitate out the product. The white precipitates (2.66 g, 83%) were collected via filtration and dried under vacuum. M.p. > 200°C; ^{1}H NMR (360 MHz, $CDCl_3$): δ = 7.75–7.73 (m, 3H), 7.66 to 7.63 (m, 12H), 6.68 (s, 1H), 5.34 (d, J = 12.7 Hz, 2H), 2.99 (t, J = 5.8 Hz, 2H), 1.32 to 1.19 (m, 5H), 1.13 to 1.04 (m, 5H), 0.90 (t, J = 6.7 Hz, 3H); ^{13}C NMR (90 MHz, $CDCl_3$): δ = 150.4, 134.7, 134.2,

134.14, 134.09, 130.0, 129.95, 129.88, 118.5, 117.5, 116.3, 115.8, 67.8, 31.7, 29.2, 29.1, 28.6, 25.7, 22.5, 14.0.

PPyPV. 0.73 mL of 2.5% NaOEt in EtOH solution (0.7 mmol) was added dropwise to a solution of 4 (0.21 g, 0.22 mmol) and 2,6-pyridinedicarboxaldehyde (0.03 g, 0.22 mmol) in a mixture of anhydrous EtOH (1 mL) and THF (3 mL) at room temperature. The reaction mixture was stirred for additional 26 h. The resulting polymer was precipitated twice from MeOH and then dried to afford mixed PPyPV (0.05 g, 65%) as a yellow resin. ^{1}H NMR (200 MHz, $CDCl_3$): δ = 7.90 to 7.50 (m), 7.30 to 6.90 (m), 6.80 to 6.60 (m), 4.01 (brs, 2H (*trans* fragment)), 3.51 (brs, 2H (*cis* fragment), 1.83 (brs, 2H), 1.48 (brs, 2H), 1.64 (brs, 8H), 0.78 (brs, 3H).

PPyPV: A sample of mixed PPyPV (0.03 g) and I_2 (11 µL of 0.01% iodine in PhMe solution) were refluxed in PhMe (3.5 mL) under argon atmosphere for 6 h. The solvent and iodine were evaporated off under reduced pressure and the product was dissolved in $CHCl_3$ and precipitated out with MeOH. The resulting precipitate was dried to afford PPyVPV as yellow resin (0.02 g). ^{1}H NMR (200 MHz, $CDCl_3$): δ = 7.89 (s,1H), 7.81 (s, 1H), 7.59 (brs, 1H), 7.40 to 7.15 (m, 7H), 4.01 (brs, 2H), 1.84 (brs, 2H), 1.49 (brs, 2H), 1.22 (brs, 8H), 0.80 (brs, 3H); calculated for $C_{31}H_{43}NO_2$ (461.7): C, 80.65; H, 9.39; N, 3.03; found: C, 78.69; H, 9.17; N, 2.83; calculated for HCl protonated once every three repeat units: C, 78.58; H, 9.22; N, 2.96.

Molecular Weight Definition. The molecular weights and polydispersity (PDI) of PPyPV (M_w = 24,246; PDI = 1.8) were determined in THF by using size exclusion chromatography (SEC) equipped with a UV detector. The SEC system was calibrated by using polystyrene standards prior to use. The GPC measurements of the polymer show that the number-average molecular weight (M_n) is 13,543 corresponding to 29 repeating units.

UV-Visible Measurements. The polymer that was used in these experiments was synthesized shortly before use. The solutions were placed in a 1 mm path length quartz cell. The solid-state samples were produced shortly before they were tested in order to reduce polymer oxidation. The solid-state samples were created by spin-coating the polymer onto a cleaned glass substrate. The UV-Vis experiments were performed on Jasco 7800 UV-Vis spectrophotometer.

14.1.2 Results and Discussion

Synthesis of the Conjugated Polymer. The basic strategies employed for synthesizing PPyPV are based on Wittig-type ethylenic group formation methodology. In this regard, the corresponding diphosphonium salt was prepared first. Scheme 14.1 illustrates the synthetic sequences for making the diphosphonium salt.

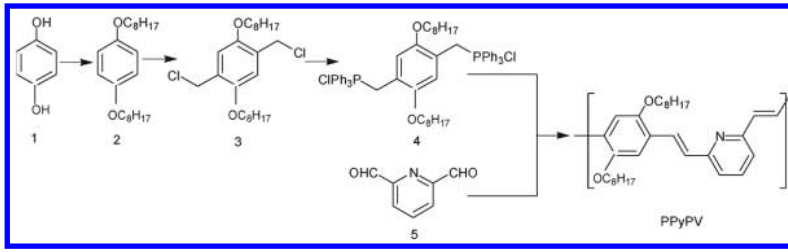

Scheme 14.1 Synthesis of PPyPV.

Specifically, heating 1,4-dihydroquinone 1 with 1-chlorooctane in DMF at 90°C in the presence of K_2CO_3 readily afforded 1,4-bis(octyloxy)benzene 2 in 71% yield. Subsequent chloromethylation of 2, using a general chloromethylation procedure for aromatic compounds, provides 3 (77% yield). The soluble diphosphonium salt 4 was made from its bis-(chloromethyl) precursor 3 in hot DMF. PPyPV polymer was prepared using multiple Wittig condensation with 2,6-pyridinedicarboxaldehyde. Like typical Wittig-type reactions, this reaction also yielded a mixture of *trans*- and *cis*-vinylene isomers. So mixed *trans*- and *cis*-polymers under these reaction conditions were observed. The isomerization of the mixed polymers to all *trans*-polymer was achieved by refluxing in toluene with a catalytic amount of iodine. The isomerization process was followed by ^{1}H NMR. ^{1}H NMR of the polymers showed the resonance signals at about 3.5 and 4.0 ppm, which are attributed to the $-OCH_2$ unit and are related to *cis*- and *trans*-olefins, respectively. The assignment of ^{1}H NMR signals was confirmed by comparing with the spectrum of the pure *trans*-isomer. The molecular weight of PPyPV was determined in THF by using size exclusion chromatography equipped with an UV detector. The number-average degree of polymerization was estimated to be $n \approx 29$ for

PPyPV by using Mn and the molecular weight of the repeating unit (461 for PPyPV).

Basic Character. PPyPV polymer was found to be easily protonated with acids on its nitrogen atoms in the pyridine unit (Scheme 14.2).

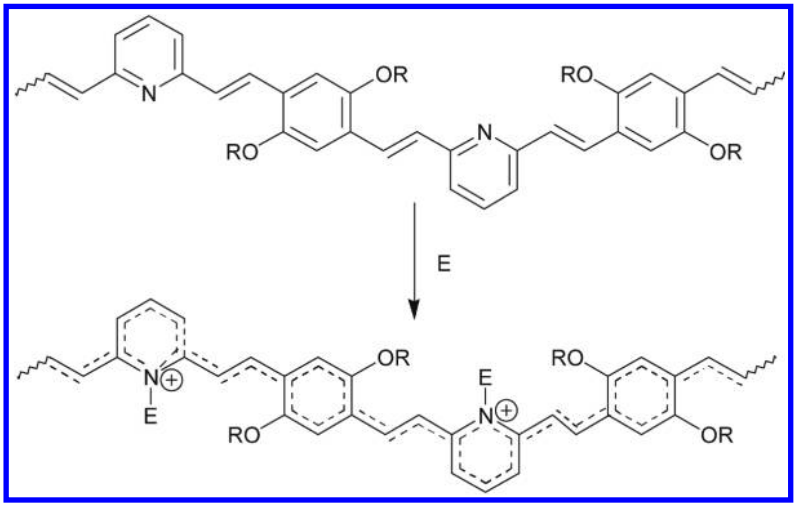

Scheme 14.2 Electrophilic attack on the PPyPV polymer (E is H^+ or $CHCl_3$).

A positive charge in the resulted pyridinium cation is delocalized in fully conjugated polymer backbone. The protonation process is accompanied with a drastic color change. While neutral PPyPV possess a green-yellow color, the acid-treated PPyPV is strongly red. Base treatment (ammonia) regenerates the original green-yellow color. The charge delocalization in the protonated form makes this polymer very basic and it behaves as a proton sponge. PPyPV turns a red color even in chloroform. Elemental analysis of PPyPV reveals that the polymer is HCl-protonated once every three repeat units.

Recent studies have shown how in conjugated oligomers containing pyridine units, it was possible to obtain a p-doped conjugated polymer without the removal of electrons, interconverting from p-doped and undoped form simply using an acid–base reaction (12).

14.2 UV-Vis Absorption Studies

14.2.1 Liquid vs. Solid-State absorption of PPyPV

Both liquid and solid-state samples were probed using UV-Vis spectroscopy to characterize the different interactions in the system. UV-Vis spectra of PPyPV were recorded in both liquid and solid states and are presented in Fig. 14.1.

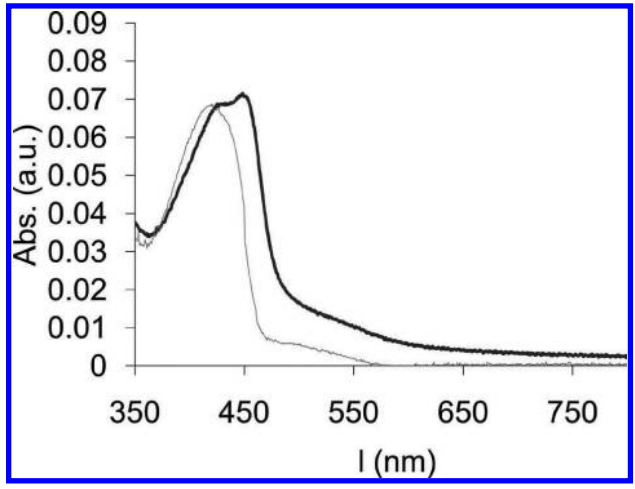

Figure 14.1 UV-Vis absorption spectra of PPyPV in CH_3Cl solution (blue line) and in solid state (red line).

The meta substitution in the pyridine unit leads to a dihedral angle in the polymer main chain that reduces the π orbital overlap accordingly. The achievement of smaller conjugation lengths results in a blue shifted π–π^* absorption with respect to the parent PPV. The π–π^* absorption in the liquid phase results in a featureless peak indicating that no vibronic transitions occur in PPyPV. The absence of vibronic transitions confirms the existence of a significant dihedral angle caused by the ring distortions in the polymer backbone. The solid-state spectrum is red-shifted by approximately 20 nm and shows vibronic structures indicating the presence of local domains with increased conjugation length, which is a consequence of the aggregation process.

14.2.2 Acid–Base Process

The optical properties of this conjugated polymer can be varied by chemical protonation of the system. The pyridine unit in PPyPV makes this polymer a Lewis base. The lone pair of the pyridine rings is a sp^2 orbital, orthogonal to the π system, but in the 2,5-pyridine vinylene systems the action of protonation renders the macromolecule "p-doped" (12).

14.2.3 Liquid Phase

The protonation process was conducted by adding an aqueous HCl solution into a chloroform solution of the PPyPV. The process was monitored by UV-Vis absorption spectroscopy as shown in Fig. 14.2.

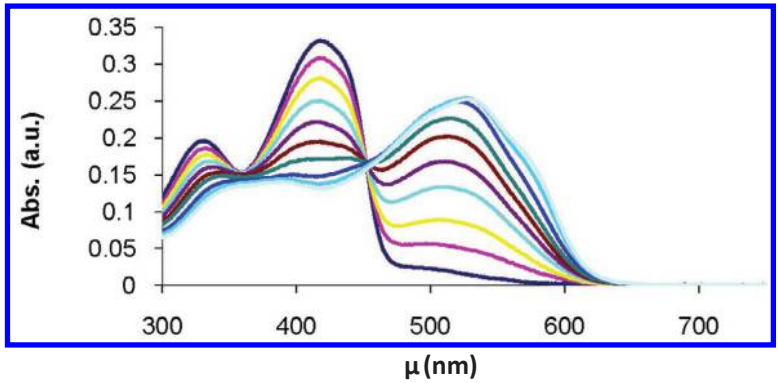

Figure 14.2 UV-Vis absorption spectra of PPyPV in CH_3Cl during the protonation process with HCl. The polymer concentration is 0.05 mg/mL, the protonation was performed adding 0.5 mL aliquots of a 1.0 N HCl solution. The spectra are collected at every aliquot.

The spectra clearly show that increasing the amount of HCl in the polymer solution leads to a decrease in the π–π^* transition peak at 420 nm as well as the appearance and increase of a new peak at 510 nm relative to the protonated form. The solution turns from a yellow color to deep red for the neutral and protonated forms, respectively. The spectra in Fig. 14.2 show that a saturation point is reached where no more charged species can be supported by the system; so additional HCl has no effect.

14.2.4 Solid State

The acid–base process in solid state was conducted by dipping a film of PPyPV on a glass substrate into a HCl 0.1 N solution. The protonation was followed by time. The UV-Vis spectra reported in Fig. 14.3 confirm all the features found in the solution phase.

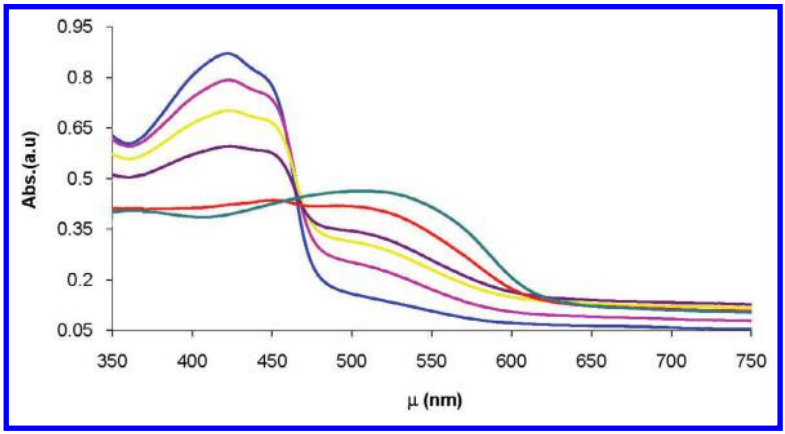

Figure 14.3 UV-Vis absorption spectrum of PPyPV solid state doping. PPyPV in film during the protonation process with HCl gas. The spectra are collected increasing the exposition time to HCl vapors.

14.2.5 Role of Concentration-Polymer Interchain Interaction

It is well known that when a charge on a molecule is dispersed over a large area of its structure, a stabilization of the entire system occurs. This property is typical of π-conjugated systems in general. In particular, conjugated polymers that have low dimensionality are able to change their local geometric structure upon the formation of the charged state of the molecule leading to the charged species (13). Recent studies have shown that interchain interactions (14–16) play a fundamental role in the excited states of conjugated polymers allowing the delocalization of the charge over different chains. In particular, it was shown that polarons in PmPV are predominately formed through interchain species and by separating the polymer chains the polaron population is reduced (17).

Until this work, all the experimental evidence has been deduced mainly through photoluminescence and photoinduced absorption data. As far as we know, there has been no experimental data based on UV-Vis spectroscopy that shows evidence for the stabilization of the charged species due to the interchain interaction has been reported in literature. In this chapter, we report the spectroscopic evidence based on UV-Vis absorption of this phenomena.

In the beginning, we observed that the polymer chloroform solutions drastically changed their color depending on the concentration, from a light yellow for the more dilute ones to a deep red for the most concentrated.

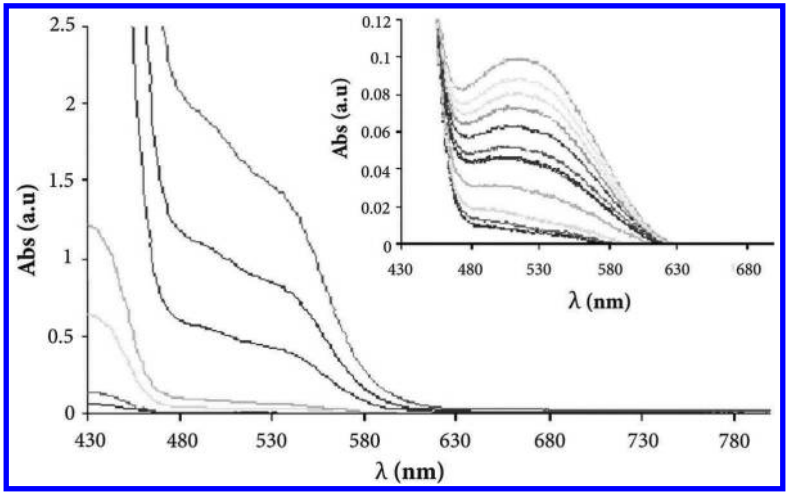

Figure 14.4 UV-Vis absorption spectra of PPyVPV in $CHCl_3$ solutions at different concentrations. Insert: The spectra show the detail of the absorption at 510 nm relative to the protonated form by HCl adding. It is possible to see that the absorption at the first stage of the titration has the feature of a shoulder and became a real peak after several additions of HCl solution.

Figure 14.4 shows the spectra for the polymer in a chloroform solution at different concentrations. The increase in the absorption at 510 nm corresponds to the protonated form, which follows the increase in polymer concentration. It is interesting to observe the insert in Fig. 14.4, which shows the formation of the doping peak

after the addition of HCl to the polymer solution. Before the formation of the peak, the absorption at 510 nm showed a slight shoulder, which has the same shape that was seen by increasing the concentration. To prove that this shoulder/peak comes from the acid–base process, we simply added a few drops of aqueous ammonia solution to the concentrated polymer chloroform solution, and immediately the color turned from red to light yellow. This process was also followed by UV-Vis absorption, as shown in Fig. 14.5.

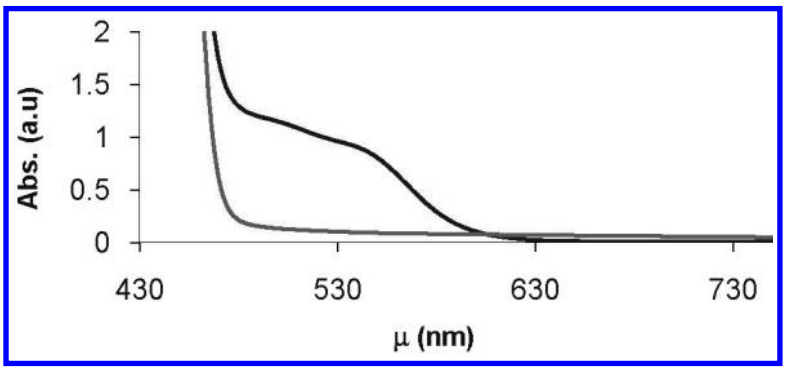

Figure 14.5 The reversible doping process is shown in the UV-Vis absorption spectra of a concentrated PPyPV-chloroform solution (blue line) and the same solution after treatment with aqueous ammonia (red line). It possible to see that after the base treatment the shoulder disappears.

The basicity of the pyridine unit is increased by the presence of the conjugation system. The basicity strength is also strongly enhanced by interchain interactions, because of the delocalization of the charged states over the chains following the protonation process leads to a stabilization of the protonated form. The increase in the basicity strength was large enough to allow the PPyPV to be doped by the weakly acidic chloroform solution, according with the following equilibrium:

$$\mathrm{PPyPV} + \mathrm{CHCl_3} \underset{\leftarrow}{\rightarrow} \left[\mathrm{PPyPV} * * \mathrm{CHCl_3}\right]^{\oplus}$$

$$K_{\mathrm{b}} = \frac{\left[\mathrm{PPyPV} * * \mathrm{CHCl_3}\right]^{\oplus}}{\left[\mathrm{PPyPV}\right]\left[\mathrm{CHCl_3}\right]}$$

assuming $[CHCl_3]$ is constant, we obtain

$$K_b' = \frac{\left[PPyPV ** CHCl_3\right]^{\oplus}}{\left[PPyPV\right]}.$$

We can study this equilibrium by measuring the absorption of the neutral and complexed-charged species at 418 nm and 510 nm, respectively, upon complexation with the base. This allows us to obtain the basicity constant, K_b, in a non-aqueous solvent, chloroform, as a function of the polymer concentration as shown in Fig. 14.6. This allows us to compare and follow the doping process from sample to sample varying the concentration.

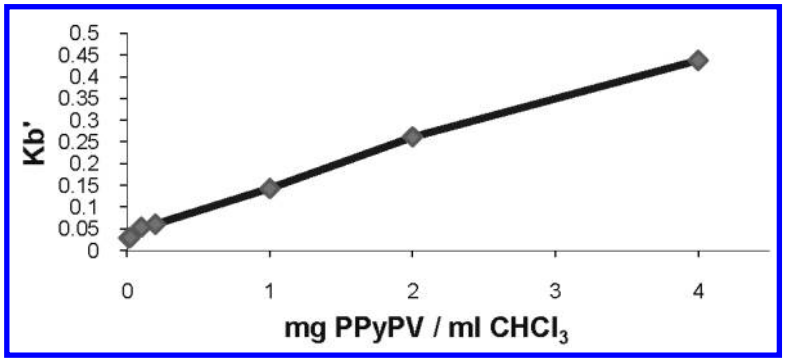

Figure 14.6 K_b' at different PPyPV concentrations in $CHCl_3$ solutions.

14.3 Conclusions

We have investigated the optical properties and the chemical doping process in a conjugated polymer, PPyPV with basic properties. We studied the influence of interchain interactions in the ground state and on the stabilization of charged states. The acid–base process was followed by UV-Vis spectroscopy. It was found that the basic strength of the PPyPV depends on the polymer concentration. The key point is that as the polymer concentration is increased, the charged state is stabilized by interchain interactions, and becomes doped more readily. By increasing the polymer concentration, we increase the interchain interaction, which stabilizes the charged states, and leads to an enhancement of the basicity strength.

It was concluded that interchain interaction plays a fundamental role in the stabilization of the polaron populations in PPyPV. There was no significant strong electronic interaction in the polymer in the ground state.

The high basicity strength makes this polymer an interesting candidate for active material in sensors for food industry, environment and quality control such as electronic nose and tongue.

Acknowledgments

This work was supported by a postdoctoral fellowship to Narizzano by the Organic Nanosciences and Nanotechnology FIRB Grant to Claudio Nicolini (RBNE01X3CE) and by Research National Program "Biocatalysis" (BTA6 project) from MIUR (Italy) to Fondazione Elba Nicolini (Bergamo) and to University of Genova, both to Claudio Nicolini.

References

1. Friend, R. H., Gymer, R. W., Holmes, A. B., Burroughes, J. H., Marks, R. N., Taliani, C., Bradley, D. D. C., Dos Santos, D. A., Bredas, J. L., Logdlund, M., and Salaneck, W. R., Electroluminescence in conjugated polymers, *Nature*, **397**, 121–128, 1999.
2. Gustafsson, G., Cao, Y., Treacy, G. M., Flavetter, F., Colinari, N., and Heeger, A. J., Flexible light-emitting-diodes made from soluble conducting polymers, *Nature*, **357**, 477–479, 1992.
3. Nicolini, C., Erokhin, V., and Ram, M. K., Supramolecular layer engineering for industrial nanotechnology, In *Nano-Surface Chemistry* (ed. M. Rosoff), Marcel Dekker New York, pp. 141–212, 2001.
4. Dai, L., Advanced syntheses and microfabrications of conjugated polymers, C_{60}-containing polymers and carbon nanotubes for optoelectronic applications, *Polymer Adv*. *Technol*., **10**, 357–420, 1999.
5. Kraft, A., Grimsdale, A. C., and Holmes, A. B., Electroluminescent conjugated polymers—Seeing polymers in a new light, *Angew*. *Chem*. *Int*. *Ed*., **37**, 402–428, 1998.
6. Huitema, H. E. A., Gelinck, G. H., van der Putten, P. H., Kuijk, K. E., Hart, C. M., Cantatore, E., Herwig, P. T., van Breemen, A. J. J. M., and de Leeuw, D. M., Plastic transistors In active-matrix displays—The

handling of grey levels by these large displays paves the way for electronic paper, *Nature*, **414**, 599–599, 2001.

7. Cravino, A., and Sariciftci, N. S., Double-cable polymers for fullerene based organic optoelectronic applications, *J. Mater. Chem.*, **12**, 1931–1943, 2002.
8. Schwartz, B. J., Conjugated polymers as molecular materials: How chain conformation and film morphology influence energy transfer and Interchain Interactions, *Ann. Rev. Phys. Chem.*, **54**, 141–172, 2003.
9. Yan, M., Rothberg, L. J., Kwock, E. W., and Miller, T. M., Interchain excitations In conjugated polymers, *Phys. Rev. Lett.*, **75**, 1992–1995, 1995.
10. Van Hutten, P. F., Krasnikov, V. V., and Hadziioannou, G., A model oligomer approach to light emitting semiconducting polymers, *Acc. Chem. Res.*, **32**, 257–265, 1999.
11. Cornil, J., Beljonne, D., Brédas, J. L., and Calbert, J. P., Interchain interactions in organic π-conjugated materials. Impact on electronic structure, optical response, and charge transport, *Adv. Mater.*, **13**, 1053–1067, 2001.
12. Wang, W. L., Helgeson, R., Ma, B., and Wudl., F., Synthesis and optical properties of cross-conjugated bis(dimethylaminophenyl)pyridylvinylene derivatives, *J. Org. Chem.*, **65**, 5862–5867, 2000.
13. Salaneck, W. R., Friend, R. H., and Brédas, J. L., Electronic structure of conjugated polymers: consequences of electron-lattice coupling, *Phys. Rep. Rev. Sec. Phys. Lett.*, **319**, 231–251, 1999.
14. Brédas, J. L., Cornil, J., Beljonne, D., Dos Santos, D. A., and Zhigang, S., Excited-state electronic structure of conjugated oligomers and polymers: a quantum-chemical approach to optical phenomena, *Acc. Chem. Res.*, **32**, 267–276, 1999.
15. Nguyen, T. Q., Doan, V., and Schwartz, B. J., Conjugated polymer aggregates in solution: Control of interchain interactions, *J. Chem. Phys.*, **110**, 4068–4078, 1999.
16. Nguyen, T. Q., Martini, I. B., Liu, J., and Schwartz, B. J., Controlling interchain interactions in conjugated polymers: The effects of chain morphology on exciton-exciton annihilaton and aggregation In MEH-PPV films, *J. Phys. Chem. B*, **104**, 237–255, 2000.
17. Lipson, S. M., Cadby, A. J., Lane, P. A., O'Brien, D. F., Drury, A., Bradley, D. D. C., and Blau, W. J., The photophysics of thin polymer films of poly-(*meta*-phenylene-*co*-2,5-dioctoxy-*para*-phenylenevinylene), *Monatshefte fur Chemie*, **132**, 151–158, 2001.

Chapter 15

Octopus Rhodopsin for Nanobioelectronics

Eugenia Pechkova,[a,d] Mikhail Ostrovsky,[b,c] Oksana Nekrasova,[b] Anastasia Shebanova,[c] Victor Sivozhelezov,[b,d] Mikhail Kirpichnikov,[b,c] and Claudio Nicolini[a,b,c,d]

[a]*University of Genova,*
[b]*Russian Academy of Sciences,*
[c]*Moscow State University,*
[d]*Fondazione Nanoworld Institute ELBA Nicolini, Pradalunga, Bergamo, Italy*

claudio.nicolini@unige.it

Physiological, evolutionary, and structural properties of octopus rhodopsin are summarized in this chapter along with their utilization for nanobioelectronics, based on the optical reversibility and photoregeneration of rhodopsins themselves. The fundamental properties of thin Langmuir–Blodgett films of octopus and bovine rhodopsins presented in this chapter appear essential for their use in nanobioelectronics. Applications that utilize both wild-type and recombinant octopus rhodopsin are, furthermore, shown, such as quantum computation and photodevices.

Nanobiotechnology in Energy, Environment, and Electronics: Methods and Applications
Edited by Claudio Nicolini

ISBN 978-981-4463-96-6 (Hardcover), 978-981-4463-97-3 (eBook)
www.panstanford.com

15.1 Fundamental Properties of Octopus Rhodopsin for Its Use in Nanobioelectronics

15.1.1 Physiological, Evolutionary, and Structural Background of Octopus Rhodopsin Use for Nanobioelectronics

Octopus eye has the ability to rotate and maintain a constant orientation with respect to gravity. Consequently, the brain can always safely interpret visual information on the basis that the eyes are horizontally aligned, though the body may be at any angle (Land, 2011).

The main difference between the eyes of invertebrates and vertebrates is that the former comprises numerous small eye units (ommatidia), each with its own photoreceptor cells (rhabdoms). Particularly, octopuses have a chamber eye similar to vertebrates; however, their photoreceptor cells are the same as in invertebrates (rhabdomeres). Instead, in chamber eye of the vertebrates, the retina contains photoreceptor cells of another, nonrabdomere type.

In most vertebrates, including primates and humans, the retina has ciliary photoreceptor cells, namely rods for highly sensitive twilight vision, and evolutionarily older cones, for daylight and color vision. Despite all the diversity of the eyes of invertebrates and vertebrates, their visual pigment remains the same, rhodopsin, one of the oldest proteins of the animal kingdom (Ostrovsky and Feldman, 2012).

Its unique photochemical and spectral characteristics are determined by one of its most conserved domains, the chromophore center, and the chromophore group 11-*cis* retinal, which interacts with its nearest protein environment.

Rhodopsin has a molecular weight of 40 kDa and consists of an apoprotein, opsin (348 amino acid residues); a chromophore, 11-*cis* retinal, covalently bound to Lys296 via a protonated Schiff base (PSB), and two oligosaccharide chains.

It crosses the membrane with seven alpha-helices, which constitute as much as 60% of its secondary structure and which appear oriented mostly perpendicular to the plane of the disk membrane.

The rhodopsin chromophore, 11-*cis* retinal, is located in a hydrophobic pocket between the helices and covalently attached to lysine 296 in helix VII via a PSB linkage. The covalent bond of the chromophore contributes to the tightly held rhodopsin in a nonsignaling conformation. The extracellular domain of rhodopsin is relatively rigid, which may help to reduce spontaneous activation of the receptor in the absence of light.

Rhodopsin is the first membrane protein of animal origin whose two-dimensional (Hargrave et al., 1983; Ovchinnikov et al., 1982) and three-dimensional (Palczewski et al., 2000) structures have been determined. The visual rhodopsin is a typical representative not only of the retinal-containing proteins, but also concurrently of a large family of G protein–coupled receptors (class A G protein–coupled receptors). The vertebrate retina is inverted in the sense that the light-sensing cells sit at the back side of the retina, so that light has to pass through layers of neurons and capillaries before it reaches the rods and cones. By contrast, the cephalopod retina has the photoreceptors at the front side of the retina, with processing neurons and capillaries behind them. Because of this, cephalopods do not have a blind spot (an area where axons from the ganglion cells can go back through the retina to the brain).

Octopus eye, like those of other invertebrates, develops as an invagination, or in-pocketing, of the skin, and not, as in the case of the vertebrate eye, as an extension of the brain (Roth, 2013, and references therein).

That is why it has to be a "smart" eye, functioning in a more efficient and versatile manner (Snowden et al., 2012, and references therein).

Cephalopods are sensitive to the polarization of light (which allows cephalopods to detect otherwise transparent prey such as jellyfish) (Pignatelli et al., 2011; Talbot and Marshall, 2011).

The rhodopsin family also includes proteorhodopsin, a bacterial version of rhodopsin, recently discovered in dinoflagellates (Fuhrman et al., 2008), sensory rhodopsins; and halorhodopsin and bacteriorhodopsin of the halophilic archaebacteria (Consani et al., 2011; Grote and O'Malley, 2011). Bacteriorhodopsin, also considered for use in bioelectronics, belongings to type 1 rhodopsins and functions in anoxygenic photosynthesis (energy conversion), emerged in prokaryotic cells about 3.5 billion years ago.

As mentioned above, the visual pigment rhodopsin, which belongs to type 2 rhodopsins (a G protein–coupled receptor) and performs photoreception (a sensory or information conversion process), emerged in the eukaryotic cells of multicellular organisms, about 1 billion years ago (Lamb et al., 2007). Primarily, the choice of those proteins for bioelectronics is dictated by the fact that the degree of conservation and functional selectivity as well as efficiency of the chromophore center in retinal-containing proteins are really amazing.

The chromophore-binding domain, formed at the earliest stages in the evolution of biosphere, contains all-*trans* retinal covalently bound to the apoprotein opsin in the case of bacteriorhodopsin and 11-*cis* retinal in the case of rhodopsin while none of the other 16 possible natural retinal isomers is a natural chromophore of the visual rhodopsin.

The uniquely organized chromophore center offers stereospecificity for an 11-*cis* isomer of retinal, as well as an exclusively high rate and efficiency of the photochemical reaction. After a photon is absorbed, the retinal chromophore is photoisomerized in about 100 fs in the case of both the vertebrate (bovine) (Nadtochenko et al., 2012; Polli et al., 2010) and invertebrate (octopus) (Yabushita et al., 2012) rhodopsins.

This suggests that by this time, approximately 100 fs, the system passes from the excited state to the ground state of the first photoproduct, photorhodopsin, which is completely formed by 200 fs (Polli et al., 2010; Schoenlein et al., 1991; Smitienko et al., 2010; see review: Ostrovsky and Feldman, 2012).

Moreover, we have demonstrated at the first time the photochromism of bovine rhodopsin on the femtosecond time scale at room temperature (Mozgovaya et al., 2010).

We have shown also the coherent regulation of this reverse photoreaction of chromophore group photoisomerization in the chromophore site of rhodopsin molecule.

The kinetics and efficiency of chromophore photoisomerization in the retinal-containing proteins is comparable to the theoretically computed rate of retinal isomerization in a gas phase (Martinez, 2010).

Efficiency of rhodopsin determined by the fact that retinal isomerization in a tight protein environment is comparable in the rate to its isomerization in a free volume. This amazing

phenomenon demonstrates the ideal structure of the chromophore center and the most efficient interaction of the chromophore with its nearest protein environment.

Actually, the chromophore center or chromophore pocket of opsin creates exactly the free space (660 $Å^3$ according to (Edwards et al., 2004)) for efficient 11-*cis* retinal isomerization.

There is no doubt of the importance of protein environment in the formation of an energy-unfavorable (nonplanar, distorted, and twisted) conformation of 11-*cis* retinal as a chromophore in the molecule of visual rhodopsin (Smith et al., 2010).

Owing to the successful crystallization of rhodopsin and its X-ray structure analysis, a three-dimensional structure of the rhodopsin molecule and its chromophore center have been described in sufficient detail (Ostrovsky and Feldman, 2012; Zhou et al., 2012). The first X-ray structure studies initiated a series of theoretical works (quantum mechanical computations and molecular simulation) that have attempted to describe the rhodopsin molecule in the dark, as well as after photon absorption (Mertz et al., 2012; Schapiro et al., 2011). Currently, the chromophore center, namely, a spatial position of 11-*cis* retinal and its interaction with the adjacent amino acid residues, is described in sufficient detail (Hubbell et al., 2003; Liang et al., 2003; Menon et al., 2001).

Such descriptions are fundamentally important for our understanding of the mechanisms involved in the spectral tuning of the visual pigments and explanation of their unique photochemical and physiological properties.

One of the unsolved problems in the description of 11-*cis* retinal spatial configuration as a chromophore is the question on the role of a nonplanar, disported, and twisted conformation of the chromophore in the acquisition of unique photochemical properties by the molecule of visual pigment. Very likely, the 11-*cis* retinal in rhodopsin acquires such a configuration due to the rotation of the β-ionone ring by approximately 65° relative to the plane of polyene chain (Feldman et al., 2009; Feldman et al., 2012; Kholmurodov et al., 2005; Kholmurodov et al., 2006).

Particularly, we have demonstrated the mutual "tuning" of 11-*cis* retinal and its nearest protein environment. A change in the 11-*cis* retinal spatial configuration, in particular, a turn of β-ionone ring around C6–C7 bond by 60° relative to the initial configuration, is observed as early as 300–400 ps after the beginning of simulation.

The rotation of β-ionone ring by 60° relative to the plane of the polyene chain leads to a change in the steric interaction between this ring and the amino acid residues forming an "aromatic cluster" and Leu266 where the distance between the β-ionone ring and Leu266 falls from 10 to 3.5 Å.

This agrees well with both theoretical computations (Saam et al., 2002) and experimental data (Salgado et al., 2004), according to which the β-ionone ring in the dark state of rhodopsin is turned by approximately 50–65° relative to the plane of the polyene chain.

In addition to the turn of β-ionone ring, a significant contributor to the formation of a twisted and strained 11-*cis* retinal configuration is the central part of the retinal polyene chain (C10–C13) (Gröbner et al., 1998; Lin et al., 1998; Verdegem et al., 1999). The question of how and in which spatial configuration 11-*cis* retinal enters the opsin chromophore center during rhodopsin regeneration should also be answered.

Note that the opsin chromophore center is rather spacious and can also accommodate other retinal isomers (for example, 9-*cis* retinal; in this case, the so-called isorhodopsin is formed, but this isomer has not been found in any natural visual pigment) (Singh et al., 2001) as well as its modifications (Imamoto et al., 1996).

Presumably, the configuration of 11-*cis* retinal when it enters the chromophore center is close to a planar one and only later, during its interaction with the adjacent amino acid residues, is the β-ionone ring rotated and the polyene chain twisted. 11-*cis* Retinal in such an unfavorable energy situation is in a state of increased preparedness to highly efficient photoisomerization and, on the other hand, stabilizes the G protein–coupled rhodopsin in its physiologically inactive dark state as an inverse agonist.

The question of why an 11-*cis* isomeric configuration of retinal was selected at the earliest stages of evolution as a chromophore of the entire visual protein family is also of interest and has been long discussed. One of the latest attempts to answer this question involved integrated quantum-mechanics and molecular-dynamics approaches (Sekharan and Morokuma, 2011). The structure, stability, energetics, and spectroscopy of 7-*cis*, 9-*cis*, 11-*cis*, and 13-*cis* retinal isomers in the vertebrate (bovine and monkey) and invertebrate (squid) rhodopsins were subject to comprehensive analysis. The obtained data suggest that one of the key factors during the

natural selection was the optimization of the electrostatic interaction between retinal and its nearest protein environment.

Certainly, we should keep in mind that other factors were also important in the selection of this particular isomer.

Among these factors are the efficient enzymatic synthesis of 11-*cis* retinal from all-*trans* retinal with the help of the protein RPE65 (retinol isomerase) in cells of the retinal pigment epithelium, the rate of 11-*cis* retinal binding to opsin and its integration into the chromophore center, stability of the dark rhodopsin at a physiological temperature, the efficiency of 11-*cis* retinal as an inverse agonist, and, naturally, the quantum yield and stereoselectivity of the ultrafast photoisomerization reaction.

15.1.2 Optical Reversibility and Photoregeneration of Rhodopsins

Studies of the forward and reverse (photochromic) reactions of rhodopsin were commenced as early as the beginning of the 1960s, when the laboratory of Wald demonstrated that a phototransition of bathorhodopsin (*trans* form of retinal) back to rhodopsin (11-*cis* retinal) with an insignificant amount of isorhodopsin (9-*cis* retinal) was possible at a temperature of liquid nitrogen (Yoshizawa, and Wald, 1963).

Indeed, the products of rhodopsin photolysis are photoactive. Photon absorption by photolysis intermediates can lead to a reverse *trans*–*cis* isomerization of retinal and the regeneration of rhodopsin (11-*cis* retinal–opsin) or, to a lesser degree, isorhodopsin (9-*cis* retinal–opsin) that is stable at a room temperature.

In the physiological literature, the restoration of a dark state of rhodopsin after absorbing a photon is referred to as rhodopsin "regeneration." In the case of vertebrates and humans, we speak about biochemical rhodopsin regeneration after its photolysis. In the case of invertebrates, when the rhodopsin molecule is not subject to photolysis, the physiological process of rhodopsin regeneration is, as a rule, represented by its photoregeneration after a comparatively long-lived intermediate (metarhodopsin) absorbs the second photon.

However, the photoregeneration of vertebrate rhodopsin from the intermediate stages of its photolysis is quite feasible and has

been experimentally demonstrated, although it hardly has any physiological importance.

Nonetheless, a study of the reverse photoreactions of rhodopsin is important for a better understanding of its photochemical transformations and has recently attracted considerable interest with the prospect of the application of the principle of photochromism of visual pigments in bionanotechnology.

Thus, rhodopsin photoregeneration is observed at almost all stages of its phototransformation.

In the case of vertebrate rhodopsin, the later photolysis products regenerate into rhodopsin (11-*cis* retinal) or isorhodopsin (9-*cis* retinal) with a lower efficiency than the early products.

In particular, the early product bathorhodopsin regenerates almost completely (Kim and Mathies, 2002) versus the 45% regeneration of metarhodopsin II (Shelyakin et al., 2012). It is important that no intermediates are formed in the reverse reaction, as is demonstrated by the presence of an isosbestic point in the absorption spectra recorded at different time moments (Krongauz et al., 1975a). An in vitro study of photoregeneration is a good tool for assessing the conformational changes in both the chromophore and protein moieties of the rhodopsin molecule at different stages of photolysis.

The mechanism of retinal *cis–trans* isomerization induced by a photon absorbed by rhodopsin was later confirmed mainly with the help of spectrometry (Kliger et al., 1984) and also by structural methods (using the rhodopsin analogs containing the 11-*cis* retinal with a fixed structure of the polyene chain (Mao et al., 1981; Mizukami et al., 1993)).

The phenomenon of isochromism was discovered when studying the forward and reverse reactions of rhodopsin. Its essence is that two spectrally indistinguishable forms of metarhodopsin I are generated in photolysis, one of which is able to photoregenerate and the other is not (Baker and Williams, 1971). Our further studies into photochromic reactions at low temperatures have demonstrated that, when rhodopsin is regenerated from metarhodopsin I, two spectrally identical (isochromic) rhodopsin forms are produced, one of which is stable at room temperature and the other is not (Krongauz et al., 1975b,c).

Using ESR spectroscopy with saturation transfer and spin labels covalently bound to the available (hydrophilic) SH groups

of the cysteine residues in rhodopsin (Cys140 and Cys316), we pioneered the recording of a photoreversible change in the conformation of rhodopsin protein moiety some time ago (Pogozheva et al., 1985) (as shown in Fig. 15.1).

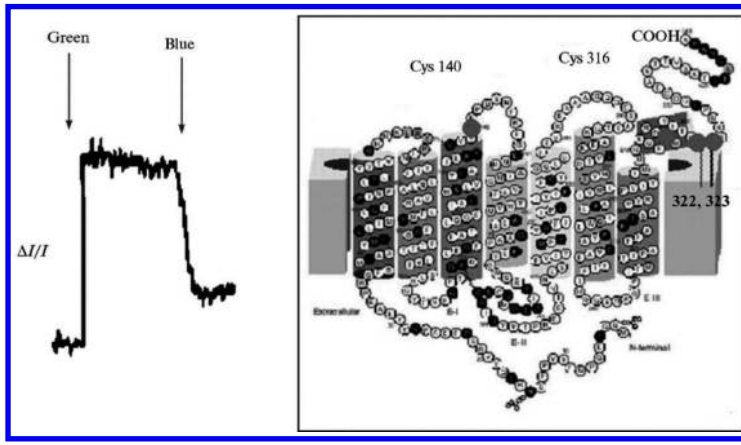

Figure 15.1 Photoreversible increase in spin label mobility at Cys140 during rhodopsin transition into metarhodopsin II induced by a green light and its decrease during metarhodopsin II transition into a mixture of rhodopsin and metarhodopsin III induced by blue light. (Left) Photoreversible increase in spin label mobility induced by green light and its decrease induced by blue light. (Right) Two-dimensional rhodopsin structure with indicated cysteine residues (Cys140 and Cys316) carrying covalently bound spin labels (Pogozheva et al., 1985).

We have demonstrated that the transition of rhodopsin into metarhodopsin II is accompanied by an increase in the conformational mobility of the cytoplasmic loops, while the reverse transition of metarhodopsin II into a mixture of products, including the photoregenerated rhodopsin and metarhodopsin III, is accompanied by a decrease in loop mobility (Pogozheva et al., 1985).

The dark regeneration of rhodopsin—the return of 11-*cis* retinal back to the chromophore center of opsin—leads to the restoration of a dark conformational state of rhodopsin; thus, the impact of light again causes a photoinduced conformational response of rhodopsin, now being regenerated (Shelyakin et al., 2012).

We have demonstrated the possibility of multiple in vitro phototransitions of octopus rhodopsin into metarhodopsin and back into rhodopsin at room temperature (Ostrovsky and Weetall, 1998) (as shown in Fig. 15.2).

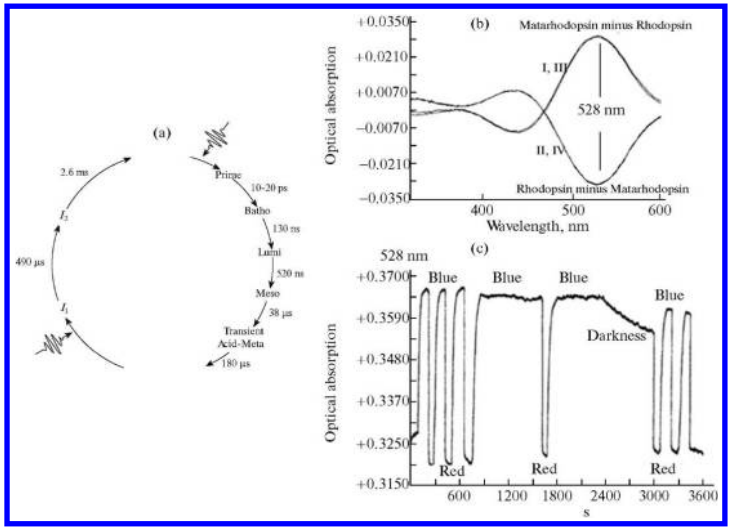

Figure 15.2 Photoreversibility of invertebrate (octopus) rhodopsin: (a) a photocycle of octopus rhodopsin; (b) differential spectra (four photocycles); and (c) multiple rhodopsin metarhodopsin phototransitions (t = 20°C) (Ostrovsky and Weetall, 1998).

A promising new direction in research utilizing femtosecond laser spectroscopy may be the study of specific features of the photoreactions taking place in rhodopsin with a genetically modified chromophore center. Such studies will attempt to clarify the specific structural features of the opsin chromophore center as an ideal protein environment providing and enhancing the photoisomerization of retinal chromophore, which is unique in its rate and efficiency.

15.2 Thin Films of Octopus and Bovine Rhodopsins

Bacteriorhodopsin (bR) and other light-sensitive proteins, including visual pigments (rhodopsin) from bovine (Maxia et al., 1995; Pepe et al., 1996; Pepe et al., 1998; Pepe and Nicolini, 1996), photosynthetic

reaction centers (Facci et al., 1994) are of interest for use in biomolecular electronic applications (Hampp et al., 2002; Maccioni et al., 1996; Nicolini et al., 1998, 1999; Paternolli et al., 2004). The unique combination of photochromic, photoelectric and electro-optical properties of these proteins is of great fundamental and applied interest.

Bacteriorhodopsin is a promising candidate for information processing because of its astonishing stability against chemical, thermal, and photochemical degradation as well as its efficient photochemistry and excellent reversibility (Birge, 1995). Retinal analogs of bR (Stryer, 1986) and genetic modification are the keys for utilization of this photochromic compound in biomolecular electronic applications.

There are few data indicating that the rhodopsin molecule can be stabilized in some of the intermediates of its photoreversible transformation. Rhodopsin, an integral membrane protein consists of a chromophore, the 11-*cis* isomer of retinal, covalently bound via a PSB to the E-amino group of a lysine residue of the apoprotein opsin. Light isomerizes the 11-*cis* chromophore to the all-*trans* form, resulting in protein conformational changes in rhodopsin that initiate the enzymatic cascade, resulting in the electrical excitation of the photoreceptor cell (Druzhko et al., 1996; Tsuda et al., 1986; Tsuda, 1987).

Although the primary photochemistry of vertebrate and invertebrate rhodopsins are similar, vertebrate rhodopsins eventually hydrolyze to free retinal and opsin, whereas invertebrate ones reach a stable pigment, metarhodopsin.

The photostability and photoreversibility of the OR protein extracted by this procedure is reported in solution in (Ostrovsky and Weetall, 1998), which, however, do appear to work only in solution. No more than one or two cycles were observed in the polymeric matrix (Ostrovsky and Weetall, 1998).

In this work, we report a new biomaterial obtained by means of an easy and fast method of extraction of the rhodopsin from retinas and characterized by several biophysical probes in order to test the photoreversibility and the photostability of the octopus rhodopsin in an extract obtained starting from octopus eyes (demonstrating that the isolation procedure is preserving the function of OR) and for octopus rhodopsin films prepared by gel-matrix entrapment method.

For extraction and purification of rhodopsin from Octopus eyes frozen eyes were hemisected, the retinas collected and washed in dim red light. Then retina samples were sonicated in darkness with a microtip in a falcon tube under external ice-cooling (65% amplitude, 1 s pulse duration, 15 s pause, 5 min exposure). Maximum temperature of sample: did not exceed 12°C during this procedure. After sonication, the sample was loaded onto a sucrose cushion and centrifuged, then only the supernant sample was used for all the measurements. Rhodopsin concentration was determined spectrophotometrically at and resulted in sample concentration was found to be of circa 100 μM. Mass spectrometry was further used to verify the presence of the rhodopsin characteristic mass peak.

To prepare optical films based on octopus rhodopsin, aliquots of rhodopsin solution were diluted with purified water and were centrifuged and the pellet resuspended in polyvinyl alcohol. Then the films were obtained by casting, gel-matrix entrapment method (Antonini et al., 2004), and dried in controlled atmosphere overnight.

Protein concentration was determined from UV/Vis spectra, and extraction of octopus rhodopsin (OR) was performed by SDS-PAGE as described in (Laemmli, 1970). The concentration of OR was found to be 3.15 mg/mL, and purity grade determined as in (Nakagawa et al., 1997) from absorbance values at A280 and absorbance maximum at A482 was estimated as 18.6%.

The photochromism was investigated by illuminating the sample via flashlights, using at wavelengths of 431 and 546 nm. The difference spectra were obtained subtracting the rhodopsin to the acid metarhodopsin, namely from illuminated sample spectrum minus spectrum of the same sample kept in dark until no further spectral changes were observed. The photostability tests were performed utilizing the filters in continuous cycles.

Morphology was characterized by atomic force microscopy (AFM) in intermittent contact mode in air by using a standard silicon cantilever.

Photoelectrical measurements of the activity of the extracted and purified OR was made on water-dissolved material electrodeposited upon an indium-tin oxide (ITO) covered glass, applying a positive voltage of 20 V for 20 min., with a platinum counter-electrode. The ITO glass was as a result covered with a

purple layer, the excess water was removed using a syringe and evaporation. The completely dried ITO glass was aluminum electrode-evaporated and photovoltage response was measured using an electrometer.

Details of experimental procedures may be found in (Paternolli et al., 2009).

Figure 15.3 shows the photoreversibility of the gel-matrix films. It is possible to observe that absorbance signal in gel-matrix film is ten times lower than in solution one, probably because of the presence of the PVAL that partially screen the light.

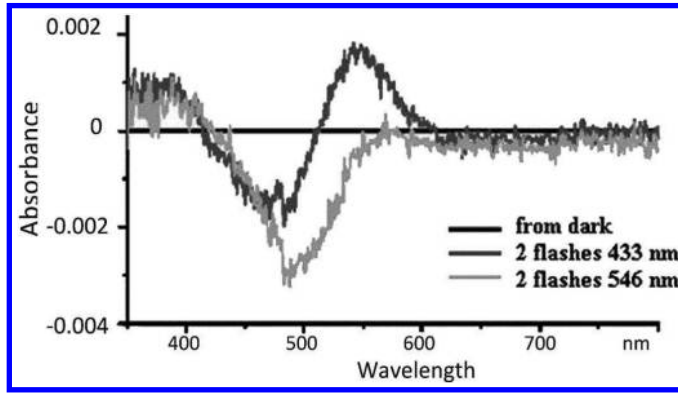

Figure 15.3 Photoreversibility of the gel-matrix OR films.

In Fig. 15.4, the photostability of the gel-matrix sample is reported. It is possible to observe that the behavior of the rhodopsin is the same in solution and in gel-matrix films. This demonstrates that the peculiar characteristics of the octopus rhodopsin purified by this method are maintained in solution and in films. No significant changes in absorption spectra have been found working with gel-matrix films leaved at room temperature and even with films 3 days old.

The AFM image of an isolated membrane is shown in Fig. 15.5 showing that about 9 nm-wide areas are randomly distributed over the membrane.

Finally, positive tests of light response of the extracted and above purified OR were carried out in a dark room using a standard incandescence bulb, placed 30 cm far from the sample. A significant photovoltaic activity can indeed be observed in Fig. 15.6, despite the low degree of purity of only 18%. The observed photovoltaic

response of rhodopsin from octopus represents an adequate proof of photoelectric activity bound to improvement with increasing the OR degree of purity (in progress).

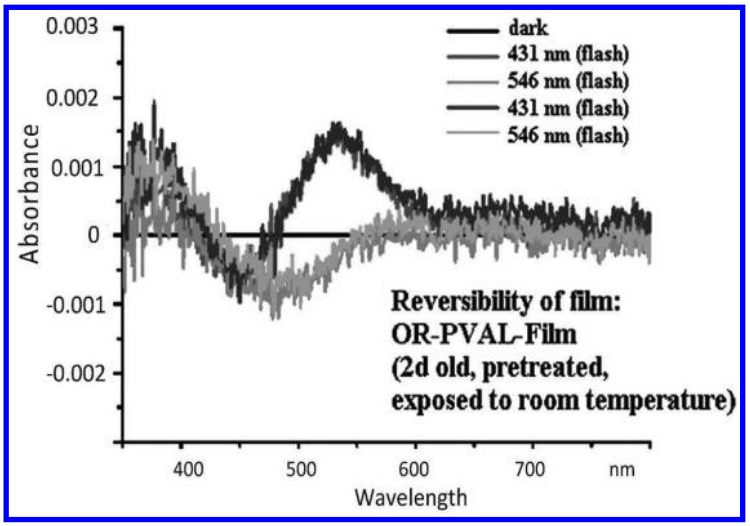

Figure 15.4 Photostability of the gel-matrix OR films.

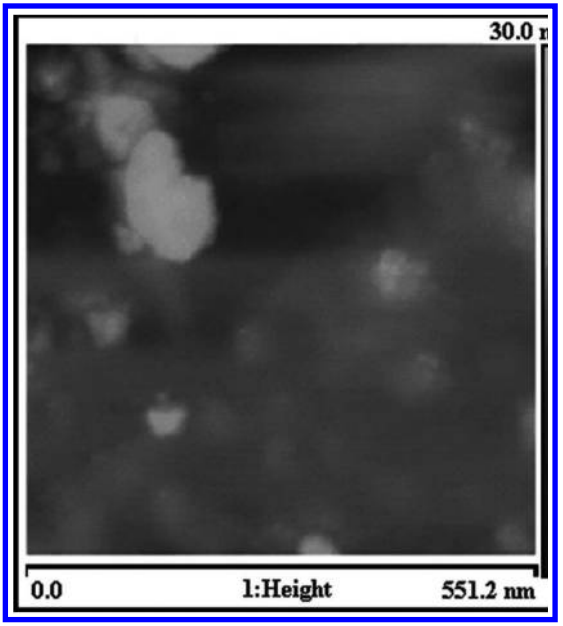

Figure 15.5 AFM image of one of the octopus retinas.

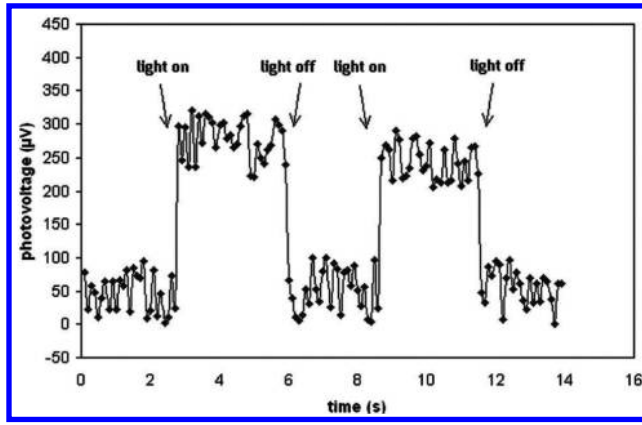

Figure 15.6 Photovoltaic response of the extracted and above purified OR.

L-B films of *bovine* rhodopsin were prepared by spreading rhodopsin, solubilized into 0.75% octylglucoside, at the air-water interface. As this preparation was performed in room light, the term opsin will be used instead of rhodopsin. The resulting monolayer was compressed by two moving barriers and consequently the surface pressure of the film increased from 20 to 35 mN/m. Depositions were then performed at a surface pressure of 35 mN/m. The surface density of the monolayer was measured by depositing opsin L-B film (up to 10 layers) on the quartz resonator of a nanogravimetric gauge. Result of the surface density of the monolayer was –5.9 ± 1.3 ng/mm^2 (SD of 10 measurements). Assuming that most of the material deposited was opsin, the area per molecule was deduced from this value.

The molecular mass of bovine rhodopsin bR being 39,000 g/mol (Dratz and Hargrave, 1983), which is -6.5×10^{-20} g/molecule, the number of opsin molecule per square millimeter resulted in 0.908×10^{11} molecules/mm^2 and therefore the area occupied by one molecule of opsin in the L-B film was 1.1×10^{-11} mm^2 = 1100 Å^2. This value is close to that of the area occupied by a molecule with a diameter of 40 Å, such as the molecule of rhodopsin, which is thought to have a cylinder shape of roughly 40 Å × 60 Å with the larger dimension perpendicular to the plane of the disk membrane (Dratz and Hargrave, 1983; Schertler et al., 1993).

The X-ray diffraction pattern of 30 layers of opsin L-B film at room temperature shows a wide reflection at –20 = 1.5 from

which, using the Bragg relation, a periodicity of –59 Å ± 3 Å was obtained. This value is in agreement with the longer dimension of rhodopsin—60–65 Å, as reported in the literature (Dratz and Hargrave, 1983), which suggests that the assembly of opsin in L-B films could be similar to that in disk membranes.

The data shown in Tables 15.1 and 15.2 at 25°C suggest that the L-B film organization caused only small modifications of the secondary structure of opsin.

Table 15.1 Temperature dependence of rhodopsin secondary structure in L-B film calculated from CD spectra of rhodopsin L-B film (30 layers) at different temperatures

T (°C)	Alpha-helix(%)	Beta-sheet(%)	Beta-turn(%)	Random coil(%)
25	68	13	7	12
100	68	14	4	14
125	66	10	5	19
150	66	7	5	22
175	58	5	1	36
200	50	3	5	42

Table 15.2 Temperature dependence of rhodopsin secondary structure in solution calculated from CD spectra of rhodopsin solution at different temperatures

T(°C)	Alpha-helix (%)	Beta-sheet (%)	Beta-turn (%)	Random coil (%)
25	68	12	9	11
45	63	12	9	16
65	59	14	10	17
85	42	24	14	20
95	40	20	13	27

The thermal stability of the secondary structure of opsin in the L-B film was studied by CD in the range between 25 and 200°C. CD spectra were used for computation of the percentage of alpha-helix, beta-sheet, beta-turn, and random coil of rhodopsin by a modified Hennessey–Johnson procedure (Carrara et al., 1992).

Although these calculations are based on a set of standard globular proteins (Chang et al., 1978), they merely indicate (see Table 15.1) that opsin in the L-B film maintained its secondary structure up to at least 150°C with no significant loss of the helix

structure, as a partial unfolding process was evident only at 175°C. The small changes in the secondary structure shown from 25 to 150°C were irreversible, as there was no change in the CD spectra of the heated samples when they were brought to room temperature.

When the preparation and deposition of rhodopsin films were made in dim red light, the secondary structure of the protein remained unchanged up to at least 200°C. As a comparison, the thermal stability of the secondary structure of bleached rhodopsin in solution is shown in the calculations of the percentage of secondary structure, based on these spectra, are shown in Table 15.2. The results indicate that opsin in solution as in L-B film had an alpha-helix content of 68% at 25°C, close to the value of –62% reported in the literature (Shichi, 1971) which decreased gradually from 45 to 95°C. At 95°C the alpha-helix content was 40% and the random coil 47%, whereas opsin in L-B film at 100°C showed negligible variation of its secondary structure.

The order of opsin molecules in the direction normal to the film plane was also maintained in the heated multilayers as suggested by the low-angle X-ray scattering measurements. The Bragg reflection at 2θ = 1.5 measured at room temperature remained almost unchanged up to 150°C and began to disappear at 175°C corresponding with the loss of secondary structure shown by the CD measurements.

The preservation of the secondary structure of rhodopsin in L-B film does not necessarily mean the preservation of its functionality such as its ability to absorb photons in the visible range. To obtain spectrophotometric information, the preparation and the deposition of rhodopsin L-B film were performed under dim red light. The UV visible spectrum of 90 layers of rhodopsin was recorded in the dark at different temperatures. The curves show that the characteristic absorbance at 500 nm was preserved up to at least 80°C (Fig. 15.7c) and began to have a small decrease at 90°C (Fig. 15.7d). The increase of temperature was accompanied by an increase of light scattering. However, the absorbance maximum at 500 nm was still present at 1000°C and the recorded spectrum remained identical when the sample was kept in room light for hours, showing no bleaching process. The same rhodopsin solution used to make the L-B film showed instead a collapse of the 500 nm absorbance maximum at –700°C in the dark (data not

shown), as already reported in the literature from calorimetric measurements on rhodopsin in disk membranes (Khan et al., 1991).

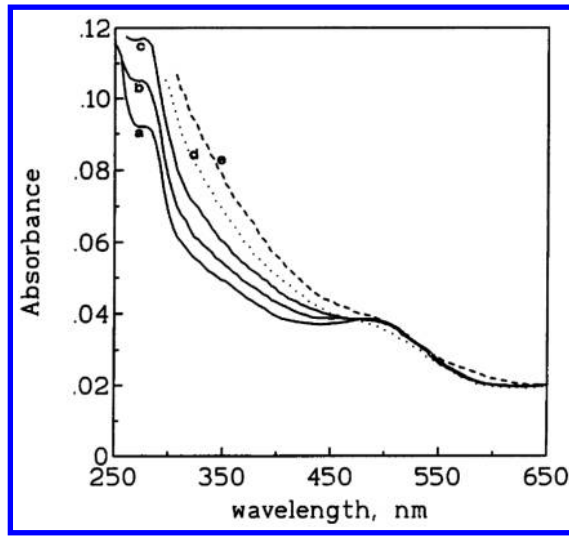

Figure 15.7 Absorbance spectra of rhodopsin L-B film (90 layers) at room temperature (a), 60°C (b), 80°C (c), 90°C (d), and 100°C (e). Rhodopsin film was prepared, deposited and dried in vacuum in dim red light, and then put in the oven for 10 min at the temperatures indicated. The spectrophotometric measurements were made at room temperature.

Thus, L-B films were made by spreading opsin solubilized in 0.75% 03-octylglucoside on the surface of the subphase in the L-B trough and then compressing them isothermically with two moving barriers. As reported in the literature (Hann, 1990; Lvov et al., 1991), it seems well established that the detergent molecules with short hydrocarbon chains such as the 13-octylglucoside used in these experiments, do not form stable monolayers at relatively high surface pressure, so that during compression they are transferred to the subphase in the form of micelles. Therefore, it is very likely that in these conditions a homogeneous film made up of mainly opsin was formed, with each molecule in close contact with the other, as suggested by the surface per molecule of 1100 $Å^2$ deduced from nanogravimetric measurements. This value, which is affected by an error of –20%,

is in accordance with those reported for the area occupied by one molecule of rhodopsin without the surrounding lipids: –800 $Å^2$ was obtained for frog rhodopsin (Dratz and Hargrave, 1983) and –1100 $Å^2$ was deduced from the measurements of surface pressure on bovine rhodopsin films (Salesse et al., 1990). Furthermore, the opsin molecule in the L-B layer would have the longer cylindrical axis perpendicular to the plane of the film as in native disk membranes. This was suggested by the X-ray diffractometric measurements, from which a periodicity of –59 ± 3 Å can be deduced. This value is comparable with 60–65 Å as reported for the longer dimension of the rhodopsin molecule (Dratz and Hargrave, 1983). The same conclusion was reached by Salesse et al. (1990); that is, the orientation of bovine rhodopsin in films compressed at lateral pressure of 38 mN/m (very near the deposition pressure of 35 mN/m used in our experiments) was the same as in intact disk membranes. From these data, a picture emerges of a two-dimensional L-B layer mainly made up of opsin molecules that are packed closer than in the already crowded disk membranes. In the latter ones, in fact, the molecules of rhodopsin per square millimeter are -2.7×10^{10} (Stryer, 1986) and the disk membrane area per molecule occupied by one molecule of rhodopsin with the surrounding lipids was calculated to be –3400 $Å^2$ (Dratz and Hargrave, 1983).

The CD spectra of opsin solutions were very similar to those of L-B films, suggesting that opsin did not alter its secondary structure significantly when assuming a two-dimensional quasi-crystalline configuration of the film.

The most striking property of rhodopsin in L-B films was the thermal stability of its secondary structure, which was maintained up to 150°C in room light and up to at least 2000°C in dim red light. This improvement of stability was also measured in disk membranes where the temperature of rhodopsin denaturation was –56°C for bleached samples and –72°C for samples kept in the dark (Khan et al., 1991). This is because of the more compact conformation of rhodopsin when it binds its chromophore compared with that of bleached rhodopsin in which the linkage between opsin and retinal is broken.

The thermal stability of opsin layers was also supported by X-ray diffraction measurements. The periodicity of –59 Å was maintained almost unchanged up to 150°C, showing a good

correlation with the negligible changes of the CD spectra in the same range of temperatures. At 175°C, however, the periodicity of the opsin layers was partially lost probably because of a kind of melting of the protein in correspondence with the change in the secondary structure shown by the CD spectra at the same temperature.

The increased thermal stability of opsin in L-B films seems to be a general property shared by other proteins (Erokhin et al., 1994; Nicolini et al., 1993; Shen et al., 1993) and is likely a result of the molecular order induced by the L-B film formation. In a CD study on anti-insulin antibody, a lyophilized sample was found more resistant to temperature than the corresponding antibody solution but less resistant than the same antibody in L-B films, which led to the conclusion that although dehydration plays an important role in structure preservation, the main stabilizing factor is the molecular close packing of the L-B film (Erokhin et al., 1994; Nicolini, 1995).

The characteristic absorbance maximum at 500 nm, on the other hand, was less stable, as it began to decrease between 90 and 100°C. When exposed to light, rhodopsin in L-B films did not bleach, as expected, because the binding between retinal and opsin does not hydrolyze in dry conditions. After flash illumination at room temperature, rhodopsin embedded in dry gelatin films (Wald et al., 1950) or in air-dried phospholipid multilayers (Applebury et al., 1974; Korenbrot and Pramik, 1977) was converted into thermally stable metarhodopsin I (absorbance maximum at 480 nm).

In our experiment, however (see Fig. 15.7), the exposure of rhodopsin L-B films to the room light apparently did not affect the 500 nm absorbance maximum. Therefore, this result could be interpreted as if rhodopsin had reached a kind of photostability when assembled in L-B films, unless rhodopsin was converted into its intermediate lumirhodopsin, which has a maximal absorbance at –497 nm. The latter is so close to the absorbance maximum of rhodopsin as to be indistinguishable in our experimental conditions.

This last interpretation would be in accordance with the results reported by Guerette et al. (1988) on the photochemical activity of the dried, aggregated form of bovine rhodopsin depleted of detergent. In conditions that share some similarities with ours, these authors found that the bleaching sequence of rhodopsin

when exposed to daylight reached the step of lumirhodopsin, which then remained stable at room temperature. The increase in light scattering of rhodopsin films with the temperature (see Fig. 15.7) was unexpected. It might have been a result of some degree of aggregation of rhodopsin molecules during heating.

15.2.1 Computer Modeling toward Use of Octopus Rhodopsin for Quantum Computation

Functionally, octR is a light transducer that captures single light quanta, while bR is a light harvester that does not require high sensitivity.

Structurally, octR and bR belong to the structural superfamily of rhodopsin-like proteins sharing the overall seven transmembrane helix topology of BR except for some details in distances and relative orientations of the helices (Faulon et al., 2003). This allows one to use bR as the primary template for all structure/function studies.

Similarities and differences between visual rhodopsins and bacteriorhodopsins are extensively discussed elsewhere (Bryl, 2003), mainly using bovR as an example. Less attention has been paid to cephalopod rhodopsins, in which rhodopsin is the main component of microvillar membranes, microvilli being cylindrical extensions of the cell membrane, arranged hexagonally within the rhabdome (photoreceptor) (Pepe and Cugnoli, 1992).

As the first step, we build a 3D model of octR using bovR as a template and compare it with the structure of bR (Fig. 15.8). We also discuss this comparison in terms of nanotechnology applications that have been reported for bR (Nicolini et al., 1998) but can also be implemented in octR. We also built a model for mutant protein aimed at ocrR/bR interconversion. We decided to explore only possible mutations in the immediate surroundings of the retinal, while mutations affecting the overall fold will be addressed elsewhere.

Selecting a tool for modeling the 3D structure of octR. For a transmembrane GPCR protein like octR, this is not a trivial task. While classical homology modeling is still successfully used (Miedlich et al., 2004), two other approaches were implemented, one based on intraprotein hydrogen-bond optimization (Pogozheva et al., 1997) and the other based on first principles of transmembrane protein assembly (Trabanino et al., 2004). As for the hydrogen-

bond optimization approach, it seems to be working well if experimentally derived constraints are used, but the experimental data underlying these constraints are themselves under discussion for octR. Besides, the presence of retinal within the transmembrane part of the molecule could hamper correct hydrogen bond assignment, which is crucial for accuracy of the method.

```
brGround  5                                          TGRPEWI WLALGTALMG
ModelHel  1     MVESTTLVNQ TWWYNPTVDI HPHWAKFDPI PDAVYYSVGI FIG-------

brGround  22    LGTLYFLVKG MGVSDPDAKK FYAITTLVPA IAFTMYLSML LGYGLTMVPF
ModelHel        ---------- ---------- ---------- ---------- ----------

brGround  72    GGEQNPIYWA RYADWLFTTP LLLLDLALLV DADQGTILAL VGADGIMIGT
ModelHel        ---------- ---------- ---------- ---------- ----------

brGround  122   GLVGALTKVY SYRFVWWAIS TAAMLYILYV LFFGFTSKAE SMRPEVASTF
ModelHel        ---------- ---------- ---------- ---------- ----------

brGround  172   KVLRNVTVVL WSAYPVVWLI GSEGAGIVPL NIETLLFMVL DVSAKVGFGL
ModelHel        ---------- ---------- ---------- ---------- ----------

brLstate  222   ILLRSRAIFG ETGRPEWIWL ALGTALMGLG TLYFLVKGMG VSDPDAKKFY
ModelHel  44    ---------- ---------- -VVGIIGILG NGVVIYLFSK TKSLQTPANM

brLstate  44    --AITTLVPA IAF--TMYLS MLLGYGLTMV P-FGGEQNPI YWARYADWLF
ModelHel  73    FIINLAMSDL SFSAINGFPL KTISAFMKKW IFGKVACQLY GLLGGIFGFM

brLstate  89    TTPLLLLDLA LLVDAD---- ---------- ---------- -----QGTIL
ModelHel  123   SINTMAMISI DRYNVIGRPM AASKKMSHRR AFLMIIFVWM WSIVWSVGPV

brLstate  110   ALVGADGIMI GTGLVGALTK VYSYRFVW-- WAISTAAMLY ILYVLFFGFT
ModelHel  173   FNWGAYVPEG ILTSCSFDYL STDPSTRSFI LCMYFCGFML PIIIIAFCYF

brLstate  158   SK-------- ---------- -------AES MRPEVASTFK VLRNVTVVLW
ModelHel  223   NIVMSVSNHE KEMAAMAKRL NAKELRKAQA GASAE-MKLA KISMVIITQF

brLstate  183   SAYPVVWLIG SEGAGI---- ----VPLNIE TLLFMVLDVS AKVGFGLILL
ModelHel  272   MLSWSPYAII ALLAQFGPAE WVTPYAAELP VLFAKASAIH N-PIVYSVSH

brLstate  225   RSRAIFGE--
```

Figure 15.8 Structural alignment of octopus rhodopsin with the ground state and the L state of bacteriorhodopsin. The start of the L state sequence is marked in bold.

The first principles approach is more attractive considering also that it has already been tested on bovine rhodopsin. Since it is mostly based on assigning the transmembrane helices, we started by predicting positions of the helices and then manually adjusting the resulting alignment of octR versus bR using sequence identity and similarity. The resulting approach is therefore a hybrid between homology modeling and first-principles modeling.

Model quality estimated by comparison of the model with its template. One can see that the model reproduces the positions of the residues surrounding the chromophore (retinal) correctly,

particularly the Lys306 residue providing the Schiff base connection of the protein to the retinal. Notably, the model shows higher alpha helical content than its template (203 versus 190 alpha helical residues), a rare occasion in comparative modeling. Definitely some factor other than the rhodopsin structure itself is responsible for the high ordering of octR in vitro, and, as further analysis will suggest, this could be the interaction with another transmembrane protein present in membranes together with octR.

Since all visual pigments described to date have distinctive features (Nathans, 1992), the quality of the model can be assessed by the model's ability to reproduce those features. The first is a lysine in the middle of the seventh putative transmembrane segment, corresponding to Lys-296 in bovine rhodopsin, which is the site of covalent binding of the chromophore via a retinylidene Schiff base. In our case, it is Lys306. The next feature is a pair of cysteines corresponding to Cys-110 and Cys-187 in bovine rhodopsin, which are presumed to form a disulfide bond connecting the first and second extracellular loops. These are present in our model as Cys109 and Cys187. Another quality indicator is the presence of the sequence (Glu/Asp)–Arg–Tyr, or a close match to this sequence, at the beginning of the second cytosolic loop, in our case it is Asp133, Arg134, and Tyr135. Finally, one or more serine or threonine residues should be located in the cytosolic carboxyl terminus, which in bovR are the sites of light-dependent phosphorylation by rhodopsin kinase. In our model, those are threonines 329, 330, and 336.

Identity of the counterion is another important issue with respect to both the structure/function relationships and nanotechnology applications. Indeed, in both octR and bR, the conformational rearrangements required for function (proton pumping for bR, signal transduction for octR) demand precedent storage of energy, which is in both cases achieved by separating the charge of the retinal/lysine Schiff base from its counterion, acting also as a starting point for proton pumping in bR. Our model predicts that the position equivalent to the bovR counterion (Glu113) is occupied by Tyr112. This tyrosine 191 always remains neutral (Nakagawa et al., 1999) so its role as the counterion is ruled out. However, our model predicts that the residue Glu181 is within 5 Å of the Schiff base nitrogen and can, therefore, serve as the counterion. This is in perfect agreement with the recent mutational

analyses proving that it is the Glu181 that is the counterion in invertebrate rhodopsins (Terakita et al., 2004) while the vertebraterhodopsin counterion (Glu113 in bovR) was acquired later in the course of evolution. For comparison of the octR model with bR and mutations suggested for octR/bR interconversion, considering that the ground-state isomers of retinal are 11-*cis* for octR and all-*trans* in bR (Fig. 15.8), we attempted to accommodate an all-*trans* retinal in the octopus opsin by means of molecular modeling. We tried to introduce all-*trans* retinal into a new cavity in which it would have the same surroundings as in bR. The latter was done by introducing putative mutations. The resulting mutant octR should possess similar properties to bR, at least in the immediate vicinity of the retinal environment. The mutations suggested to graft the bR-like retinal binding pocket to octR are Gly120Trp, Phe121Met, Ile124Trp, Gly209Ser, Tyr278Trp, Val302Lys, Ala305Tyr, and Lys306Phe. The resulting retinal-binding pocket is presented in Fig. 15.9.

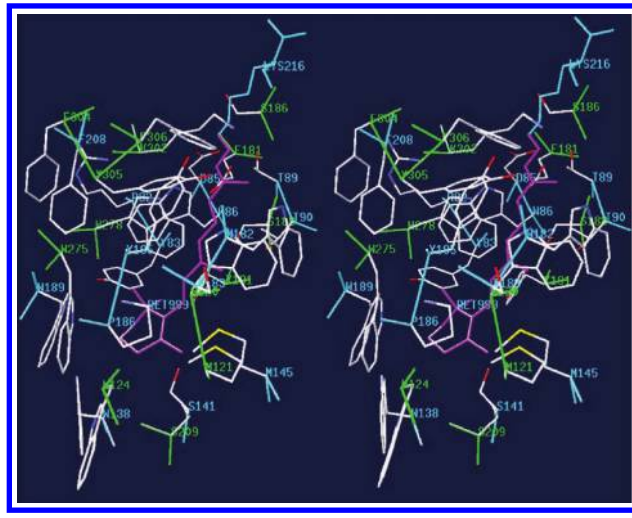

Figure 15.9 Stereo view of the retinal-binding pocket in the putative mutant octopus rhodopsin superimposed on the retinal pocket of bacteriorhodopsin. Backbones of the octR and bR as well as residue numbers are in green and cyan, respectively. Side chains are CPK-colored.

One can see that no mutation is required to insert the counterion into octR at the spatially equivalent position of bR.

Indeed, the Asp83 of bR and Glu181 of OctR are less than 3 Å apart. The mutation Gly120Trp is required to insert a tryptophan residue at the position identical to that of Trp182 of bR. The Trp182 is known to be responsible for the functionally important interaction with the retinal 9-methyl group in the L intermediate (Maeda et al., 1995). The mutation Phe121Met in octR reproduces the Met145 of bR, for which computer simulations predict involvement in the binding pathway of retinal (Israleweitz et al., 1997). The mutation Ile124Trp introduces a tryptophan equivalent to Trp138 in bR, which is involved in a functionally important pi-cloud H-bond with Trp189 in bR while the Tyr278Trp is designed to provide the equivalent of Trp189 of bR, which exhibits marked UV Raman spectroscopy-detected changes in its environment during the photocycle (Rouhani et al., 2001). The Val302Lys and Lys306Phe are the crucial mutations shifting the retinal attachment site. The Lys302 now provides the Schiff base link to the retinal, while Phe306 should block the retinal isomerization to 11-*cis*. The Ala305Tyr mutation is introduced to mimic the bR residue Tyr185. The remaining residues neighboring the retinal already have their structural counterparts in the native octR and require no mutation. One can see that three new tryptophan residues are proposed to be introduced in the mutant octR. According to our model, the mutations proposed for moving the Schiff base linkage to another position should result in absorbance spectrum changes, as well as change of the time scale of the earliest photoprocess detected.

To find out if the native octR could accommodate retinal that is the excited state for octR but the ground state in bR, we inserted all-*trans* retinal into the native octR retinal cavity. This allowed checking if octR could bind all-*trans* retinal in the same way as it binds its native ground-state 11-*cis* retinal. These very simplified strategies are dictated primarily by the approximate nature of homology modeling.

As follows from Fig. 15.10, octopus opsin should readily recombinate with all-*trans* retinal. The superimposed structures allow one to see that octR opsin can accommodate retinal both in its native 11-*cis* conformation and in the all-*trans* conformation. This is supported by the experimental data (Koutalos et al., 1989) showing that while both bovR and octR are easily regenerated with their native 11-*cis* retinal, octR can be additionally regenerated with all-*trans* retinal and moreover the 13-*cis* retinal which is the native

ground-state chromophore for bR. It is further supported by the recent finding that rhodopsin from lancelet (amphioxus), a primitive chordate, is, like octR and unlike bovR, able to bind all-*trans* retinal, and mutational analyses revealed that Trp265 is responsible for this property (Tsukamoto et al., 2005). We found that the pairwise homologies between rhodopsins from lancelet and octopus, as well as bovine and octopus rhodopsins, are similar (about 30% identity) but the 275th amino acid position in our octR model equivalent to the 265th position of lancelet rhodopsin is also occupied by tryptophan (data not shown). In contrast, there are no tryptophans at the corresponding position of bovine rhodopsin or positions close in its amino acid sequence.

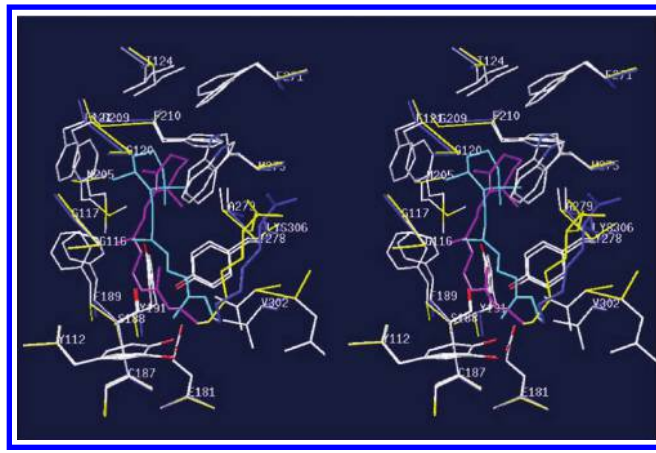

Figure 15.10 Stereo view of the superimposed retinal-binding pocket for 11-*cis* (left) and all-*trans* (right) retinal. The retinal is colored in magenta and cyan respectively, backbone atoms in yellow and blue, respectively, and side-chain atoms, according to the CPK scheme.

On the one hand, this adds to the validity of our octR model since it predicts not only the experimentally known effect, i.e., the ability of octR to bind all-*trans* retinal, but also its cause, i.e., the tryptophan at the 275th position. On the other hand, none of the mutations proposed in this paper is at the 275th position, so they are unlikely to affect this property. Besides, the mutation of the neighboring Tyr278 to Trp, proposed herein, is unlikely to affect the conformation of Trp275 because both Tyr and Trp residues have aromatic side chains.

However, the conformations of the ionone ring in the model of all-*trans* reconstituted octR and the 11-*cis* dark-state octR are not easily interconvertible within the protein because of contacts with protein side chains.

This is supported by the fact that intraprotein conversion of 11-*cis* to all-*trans* conformation in any rhodopsin requires the entire range of the photoprocess, which has the time scale of milliseconds. Upon activation by light followed by transition through batho- and mesoto limi-rhodopsin, the retinal molecule dissociates from octR to form the free retinal and the octopus opsin, so octR regenerates again only after the retinal has been converted into the 11-*cis* configuration. However, our data, as well as evidence for the presence of alternative binding sites for retinal on opsin (Schädel et al., 2003), suggest that unless the all-*trans* retinal is quickly transformed into 11-*cis* retinal upon release into the lipidic matrix or bound to some transporter protein delivering it to and from the isomerization site, it will be very likely sequestered by the same octopus opsin, thus leading to the inactive form of octR, thereby terminating the visual cycle. In reality, the visual cycle is not terminated, which implies that the all-*trans* retinal release from octR is followed by its uptake by a protein other than rhodopsin.

The body of experimental data available for invertebrate rhodopsins suggest that the retinochrome is located away from the rhodopsin but linked to it via a shuttle protein RALBP (Terakita et al., 1989). We will now consider the distance from the site of retinal release from octR at which retinal uptake by RALBP must take place.

Assume the excessively high diffusion coefficient of $D = 10^{-7}$ cm^2/s for retinal in the membrane. Assume also that the time available for the all-*trans* retinal before it is sequestered by the octopus opsin as $t = 10^{-7}$ s, again unrealistically large because such a process should be limited by side-chain and main-chain torsional motions of the opsin and/or torsional motions of the retinal, all of which are at the nanosecond to picosecond time scale. Then, the maximal distance to which such "free" all-*trans* retinal can travel will be given by the Einstein–Smoluchowski equation $d = (2\,Dt)^{1/2} = 1.5 \times 10^{-7}$ cm, which is only 15 Å. Therefore, the RALBP protein must be located very near the rhodopsin. Importantly, in other invertebrates like honeybee, such a retinal

binding protein has also been detected and, moreover, is able to perform the function of retinochrome (Pepe et al., 1990).

15.3 Preliminary Conclusions on Fundamental Properties of Rhodopsins Essential for Use in Nanobioelectronics

Image processing by octopus rhodopsin is done at the optic lobe of the brain (Thompson, 2011). There is no separate optic nerve in the octopus eye; rather photoreceptors are connected directly to the optic lobe by passing over the surface of the eye. Accordingly, octopus rhodopsin (octR) is exceptionally well ordered in their membranes in vivo so the regular structure of the photoreceptors in the octopus eye has been used as a model for an artificial retina (Kim, 2011), have neither 3D structures nor suitable crystals.

The close relative of octopus rhodopsin, Bovine rhodopsin (bovR), been crystallized, both in 2D and 3D, even though it does not form regular arrays in vivo. Instead, octopus rhodopsin (octR), failed to crystallize, though it does not form regular arrays in vivo, though its close homolog, squid rhodopsin, has been crystallized both in 2D and 3D (Sugihara et al., 2011, and references therein). This apparent contradiction obviously still merits clarification.

15.4 Applications

15.4.1 Photoreversibility and Photostability of Octopus Rhodopsin in Thin Films and Application to Photovoltaic Cells

A new biomaterial obtained by means of a new method of extraction and purification of rhodopsin from octopus membranes was presented. It was found that this procedure is faster and cheaper than the method earlier reported (Tsuda et al., 1986). The purity of the resulting biomaterial is not high grade, but the photo induced characteristic measurements highlight that the process of photoreversibility is present in this type of rhodopsin. Furthermore films of octopus rhodopsin were also obtained employing the gel-matrix method with PVAL solution. In these films, the protein

maintains its photocromatic properties and the films can be handed at room temperatures without problems. The ability of octopus rhodopsin to photorecycle and slowly to decay to equilibrium shows that this material has characteristics similar to those observed in the D96N mutant bacteriorhodopsin (Hampp et al., 2002). The observation of the same properties in thin films suggest the possibility to employ this new biomaterial in biomolecular electronic applications, as confirmed by its photovoltaic response.

Molecular switch

The maximal rate of the reverse (photochromic) reaction can be reached at the earliest stages of rhodopsin photolysis, namely, the formation of photo- and bathorhodopsins. We have started work in this field and are actively continuing it (Mozgovaya et al., 2010; Smitienko et al. 2010)). The coherent dynamics of the photoisomerization of 11-*cis* retinal chromophore in bovine rhodopsin was studied with the help of high-resolution laser absorption spectroscopy. A double-pulse system was used to comprehensively examine the absorption spectrum dynamics of the rhodopsin exposed to femtosecond excitation light pulse on a femto–picosecond scale. This study confirmed and refined the coherent nature of the retinal chromophore photoisomerization in the rhodopsin molecule. A specially designed triple-pulse femtosecond laser system allowed us for the first time to record an ultrafast photochromic reversible reaction of rhodopsin in a femtosecond range, namely, the transition of dark-state rhodopsin (11-*cis* retinal) into a primary photoinduced intermediate, photorhodopsin, in its ground electronic state (*trans* retinal) and then a reverse photoinduced transition of photorhodopsin into rhodopsin. Photoreversibility of invertebrate (octopus) rhodopsin is presented in Fig. 15.2.

These studies allowed to demonstrate the possibility of the coherent control of the reverse reaction after the impact of the second light pulse on photorhodopsin in its oscillatory excited state at different time moments. Thus, we were the first to demonstrate the feasibility of the ultrafast photochromic reaction of rhodopsin at room temperature in a manner described in (Schapiro et al., 2011). This result allows the visual pigment rhodopsin to be regarded as a prototype of an ultrafast molecular photoswitch.

Quantum computation

In terms of the application of octR in quantum or optical computations, this work has explored only one of two possible directions, namely, increasing stability and crystallizability of the octR-based systems that are, intrinsically, highly sensitive light sensors. The other option, that is, grafting the properties of octR to the already stable and crystallizable protein, remains to be explored. Our calculations suggest that mutagenesis can practically arbitrarily be used to modify the immediate surroundings of the octR's photosensitive molecule, retinal, thus allowing one to graft the properties of bR to octR and vice versa. This is mostly done by incorporating tryptophans into the vicinity of the retinal, in the same way increasing the protein stability.

The nature of stability of octR in vivo, however, is probably caused by the presence of another protein in addition to octR (possibly RALBP), which should be located in the immediate vicinity to octR in vivo. The presence of this protein can yield better stability and ordering of the octR-based assemblies, including crystals. Obtaining such structures containing rhodopsin and the other retinal-binding protein will give rise to a novel type of optical computation device. Indeed, the key property of bR allowing one to utilize it in optical memory device is its existence in two stable forms. The same property is utilized in the existing optical computer (Lewis et al., 1997), in which two lasers are used to encode signals on bR films, so that the signals can be added and subtracted according to the trinary logic system, where positive unity, negative unity, and zero are designated by a high concentration of purple form, a high concentration of yellow form, and equal amounts of the two forms, respectively. Obviously, this device is purely passive. If regularly structured octR/retinochrome films are obtained, they will contain two different proteins that can be manipulated independently. This will open the road to a new formulation of classical optical computing, now including active optical elements. Considering that the power of nanobiotechnology allows atomic level manipulation of proteins, this could allow embedding quantum computation units into the rhodopsin-based active computation media.

Toward recombinant octopus rhodopsin

Cloning and expression of recombinant octopus rhodopsin protein with the same (or even improved) structural and functional properties is of great interest due to perspective of its biotechnological applications. Attempts for recombinant octopus rhodopsin cloning and expression have already been made (Harada et al., 1991, 1994), but in these studies the yield of full-length rhodopsin with desired optical properties was very low. The problems could be associated with inefficient reconstitution of the full-length protein, which was solubilized from inclusion bodies, and binding of retinal group to wrong lysine residues could also occur. Cephalopod rhodopsins, in comparison to vertebrate rhodopsins, have C-terminal cytoplasmic extension (about 90 amino acid) that is proline-rich. This C-terminal tail could prevent the right folding of recombinant octopus rhodopsin. Absence of this part of protein as it was shown in the study on native octopus rhodopsin (Ashida et al., 2004) did not influence either its optical properties or G-protein activation. That is why cloning and expression of octopus rhodopsin lacking C-terminal region could open a wide avenue for facilitation of production of recombinant octopus rhodopsin with desired structural-functional properties.

Previously, a method for high-yield production in *E. coli* of recombinant bacteriorhodopsin (BR) from *Halobacterium salinarum* was developed (Institute of Bioorganic Chemistry, RAS, Bioengineering Department) (Nekrasova et al., 2010). Expression was based on a hybrid protein approach using Mistic as a carrier for insertion of recombinant bacterio-opsin (bO) into cytoplasmic membrane of *E. coli*. Mistic, a small membrane protein from *Bacillus subtilis* composed of four transmembrane alpha-helices, was shown to enhance expression of a series of eukaryotic membrane proteins, e.g., Kv channels, GPCRs, and others (Kefala et al., 2007; Roosild, 2005). Bacterio-opsin, which was over-expressed in the form of an N-terminal hybrid protein Mistic-bO, was embedded in the plasma membrane and acquired nearly native conformation since it was able to bind exogenuous retinal. Membrane location of the hybrid protein resulted in increased stability of the target protein in the bacterial cell and, furthermore, favored its effective

solubilization in detergents and subsequent reconstitution with retinal in vitro.

This expression system was used by us for cloning and expression of the gene coding for octopus rhodopsin. Basing on the full-length synthetic gene for Octopus dofleini rhodopsin designed by Harada et al. (Harada et al., 1991) we constructed a truncated gene, which encoded a recombinant protein comprising the first 372 amino acid residues of octopus rhodopsin and lacking its C-terminal proline-rich region. We performed codon optimization of existing nucleotide sequence and introduced a number of changes for cloning into expression vector. The Glu372 is the putative site of protease V8 digestion, and it was shown that this digestion did not affect octopus rhodopsin optical properties (Ashida et al., 2004). Besides, the fact that truncated variant of squid rhodopsin (1–360), which is highly homologous to octopus rhodopsin was obtained for crystallization provided additional reason for preparing recombinant octopus rhodopsin lacking its C-terminus (Murakami and Kouyama, 2008). The apoprotein amino acid sequence encoded by truncated synthetic gene is shown in Fig. 15.11.

```
1-50    MVESTTLVNQTWWYNPTVDIHPHWAKFDPIPDAVYYSVGIFIGVVGIIGI
51-100   LGNGVVIYLFSKTKSLQTPANMFIINLAMSDLSFSAINGFPLKTISAFMK
101-150 KWIFGKVACQLYGLLGGIFGFMSINTMAMISIDRYNVIGRPMAASKKMSH
151-200 RRAFLMIIFVWMWSIVWSVGPVFNWGAYVPEGILTSCSFDYLSTDPSTRS
201-250 FILCMYFCGFMLPIIIIAFCYFNIVMSVSNHEKEMAAMAKRLNAKELRKA
251-300 QAGASAEMKLAKISMVIITQFMLSWSPYAIIALLAQFGPAEWVTPYAAEL
301-350 PVLFAKASAIHNPIVYSVSHPKFREAIQTTFPWLLTCCQFDEKECEDAND
351-372 AEEEVVASERGGESRDAAQMKE
```

Figure 15.11 Truncated octopus rhodopsin apoprotein sequence encoded by synthetic gene.

15.5 Conclusion

A set of overlapping oligonucleotides, which corresponded to both DNA strands was synthesized, and these oligonucleotides were annealed and amplified in a polymerase chain reaction, PCR. The

nucleotide sequence of a gene was verified by sequencing, and the gene was further cloned into expression vector. Procedures for purification and reconstitution of functionally active octopus rhodopsin are now under investigation.

With respect to photoreversibility, photostability, and application to photovoltaic cells, a new biomaterial resulting from the isolation of OR starting from octopus photoreceptor membranes was characterized by mass spectroscopy verifying the presence of rhodopsin in the extract. Photoreversibility and photochromic properties were investigated utilizing spectrophotometric measurements and pulsed light. Thin films of octopus rhodopsin were realized, utilizing the gel-matrix entrapment method in polyvinyl alcohol solution. The results indicate that the photoreversibility and the photostability of the octopus rhodopsin in gel-matrices are maintained. Several measurements were performed to test the stability of the resulting biomaterial in time and at room temperature. Preliminary tests demonstrate that the photo reversibility and the photostability are still found after few days from the biomaterial preparation and after the exposure for several hours at room temperature.

For bovine rhodopsin, nanogravimetric and small-angle X-ray diffraction measurements suggest that the assembly of rhodopsin in LB films is similar to that in disc membranes, with the longer dimension perpendicular to the plane of the film, but with the important difference that the molecules of rhodopsin in the LB film are closer together than in the disc membrane. Indeed, each molecule of rhodopsin occupies an area of only about 1000 Å compared with a value of about 3400 Å for the area occupied by rhodopsin and surrounding lipids in the disc membrane. In this kind of artificial monolayer, the molecules of rhodopsin may have lost most of their mobility so as to form a state very similar to a solid state. As the orientation of the retinal chromophore presumably remains the same as in the disc membrane, i.e. with the molecules parallel to the plane of the layer, the close packing of retinal molecules may form the basis for excitonic conductance. This property, together with the high thermal stability of the rhodopsin film, makes this material very interesting for the construction of bioelectronic devices.

In terms of application of octopus rhodopsin for molecular switch, we found possible to incorporate the crude extract of octopus

rhodopsin into sol-gel glass using procedure described previously for incorporation of bR. This procedure does not lead to rhodopsin destruction; however, only one non-photoreversible transition from rhodopsin to alkaline or acid metarhodopsin was observed. Metarhodopsins trigger the enzymatic amplification cascade of phototransduction, while the photoswitch of metarhodopsins back to rhodopsin should stop the activity of the cascade. Then, rhodopsin could be considered as prototype of enzymatic processes photoswitcher.

For application of octR in quantum or optical computations, visual membranes of octopus, whose main component is the light-sensitive signal transducer octopus rhodopsin (octR), are extremely highly ordered, easily capture single photons, and are sensitive to light polarization, which shows their high potential for use as a QC detector. However, artificial membranes made of octR are neither highly enough ordered nor stable, while the bacterial homolog of octR, bR, having the same topology as octR, forms both stable and ordered artificial membranes but lacks the optical properties important for optical QC. In this study, we investigate the structural basis for ordering of the two proteins in membranes. We compare the atomic resolution 3D structures of octR and bR and show the possibility for structural bR/octR interconversion by mutagenesis. We also show that the use of nanobiotechnology can allow (1) high-precision manipulation of the light acceptor, retinal, including converting its surrounding into that of bacterial rhodopsin, the protein already used in optical-computation devices and (2) development of multicomponent and highly regular 2D structures with a high potential for being efficient optical QC detectors.

Overall, considering the functional efficiency and versatility of octopus rhodopsin, its nanobioelectronics application seems plausible, that is, bioelectronics with control at atomic scale. Although usage of OctR is about mostly bioelectronics, it expands also to energy application (see photovoltaic cells below), which is not surprising considering the known use of bR, a close relative of OctR. To ensure atomic scale control, approaches to crystallization and forthcoming 3D structure resolution as suggested in (Sivozhelezov and Nicolini, 2006), should be considered.

References

Antonini M., Ghisellini P., Paternolli C., Nicolini C. (2004). Electrochemical study of the engineerized cytochrome P450scc interaction with free and in lipoproteins cholesterol, *Talanta*, **62**, 945–950.

Applebury, M. L., Zuckerman, D. M., Lamola, A. A., Jovin, T. M. (1974). Rhodopsin: Purification and recombination with phospholipids assayed by the metarhodopsin I metarhodopsin II transition. *Biochemistry*, **13**, 3448–3458.

Ashida, A., Matsumoto, K., Abrey, T. G., Tsuda, M. A. (2004). Purified agonist-activated G-protein coupled receptor: Truncated octopus acid metarhodopsin. *Zoolog*. *Sci*., **21**, 245–250.

Baker, B. N., Williams, T. P. (1971). Photolysis of metarhodopsin I: Rate and extent of conversion to rhodopsin. *Vis*. *Res*., **11**(5), 449–458.

Birge, R. (1995). Protein-based computers. *Sci*. *Am*., **3**, 90–95.

Bownds, D. (1967). Site of attachment of retinal in rhodopsin. *Nature*, **216**, 1178–1181.

Bryl, K. (2003). Visual and archaeal rhodopsins: Similarities, differences, and controversy. *Cell*. *Mol*. *Biol*. *Lett*., **8**, 285–296.

Carrara E., Gavotti, C., Catasti, P., Nozza, F., Berruti-Bergotti, L., Nicolini, C. (1992). Improvement of protein secondary structure prediction by combination of statistical algorithms of circular dichroism. *Arch*. *Biophys*. *Biochem*., 294.1, 107–114.

Chang, C. T., Wu, C.-S. C., Yang, J. T. (1978). Circular dichroic analysis of protein conformation: Inclusion of the, 3-turn. *Anal*. *Biochem*., **91**, 13–31.

Consani, C., Braem, O., Ajdarzadeh Oskouei, A., van der Veen, R. M., ElNahhas, A., Cannizzo, A., Chergui, M. (2011). Ultrafast (Bio) physical and (Bio) chemical Dynamics. *Chim*. *Int*. *J*. *Chem*., **65**(9), 683.

Dratz, E., Hargrave, P. A. (1983). The structure of rhodopsin and the rod outer segment disk membrane. *Trends Biochem*. *Sci*., **8**, 128–151.

Druzhko, A. B., Vanderah, D. J., Robertson, B., Weetall, H. H. (1996). An azulenic bacteriorhodopsin analog has photoinduced activity. *Photochem*. *Photobiol*., **64**, 867–869.

Edwards, P. C., Li, J., Burghammer, M., Hugh McDowell, J., Villa, C., Hargrave, P. A., Schertler, G. F. (2004). Crystals of native and modified bovine rhodopsins and their heavy atom derivatives. *J*. *Mol*. *Biol*., **343**(5), 1439–1450.

Erokhin, V., Facci, P., Nicolini, C. (1994). Two-dimensional order and protein thermal stability: High temperature preservation of structure and function. *Biosens*. *Bioelectron*., **10**, 25–34.

Facci, P., Erokhin V., Nicolini C. (1993). Nanogravimetric gauge for surface density measurement and deposition analysis of Langmuir Blodgett films. *Thin Solid Films*, **231**, 86–89.

Facci, P., Erokhin, V., Nicolini, C. (1994). Scanning tunneling microscopy of a monolayer of reaction centers. *Thin Solid Films*, **243**, 403–406.

Faulon, J. L., Sale, K., Young, M. (2003). Exploring the conformational space of membrane protein folds matching distance constraints. *Protein Sci*., **12**(8), 1750–1761.

Feldman, T. B., Kholmurodov, K. T., Ostrovsky, M. A., Khrenova, M. G., Nemukhin, A. V. (2009). Studies on the conformational state of the chromophore group (11-*cis*-retinal) in rhodopsin by computer molecular simulation methods. *Biophysics*, **54**(4), 465–470.

Feldman, T., Ostrovsky, M., Kholmurodov, K., Yasuoka, K. (2012). Model of abnormal chromophore-protein interaction for E181K rhodopsin mutation: Computer molecular dynamics study. *Open Biochem*. *J*., **6**, 94.

Findlay, J. B., Brett, M., Pappin, D. J. (1981). Primary structure of C-terminal functional sites in bovine rhodopsin. *Nature*, **293**(5830), 314–316.

Fuhrman, J. A., Schwalbach, M. S., Stingl, U. (2008). Proteorhodopsins: an array of physiological roles? *Nat*. *Rev*. *Microbiol*., **6**(6), 488–494.

Gröbner, G., Choi, G., Burnett, I. J., Glaubitz, C., Verdegem, P. J., Lugtenburg, J., Watts, A. (1998). Photoreceptor rhodopsin: Structural and conformational study of its chromophore 11-*cis* retinal in oriented membranes by deuterium solid state NMR. *FEBS Lett*., **422**(2), 201–204.

Grote, M., O'Malley, M. A. (2011). Enlightening the life sciences: The history of halobacterial and microbial rhodopsin research. *FEMS Microbial*. *Rev*., **35**(6), 1082–1099.

Guerette, L., Tessier, M., Boucher, F. (1988). The limited photochemical activity of solid aggregated form of bovine rhodopsin. *Biochem*. *Cell Biol*., **66**, 161–166.

Hampp, N., Fischer, T., Neebe, M. (2002). Bacteriorhodopsin-based photochromic pigments for optical security applications. *Proc*. *SPIE*, **4677**, 121–128.

Hampp, N. (1993). Heat proof protein. *Nature*, **366**, 12.

Hann, R. A. (1990). Molecular structure and monolayer properties. In *Langmuir Blodgett Films*. (Roberts, G., ed.), Plenum Press, New York, pp. 19–22.

Harada, Y., Sakamoto, T., Shinomura, T., Takamoto, K., Senda, T., Tsuda, M. (1991). Total synthesis of a gene for octopus rhodopsin and its preliminary expression. *J. Biochem.*, **110**, 501–507.

Harada, Y., Senda, T., Sakamoto, T., Takamoto, K., Ishibashi, T. (1994). Expression of octopus rhodopsin in *Escherichia coli*. *J. Biochem*, **115**, 66–75.

Hargrave, P. A. (1977). The amino-terminal tryptic peptide of bovine rhodopsin a glycopeptide containing two sites of oligosaccharide attachment. *Biochim. Biophys. Acta (BBA)-Protein Struct.*, **492**(1), 83–94.

Hargrave, P. A., McDowell, J. H., Curtis, D. R., Wang, J. K., Juszczak, E., Fong, S. L., Argos, P. (1983). The structure of bovine rhodopsin. *Biophys. Struct. Mech.*, **9**(4), 235–244.

Hubbell, W. L., Altenbach, C., Hubbell, C. M., Khorana, H. G. (2003). Rhodopsin structure, dynamics, and activation: A perspective from crystallography, site-directed spin labeling, sulfhydryl reactivity, and disulfide cross-linking. *Adv. Protein Chem.*, **63**, 243–290.

Imamoto, Y., Sakai, M., Katsuta, Y., Wada, A., Ito, M., Shichida, Y. (1996). Structure around C6-C7 bond of the chromophore in bathorhodopsin: low-temperature spectroscopy of 6*s*-*cis*-locked bicyclic rhodopsin analogs. *Biochemistry*, **35**(20), 6257–6262.

Israelewitz, B., Izrailev, S., Schulten, K. (1997). Binding pathway of retinal to bacterio-opsin: A prediction by molecular dynamics simulations. *Biophys. J.*, **73**(6), 2972–2979.

Kandori, H., Ichioka, T., Sasaki, M. (2002). Photoisomerization of the rhodopsin chromophore in clay interlayers at 77 K. *Chem. Phys. Lett.*, **354**(3), 251–255.

Kefala, G., Kwiatkowski, W., Esquivies, L., Maslennikov, I., Choe, S., (2007). Application of Mistic to improving the expression and membrane integration of histidine kinase receptors from *Escherichia coli*. *J. Struct. Funct. Genom.*, **8**, 167–172.

Khan, M. A., Bolen, W., Hargrave, P. A., Santoro, M. M., McDowell, J. H. (1991). Differential scanning calorimetry of bovine rhodopsin in rod outer segment disk membranes. *Eur. J. Biochem.*, **200**, 53–59.

Kholmurodov, K. T., Feldman, T. B., Ostrovsky, M. A. (2005). Molecular dynamics simulation and experimental studies on the visual pigment rhodopsin: Multiple conformational states and structural changes (No. JINR-E19-2005-20).

Kholmurodov, K. T., Feldman, T. B., Ostrovsky, M. A. (2006). Visual pigment rhodopsin: A computer simulation of the molecular dynamics of 11-*cis*-retinal chromophore and amino-acid residues in the chromophore centre. *Mendeleev Commun*., **16**(1), 1–8.

Kim, J. (2011). U.S. Patent Application (13/180,668).

Kim, J. E., Mathies, R. A. (2002). Anti-Stokes Raman study of vibrational cooling dynamics in the primary photochemistry of rhodopsin. *J*. *Phys*. *Chem*. *A*, **106**(37), 8508–8515.

Kliger, D. S., Horwitz, J. S., Lewis, J. W., Einterz, C. M. (1984). Evidence for a common BATHO-intermediate in the bleaching of rhodopsin and isorhodopsin. *Vis*. *Res*., **24**(11), 1465–1470.

Korenbrot, J. I., Pramik, M. J. (1977). Formation, structure and spectrophotometry of air-water interface films containing rhodopsin. *J*. *Membr*. *Biol*., **37**, 235–262.

Koutalos, Y., Ebrey, T. G., Tsuda, M., Odashima, K., Lien, T., Park, M. H., Nakanishi, K. (1989). Regeneration of bovine and octopus opsins in situ with natural and artificial retinals. *Biochemistry*, **28**(6), 2732–2739.

Krongauz, V. A., Shifrina, R. R., Fedorovich, I. B., Ostrovskiĭ, M. A. (1975a). Photochromism of visual pigments. I. Formation of isochrome products during reversible transformations of frog rhodopsin. *Biofizika*, **20**(2), 219.

Krongauz, V. A., Shifrina, R. R., Fedorovich, I. B., Ostrovskiĭ, M. A. (1975b). Photochromism of visual pigments. II. Kinetics of photoconversion of frog rhodopsin. *Biofizika*, **20**(3), 419.

Krongauz, V. A., Shifrina, R. R., Fedorovich, I. B., Ostrovskiĭ, M. A. (1975c). Photochromism of visual pigments. III. Comparative study of photoconversions in bovine and frog rhodopsin. *Biofizika*, **20**(3), 426.

Laemmli U. (1970). Cleavage of structural proteins during the assembly of the head of bacteriophage T4. *Nature*, **227**, 680–685.

Lamb, T. D., Collin, S. P., Pugh, E. N. (2007). Evolution of the vertebrate eye: opsins, photoreceptors, retina and eye cup. *Nat*. *Rev*. *Neurosci*., **8**(12), 960–976.

Land, M. F. (2011). Oculomotor behaviour in vertebrates and invertebrates. In *The Oxford Handbook of Eye Movements*, p. 1.

Langmuir, I., Shaefer, V. (1938). Activities of urease and pepsin monolayers. *J*. *Am*. *Chem*. *Soc*., **60**, 1351–1360.

Lewis, A., Albeck, Y., Lange, Z., Benchowski, J., Weizman, G. (1997). Optical computation with negative light intensity with a plastic bacteriorhodopsin film. *Science*, **275**(5305), 1462–1464.

Liang, Y., Fotiadis, D., Filipek, S., Saperstein, D. A., Palczewski, K., Engel, A. (2003). Organization of the G protein-coupled receptors rhodopsin and opsin in native membranes. *J. Biol. Chem.*, **278**(24), 21655–21662.

Lin, S. W., Groesbeek, M., van der Hoef, I., Verdegem, P., Lugtenburg, J., Mathies, R. A. (1998). Vibrational assignment of torsional normal modes of rhodopsin: Probing excited-state isomerization dynamics along the reactive C11-C12 torsion coordinate. *J. Phys. Chem. B*, **102**(15), 2787–2806.

Litman, B. J. (1982). Purification of rhodopsin by concanavalin a affinity chromatography. *Methods Enzymol.*, **81**, 150–154.

Lvov, Y., Erokhin, V., Zaitsev, S. (1991). Protein Langmuir Blodgett films. *Bio. Membr.*, **4**(9), 1477–1513.

Maccioni, E., Radicchi, G., Erokhin, V., Paddeu, S., Facci, P., Nicolini, C. (1996). Bacteriorhodopsin thin film as a sensitive layer for an anaesthetic sensor. *Thin Solid Films*, **284–285**, 898–900.

Maeda, A., Yamazaki, Y., Sasaki, J., Hatanaka, M., Kandori, H., Needleman, R., et al. (1995). Interaction of tryptophan-182 with the retinal 9-methyl group in the L intermediate of bacteriorhodopsin. *Biochemistry*, **34**(2), 577–582.

Mao, B., Tsuda, M., Ebrey, T. G., Akita, H., Balogh-Nair, V., Nakanishi, K. (1981). Flash photolysis and low temperature photochemistry of bovine rhodopsin with a fixed 11-ene. *Biophys. J.*, **35**(2), 543–546.

Martinez, T. J. (2010). Physical chemistry: Seaming is believing. *Nature*, **467**(7314), 412–413.

Maxia, L., Radicchi, G., Pepe, I. M., Nicolini, C. (1995). Characterization of Langmuir-Blodgett films of rhodopsin. *Thermal Stability Stud. Biophys. J.*, **69**, 1440–1446.

Menon, S. T., Han, M., Sakmar, T. P. (2001). Rhodopsin: Structural basis of molecular physiology. *Physiol. Rev.*, **81**(4), 1659–1688.

Mertz, B., Struts, A. V., Feller, S. E., Brown, M. F. (2012). Molecular simulations and solid-state NMR investigate dynamical structure in rhodopsin activation. *Biochim. Biophys. Acta (BBA)-Biomembr.*, **1818**(2), 241–251.

Miedlich, S. U., et al. (2004). Homology modeling of the transmembrane domain of the human calcium sensing receptor and localization of an allosteric binding site. *J. Biol. Chem.*, **279**, 7254–7263.

Mizukami, T., Kandori, H., Shichida, Y., Chen, A. H., Derguini, F., Caldwell, C. G., et al. (1993). Photoisomerization mechanism of the rhodopsin chromophore: Picosecond photolysis of pigment containing 11-*cis*-locked eight-membered ring retinal. *Proc. Nat. Acad. Sci.*, **90**(9), 4072–4076.

Mogilevski, L. Y., Dembo, A. T., Svergun, D. I., Feigin, L. A. (1984). Automatic small-angle x-ray diffractometer with linear position sensitive detector. *Crystallography*, **29**, 587.

Montal, M., Darszon, A., Trissl, H. W. (1977). Transmembrane channel formation in rhodopsin-containing bilayer membrane. *Nature*, **267**, 221.

Mozgovaya, M. N., Smitienko, O. A., Shelaev, I. V., Gostev, F. E., Feldman, T. B., Nadtochenko, V. A., Sarkisov, O. M., Ostrovsky, M. A. (2010). Photochromism of visual pigment rhodopsin on the femtosecond time scale: Coherent control of retinal chromophore isomerization. *Doklady Biochem. Biophys*, **435**, 302–306. Original Russian text © Mozgovaya, M. N., Smitienko, O. A., Shelaev, I. V., Gostev, F. E., Feldman, T. B., Nadtochenko, V. A., Sarkisov, O. M., Ostrovsky, M. A. (2010). Published in *Doklady Akademii Nauk*, 2010, **435**(2), 262–266.

Murakami, M., Kouyama, T. (2008). Crystal structure of squid rhodopsin. *Nature*, **453**, 363–367.

Nadtochenko, V. A., Smitienko, O. A., Feldman, T. B., Mozgovaya, M. N., Shelaev, I. V., Gostev, F. E., Sarkisov, O. M., Ostrovsky, M. A. (2012). Conical intersection participation in femtosecond dynamics of visual pigment rhodopsin chromophore *cis_trans* photoisomerization. *Doklady Biochem. Biophys*., **446**, 242–246. Original Russian text © Nadtochenko, V. A., Smitienko, O. A., Feldman, T. B., Mozgovaya, M. N., Shelaev, I. V., Gostev, F. E., Sarkisov, O. M., Ostrovsky, M. A. (2012). Published in *Doklady Akademii Nauk*, 2012, **446**(4), 460–465.

Nakagawa, M., et al. (1999). How vertebrate and invertebrate visual pigments differ in their mechanism of photoactivation, *Proc. Nat. Acad. Sci. USA*, **96**, 6189–6192.

Nakagawa, M., Kikkawa, S., Iwasa, T., Tsuda, M. (1997). Light-induced protein conformational changes in the photolysis of octopus rhodopsin. *Biophys. J*., **72**, 2320–2328.

Nathans, J. (1992). Rhodopsin: Structure, Function, and Genetics, *Biochemistry*, **31**, 4923–4931.

Nekrasova, O. V., Wulfson, A. N., Tikhonov, R. V., Yakimov, S. A., Simonova, T. N., Tagvey, A. I., Dolgikh, D. A., Ostrovsky, M. A., Kirpichnikov, M. P. (2010). A new hybrid protein for production of recombinant bacteriorhodopsin in *Escherichia coli*. *J. Biotechnol*., **147**, 145–150.

Nicolini, C. (1995). From neural chip and engineered biomolecules to bioelectronic devices: An overview. *Biosens. Bioelectron*., **10**, 105–127.

Nicolini, C., Erokhin, V., Antolini, F., Catasti, P., Facci, P. (1993). Thermal stability of protein secondary structures in L-B films. *Biochim. Biophys. Acta*, **1158**, 273–278.

Nicolini, C., Erokhin, V., Paddeu, S., Paternolli, C., Ram, M. K. (1999). Towards light-addressable transducer bacteriorhodopsin based. *Biosens. Bioelectron*., **14**, 427–433.

Nicolini, C., Erokhin, V., Paddeu, S., Sartore, M. (1998). Towards light-addressable transducer bacteriorhodopsin based. *Nanotechnology*, **9**, 223–227.

Nicolini, C., et al. (1998). Towards light-addressable transducer bacteriorhodopsin based, *Nanotechnology*, **9**, 223–227.

Oesterhelt, D., Brauchle, C., Hampp, N. (1991). Bacteriorhodopsin: a biological material for information processing. *Q. Rev. Biophys*., **24**, 425–478.

Ostrovsky M. A., Feldman T. B. (2012). Chemistry and molecular physiology of vision: light-sensitive protein rhodopsin. *Russ. Chem. Rev*., **81**(11), 1071–1090.

Ostrovsky, M. A., Weetall, H. H. (1998). Octopus rhodopsin photoreversibility of a crude extract from whole retina over several weeks' duration. *Biosens. Bioelectron*., **13**(1), 61–65.

Ovchinnikov, Y. A., Abdulaev, N. G., Feigina, M. Y., Artamonov, I. D., Zolotarev, A. S., Kostina, M. B., et al. (1982). The complete amino acid sequence of visual rhodopsin. *Bioorg. Khim*., **8**, 1011–1014.

Palczewski, K., Kumasaka, T., Hori, T., Behnke, C. A., Motoshima, H., Fox, B. A., Miyano, M. (2000). Crystal structure of rhodopsin: AG protein-coupled receptor. *Sci. Signal*., **289**(5480), 739.

Paternolli, C., Antonini, M., Ghisellini, P., Nicolini, C. (2004). Recombinant cytochrome P450 immobilization for biosensor application. *Langmuir*, **20**, 11706–11712.

Pepe, M., Cugnoli, C. (1992). Retinal photoisomerase: Role in invertebrate visual cells, *J. Photochem. Photobiol. B*, **13**, 5–17.

Pepe, I. M., Cugnoli, C., Schwemer, J. (1990). Rhodopsin reconstitution in bleached rod outer segment membranes in the presence of a retinal-binding protein from the honeybee. *FEBS Lett*., **268**(1), 177–179.

Pepe, I. M., Maxia, L., Nicolini, C. (1996). Properties of Langmuir-Blodgett Films of rhodopsin. *Thin Solid Films*, **284–285**, 739–742.

Pepe, I. M., Nicolini, C. (1996). Langmuir-Blodgett films of photosensitive proteins. *J. Photochem. Photobiol. B: Biol*., **33**, 191–200.

Pepe, I., Ram, M. K., Paddeu, S., Nicolini, C. (1998). Langmuir-Blodgett films of rhodopsin: An infrared spectroscopic study. *Thin Solid Films*, **327–329**, 118–122.

Pignatelli, V., Temple, S. E., Chiou, T. H., Roberts, N. W., Collin, S. P., Marshall, N. J. (2011). Behavioural relevance of polarization sensitivity as a target

detection mechanism in cephalopods and fishes. *Philos. Trans. R. Soc. B: Biol. Sci.*, **366**(1565), 734–741.

Pogozheva, I. D., Kuznetsov, V. A., Livshits, V. A., Fedorovich, I. B., Ostrovskii, M. A. (1985). Light-induced changes in the hydrophilic region of the rhodopsin molecule. EPR spectroscopic study with saturation transfer. *Biol. Membrany*, **2**(9), 880–896.Pogozheva I. D., Lomize A. L., Mosberg H. I. (1997). The transmembrane 7-alpha-bundle of rhodopsin: Distance geometry calculations with hydrogen bonding constraints. *Biophys. J.*, **72**, 1963–1985.

Polli, D., Altoè, P., Weingart, O., Spillane, K. M., Manzoni, C., Brida, D., Cerullo, G. (2010). Conical intersection dynamics of the primary photoisomerization event in vision. *Nature*, **467**(7314), 440–443.

Roosild, T. P., Greenwald, J., Vega, M., Castronovo, S., Riek, R., Choe, S., (2005). NMR structure of Mistic, a membrane-integrating protein for membrane protein expression. *Science*, **307**, 1317–1321.

Rouhani, S., Cartailler, J. P., Facciotti, M. T., Walian, P., Needleman, R., Lanyi, J. K., et al. (2001). Crystal structure of the D85S mutant of bacteriorhodopsin: Model of an O-like photocycle intermediate. *J. Mol. Biol.*, **313**(3), 615–628.

Saam, J., Tajkhorshid, E., Hayashi, S., Schulten, K. (2002). Molecular dynamics investigation of primary photoinduced events in the activation of rhodopsin. *Biophys. J.*, **83**(6), 3097–3112.

Salesse, C., Ducharme, D., Leblanc, R. M., Boucher, F. (1990). Estimation of disk membrane lateral pressure and molecular area of rhodopsin by the measurement of its orientation at the nitrogen water interface from an ellipsometric study. *Biochemistry*, **29**, 4567–4575.

Salgado, G. F., Struts, A. V., Tanaka, K., Fujioka, N., Nakanishi, K., Brown, M. F. (2004). Deuterium NMR structure of retinal in the ground state of rhodopsin. *Biochemistry*, **43**(40), 12819–12828.

Schertler, G. F. (1999). Structure of rhodopsin. *Rhodopsins and Photo-transduction*, 54–69.

Schädel, S. A., Heck, M., Maretzki, D., Filipek, S., Teller, D. C., Palczewski, K., Hofmann, K. P. (2003). Ligand channeling within a G-protein-coupled receptor the entry and exit of retinals in native opsin. *J. Biol. Chem.*, **278**(27), 24896–24903.

Schapiro, I., Melaccio, F., Laricheva, E. N., Olivucci, M. (2011). Using the computer to understand the chemistry of conical intersections. *Photochem. Photobiol. Sci.*, **10**(6), 867–886.

Schapiro, I., Ryazantsev, M. N., Frutos, L. M., Ferré, N., Lindh, R., Olivucci, M. (2011). The ultrafast photoisomerizations of rhodopsin and bathorhodopsin are modulated by bond length alternation and HOOP driven electronic effects. *J. Am. Chem. Soc.*, **133**(10), 3354–3364.

Schertler, G. F. X., Villa, C., Henderson, R. (1993). Projection structure of rhodopsin. *Nature*, **362**, 770–772.

Schoenlein R. W., Peteanu L. A., Mathies R. A., Shank C. V. (1991). The first step in vision: Femtosecond isomerization of rhodopsin. *Science*, **4**, 412–415.

Sekharan, S., Morokuma, K. (2011). Why 11-*cis*-retinal? Why not 7-*cis*-, 9-*cis*-, or 13-*cis*-retinal in the eye? *J. Am. Chem. Soc.*, **133**(47), 19052–19055.

Shelyakin, P. V., Kovarskii, A. L., Kasparov, V. V., Feldman, T. B., Ostrovskii, M. A. (2012). A study of the photoinduced conformational mobility of spin-labeled regenerated rhodopsin by ESR spectroscopy. *Russ. J. Phys. Chem. B*, **6**(6), 694–698.

Shen, Y. C., Safinya, R., Liang, K. S., Ruppert, A. F., Rothschild, K. J. (1993). Stabilization of the membrane protein bacteriorhodopsin to 140°C in two-dimensional films. *Nature*, **366**, 48–50.

Shichi, H. (1971). Circular dichroism of bovine rhodopsin. *Photochem. Photobiol.*, **13**, 499–502.

Singh, D., Hudson, B. S., Middleton, C., Birge, R. R. (2001). Conformation and orientation of the retinyl chromophore in rhodopsin: A critical evaluation of recent NMR data on the basis of theoretical calculations results in a minimum energy structure consistent with all experimental data. *Biochemistry*, **40**(14), 4201–4204.

Sivozhelezov, V., Nicolini, C. (2006). Theoretical framework for octopus rhodopsin crystallization. *J. Theor. Biol.*, **240**(2), 260–269.

Smith, H. G., Stubbs, G. W., Litman, B. J. (1975). The isolation and purification of osmotically intact disk from rod outer segment. *Exp. Eye Res.*, **20**, 211–217.

Smith, S. O. (2010). Structure and activation of the visual pigment rhodopsin. *Ann. Rev. Biophys.*, **39**, 309–328.

Smitienko, O. A., Mozgovaya, M. N., Shelaev, I. V., Gostev, F. E., Feldman, T. B., Nadtochenko, V. A., Ostrovsky, M. A. (2010). Femtosecond formation dynamics of primary photoproducts of visual pigment rhodopsin. *Biochemistry (Moscow)*, **75**(1), 25–35. Original Russian text © Smitienko, O. A., Mozgovaya, M. N., Shelaev, I. V., Gostev, F. E., Feldman, T.

B., Nadtochenko, V. A., Sarkisov, O. M., Ostrovsky, M. A., 2010, published in *Biokhimiya*, 2010, **75**(1), 34–45.

Snowden, R., Snowden, R. J., Thompson, P., Troscianko, T. (2012). *Basic Vision: An Introduction to Visual Perception*. Oxford University Press.

Stryer, L. (1986). Cyclic GMP cascade of vision. *Annu. Rev. Neurosci.*, **9**, 87–119.

Sugihara, M., Buss, V., Entel, P., Elstner, M., Frauenheim, T. (2002). 11-*cis*-retinal protonated Schiff base: Influence of the protein environment on the geometry of the rhodopsin chromophore. *Biochemistry*, **41**(51), 15259–15266.

Sugihara, M., Fujibuchi, W., Suwa, M. (2011). Structural elements of the signal propagation pathway in squid rhodopsin and bovine rhodopsin. *J. Phys. Chem. B*, **115**(19), 6172–6179.

Talbot, C. M., Marshall, J. N. (2011). The retinal topography of three species of coleoid cephalopod: significance for perception of polarized light. *Philos. Trans. R. Soc. B: Biol. Sci.*, **366**(1565), 724–733.

Teller, D. C., Okada, T., Behnke, C. A., Palczewski, K., Stenkamp, R. E. (2001). Advances in determination of a high-resolution three-dimensional structure of rhodopsin, a model of G-protein-coupled receptors (GPCRs). *Biochemistry*, **40**(26), 7761–7772.

Terakita, A., et al. (2004). Counterion displacement in the molecular evolution of the rhodopsin family, *Nat. Struct. Mol. Biol.*, 11, 284–289.

Terakita, A., Hara, R., Hara, T. (1989). Retinal-binding protein as a shuttle for retinal in the rhodopsin-retinochrome system of the squid visual cells. *Vis. Res.*, **29**(6), 639–652.

Thomas, D. D., Stryer, L. (1982). Transverse location of the retinal chromophore of rhodopsin in rod outer segment disc membranes. *J. Mol. Biol.*, **154**(1), 145–157.

Thompson, H. W. (2011). The biological and computational bases of vision. Computational analysis of the human eye with applications, 1.

Trabanino, R. J., et al. (2004). First principles predictions of the structure and function of G-protein-coupled receptors: Validation for bovine rhodopsin. *Biophys. J.*, **86**, 1904–1921.

Tsuda, M., Tsuda, T., Terayama, Y., Fukada, Y., Akino, T., Yamanaka, G., Stryer, L., Katada, T., Ui, M., Ebreyf, T. (1986). Kinship of cephalopod photoreceptor G-protein with vertebrate transduction. *FEBS Lett.*, **198**, 5–10.

Tsuda, M. (1987). Photoreception and phototransduction in invertebrate photoreceptors. *Photochem. Photobiol.*, **45**, 915–931.

Tsukamoto, H., Terakita, A., Shichida, Y. (2005). A rhodopsin exhibiting binding ability to agonist all-*trans*-retinal. *Proc*. *Nat. Acad*. *Sci*. *USA*, **102**(18), 6303–6308.

Unger, V. M., Hargrave, P. A., Baldwin, J. M., Schertler, G. F. (1997). Arrangement of rhodopsin transmembrane α-helices. *Nature*, **389**(6647), 203–206.

Unger, V. M., Schertler, G. F. (1995). Low resolution structure of bovine rhodopsin determined by electron cryo-microscopy. *Biophys*. *J*., **68**(5), 1776–1786.

Verdegem, P. J. E., Bovee-Geurts, P. H. M., De Grip, W. J., Lugtenburg, J., De Groot, H. J. M. (1999). Retinylidene ligand structure in bovine rhodopsin, metarhodopsin-I, and 10-methylrhodopsin from internuclear distance measurements using 13C-labeling and 1-D rotational resonance MAS NMR. *Biochemistry*, **38**(35), 11316–11324.

Wald, G., Durrel, J., St. George, R. C. C. (1950). The light reaction in the bleaching of rhodopsin. *Science*, **17**, 179–182.

Wang, J. K., McDowell, J. H., Hargrave, P. A. (1980). Site of attachment of 11-*cis*-retinal in bovine rhodopsin. *Biochemistry*, **19**(22), 5111–5117.

Yabushita, A., Kobayashi, T., Tsuda, M. (2012). Time-resolved spectroscopy of ultrafast photoisomerization of octopus rhodopsin under photoexcitation. *J*. *Phys*. *Chem*. *B*, **116**(6), 1920–1926.

Yoshizawa, T., George W. (1963). Pre-lumirhodopsin and the bleaching of visual pigments. *Nature*, **197**, 1279–1286.

Zhou, X. E., Melcher, K., Xu, H. E. (2012). Structure and activation of rhodopsin. *Acta Pharmacol*. *Sin*., **33**, 291–299.

Index